A SEISMIC INVESTIGATION OF THE KENYA RIFT VALLEY

by

William John Henry B.Sc.

A thesis submitted for the degree of

Doctor of Philosophy at the University of Leicester

October, 1987

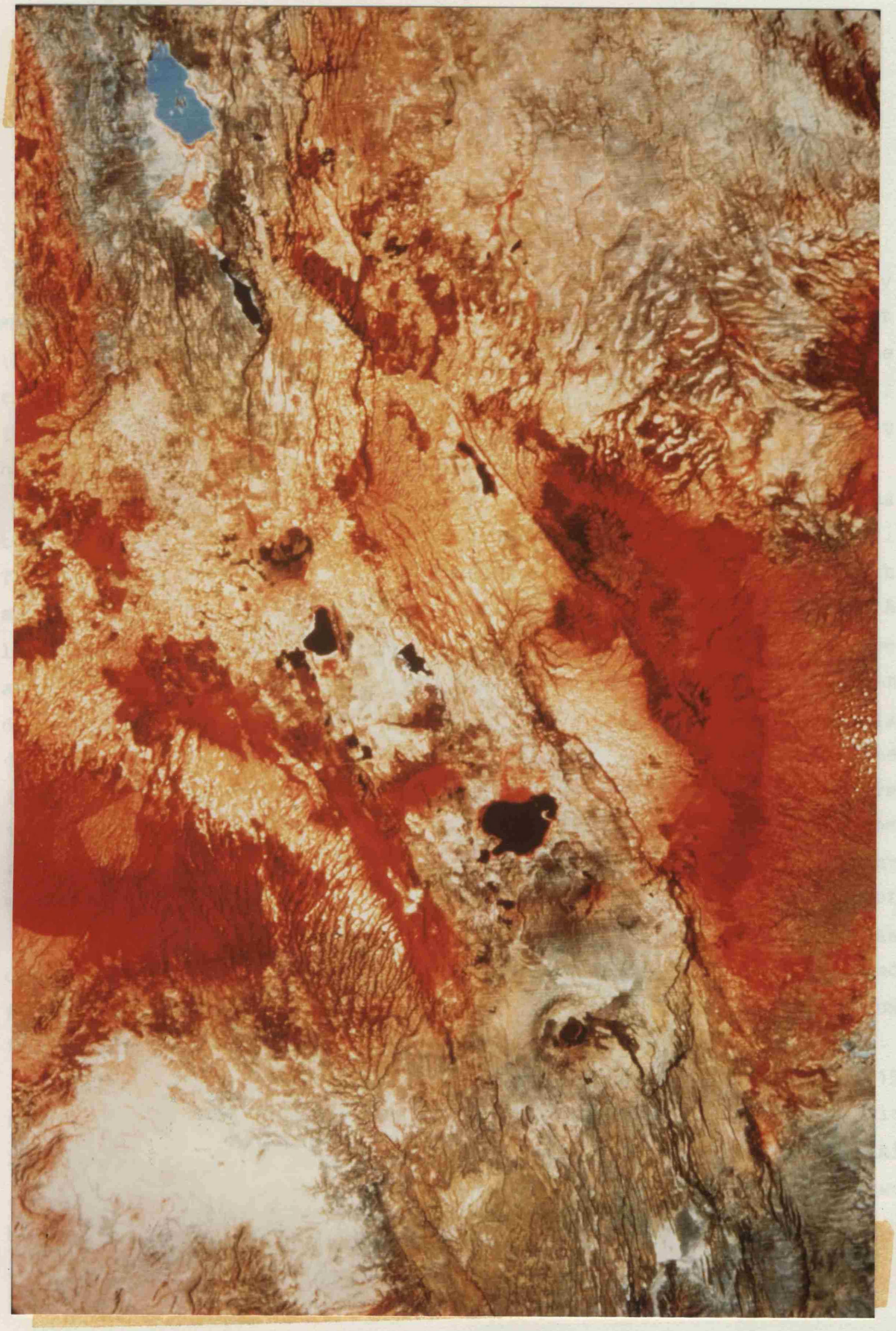

Landsat image of the Kenya rift valley
between Lake Baringo and Lake Magadi

A seismic investigation of the Kenya rift valley

by W.J. Henry

Abstract

In August of 1985 the crustal structure underlying the Kenya rift valley was investigated by long range explosion seismology. The experiment (KRISP85) consisted of two seismic lines in the central sector of the rift, one along the axis (140 km) and the other across it (50 km). Interpretation of the data, including time-term analysis and ray tracing has yielded the following information.

The thickness of rift infill varies from about 6 km below Lake Naivasha to about 2 km and 1.5 km below Lake Magadi and Lake Bogoria respectively. The underlying material has a P-wave velocity of 6.05 $\pm$ 0.03 km/s which suggests the rift is underlain by Precambrian metamorphic basement. A localised high velocity zone identified to the east of Nakuru may be associated with basic intrusive material. The P-wave velocity increases discontinuously to 6.45 $\pm$ 0.05 km/s at a depth of 12.5 $\pm$ 1.0 km. This depth is similar to that inferred for the brittle-ductile transition zone from a study of local seismicity in the Lake Bogoria region. A high P-wave velocity layer (7.1 $\pm$ 0.15 km/s) occurs at 22 $\pm$ 2 km depth which might be associated with a sill-like basic intrusion in the lower crust. An upper mantle velocity of 7.5 $\pm$ 0.2 km/s (unreversed) is reached at a depth of 34.0 $\pm$ 2.0 km. This implies that only moderate crustal attenuation has occurred beneath the central sector of the rift. No evidence was obtained for the existence of an "axial intrusion" reaching to shallow levels below the rift and causing crustal separation as suggested by previous studies.

Relative residuals determined for 46 teleseismic events recorded by a 15 station, small aperture seismic array in the vicinity of Lake Bogoria indicate considerable lateral heterogeneity in the upper crust. An Aki inversion of the relative residuals has revealed the existence of two distinct low velocity zones which may be associated with magma chambers.

ACKNOWLEDGEMENTS

This work was sponsored by the Natural Environmental Research Council.

I would like to thank:

My supervisors, Pete Maguire and Aftab Khan, for their encouragement and advice during the last three years and for their critical reading of the manuscript.

Don Griffiths, Jim Davies and Thomas Kitavi for providing excellent company during three months of preparatory work in Kenya.

Everyone involved in the implementation of the KRISP85 explosion programme.

Philippa Cooke and Nick Lafolley for keeping the Lake Bogoria array up and running for three months.

Jim Mechie for his invaluable advice on many aspects of explosion seismology.

Martin Higham for the programming and data processing he has carried out during this study.

Ian Hill, Jaafar Ali, Philippa Cooke, Martin Higham, Rob Young, Alan Pointing, Annabel Bowker, Shona Grant, Mike Norry, Dave Quirk, Hans-Albert Dalheim, Verney Green, Chris Swain, Tim Sugden, Dave Martill and Tony Rex for useful discussion.

Bill Teasdale, Paul Coward, Sue Button, Ann Montgomery and all the other technical and clerical staff of the Leicester University Geology Department.

The staff of the Leicester University Computing Centre and Central Processing Unit for their assistance.

Margaret Ansell for her critical reading (sometimes over critical) of the manuscript and all her support during the writing of this thesis.

All my friends and colleagues at Leicester University for making the last three years so enjoyable.

CONTENTS

INTRODUCTION 1

Chapter 1 : GEOLOGICAL AND GEOPHYSICAL REVIEW OF THE KENYA RIFT VALLEY

1.0 Introduction 3
1.1 The East African Rift System 3
1.2 The volcanic evolution of the Kenya rift 6
1.3 The tectonic history of the Kenya rift 9
1.4 Geophysical studies of the Kenya rift 11
1.4.1 Seismicity 12
1.4.2 Heat flow 13
1.4.3 Crustal structure 13
1.4.4 Upper mantle structure 20
1.5 Estimates of extension 21
1.6 Mechanisms of rifting 23
1.6.1 Low angle detachment systems 23
1.6.2 Diapiric injection and reverse decollements 25

Chapter 2 : THE KRISP85 EXPLOSION PROGRAMME

2.0 Introduction 27
2.1 Aims of the explosion programme 27
2.2 Locations of the seismic lines 28
2.3 Surveying 32
2.3.1 EW-line 32
2.3.2 NS-line 31
2.3.2 Accuracies of station locations and elevations .. 35
2.4 Shot points 35
2.5 Recording equipment 39
2.6 Timing 40
2.7 Huddle tests 41
2.8 Logistics 41

Chapter 3 : PROCESSING AND METHODS OF INTERPRETATION OF REFRACTION DATA

3.0 Introduction 42
3A.1 Digitising and merging 43
3A.2 Processing of Geostore data 43

3A.3 Filtering 44
3A.3.1 Frequency filtering 44
3A.3.1.1 Spectral analysis 44
3A.3.1.2 Bandpass filtering 48
3A.3.2 Polarisation filtering 48
3A.3.2.1 Theory of REMODE filtering 52
3A.3.2.2 Choice of REMODE filter parameters 53
3A.3.2.3 Effectiveness of REMODE filter 55
3A.4 Picking of first arrival times 56
3A.4.1 Sources of observational errors 56
3A.4.2 Aids to the picking of first arrivals 56
3A.4.3 Error estimation 57
3A.5 Recovery of amplitude information 59
3A.5.1 Determination of scaling factors 59
3A.5.2 True amplitude plotting 61

3B.1 Least squares analysis 62
3B.2 Ray tracing using SEIS81 62
3B.2.1 Theory of 2-point ray tracing 63
3B.2.1.1 Medium with a continuous velocity function 63
3B.2.1.2 Geometrical spreading 64
3B.2.1.3 First order interface 65
3B.2.1.4 Source characteristics 66
3B.2.2 Operation of SEIS81 67
3B.2.3 Example of SEIS81 in use 67
3B.3 Time-term analysis 69
3B.3.1 Theory of time-term analysis 69
3B.3.2 Example of the time-term method 72

<u>Chapter 4</u> : INTERPRETATION OF THE REFRACTION DATA

4.0 Introduction 75
4.1 NS-line interpretation 76
4.1.1 Phase correlations 76
4.1.2 Analysis of uppermost crustal phases 76
4.1.3 Analysis of Pg phase 85
4.1.4 Upper crustal high velocity zone 87
4.1.5 Time-term analysis of basement refraction 89
4.1.6 Modelling of shallow velocity structure by ray tracing 93

4.1.7 Description of later phases 98
4.1.8 Modelling of deep velocity structure by ray tracing. 99
4.2 Reinterpretation of some KRISP75 data 107
4.3 EW-line interpretation 110
4.3.1 Interpretation of shots EWA and NTU 110
4.3.2 Interpretation of shots SU1 and MAR 116
4.4 S-wave analysis 117

Chapter 5 : SHOT EFFICIENCIES AND DIURNAL NOISE VARIATION STUDY

5.0 Introduction 122
5.1 Shot point efficiencies 122
5.2 Study of diurnal noise variation 136
5.3 Recommendations for future refraction experiments in the area 142

Chapter 6 : INTERPRETATION OF TELESEISMIC EVENTS RECORDED BY THE LAKE BOGORIA ARRAY

6.0 Introduction 143
6.1 Local geology and description of the seismic network .. 144
6.2 Teleseismic events 146
6.3 Measurement of absolute and relative arrival times 147
6.4 Calculation of absolute and relative residuals 155
6.5 Discrimination between core phases 159
6.6 Absolute residuals 160
6.7 Relative residuals 163
6.8 Aki inversion method 168
6.9 Inversion of the teleseismic data 170
6.10 Results of Aki inversion 173

Chapter 7 : DISCUSSION

7.1 The depth to basement 179
7.2 The nature of the basement 180
7.3 The existence of the axial intrusion 184
7.4 The origin of reflection B. Brittle-ductile transition zone? 187
7.5 Intrusion in the lower crust 190
7.6 Crustal thickness below the rift 191

Chapter 8 : CONCLUSIONS AND RECOMMENDATIONS

8.1 Conclusions 192
8.2 Recommendations 193

Appendices

A First arrival times 194
B Computer programs 200
C Relative residuals and Aki inversion output 206

References 216

LIST OF FIGURES

CHAPTER 1

1.1 Map of Africa showing Afro-Arabian Rift System 4

1.2 Map of East Africa showing the Kenya dome and Kenya rift valley 5

1.3 Geological map of Kenya. Overlay shows major faults that delineate rift valley 7

1.4 Miocene to Recent volcanism of the Kenya rift valley 8

1.5 Fault pattern of the Kenya rift valley (after Baker et al, 1972) 10

1.6 Velocity models determined for the Kenya rift valley and its flanks 14

1.7 Location map of previous seismic experiments in the vicinity of the Kenya rift valley 16

1.8 Bouguer anomaly across the Kenya rift valley at latitude 1.1°S showing regionals of Searle (1970) and Fairhead (1976) (after Fairhead, 1976) 18

1.9 Teleseismic delay times observed in Kenya 22

1.10(a) Schematic cross section through the Baringo-Bogoria subbasin of the Kenya rift (after Bosworth, 1986) 24

1.10(b) Morphotectonic interpretation of the Kenya rift valley (after Bosworth, 1986) 24

1.11 Stages in Mohr's hypothesis for rifting in Ethiopia and Kenya (after Mohr, 1987) 26

CHAPTER 2

2.1 Bouguer gravity anomaly map showing locations of KRISP85 seismic refraction lines 29

2.2 Location map of KRISP85 seismic refraction experiment showing lines and shot points 30

2.3 Location map of KRISP85 seismic refraction experiment showing station locations and access roads 31

CHAPTER 3

3.1(a) Three vertical component recordings of the Baringo 1 shot with accompanying energy spectra of noise and seismic signal 45

3.1(b) Three vertical component recordings of the Baringo 2 shot with accompanying energy spectra of noise and seismic signal 46

3.1(c) Three vertical component recordings of the Naivasha shot with accompanying energy spectra of noise and seismic signal 47

3.2(a) Unfiltered portion of the Baringo record section 49

3.2(b) Portion of the Baringo record section after the application of a 0.5 - 20.0 Hz bandpass filter 49

3.2(c) Portion of the Baringo record section after the application of a 0.5 - 15.0 Hz bandpass filter 50

3.2(b) Portion of the Baringo record section after the application of a 0.5 - 10.0 Hz bandpass filter 50

3.3 Three component records from stations 18 and 35 of the second Baringo shot with accompanying ground motion plots .. 51

3.4 Rotation required to obtain $\bar{z}$ and $\bar{r}$ components. The particle motions of incident P and SV waves are shown along side 52

3.5 Six examples of the signal enhancement resulting from the application of the REMODE polarisation filter 54

3.6 The effect of angle of rotation on signal enhancement resulting from REMODE filtering 55

3.7 A.C. contaminated traces before and after "A.C. removal" ... 58

3.8 Vertical component recordings of the second Susua huddle test shot 60

3.9 Ray-tracing diagrams and reduced velocity plots obtained from the KRISP68 velocity model 68

3.10 Raypath of a refracted arrival 70

3.11 Ray-tracing diagrams and reduced velocity plots for 4 simulated shots into a simple velocity model 73

3.12 Depths determined by the time-term method after: (a) 1 iteration; and (b) 2 iterations 74

CHAPTER 4

4.1(a) Baringo 1 record section (NS-line) 77

4.1(b) Baringo 1 record section - stations near Lake Magadi (NS-line) 78

4.2 Baringo 2 record section (NS-line) 79

4.3 Naivasha record section (NS-line) 80

4.4 Chepkererat record section (NS-line) 81

4.5 Solai record section (NS-line) 82

4.6 Elmenteita record section (NS-line) 83

4.7 Magadi record section (NS-line) 84

4.8 Planar P-wave velocity models for the NS-line 86

4.9 Velocity vs width of the HVZ for a travel time advance of 0.18 secs 88

4.10 Time-term depths determined for the NS-line 92

4.11 Shallow P-wave velocity model determined from ray-tracing for the NS-line 94

4.12(a) Observed and synthetic travel times for the Baringo 1 shot and accompanying ray tracing diagram (Vr = 6 km/s) 95

4.12(b) Observed and synthetic travel times for the Baringo 2 shot and accompanying ray tracing diagram (Vr = 6 km/s) 95

4.12(c) Observed and synthetic travel times for the Naivasha shot and accompanying ray tracing diagram (Vr = 6 km/s) 96

4.12(d) Observed and synthetic travel times for the Magadi shot and accompanying ray tracing diagram (Vr = 6 km/s) 96

4.12(e) Observed and synthetic travel times for the Chepkererat shot and accompanying ray tracing diagram (Vr = 6 km/s) 97

4.12(f) Observed and synthetic travel times for the Solai shot and accompanying ray tracing diagram (Vr = 6 km/s) 97

4.13 Three classes of velocity-depth functions which gave arrival times consistent with those observed 101

4.14 Synthetic seismograms generated for models 1, 2 and 3 of figure 4.13 102

4.15 Synthetic seismogram and ray tracing diagram for the Baringo shots 104

4.16 Synthetic seismogram and ray tracing diagram for the Naivasha shot 105

4.17 Synthetic and observed amplitude ratios for the Baringo 2 shot 106

4.18 Map showing location of KRISP75 NS-line with overlay showing extent of alluvial deposits 108
4.19 Reduced velocity plots of the shots fired into the KRISP75 NS-line 109
4.20 Ewaso Ngiro record section (EW-line) 111
4.21 Ntulelei record section (EW-line) 112
4.22 Susua 1 record section (EW-line) 113
4.23 Mt Margaret record section (EW-line) 114
4.24 Schematic velocity cross-section showing results obtained from the EW-line 115
4.25 Baringo 2 S-wave record section (NS-line) 118
4.26 Naivasha S-wave record section (NS-line) 119
4.27 Chepkererat S-wave record section (NS-line) 120
4.28 Ewaso Ngiro S-wave record section (EW-line) 121

CHAPTER 5

5.1 True amplitude record section for the Baringo 2 shot 123
5.2 Map showing the locations of shot points used in the KRISP68, KRISP75 and KRISP85 experiments 125
5.3 Amplitude vs scaled distance plot for various shot points .. 126
5.4 Diurnal variation of r.m.s. noise for 11 of the Lake Bogoria network stations 138
5.5 Histograms of r.m.s. noise levels for 03:00 - 06:00 hours and 06:00 - 09:00 hours 141

CHAPTER 6

6.1 Map showing locations of the Lake Bogoria network 144
6.2 Epicentres of the 46 teleseismic events used in this study on a zenithal equidistant map of the world 149
6.3(a) Vertical component records of event 39 150
6.3(b) Vertical component records of event 41 151
6.3(c) Vertical component records of event 35 152
6.4 Diagram showing the relative arrival times measured for events VAN1, VAN2 and VAN3 using methods (1), (2) and (3) .. 154
6.5 Ray paths of core phases bottoming in the outer core (branches BC and AB) and those passing through the inner core (branch DEF) (after Morrelli and Dziewonski, 1987) 159

6.6 Form of the travel time curves for core phases between epicentral distances 140 and 152 degrees 161
6.7 Mean relative residuals calculated for events observed by the Lake Bogoria network 165
6.8 Diagram showing blocks sampled by incident teleseismic waves recorded at two receiving stations (After Aki et al, 1977) . 169
6.9(a) Contoured velocity perturbations for layer 2 174
6.9(b) Contoured velocity perturbations for layer 3 175
6.9(c) Contoured velocity perturbations for layer 4 176

CHAPTER 7

7.1 Bouguer gravity anomaly for stations 20 to 31 of the NS-line 183
7.2 Hypocentre locations and focal depths of local earthquakes recorded by the Lake Bogoria seismic array 188

INTRODUCTION

During 1985 the Kenya rift valley was the site of four seismic investigations: one explosion seismology programme followed by three passive seismic monitoring programmes. Collectively, they are known as KRISP85 (Kenya Rift International Seismic Project, 1985). This study is based on data arising from two of the above: (1) the explosion seismology programme and (2) the Lake Bogoria Earthquake Project involving recording from a temporary, small aperture, 15 station seismic array. The contents of the eight chapters are summarised below.

Chapter 1 - Geological and geophysical review of the Kenya rift valley.

Previous geological and geophysical studies of the Kenya rift are reviewed. This serves as a basis for later comparison with the results of this study.

Chapter 2 - The KRISP85 explosion programme.

This is dedicated to a comprehensive account of the implementation of the explosion seismology programme. It includes details of the seismic lines, the shot points used, their survey and the instrumentation used.

Chapter 3 - Processing and methods of interpretation of the refraction data.

This chapter is divided into two parts: 3A and 3B. The first part deals with the processing of the data obtained from the explosion programme. The second part consists of descriptions of the various methods used to interpret the refraction data.

Chapter 4 - Interpretation of refraction data.

The KRISP85 record sections are presented and an account is given of how time-term analysis and ray theoretical forward modelling were used to obtain P-wave velocity information for the crust and upper mantle beneath the rift.

Chapter 5 - Shot efficiencies and diurnal noise variation study.

One of the aims of the KRISP85 explosion seismology programme was to gain experience for a larger scale experiment planned for the future. This chapter deals with some of the lessons learned from KRISP85 as regards the choice of shot points and charge sizes and the optimum time for shooting.

Chapter 6 - Interpretation of teleseismic events recorded by the Lake Bogoria seismic array.

An account is given of the determination of relative residuals for 46 teleseismic events recorded by the Lake Bogoria seismic array. The Aki inversion method is used to invert the relative residuals determined for P-wave velocity structure below the array.

Chapter 7 - Discussion.

Results from Chapters 4, 5 and 6 are put into a geological context. Comparison is made with previous studies in the area and existing models proposed for the rift valley are critically examined.

Chapter 8 - Conclusions and recommendations.

This includes a very brief summary of the most important conclusions made and a few suggestions for further work.

CHAPTER (I)

GEOLOGICAL AND GEOPHYSICAL REVIEW OF THE KENYA RIFT VALLEY

1.0 Introduction.

This introductory chapter comprises a review of current geological and geophysical understanding of rifting in East Africa. Emphasis is placed on aspects of rifting most relevant to this study, thus providing a basis for later comparison. It is divided into six sections:

(1.1) The location of the Kenya rift within the East African Rift System.

(1.2) Volcanic history.

(1.3) Structural history.

(1.4) Previous geophysical studies.

(1.5) Estimates of extension.

(1.6) Mechanisms of rifting.

Since Kenya's independence several place names have changed which could lead to some confusion. In this thesis the more recent names are used whenever possible. Thus what was formerly "Lake Rudolf" is referred to as "Lake Turkana", "Lake Hannington" is referred to as "Lake Bogoria", the "Kavirondo rift" is referred to as the "Nyanza trough" and the "Gregory rift" itself is referred to as the "Kenya rift".

1.1 The East African Rift System.

The Cainozoic Rift System of East Africa comprises a series of rift "zones" (Rosendahl, 1987) stretching approximately 3200 km from the Afar Triple Junction at the Red Sea - Gulf of Aden intersection to the Zambesi River in Southern Africa (Fig. 1.1). It is normally considered to be a continental extension of the world-wide rift system (Rothe, 1954; Baker and Wohlenberg, 1971; McKenzie et al, 1970) being associated with a zone of shallow seismicity continuous with the Gulf of Aden and hence the Carlsberg Ridge of the NW Indian Ocean.

The physiographic character of the system varies considerably along its length. In the north a single rift valley, the Ethiopian rift, transects the Ethiopian dome, separating the Ethiopian plateau to the west from the Somalian plateau in the east. The bifurcation of the rift system in the vicinity of Lake Victoria results in the formation of eastern and western branches (Fig. 1.2). This bifurcation has been attributed to the Tanganyikan Shield, which shows EW structural trends, acting as a resistant block and deflecting the rifting to either side (McConnel,

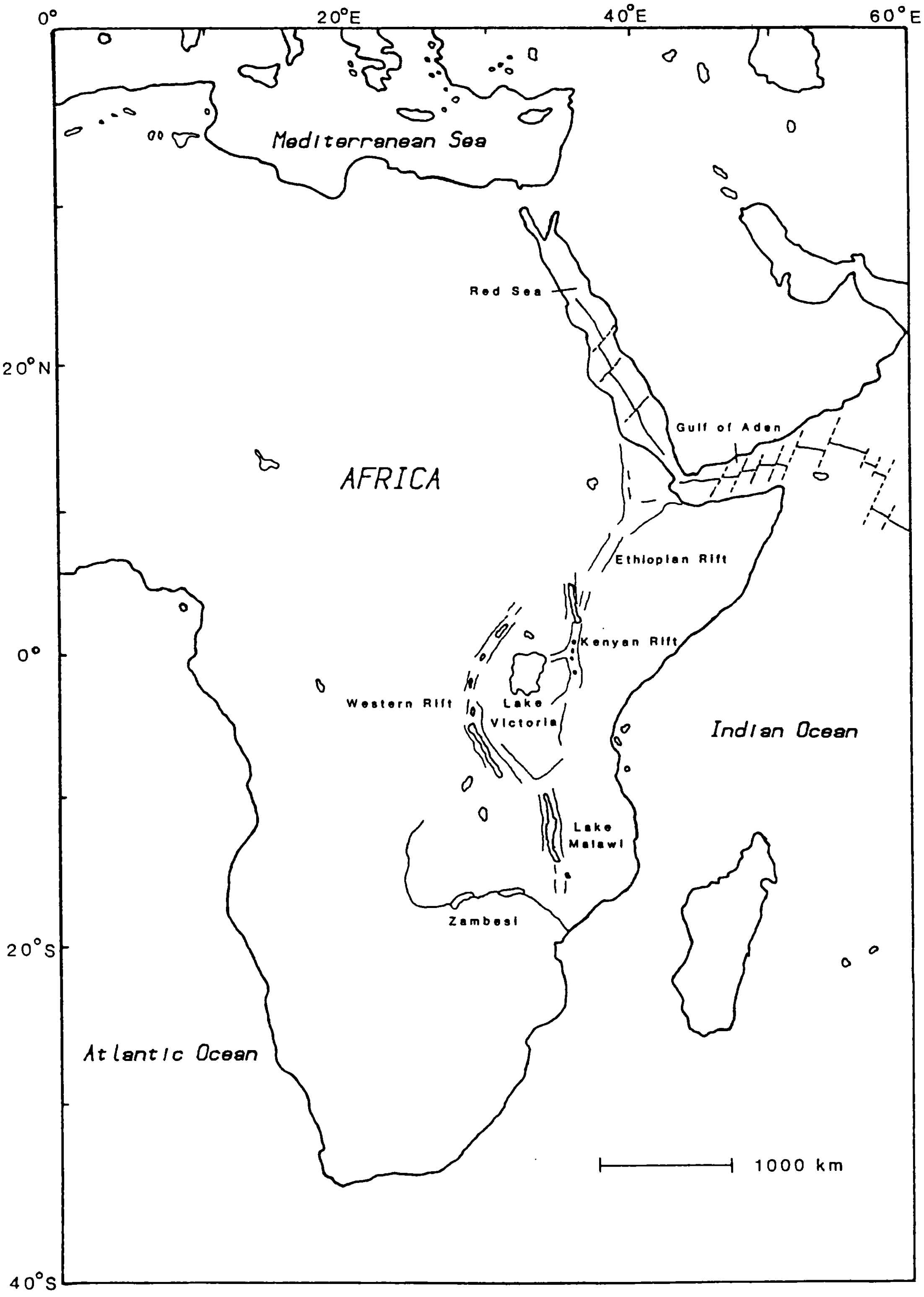

Figure 1.1 : Map of Africa showing Afro-Arabian Rift System.

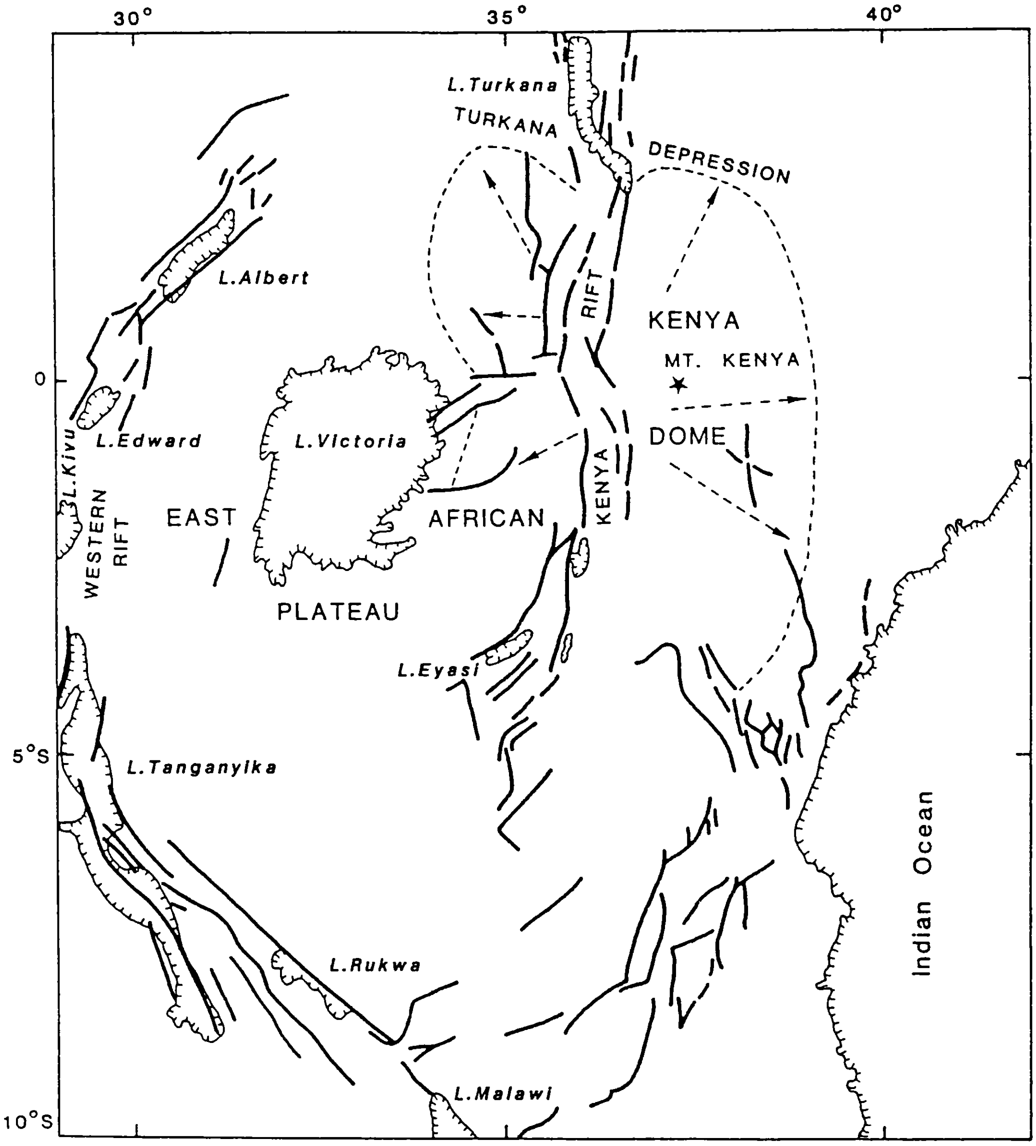

Figure 1.2 : Map of East Africa showing Kenya dome and Kenya rift valley.

1967). The Malawi rift to the south has much in common with the western branch and is often considered to be an extension of it (Rosendahl, 1987). Volcanism and faulting patterns are also highly variable: Along the eastern branch volcanism has been voluminous making it one of the worlds "wettest" rifts, whereas there has been little volcanic activity associated with the western branch (Mohr, 1982).

This study is concerned with the Kenya rift valley, a section of the eastern branch that transects the Kenya dome, a local culmination of the East African plateau (Fig. 1.2). Between latitudes $2^{o}S$ and $2^{o}N$ (approx 450 km) the rift valley approximates to a fault-bounded graben, of width between 50 km and 70 km and topographic relief of up to 2 km. To the north and south, however, the fault structures splay out over widths of 200 km or more and it loses its graben like appearance (King, 1978). The Precambrian basement underlying the rift can be subdivided into the Tanganyikan Shield to the west of $35.5^{o}E$ and the younger Mozambique Belt to the east. In the vicinity of the rift it is overlain by thick piles of Cainozoic volcanics and lake sediments, the volcanics extending well beyond the rift boundaries (Fig. 1.3).

1.2 The volcanic evolution of the Kenya rift.

The volcanic history of the Kenya rift has been documented by numerous authors (Baker and Wohlenberg, 1971; Baker et al, 1972; Logatchev et al, 1972; King and Chapman, 1972; King, 1978). In order to summarise this information it is convenient to divide the complex series of events into 5 major phases of volcanic activity (Fig. 1.4). This may in some instances lead to over simplification but is sufficiently detailed for this particular study.

(1) 23 - 16 Ma.

The first volcanism of the region occurred in the north of Kenya when the subsidence of the Lake Turkana region was accompanied by voluminous basaltic fissure eruptions resulting in the Samburu and Turkana basalts. Further to the west there was contemporaneous but autonomous alkaline-carbonatitic activity giving rise to volcanoes in the vicinity of the Kenya-Uganda border (e.g. Mt Elgon) and the Nyanza trough.

(2) 13.5 - 10 Ma.

Volcanism shifted southwards as highly mobile plateau phonolites were extruded over a large part of central Kenya. The area covered is roughly coextensive with that of the Kenya dome. Activity originated within the

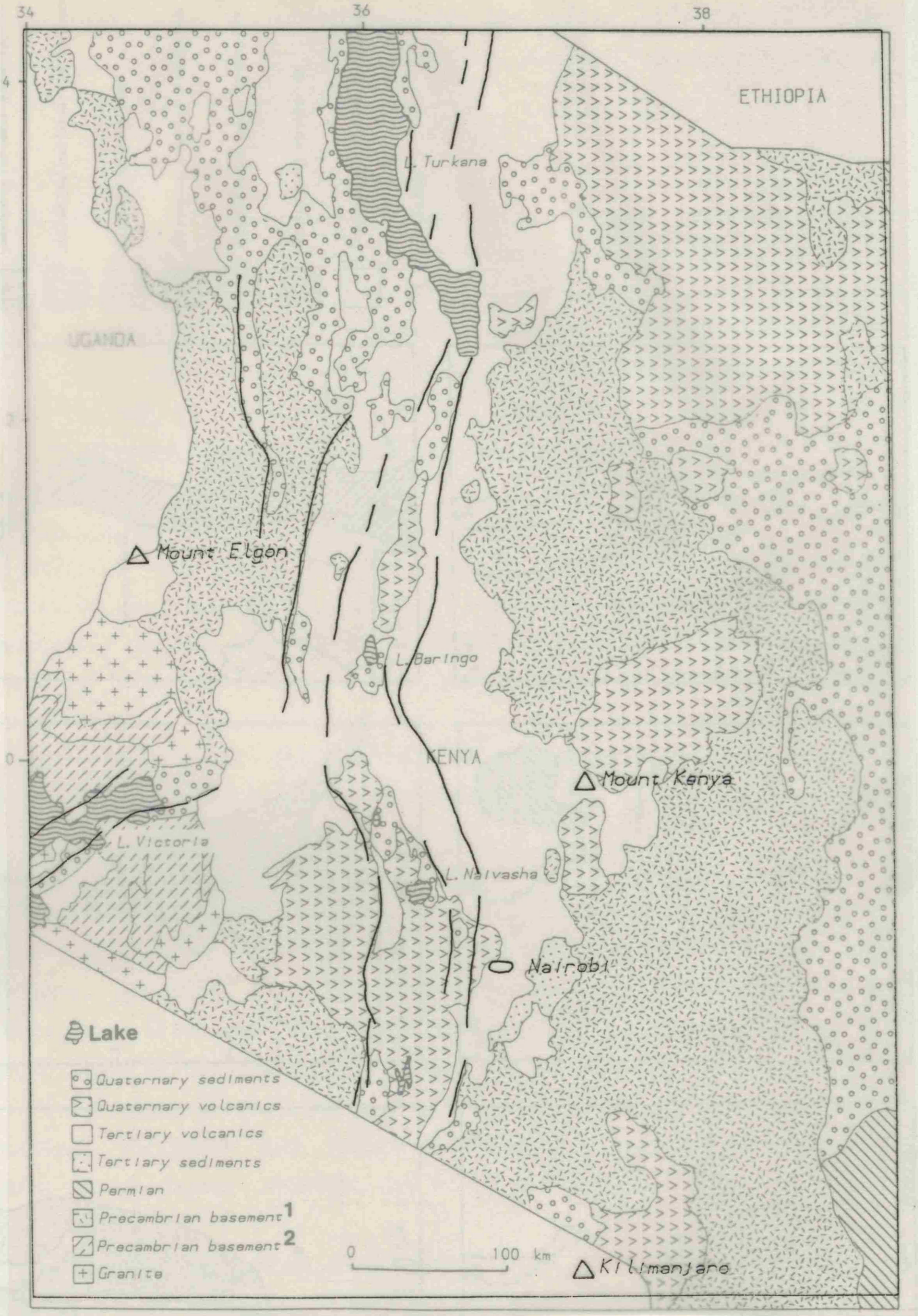

1 : Mozambique Belt

2 : Tanganyika Shield

Figure 1.3 : Geological map of Kenya. Overlay shows major faults that delineate rift valley.

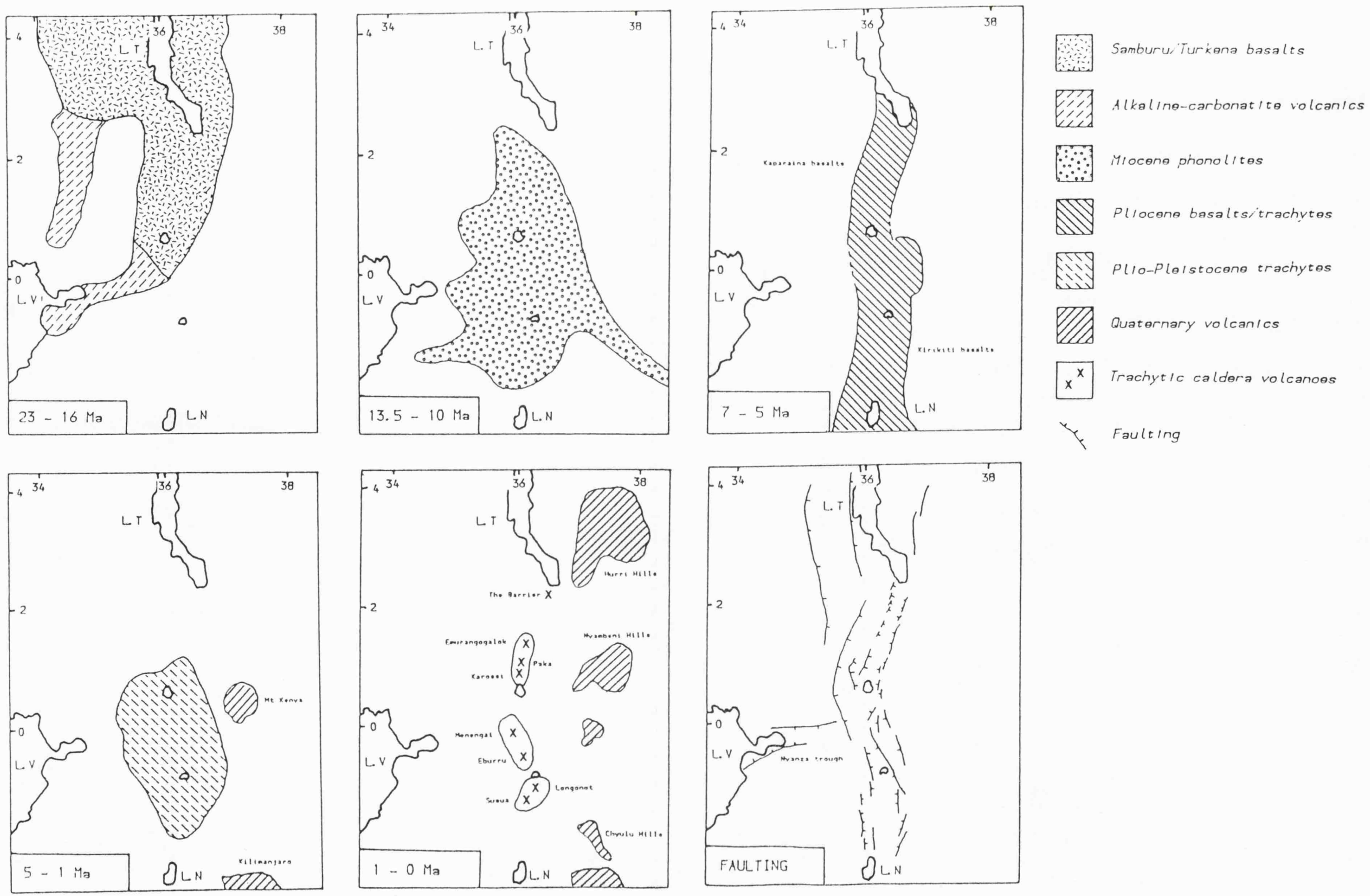

Figure 1.4 : Miocene to Recent volcanism of the Kenya rift valley.

proto-rift zone but infilling of the early rift depression allowed flooding over the flanks to occur. Magmatic productivity was at its highest during this period.

(3) 7 - 5 Ma.

Following the eruption of the Miocene plateau phonolites there was a period of major fault development forming a N-S asymmetric trough. Flood basalts and trachytes were then erupted and confined mainly to the trough. These basalts are called the Kaparaina basalts and the Kirikiti basalts in the north and south respectively. There is some disagreement about the precise age of this basalt series. Logatchev (1972) dates them as 5.0 - 2.0 Ma whereas King and Chapman (1972) give an age of 6.5 - 5.0 Ma.

(4) 5 - 1 Ma.

Most of the floor of the central and southern parts of the rift is occupied by lavas and tuffs of trachytic composition. Tuffs and, less commonly, lavas also occur on the flanking plateaus. This series can be broadly divided into a lower part made up of tuffs and an upper part composed mainly of trachyte lavas.

Mount Kenya and Kilimanjaro, built up of phonolites, trachytes and basalts, are late Pliocene - Pleistocene in age (3.5 - 2.0 Ma).

(5) 1 - 0 Ma.

When fissure type eruptions ceased, volcanism along the rift floor disintegrated into several areas of mainly trachytic caldera volcanoes (Susua, Longonot, Eburru, Menengai, Karossi, Paka, Emuruangogalok and The Barrier). Eruptions were often violent giving rise to pyroclastics which cover much of the present day rift floor and western escarpment.

The remaining Quaternary activity involved the development of large central volcanoes and basalt lava fields to the east of the rift giving rise to the Chyulu, Nyambeni and Hurri Hills (Fig. 1.4).

1.3 The tectonic history of the Kenya rift.

The oldest tectonic features of the area are of lower Miocene age. Uplift of the regions surrounding the present day Ugandan escarpment and Nyanza trough occurred with complementary subsidence forming the Turkana depression and the generation of the Turkwel Fault (fig. 1.5). Three major episodes of rift faulting have been documented (Baker et al, 1972; Logatchev et al, 1972; King, 1978). The first took place in late Miocene (7 Ma) and was responsible for the development of the Elgeyo Fault and the

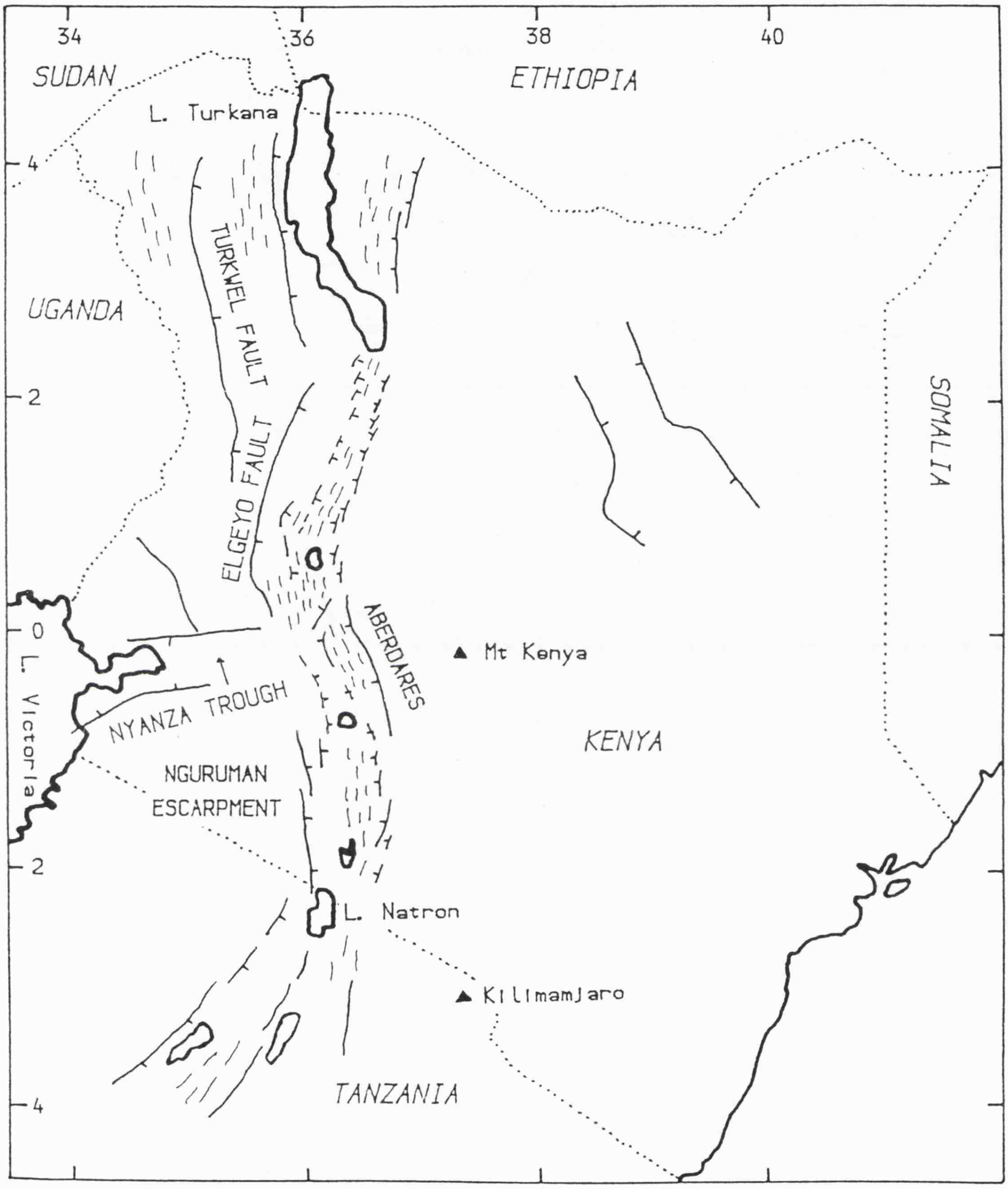

Figure 1.5 : Fault pattern of the Kenya rift valley (after Baker et al, 1972).

Nyanza trough faulting. It was most marked in the north where it was confined mainly to the western side of the present day rift, resulting in the development of an asymmetrical trough. The current morphology of the rift resulted largely from the second episode of faulting during late Pliocene (2.0 - 1.5 Ma) which incorporated rejuvenation of existing faults, more extensive marginal faulting on both the eastern and western sides and intense fracturing of the crust at the northern and southern extremities of the rift. Finally, around 0.5 Ma, grid faulting inside the rift produced numerous minor faults, aligned parallel with the axis of the rift, forming miniature graben and horsts. Such faulting has continued until present day as is evident from recent seismicity studies (e.g. Pointing et al, 1985).

Virtually all faults are normal, dip-slip (Baker, 1958; Baker, 1963), with throws ranging from kilometres (3.5 km for the Elgeyo Fault) to a few metres (Pleistocene grid faulting). Rift margins are formed by various modes of faulting including major boundary faults, downwarps and stepped faults. Bosworth et al (1986) noted that cross sections of the rift are half graben in form with much larger throws on one margin than the other and that the sense of this asymmetry tends to alternate along the rift producing the lazy "S" configuration observed (Fig. 1.5). He identified three "detachment systems" (Elgeyo, Aberdare and Nguruman) (Fig. 1.10) separated by "accommodation zones". These are described in more detail in section 1.6 when mechanisms of rifting are discussed.

The Kenya dome is a striking topographic high. The highest part of the rift floor, near Lake Naivasha, is 1.4 km higher than the southern sector, south of Lake Magadi, and 1.7 km higher than Lake Turkana in the north. There is some dispute as to whether the raised topography is due mainly to epeirogenic uplift or to the massive accumulation of volcanics. Using evidence from erosion surfaces, Baker et al (1972) suggested that there have been three phases of epeirogeny since Miocene amounting to about 2000 m of uplift. King (1978), however, concluded that the raised topography is more a reflection of volcanic accumulation than of vertical uplift. This theory is supported by recent work on the mechanisms of isostatic compensation operating in the vicinity of the Kenya rift (Betchel et al, 1987).

1.4 Geophysical studies of the Kenya rift.

Numerous geophysical methods have been employed to help constrain models of the rift. These include microearthquake studies, teleseismic studies, gravity surveys, explosion seismology profiles, a magnetotelluric experiment, a geomagnetic deep sounding experiment, heat flow measurements and an aeromagnetic survey. The most recent review of geophysical studies carried out was written by Pointing (1985). It is convenient for the work to be described under the following headings: (1) Seismicity, (2) Heat flow, (3) Crustal structure and (4) Upper mantle structure.

1.4.1 Seismicity.

In a review of the seismicity associated with the East African Rift System, Fairhead and Stuart (1982) suggested that it is influenced by the structural trends of the Precambrian basement geology, following the mobile belts that surround older, more stable, cratons. Evidence from several detailed microseismicity studies in the vicinity of the Kenya rift indicates that tensile strain is being released predominantly by microearthquake activity along the axial zone of the rift. For example, 389 microearthquakes were detected during 7 months of recording at an array in Northern Kenya (Pointing, 1985). The majority of these events were confined to the rift with a more diffuse zone about 150 km to the east of it. Hamilton et al (1973) detected 169 events in 7 months recording at several sites along the rift floor between Lakes Naivasha and Bogoria. Some of these were found to be associated with known geothermal areas and many were linearly distributed along the rift floor faults. Shah (1986) collated all the teleseismic events associated with the the eastern and the western rift zones. It was confirmed that the western rift is more active, in terms of teleseismic events, than the Kenya rift. Activity along the Kenya rift was found to be maximum at about $3^{o}S$, decreasing northwards. This lack of teleseismic activity in northern Kenya has been suggested as evidence for the presence of hot, igneous material at shallow depth along the rift acting as a 'lubricant', allowing strain energy to be released by microseismic activity (Fairhead and Stuart, 1982).

Focal mechanisms derived by Cooke (1987) and Shudofsky (1984) indicate normal faulting with the least compressive stress orientated predominantly east - west, i.e. normal to the rift orientation. Shudofsky (1985) concluded that earthquakes associated with the East African Rift System can have focal depths as great as 25 - 30 km. Such observations were confined to the western branch and the northern and southern extremities of the eastern branch.

Cooke (pers. comm.) has located around 600 local earthquakes recorded by a 15 station array in the vicinity of Lake Bogoria. Most of the focal depths were found to lie above 12 km below sea level but a small number of events of low frequency yielded focal depths of up to 25 km.

1.4.2 Heat flow.

Heat flow measurements across the Kenya rift have been reported by Morgan (1973), Williamson (1975) and Morgan and Wheildon (1981). Morgan (1982) summarises the results as follows:

rift floor : mean heat flow = 105 ± 51 mW m^{-2}

rift flanks : mean heat flow = 52 ± 17 mW m^{-2}

It is evident that there is a significant heat flow anomaly across the rift. The high standard deviation obtained for the rift floor measurements shows the heat flow pattern to be erratic, indicative of a thermal regime dominated by recent volcanism and hydrothermal circulation along faults (Morgan, 1982). The values obtained for the rift flanks are similar to those determined for the coastal region of East Africa (Evans and Tammemagi, 1974; Williamson, 1975).

1.4.3 Crustal stucture.

Away from zones of rifting the crustal structure of East Africa appears to be that expected for normal stable shield areas (Gumper and Pomeroy, 1970; Mueller and Bonjer, 1973; Long et al, 1972). The "AFRIC" model (Fig. 1.6(a)) determined by Gumper and Pomeroy (1970) can be considered as a standard against which other models can be compared.

Several seismic investigations have contributed to current knowledge of crustal structure of the Kenya rift valley, the results of which are summarised in figure 1.6.

(1) Rykounov et al (1972) recorded microearthquakes in the southern part of the rift between Lake Magadi, Kenya and Mount Hanang, Tanzania (Fig. 1.7). Using the relative arrival times of different phases observed, a 2 layer crustal model (35 - 37 km thick) was determined (Fig. 1.6(b)).

(2) Bonjer at al (1972) investigated the crustal structure of the eastern flank under Nairobi. Crustal response ratios were determined by spectral analysis of long period body waves and compared with synthetic ratios for various models. A 2 layer crust (42 km thick) gave best agreement (Fig. 1.6(c)).

(3) The crustal structure below Nairobi was also investigated by Herbert and Langston (1985) using teleseisms. The relative arrival times of observed P and P_s conversions were compared with those obtained synthetically from horizontally layered models. A crustal thickness

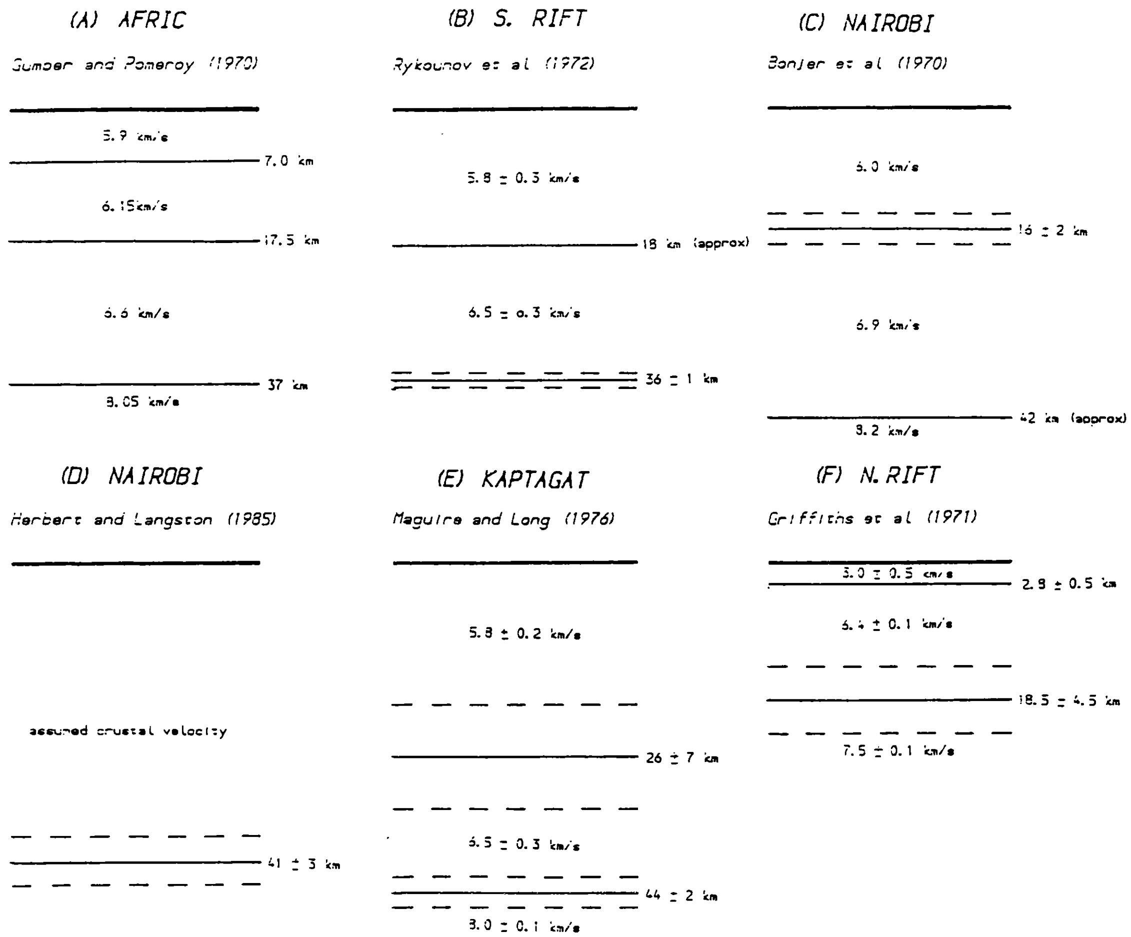

Figure 1.6 : Velocity models determined for the Kenya rift valley and its flanks.

of 41 $\pm$ 3 km was obtained, assuming reasonable crustal velocities (Fig. 1.6(d)).

(4) Analysis of first arrivals of local and regional earthquakes recorded by a seismic array on the western rift flank at Kaptagat (Fig. 1.7) provided a crustal model across the rift margin (Maguire and Long, 1976). It was concluded that shield crust of normal thickness occurs below Kaptagat (Fig. 1.6(e)), separated from anomalously high velocity material beneath the rift by a steep structural boundary.

(5) Griffiths et al (1971) reported the results of a seismic refraction experiment conducted in the rift. It consisted of a reversed line located approximately along the rift axis with end shot points at Lake Bogoria and Lake Turkana and 10 fine element receiving arrays at about 20 km intervals (Fig. 1.7). Although the line was reversed, first arrivals observed from Turkana were almost certainly from a deeper layer than those from Bogoria and thus the velocities obtained are apparent and interpretation was limited to the determination of a horizontally layered model. The crustal structure determined is quite different from any of the other models (Fig. 1.6(f)). A high crustal velocity (6.4 km/s) is present at relatively shallow depth and highest velocity measured is only 7.5 km/s which occurs at a depth of 18.5 km. The occurrence of the 6.4 km/s layer at such shallow depth has often been cited as evidence for the presence of a linear, basic intrusion running along the axis of the rift (Baker et al, 1972; Maguire and Khan, 1980; Swain et al, 1981).

(6) Swain et al (1981) describe a small-scale seismic refraction experiment designed to confirm the presence of the 6.4 km/s layer found by Griffiths et al (1971) and if possible establish its lateral extent. It comprised 2 lines, the first running from Lake Baringo to Chebloch Gorge (50 km west) and the second from Lake Baringo to Lake Bogoria (35 km south) (Fig. 1.7). Results from the first line only have been fully documented (Swain, 1979; Swain et al, 1981). A 2 layer interpretation indicated a near constant refractor velocity of about 5.7 km/s with an overburden whose velocity varies between 2.35 km/s and 3.7 km/s. The 5.7 km/s velocity was attributed to metamorphic basement and the lower velocities to Cainozoic volcanics and lake sediments. It should be

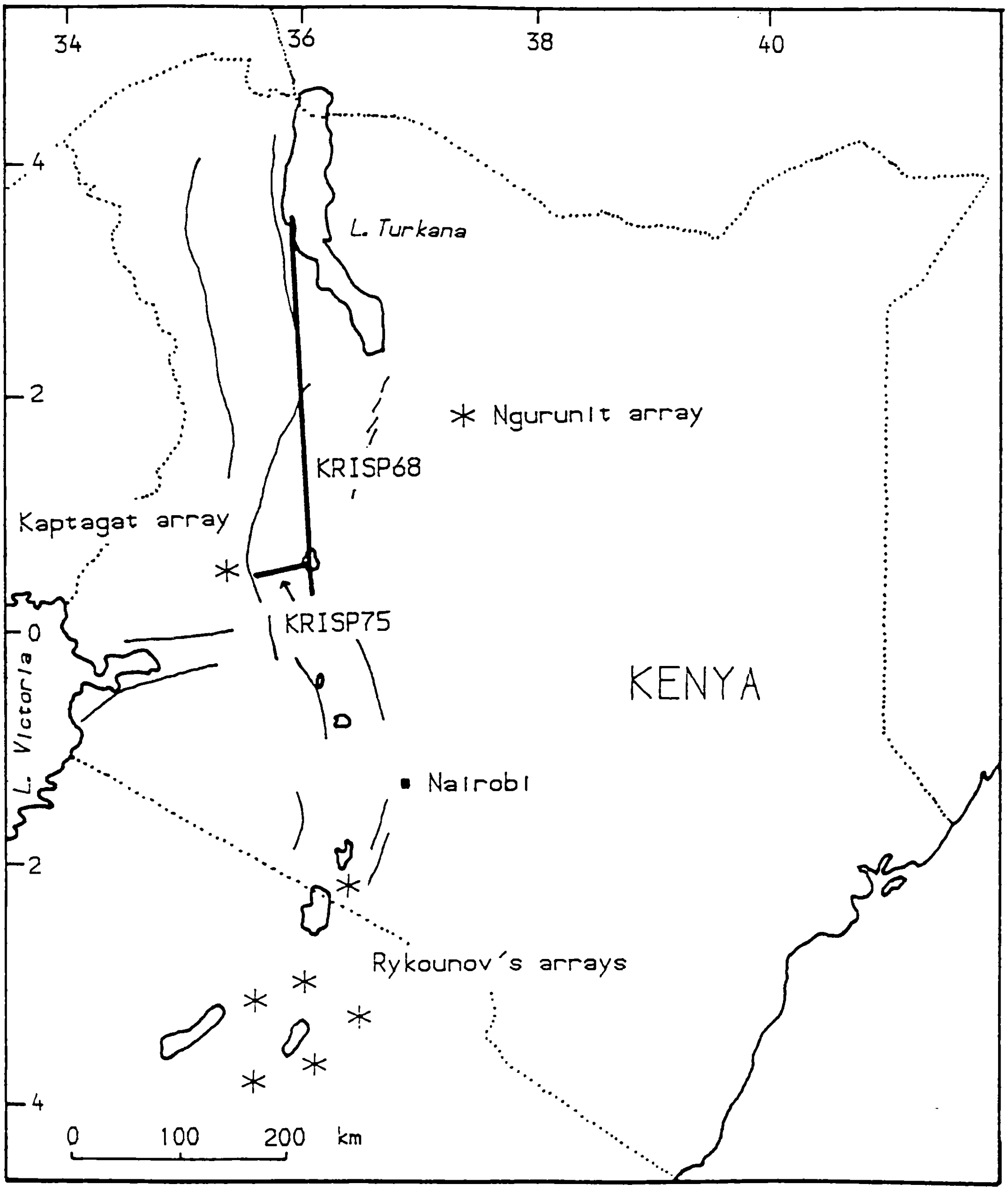

Figure 1.7 : Location map of previous seismic experiments in the vicinity of the Kenya rift valley.

noted that no velocity higher than 5.7 km/s was detected.

(7) Pointing (1985) used the apparent velocities of local and regional events recorded at the Ngurunit array, N. Kenya, (Fig. 1.7) to determine crustal structure. A 2 layer crustal model was derived. The velocity of the upper crustal layer increases linearly with depth (Z) according to the function $V = 5.8 + 0.024Z$ while the velocity of the lower layer is 6.5 ± 0.2 km/s. The interface between the 2 layers has a depth of approximately 24 km. The variation of apparent velocities of P_n with azimuth suggested that the Moho is dipping to the east at about 7°. The depth of the Moho was calculated to be about 46 km and the velocity of the sub-Moho material to be 8.3 ± 0.2 km/s.

Several authors have attempted to use gravity profiles across the rift to model crustal structure. McCall (1967) was the first to note the existence of a positive residual Bouguer anomaly over the axis of the rift near Menengai. This "axial high" is superimposed on the longer wavelength gravity low associated with the Kenya dome, which will be discussed in the next section.

Searle (1970) investigated the gravity field associated with the rift floor and shoulders between 0.25°N and 1.5°S. The axial high was found to be a continuous feature of 40 - 80 km width and 300 - 600 g.u. amplitude. Searle concluded that the geophysical and geological data are best satisfied if the anomaly is due to a dense intrusion of mantle derived material about 20 km wide and reaching to within 3 km of the surface.

Baker and Wohlenberg (1971) reinterpreted one of Searle's profiles across the rift valley, just to the south of Menengai. Their much quoted model includes a high density intra-crustal wedge, the top of which is 10 km wide and about 1.5 km below sea level under the inner graben. They suggested the body could represent a wedge shaped, basic intrusive mass.

Fairhead (1976) revised the regional Bouguer anomaly used by Searle (1970) which resulted in the amplitude of the positive residual anomaly within the rift being reduced by more than 50%. The regional Bouguer anomaly was assumed by Fairhead to follow the observed Bouguer anomaly over the exposed sections of the Precambrian basement both east and west of the rift (Fig. 1.3). Over the Cainozoic volcanics and sediments associated with the rift, it was assumed to be a smooth interpolation of the regional on either side (Fig. 1.8). The resulting negative lobes were attributed to substantial thicknesses of low density pyroclastics on the rift shoulders. Fairhead suggested that the reduced positive anomaly could be due to the presence of considerable thicknesses of dense basaltic lavas

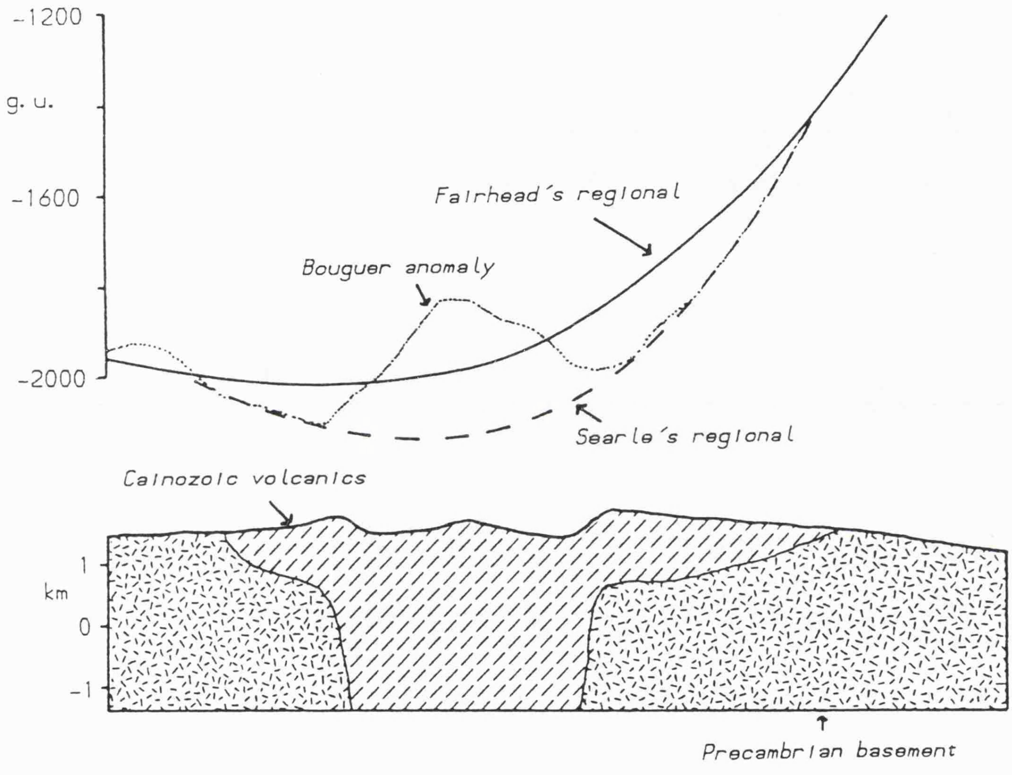

Figure 1.8 : Bouguer anomaly across the Kenya rift valley at latitude 1.1 S showing regionals of Searle (1970) and Fairhead (1976) (after Fairhead, 1976).

buried beneath the rift floor (Section 1.2). However the non-uniqueness of gravity interpretation prevented Fairhead from differentiating between the axial intrusion model and the basaltic infill model.

Swain et al (1981) interpreted 2 gravity profiles across the rift at 0.5^{o}N and 1.0^{o}N, the first of which included the KRISP75 seismic line for control. Once the gravitational effect of the overlying volcanics and sediments (derived from the seismic and geological data) had been removed, a 50 km wide, 340 g.u. positive anomaly remained. It was explained by a "lopolith" type of basic intrusion, 20 - 30 km broad and of 4 - 6 km vertical extent, within the basement.

Darracott et al (1972) interpreted a gravity survey over the rift in southern Kenya and northern Tanzania. The axial high was found to persist as far as about 2^{o}S. An interpretation similar to that of Searle's was chosen, the positive anomaly being explained by a gabbroic intrusion of about 10 km width reaching to within 4 km of the surface.

Geomagnetic anomalies over the rift valley have been mapped by both aerial and ground magnetic surveys. The aeromagnetic surveys (Wohlenberg and Bhatt, 1972) were flown over the Lake Magadi and Menengai areas at average ground clearances of 1000 and 600 metres respectively. The objective was to ascertain whether it is possible to detect the presence of the axial intrusion, suggested by gravity, using magnetic methods. In both regions, but particularly around Menengai, NW - SE trending anomalies were identified. The source of these anomalies was considered to be deep beneath the rift zone but no precise mechanism was offered. The most important result was the lack of any evidence supporting the existence of the axial intrusion. Wohlenberg (1975) has carried out ground magnetic surveys of the vertical and total magnetic field between 2°S and 1°N. The 8 profiles are characterised by numerous short wavelength anomalies. Only after smoothing did they show any correlations with the aeromagnetic profiles. Wohlenberg considered that negative anomalies observed trending NW - SE through Menengai could be due to "magnetic gaps" in the volcanic infill caused by local upwarps of the Curie isotherm, presumably lying above hot dyke intrusions. The one ground profile in the Magadi area was considered to show a distinct anomaly coinciding roughly with the positive residual gravity anomaly observed by Darracott et al (1972).

Other techniques employed to study the crustal structure include magnetotellurics ..(Rooney and Hutton, 1977) and geomagnetic deep sounding (Banks and Beamish, 1979). The magnetotelluric study, consisting of 10 measuring locations in and around the rift between the equator and 1°S, indicated the presence of not less than 5 km thickness of conductive material at a depth of less than 8 km beneath the rift floor. The only reasonable explanation for such a large volume of highly conducting upper crustal rock was considered to be the presence of electrolytic fluids in rock pores and fissures. To satisfy the long period data, conductive material was also required at depths of greater than 30 km which was thought to probably correspond to the upper mantle. The geomagnetic deep sounding experiment consisted of a grid of over 20 magnetometers in and around the rift between 0.5°N and 1.0°S. The existence of 2 zones of high conductivity associated with the rift was revealed. The shallower zone was confined to lie directly beneath the rift floor, with its upper surface no deeper than 20 km but perhaps as shallow as 5 km. The deeper conductor was found to lie at a depth of about 100 km, to the east of the rift below the Aberdare Mountains and possibly extending as far as Mount Kenya.

1.4.4 Upper mantle structure.

It has long been recognised that the mantle underlying the Kenya rift valley is anomalous.

Gravity surveys, the first of which was carried out by Bullard (1936), have indicated that the East African plateau is associated with a broad, negative Bouguer anomaly about 1000 km wide and reaching its maximum amplitude of approximately -1000 g.u. in the vicinity of the eastern branch. Several workers have produced models to explain the negative anomaly (Sowerbutts, 1969; Girdler et al, 1969; Searle, 1970; Baker and Wohlenberg,1971; Khan and Mansfield, 1971; Darracott et al,1972; Fairhead, 1976). The models differ in detail but all include the presence of anomalously low density upper mantle material, i.e. they are consistent with lithospheric attenuation or asthenospheric upwarp.

Using the reasonable gravity coverage available for Kenya, Banks and Swain (1978) were able to rigorously examine isostasy. By computing the isostatic response function (Lewis and Dorman, 1970) for the area they concluded that the Kenya dome is compensated by a region of low density mantle, the top of which being no deeper than 55 km.

The KRISP68 experiment (Griffiths et al, 1971) indicated the presence of 7.5 km/s material at about 20 km depth (Fig. 1.6) which was attributed to anomalous upper mantle material. The Kaptagat array data (Maguire and Long, 1976) also favoured a lower velocity (7.1 km/s) below the rift than below the flanks. Rayleigh wave dispersion studies (Sundaralingham, 1971; Knopoff and Schlue, 1972) of reversed paths between Addis Ababa and Nairobi (approximately along the eastern branch) indicated anomalously low shear wave velocities in the upper mantle (4.25 - 4.65 km/s) compared with the average value of 4.65 km/s for the continent, reported by Gumper and Pomeroy (1970). Slowness anomalies determined from teleseismic arrivals recorded at the Kaptagat array (Long and Backhouse, 1975) suggest a lateral variation in velocity associated with the steeply dipping upper surface of the low velocity zone.

Teleseismic delay times have been measured by several workers (Long et al, 1972; Long and Backhouse, 1975; Savage and Long, 1985; Pointing, 1985) The results of these studies are summarised in figure 1.9. It is evident that the Kenya dome is associated with large positive delays. This is consistent with the presence of low velocity mantle material beneath the rift. Positive delays over the rift were also observed in teleseismic studies carried out by U.C.L.A. and Wisconsin University (Green and Meyer, 1986; Dalheim and Davis, 1986) as part of the KRISP85 programme though final results have not yet been published.

Savage and Long (1985) used relative delay times observed across the rift (Fig. 1.9) to model the low velocity zone which they assumed to have a velocity of 7.5 km/s. Smaller positive delays observed at the centre of the rift were interpreted as indicating that the anomalous zone actually penetrates the crust to form an intrusion of relatively high velocity material along the rift axis, reaching to within about 20 km of the surface. It was stated that the 30 km width of the intrusion at the base of the crust was well constrained by the data. A reinterpretation of the data by Long (1987), using tomographic inversion, suggested that the smaller positive delays observed over the rift are the result of a 20 km wide, high velocity feature concentrated in the top 20 km of the lithosphere and not in the lower crust as previously suggested. This interpretation was said to be more consistent with the positive residual gravity anomaly.

1.5 Estimates of extension.

McKenzie et al (1970) considered the East African rift system and the Afar triple junction in terms of oceanic plate tectonics theory. The relative motion between the plates on either side of the system, Nubia and Somalia, was obtained from estimates for the opening rates of the Red Sea and Gulf of Aden. This scheme predicted crustal extension of 65 km and 30 km across the eastern rift in Ethiopia and Kenya respectively. Searle (1970) claimed that gravity data from the Kenya rift supported such an estimate for extension. His interpretation of the positive residual anomaly (axial high) comprised dense intrusions of mantle derived material, between 16 and 28 km wide, having "filled the gap between the

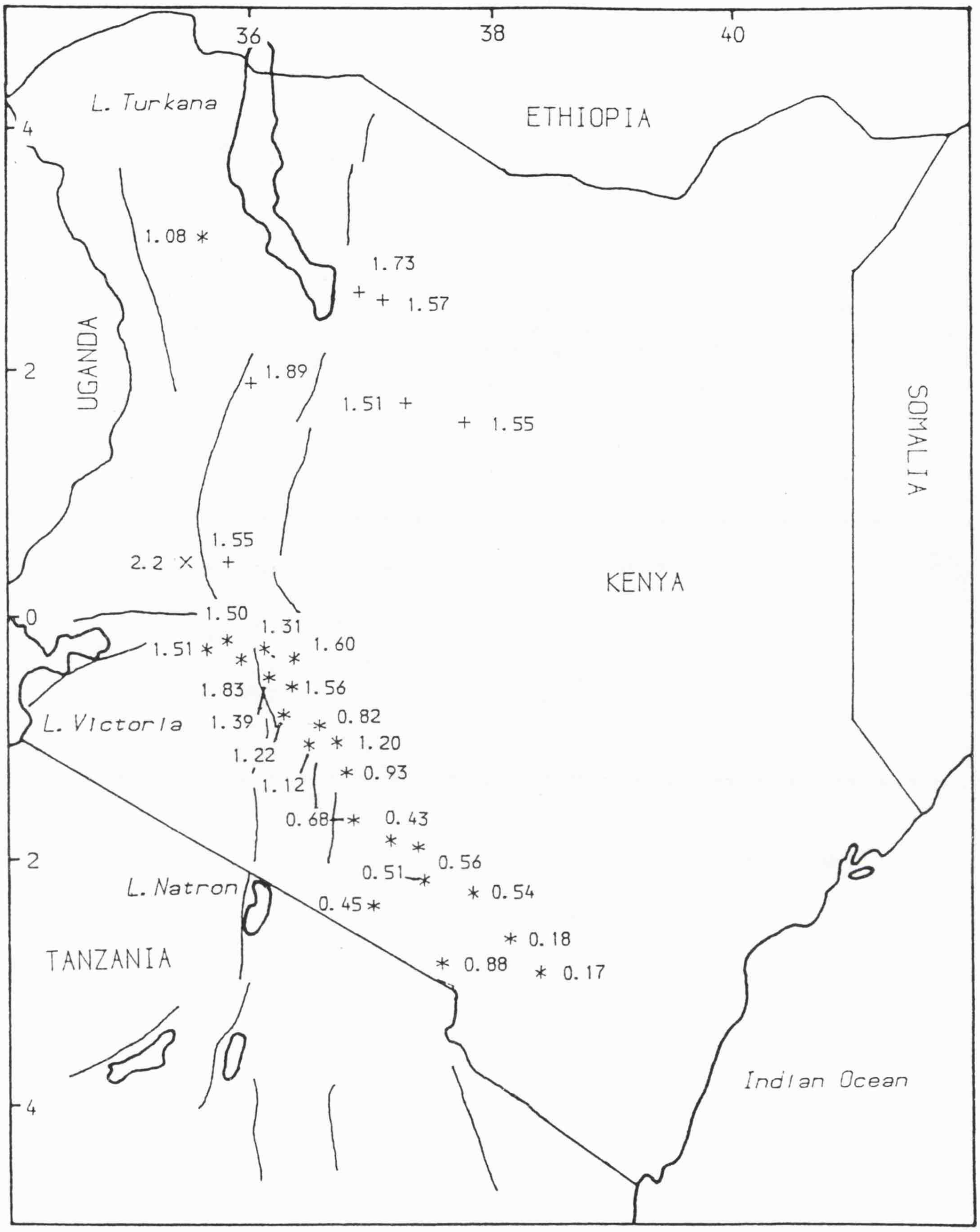

* *Savage and Long (1985)*

\+ *Pointing (1985)*

× *Long and Backhouse (1970)*

Figure 1.9 : Teleseismic delay times observed in Kenya. All have been calculated using Herrin's travel-time tables. Those of Long and Backhouse (1970) are relative to Bulaweyo while those of Savage and Long (1985) and Pointing (1985) are station delays.

separating continental blocks". However, these estimates of extension are not consistent with geological evidence. Baker et al (1972) reported that total extension is unlikely to have been more than 30 km in Ethiopia and 10 km in Kenya, and in the regions of Lake Turkana and N.Tanzania it is no more than 2 - 3 km. Revisions to the original plate tectonics scheme (Freund, 1970; Mohr, 1970; Baker et al, 1972) reduced the maximum amount of extension across the eastern rift to 25 km in central Ethiopia and 12 km in central Kenya which are more consistent with geological evidence. Other estimates of extension across the Kenya rift, based on gravity modelling and geological evidence vary between 8 and 15 km (Baker and Wohlenberg, 1971; Swain, 1976; Fairhead, 1976; King, 1978).

Emerick and Duncan (1982) calculated the relative motion across the East African rift by subtracting the Somali plate absolute motion from that of the African plate during the last 10 m.y. The resulting estimate of 320 km of total separation is completely inconsistent with all other estimates.

1.6 Mechanisms of rifting.

Many different mechanisms have been proposed for the formation of rift valleys such as the Kenya rift. These include models involving lithospheric stretching (Mckenzie, 1978), diapiric injection (Turcotte and Emerman, 1983; Mohr, 1987), wedge subsidence (Bott and Mithen, 1983), deep crustal metamorphism (Middleton, 1980) and low angle detachment systems (Bosworth, 1987). It will later be seen that the results of this study have imposed important constraints on such models. Detailed descriptions of all of the mechanisms which have been suggested for the Kenya rift are not warranted here. However, summaries of two of the most recent hypotheses are given below.

1.6.1 Low angle detachment systems.

Recent studies of failed and active continental rifts have revealed general similarities in their geometries that are not properly depicted by symmetric graben models (Bally, 1982; Bosworth, 1985; Bosworth et al, 1986; Bosworth, 1987). Bosworth et al (1986) noted that cross sections through rifts are generally half graben in form with one bounding fault system more developed than the other. Such asymmetry has been observed in seismic reflection profiles from Lake Malawi, Lake Tanganyika (Rosendahl et al, 1987) and Lake Turkana (Dunkelman, 1986). The sense of the asymmetry tends to alternate along the rift axis every 50 - 150 km producing a lazy "S" configuration in plan view. Bosworth et al (1986) proposed that such asymmetry is a feature of the Kenya rift, it being made

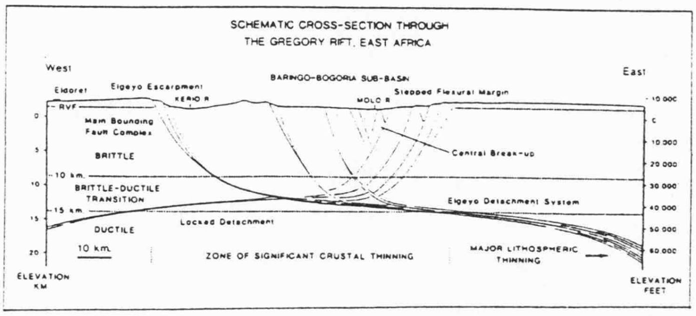

Figure 1.10 (a) : Schematic cross section through the Baringo-Bogoria subbasin of the Kenya rift (after Bosworth, 1986).

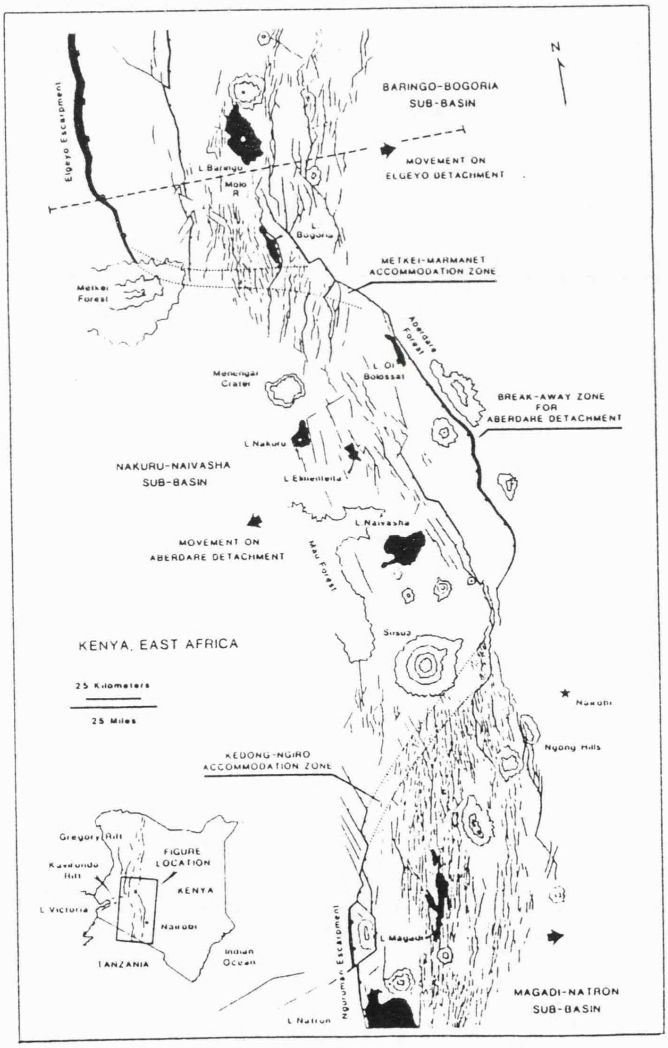

Figure 1.10 (b) : Morphotectonic interpretation of the Kenya rift valley (after Bosworth, 1986).

up of a series of linked "sub-basins" that have evolved with distinct tectonic and stratigraphic histories. Each sub-basin was said to be bordered by a major rift-bounding fault on one side and a series of more minor faults on the opposing side.

When rifting is initiated two opposing detachments were said to form, producing an initial full-graben geometry. It has been suggested that the two opposing systems of normal faults each merge into low angle detachment surfaces (Wernicke and Burchfiel, 1982) at depths of 10 - 15 km which may coincide with the brittle-ductile transition zone. If the detachments cross cut at depth then one is likely to lock resulting in the formation of a half-graben geometry (Fig. 1.10 (a)). Bosworth's morphotectonic interpretation of the Kenya rift is shown in figure 1.10 (b): The rift is divided into three, or possibly four, sub-basins separated by "accommodation zones" of complex wrench style tectonics.

Bosworth (1987) inferred that off-axis from the rift the detachment zones merge along strike and continue to the base of the lithosphere. This was suggested as being the cause of both lithospheric thinning and the development of major volcanic cones (e.g. Kilimanjaro, Mt Kenya and Mt Elgon) away from the axis of the rift.

1.6.2 Diapiric injection and reverse decollements.

Mohr (1987) suggested that Ethiopian and Kenyan rifting is a response to the forceful diapiric injection of anomalously hot and mobile asthenosphere which has most recently breached the upper crust. This injection was said to be accommodated by the outward and downward movement of lithospheric slices along reverse decollements of ductile shear. The model proposed by Mohr (1987) is shown in cross-section in figure 1.11. The reverse decollements are required by the model to explain why estimates of extension obtained from the surface geology are significantly lower than the extension at greater depth that would result from the emplacement of such an asthenolith (accepting that no significant stoping or anatexis has taken place). Rift margin faulting was said to be in response to both minor crustal extension and gravitational collapse into the depression created isostatically by the rising high density asthenolith.

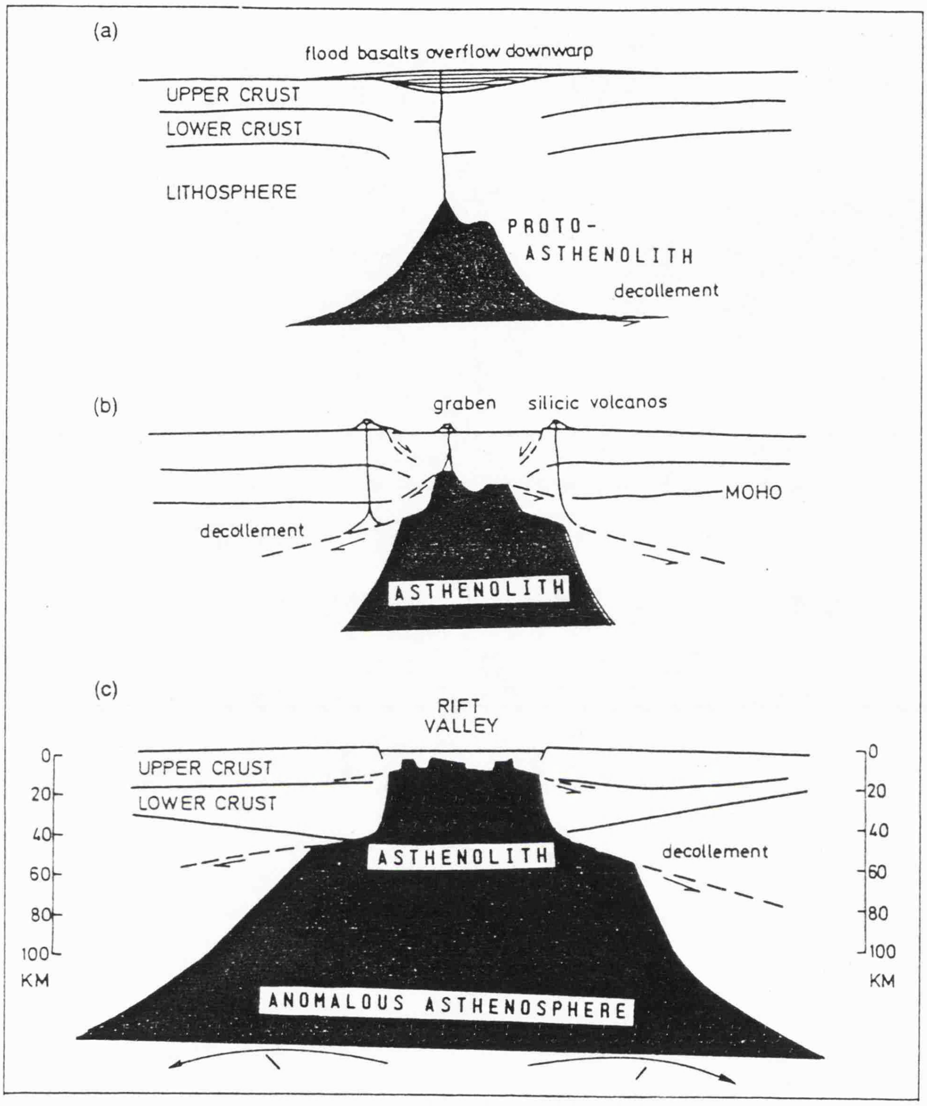

Figure 1.11 : Stages in Mohr's hypothesis for rifting in Ethiopia and Kenya (after Mohr, 1987).

(a) Mid-Tertiary: protorift downwarp and associated volcanism from newly initiated asthenospheric diapir.

(b) End of Tertiary: rifting and penetration of lower crust by asthenolith. Reverse decollements active within lithospheric mantle.

(c) Quaternary: rapid ascent of asthenolith. Reverse decollements now active within crust and along Moho.

CHAPTER (II)

THE KRISP85 EXPLOSION PROGRAMME

2.0 Introduction.

At a meeting on "Processes in Planetary Rifting", held by NASA in 1981, emphasis was placed on the need for an international effort to study one terrestrial rift in detail. The Kenya rift, often considered to be the type example of continental rifting and already the subject of preliminary geological and geophysical study, was an obvious target for a programme of seismic investigations. KRISP85 (The Kenya Rift International Seismic Project 85) was the first such international effort. Participants from the U.K., the U.S.A., West Germany, Kenya, Switzerland and Zimbabwe took part in a long range explosion seismology programme. This was followed immediately by three independent passive seismic monitoring programmes carried out by Leicester University (U.K.), U.C.L.A. (U.S.A.) and Wisconsin University (U.S.A.). This chapter is dedicated to a comprehensive description of the explosion seismology phase of KRISP85.

2.1 Aims of the explosion programme.

Seismic refraction profiling has been described as the most cost effective method for obtaining information on structure, seismic velocities and petrological conditions in the deep crust and upper mantle (Olsen, 1983). Its use has been very effective in the study of the Rhinegraben (Prodehl, 1981), the Rio Grande rift (Olsen et al, 1979) and the Baikal rift (Puzirev, 1978). As mentioned in Chapter 1, the method has already been used to study the Kenya rift (KRISP68 and KRISP75). The COCORP (The United States Consortium for Continental Reflection Profiling) and BIRPS (British Institute for Reflection Profiling Syndicate) groups have shown that the seismic reflection method is now capable of providing high resolution structural data down to upper mantle depths. However, it would currently be prohibitively expensive to use this technique on the Kenya rift valley.

The objectives of the explosion programme can be divided into two categories: (a) Those of immediate geological significance; and (b) those pertaining to future explosion seismology in the area.

In category (a) the objectives were:

(1) To determine variations in the thickness of rift infill along and across the rift.

(2) To determine the nature of the basement below the rift infill.

(3) To locate any anomalously high velocity zones in the crust which might indicate the presence of basic, mantle derived intrusives i.e. the "axial intrusion".

(4) To determine the crustal thickness (depth to Moho) below the rift.

(5) To determine the upper mantle P-wave velocity.

(6) To determine S-wave velocities where possible.

(7) To examine anelastic attenuation (Q) along and across the rift.

In category (b) they were:

(1) To test shot efficiencies.

(2) To test transmission along and across the rift.

(3) To gain logistical experience in implementing a large scale explosion seismology programme in such a remote region.

2.2 Locations of the seismic lines.

The experiment comprised 2 seismic lines: One was sited along the rift axis (NS-line) and the other across the rift (EW-line).

The NS-line was chosen to follow the positive axial Bouguer anomaly as closely as logistically possible (Fig. 2.1). There are several reasons for the choice of location between Chepkererat (CHE) and Susua (SUS) (Fig. 2.2): (1) the axial gravity high is most pronounced at these latitudes; (2) the rift south of Lake Bogoria has not been the site of any previous seismic refraction studies; (3) the region has a reasonable network of roads making access relatively straight forward (Fig. 2.3); and (4) Lake Baringo was known, from the KRISP75 experiment, to be an efficient shot point.

The EW-line ran from Mount Margaret (MAR), on the rift floor near the eastern escarpment, to Ntulelei (NTU) on the western flank. This location was chosen primarily because of the easy access provided by the Narok road (Fig. 2.3).

The NS and EW lines were 140 km and 50 km long respectively. 42 recording stations were deployed along each, resulting in station spacings of approximately 3.4 km and 1.2 km. Figures 2.2 and 2.3 show the locations of the shot points which will be discussed in detail in section 2.4 and Chapter 5. Additional recording stations were deployed between the main lines and off-end shots EWA, BAR and MAG (Fig. 2.3).

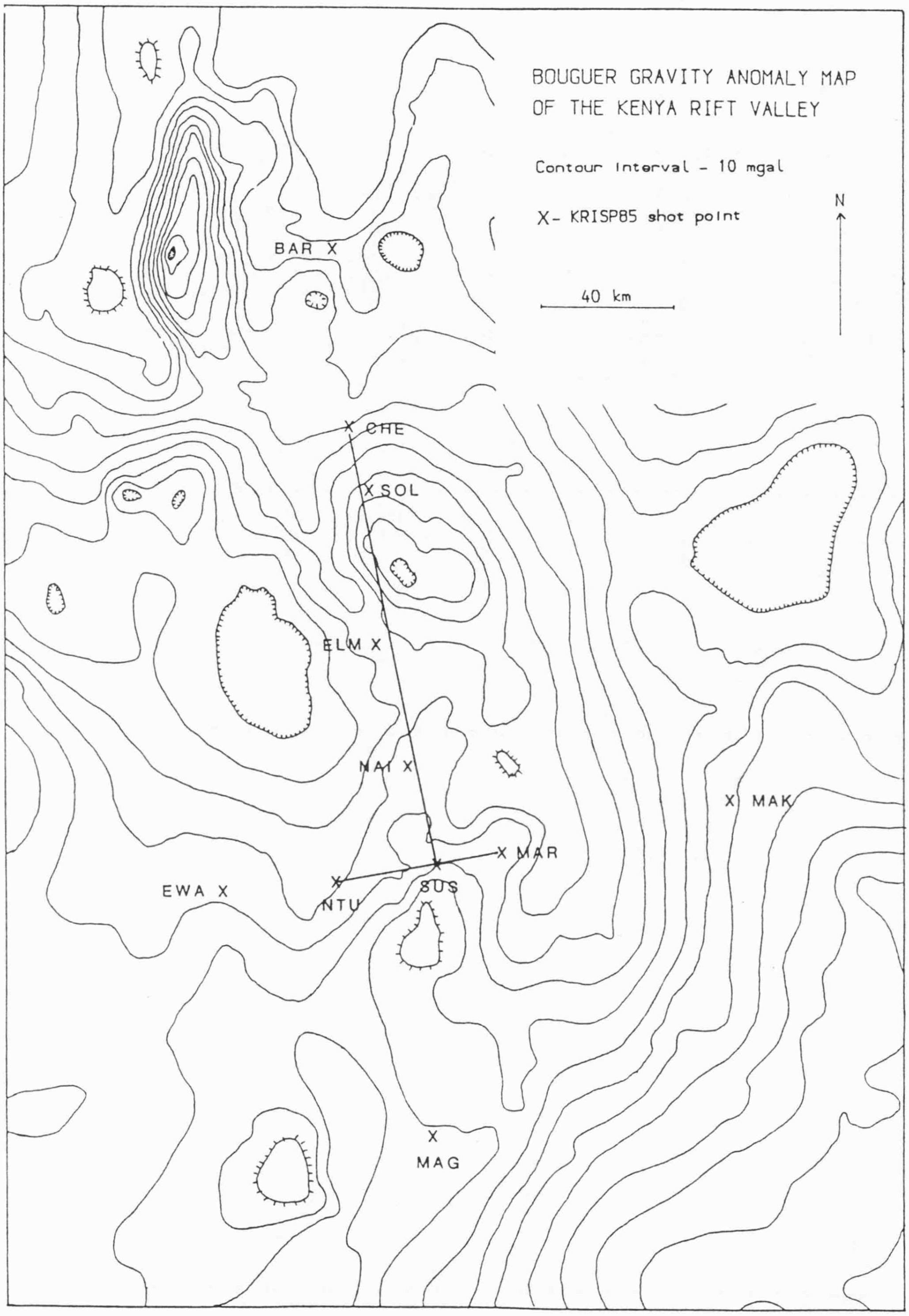

Figure 2.1 : Bouguer gravity anomaly map showing locations of KRISP85 seismic refraction lines.

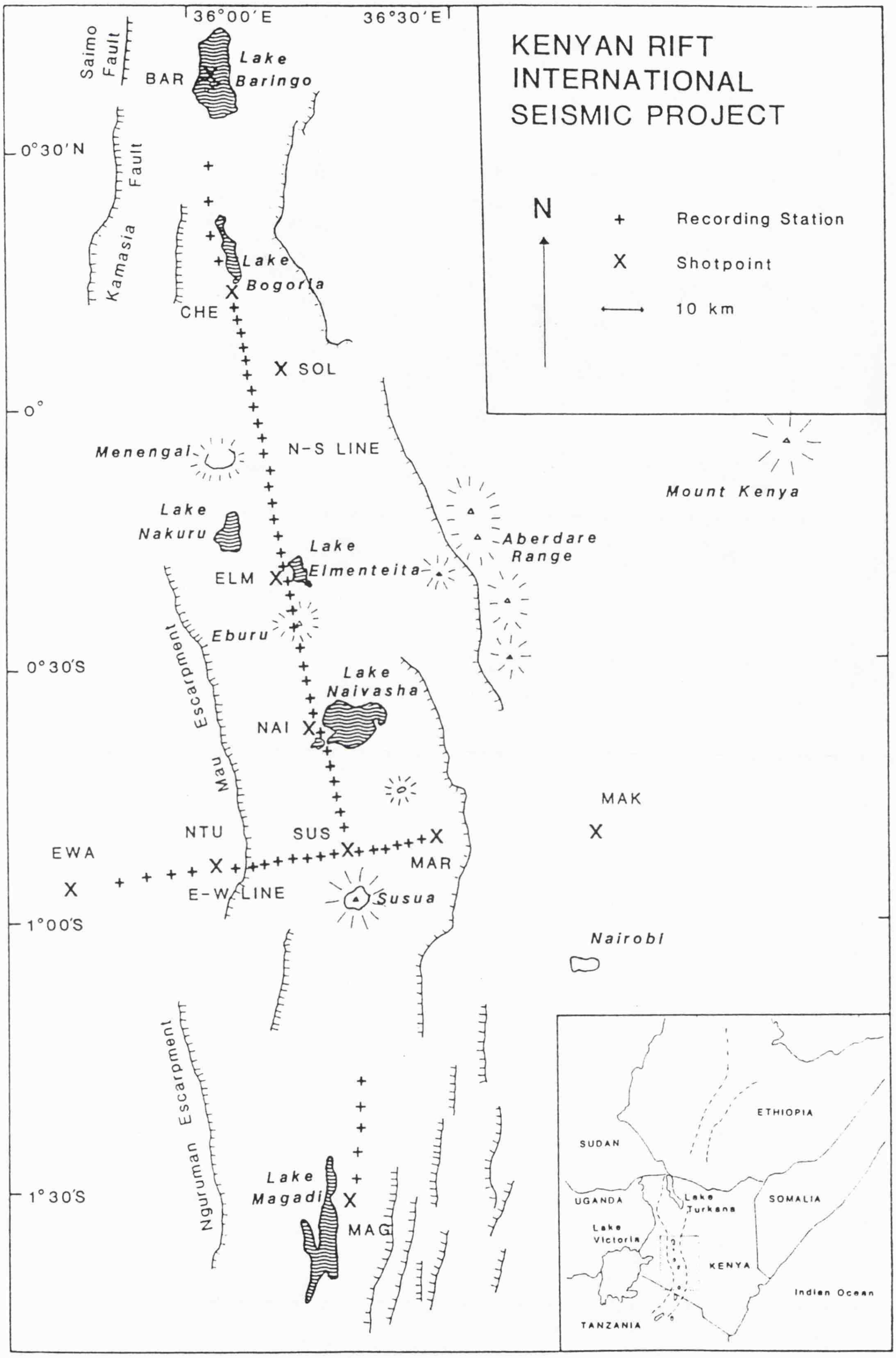

Figure 2.2 : Location map of KRISP85 seismic refraction experiment showing lines and shot points.

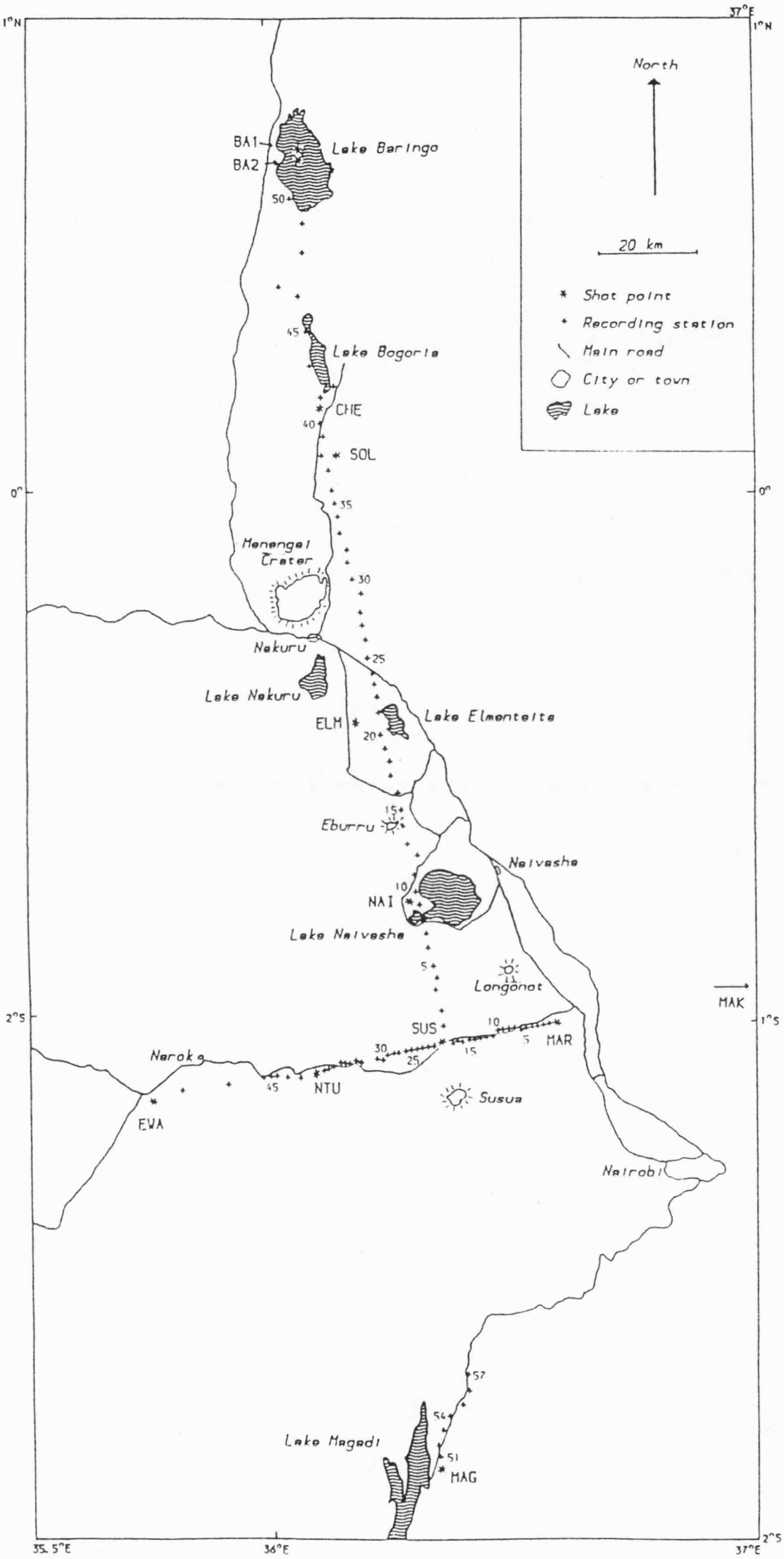

Figure 2.3 : Location map of KRISP85 seismic refraction experiment showing station locations and access roads.

2.3 Surveying.

2.3.1 EW-line.

The flat scrubland of the rift floor along the EW-line was considered to be too featureless for stations to be positioned using the available 1:50000 topographical maps and aerial photographs. For this reason a professional surveyor was contracted to set out the line. The line was divided into 2 sections: section 1 from MAR to SUS and section 2 from SUS to NTU (Fig. 2.3).

Section 1: A traverse was laid out along the Narok road and measured using an electronic distance measuring device. This was divided into 20 equal distances and the recording stations were positioned, sighting from the road. Some stations were offset from the straight line between MAR and SUS to keep them away from the road, settlements or maize fields.

Section 2: This section was started by traversing cross country, maintaining the alignment of section 1, and positioning recording stations where appropriate. This was continued as far as station 30 where, owing to severe topography and dense vegetation, the traverse was run out to the Narok road once again. It was continued as far as NTU and stations 33 - 41 were positioned in the same fashion as employed for section 1.

Station 31 was subsequently positioned with the aid of the relevant 1:50000 topographical map. The remaining gap, which coincides with the western escarpment, could not be filled owing to the impossibility of vehicular access.

Vertical angles were measured during the traverse so elevations could be calculated for stations 0 - 30 and 33 - 41. All other elevations were estimated from mapped contour heights.

2.3.2 NS-line.

The NS-line stations were roughly positioned along a straight line between SUS and CHE (Fig. 2.3) using the 1:50000 maps. Areas of high noise level were in general avoided but, as the line passed through some densely populated regions, this was not always possible.

The University of Nairobi Surveying Department advised that the 1:50000 topographical maps available could not give the level of accuracy desired for the location of recording stations (about $\pm$ 30 metres). The length of the NS-line made a conventional traverse survey impractical. The "Regional Centre For Services in Surveying, Mapping and Remote Sensing" offered to

<u>Table 2.1 : EW-line coordinates.</u>

STAT	EASTING	NORTHING	ELEV	STAT	EASTING	NORTHING	ELEV
'EW00'	226424	9888649*	1767*	'EW31'	188200	9880850~	840~
'EW01'	225189	9888402*	1755*	'EW33'	184953	9880041*	2044*
'EW02'	223903	9888202*	1732*	'EW34'	184015	9880209*	2093*
'EW03'	222689	9887921*	1717*	'EW35'	183192	9879659*	2104*
'EW04'	221456	9887780*	1710*	'EW36'	181805	9879586*	2142*
'EW05'	220143	9887511*	1704*	'EW37'	180764	9879500*	2128*
'EW06'	218982	9886995*	1692*	'EW38'	179437	9878926*	2184*
'EW07'	217658	9887145*	1696*	'EW39'	178255	9878801*	2148*
'EW08'	216392	9887000*	1698*	'EW40'	177340	9878382*	2122*
'EW09'	215077	9886860*	1685*	'EW41'	175757	9878072*	2105*
'EW10'	213899	9886514*	1681*	'EW42'	172580	9877100~	2000~
'EW11'	212745	9885778*	1657*	'EW43'	168850	9877430~	1910~
'EW12'	221150	9885537*	1644*	'EW44'	166760	9877820~	1910~
'EW13'	210231	9885502*	1631*	'EW45'	165000	9876270~	1800~
'EW14'	208962	9885243*	1615*	'EW46'	163160	9876140~	1850~
'EW15'	207759	9884808*	1607*	'EW47'	154820	9874670~	1920~
'EW16'	206512	9884566*	1603*	'EW48'	145260	9873270~	1890~
'EW17'	205227	9884519*	1598*	'EW49'	138579	9871284~	1850~
'EW18'	203980	9884275*	1603*	'EWSU1'	201315	9883387*	1620*
'EW19'	202538	9884173*	1612*	'EWEWA'	138579	9871284~	1850~
'EW20'	201486	9883790*	1620*	'EWMAR'	226399	9888614*	1767*
'EW21'	200240	9883547*	1622*	'EWNTU'	175757	9878072*	2105*
'EW22'	198983	9883289*	1625*	'EWMAK'	293000	9902000~	1400~
'EW23'	197704	9883053*	1635*				
'EW24'	196498	9882818*	1647*				
'EW25'	195236	9882572*	1667*				
'EW26'	194032	9882341*	1660*				
'EW27'	192861	9882105*	1724*				
'EW28'	191583	9881827*	1753*				
'EW29'	190631	9881816*	1826*				
'EW30'	189975	9880328*	1787*				

* from survey traverse
~ from 1:50000 map

units - metres

Table 2.2 : NS-line coordinates.

STAT	EASTING	NORTHING	ELEV	STAT	EASTING	NORTHING	ELEV
'NS00'	201489	9883797	1620	'NS36'	180325	10000640*	1590∂
'NS01'	202541	9887416*	1630∂	'NS37'	179742	10004828*	1555∂
'NS02'	202222	9891348*	1645∂	'NS38'	177694	10007431*	1540∂
'NS03'	200928	9894833*	1760∂	'NS39'	178300	10011500*	1510∂
'NS04'	201500	9897160*	1740∂	'NS40'	177725	10014170*	1510∂
'NS05'	200640	9900160*	1920∂	'NS41'	179000	10017100*	1510∂
'NS06'	199735	9903605*	2060∂	'NS42'	177620	10019710~	1110~
'NS07'	199160	9907080*	2000∂	'NS43'	179700	10022010~	1000~
'NS08'	198400	9909950*	1895∂	'NS44'	175820	10026700~	980~
'NS09'	197639	9912898*	1915∂	'NS45'	174900	10033530~	1000~
'NS10'	197018	9915813*	1900∂	'NS46'	173260	10040580~	995~
'NS11'	196978	9919752*	2010∂	'NS47'	169000	10042320~	1005~
'NS12'	197296	9923820*	2005∂	'NS48'	174330	10050370~	975~
'NS13'	195107	9925633*	2320∂	'NS49'	174000	10056240~	950~
'NS14'	194500	9929600*	2555∂	'NS50'	171580	10061500~	950~
'NS15'	193880	9932930*	2330∂	'NS51'	202060	9797020*	780~
'NS16'	193100	9936500*	1940∂	'NS52'	202378	9799890*	760~
'NS17'	191730	9940150*	1920∂	'NS53'	203038	9802760*	810~
'NS18'	191810	9942830*	1860∂	'NS54'	204953	9805487*	860~
'NS19'	190820	9945398*	1840∂	'NS55'	206714	9808925*	930~
'NS20'	189677	9948825*	1800∂	'NS56'	207960	9811080*	860~
'NS21'	189740	9953447*	1780∂	'NS57'	207720	9813720*	875~
'NS22'	188780	9956559*	1860∂	'NSMAG'	201888	9795128~	740~
'NS23'	188540	9959247*	1860∂	'NSSU2'	201486	9883790	1620
'NS24'	188149	9961720*	1880∂	'NSNAI'	195500	9913700~	1880~
'NS25'	186814	9965447*	1930∂	'NSELM'	184600	9951200~	1875~
'NS26'	186823	9968242*	1950∂	'NSSOL'	181800	10007800~	1515~
'NS27'	186100	9971900*	1990∂	'NSCHE'	179000	10017100*	1510∂
'NS28'	185700	9974500*	2030∂	'NSBA1'	173900	10070600~	950~
'NS29'	186000	9977780*	2145∂	'NSBA1'	173940	10070520~	950~
'NS30'	184180	9981112*	2120∂	'NSBA2'	173930	10071070~	950~
'NS31'	183260	9984970*	2090∂	'NSBA2'	173900	10071120~	950~
'NS32'	183205	9987730*	2140∂				
'NS33'	181808	9991279*	1920∂				
'NS34'	181400	9994900*	1750∂				
'NS35'	180922	9997606*	1710∂				

units - metres

* from resection

∂ from barometric levelling

~ from 1:50000 map

carry out an aerial survey of the line. White crosses, which would be visible from the air, were constructed at each station from SUS to CHE. These were 14 metres across and made of either white-washed boulders (where locally available) or diatomite (obtained from the Elmenteita diatomite quarry). Unfortunately, owing to unforeseen circumstances (a military coup in Uganda), the plane which was to have flown the survey was never made available and the aerial survey was not carried out.

Following the explosion programme the NS-line stations were located by resection i.e. positions were fixed by sighting from each station to at least three points of known position. Surrounding triangulation points provided this control. An accuracy of about ± 25 metres was obtained by this method. Stations 51 to 57 (near Lake Magadi) were also located by resection.

The remaining stations on the NS-line (north of CHE) were located using the relevant 1:50000 maps.

Elevations for the main line stations from SUS to CHE were determined by barometric levelling during a gravity survey of the line. Other elevations were estimated from contour heights.

2.3.3 Accuracy of station locations and elevations.

The U.T.M. grid references and elevations are presented in tables 2.1 and 2.2. The methods used to determine the position and elevation are given for each station. The following table summarises the estimated accuracies of the various methods.

Table 2.3 : Coordinate and elevation accuracy.

Method	Accuracy	Method	Accuracy
1:50000 map	± 75 m	1:50000 map	± 20 m
Survey traverse	± 5 m	Survey traverse	± 2 m
Resection	± 30 m	Barometric levelling	± 3 m

2.4 Shot points.

The shot point locations are shown in figure 2.3 and their grid references listed in table 2.4. Thirteen shots were fired in total: EWA (Ewaso Ngiro), NTU (Ntulelei), SU1 (Susua), MAR (Mount Margaret) and MAK (Makuyu) were recorded by the EW-line stations; MAG (Magadi), SU2 (Susua), NAI (Naivasha), ELM (Elmenteita), SOL (Solai), CHE (Chepkererat), BA1 and BA2 (Lake Baringo) were recorded by the NS-line stations. Of these shots, nine were fired in bore-holes (EWA, NTU, SU1, MAR, MAK, SU2, ELM, and

Table 2.4 : Shot locations and times (G.M.T.).

SHOT	EASTING(m)	NORTHING(m)	ELEV(m)	DATE	HOURS	MINS	SECS
'SU1'	201408	9883498*	1612*	11-08-85	10	11	00.60
'EWA'	138550	9871325~	1860~	11-08-85	10	16	59.83
'MAR'	226399	9888614*	1767*	14-08-85	10	14	59.65
'NTU'	175807	9877986*	2105*	15-08-85	03	41	00.01
'MAK'	293000	9902000~	1400~	15-08-85	03	46	02.52
'BA1'	173750	10071560~	950~	19-08-85	04	40	31.35
'MAG'	201873	9795125~	740~	19-08-85	04	46	30.45
'SOL'	181900	10007800~	1515~	19-08-85	04	48	32.42
'SU2'	201529	9883963*	1612*	22-08-85	05	40	59.93
'NAI'	195400	9913750~	1880~	22-08-85	05	48	01.99
'BA2'	174130	10070040~	950~	24-08-85	05	40	29.84
'ELM'	184620	9951220~	1875~	24-08-85	05	44	59.73
'CHE'	179000	10017560ə	1510+	24-08-85	05	48	31.88

* from survey traverse

ə from resection

~ from 1:50000 map

\+ from barometric levelling

CHE), three were lake shots (NAI, BA1 and BA2) and one was a surface shot (SOL).

The explosive used was Geogel, 60% strength, manufactured by ICI Explosives International. It comes in the form of 60 cm long, 60 mm in diameter, plastic coated sticks suitable for detonation under water. The sticks could be screwed together before being lowered down the bore-hole. Cordtex was used to link charges together and detonation achieved by electric detonators.

The details of all the bore-hole shots are summarised in table 2.5. The three lake shots and the surface shot are described below.

NAI: The Naivasha shot was fired in Crater Lake, a small lake in the crater of a volcanic cone to the east of Lake Naivasha. The 700 kg charge was distributed over a 20 m by 20 m area about 30 m off shore. It was divided into 16 packages of 42 kg and 1 package of 28 kg which were laid on the lake bottom (5 m deep) and linked by Cordtex. The shot instant was determined by means of a recorder on the shore line.

BA1: The Baringo shots were fired in Lake Baringo, one of the rift's fresh water lakes, which is about 20 km long and 10 km wide. Both shots were fired from Samatian, one of the lake's small islands. The charge size of the BA1 shot was 1000 kg which was divided into 10 equally sized packages. These were distributed along 2 parallel lines about 75 m long and 5 m apart, aligned approximately NS and about 350 m north of Samatian. A specially designed raft was used to lower the packages on to the lake bottom, a depth of about 20 m. They were all linked together by Cordtex. The shot instant was recorded by means of 2 geophones, situated 70 m apart, on the island.

BA2: The second Lake Baringo shot was set off about 500 m SSE of Samatian. The 600 kg charge was divided into 6 units which were deposited on the lake bottom (20 m deep) along a single line aligned approximately EW. Again the charges were linked by Cordtex and the shot instant was recorded by means of 2 geophones on the island.

SOL: The SOL shot was fired in Lake Solai which is located about 1 km east of the NS-line between stations 37 and 38. As Lake Solai is no more than a swamp, less than 20 cm deep, it constituted the only surface shot of the experiment. The 400 kg charge was laid out along 4 parallel lines about 6 m apart. The lines, each consisting of 2 rows of 25 sticks laid end to end, were linked by Cordtex.

Table 2.5 : Bore-hole shot descriptions.

Shot	No. holes	Distribution	Hole depth	Charge depth	Water depth	Charge size	Comments
SU1	1		30m	10m	dry	100kg	loose volcanic soil
EWA	2	30m apart approx EW alignment	54m,55m	30m,31m	14m,15m	500kg	firm soil
MAR	1		54.5m	31.5m	dry	248kg	loose volcanic soil
NTU	1		29 m	9m	dry	210kg	firm soil
MAK	2	40m apart	51m,60m	31,35m	4.5m,58m	1140kg	
MAG	6	150m linear array approx NS alignment	60m-75m	19m-20.5m	dry	1000kg	firm rocky soil
SU2	2	50m apart approx NS alignment	20m,22m	11m,14m	dry	400kg	loose volcanic soil
ELM	1		34m	26.5m	dry	400kg	poorly consolidated lake sediments
CHE	4	scattered over approx 50m	18m-40m	5m-9m	dry	300kg	firm laterite soil

2.5 Recording equipment.

As KRISP85 was an international project several different recording systems were employed: the Geostore system (U.K.); the Mars system (West Germany and Switzerland); and the Wisconsin recorder and the DR100 system (U.S.). A brief description of each system except the DR100 (for which no information could be obtained at the time of writing) is presented below.

Geostore system: The Geostore is a 14 track analogue magnetic tape recorder which records on 2400 ft of 1/2 inch tape at speeds of 15/640, 15/320 or 15/160 ips. It has a 32 Hz upper limit to the frequency of the recorded signal at 15/160 ips which was the speed used during the explosion programme. The recorder can be set to run in either uni-directional or bi-directional mode. In uni-directional mode, as used during KRISP85, 2 tracks record a flutter signal and another records the internal clock, leaving 11 possible data channels. As two different recording heads are used to record the odd and even channels, it is advisable to use 2 channels for the recording of an external time signal so that any head misalignment can be corrected for.

Each of the six Geostore systems deployed was capable of recording three 3-component stations; a base-station and 2 out-stations. The out-stations were linked to the base-station by telemetry. The seismometer output signals are sent via a digital autorange amplifier-modulator to a UHF radio transmitter connected to a Yagi dipole aerial. The signal is picked up by the corresponding receiver at the base station and sent to a line interface unit which separates the digital signal into 3 frequency modulated signals corresponding to the original 3 components. These are then recorded by the Geostore.

As well as the digital system described above, an older analogue system was employed at some stations. This is similar to the digital system except that 3 analogue amplifier modulators and 3 separate transmitter-receiver pairs are required for a 3-component station. Obviously, there is no need for the line interface unit required by the digital system.

The UHF radios have a line of sight range of about 30 km which is much greater than the station separations of KRISP85. However, topographic relief along the NS-line is considerable so telemetry links had to be checked prior to the experiment. It was necessary to identify suitable Geostore base-stations (those sites having radio links with adjacent sites).

Base-station and out-stations were powered by 32 amp hour batteries which were charged by solar panels.

Mars system: Twelve Mars 66 analogue recorders were used during the experiment. The main difference between the 9 German systems and 3 Swiss systems deployed is that the former record on to 1/4 inch magnetic tape and the latter on to cassette tape.

It is a single station system capable of recording 3 seismic signals and a time signal (Berckhemer, 1976). The seismometer outputs are passed through a calibrated wide-band amplifier and frequency modulated at 0.86 kHz, 2.1 kHz and 4.4 kHz (± 15%). A fourth carrier frequency (9.5 kHz ± 15%) is modulated by the time signal. All carriers together with a crystal-controlled flutter frequency (6.4 kHz) are recorded, in the case of the German MARS system, on the single track of a UHER audio tape recorder capable of recording at 4 speeds (2.4, 4.7, 9.5 and 19.0 cm/s). The Swiss MARS system records similarly on to a conventional cassette recorder.

Wisconsin system: The U.S. contingent came equipped with 15 recorders designed and built at Wisconsin University.

It is a 3-component digital system which can operate in either event triggered or programmed mode. It has a 12 digit L.E.D. display and parameters such as sample rate, amplifier gain, arm/disarm are entered via a small key pad. The digital data is recorded on 1/4 inch tape formatted as follows: 4 tracks digital; 1 track per component and 1 track for error correction. Other information, including time, is distributed with the data. It has a very high dynamic range (106 dB) and a recording capacity of 6.4 hours per tape (1800 feet).

As the Wisconsin recorder is fully programmable, several instruments could be manned by a single operator.

2.6 Timing.

Absolute timing was achieved by the recording of a radio time signal along with the seismic data. Two broadcast time signals, Omega and Radio Moscow, were employed.

Omega: This is a navigation signal transmitted by "Omega Navigation Transmitters" located around the globe. Transmissions from La Reunion and Liberia can be received in Kenya. An Omega receiver (Omega-rec), tuned to a particular transmitter, works in conjunction with an interface (Omega-face). The Omega-rec contains a clock synchronized with the time signal and generates only a minute pulse which is offset several seconds with respect to universal time. These minute pulses override the free running quartz clock of the Omega-face which then runs in parallel with the Omega-rec but with the offset corrected for. The Omega-face generates a binary coded decimal output which consists of 48 bits delivering the following information: current minute, current hour, Julian day, reception and synchronization status and identification number. This code can be repeated either once a second (bit length 20 msec) or once a minute (bit length 1 sec). The latter was recorded during KRISP85.

Radio Moscow: Several of the MARS stations received the Radio Moscow time signal. For 20 minutes of every hour second pulses are broadcast by Radio Moscow. These were used to sychronise an internal clock which generated a binary coded decimal output. Obviously, shot windows had to be chosen to coincide with the transmission times.

2.7 Huddle tests.

As it was necessary to compare the responses of the different recording units two huddle tests were carried out; one at the head-quarters near Nairobi and another on the Susua plain, near shot points SU1 and SU2. The first comprised two small shots, at about 1 km range, recorded by a Geostore, a Mars and a Wisconsin unit. During the second, all available instruments recorded 2 shots at about 700 m range. Unfortunately, the DR100 units were not available at the time of either of the huddle tests.

The results of the huddle test are used in Chapter 3 when the recovery of true amplitude information is discussed.

2.8 Logistics.

During the two week period of shooting the head-quarters and play-back centre was in Nakuru (Fig. 2.3). Three shooting parties were responsible for the loading, preparation and firing of the 13 shots. There were ten recording parties, operating from 3 to 6 recorders each. During the first stage of the experiment, the shooting of the EW-line, all the recording parties were based at a camp near Mount Margaret (MAR). During the shooting of the NS-line there were two camps; one on the north-west shore of Lake Naivasha which catered for stations south of NS23 and one near Solai for the remaining NS-line stations.

Communication between HQ and shooting and recording parties was achieved using Southcom radios. Radio scheds were run every morning and evening.

The shot times are listed in table 2.5. The first 3 shots were fired in the early afternoon. It soon became apparent that noise levels were lower in the early morning so the remaining 10 shots were fired at between 6:00 a.m. and 9:00 a.m. (local time). For reasons of safety, night shooting was not considered a feasible alternative.

CHAPTER (III)

PROCESSING AND METHODS OF INTERPRETATION OF REFRACTION DATA

3.0 Introduction.

The first part of this chapter (3A) deals with the processing of the KRISP85 refraction data. This includes details of the digitising, merging, corrections applied, filtering, picking of first arrivals and the recovery of true amplitude information.

The second part (3B) consists of descriptions of the various methods applied in the interpretation of the refraction data.

A. PROCESSING OF KRISP85 REFRACTION DATA

3A.1 Digitising and merging.

Following the explosion programme the data tapes were taken by the participating groups to their respective institutions where initial processing was carried out. For the digital recording systems this entailed the transfer of the data on to high density computer tape. The MARS tapes were digitised at 100 samples per second at the University of Karlsruhe, West Germany. Further processing included the decoding of the time signal and input of some header information. The Geostore tapes were digitised at 100 samples per second at the Global Seismology Unit of the British Geological Survey (B.G.S.), Edinburgh. As the subsequent processing of the Geostore data was performed at Leicester University it will be dealt with in more detail in the next section.

The data sets were sent to Leicester University where they were reformatted and merged. All subsequent processing has been carried out using the Leicester University "Seismic Data Processing System" (SDPS4) which is described briefly in Appendix B.

3A.2 Processing of Geostore data.

The files created at the B.G.S., Edinburgh, were first converted to SDPS4 format. They normally contained the 9 seismic traces and 2 auxiliary traces (the Omega and internal clock signals) recorded by each Geostore during recording windows. A Fortran program (GATOMG, Appendix B) was written to:

(a) decode the Omega B.C.D. time signal.

(b) calculate a stretch factor to correct the nominal sampling interval for any wow or flutter.

(c) calculate the absolute time of the first sample.

(d) delete auxiliary traces.

(e) gate the seismograms to a specified time window.

The resulting files were merged to create shot files, each one containing all the seismograms from a particular shot.

The seismograms recorded by the geostores were subject to two timing errors which had to be corrected for.

(1) The 9690 digital recording system introduces a small time delay to the recorded signal. As the external time signal is recorded directly and not subject to this delay a correction is necessary. Two independent estimates of the delay, made by B.G.S. employees, are 50 ms and 70 ms. A compromise figure of 60 ms was added to the first sample time of all the

digital station traces.

(2) As stated in Chapter 2, the odd and even Geostore channels are recorded by different recording heads. If they are not properly aligned a time difference is introduced between odd and even channels. As the external clock was normally recorded on channel 14, a correction had to be made to the traces recorded on odd channels. The correction necessary was determined by recording a square wave on the odd and even channels of each Geostore and examining the resulting time difference.

3A.3 Filtering.

As will become apparent in Chapter 4 many of the KRISP85 seismograms have low signal to noise (S:N) ratios. In order to aid the picking of first arrivals and correlation of later phases, considerable effort was devoted to enhancing the seismic signal. In particular, frequency filtering and polarisation filtering were employed with some success.

3A.3.1 Frequency filtering.

It is assumed that the reader is familiar with the theory of finite impulse response (FIR) digital filtering. A comprehensive treatment is given by Rabiner and Gold (1975). The SDPS4 system includes a routine capable of designing a wide variety of FIR filters including lowpass, highpass, bandpass, bandstop and differentiator filters. A routine is also available for the spectral analysis of time series. Energy or phase spectra can be produced for a specified section of a seismogram using the NLOGN fast fourier transform routine (Robinson, 1967).

3A.3.1.1 Spectral analysis.

Spectral analysis was carried out on selected seismograms. Figures 3.1 (a-c) show energy spectra of noise and noise + seismic signal (denoted "signal") of vertical component records from the Baringo and Naivasha shots. Inspection of such spectra led to the following conclusions.

(1) The frequency of the seismic signal is generally less than about 15 Hz.

(2) The noise is sometimes of significantly higher frequency than the signal (e.g. st30, BA1 and st23, NAI) but the spectra of noise and signal often overlap (e.g. st33, BA1 and st35, BA2).

(3) The energy spectra of the pre-signal noise of st41, BA1 and st11, NAI show a dominant frequency of 5 Hz. This is common to all the Geostore records, having resulted from 50 Hz mains pick up during digitisation. Tapes were played back at 10 times real time which

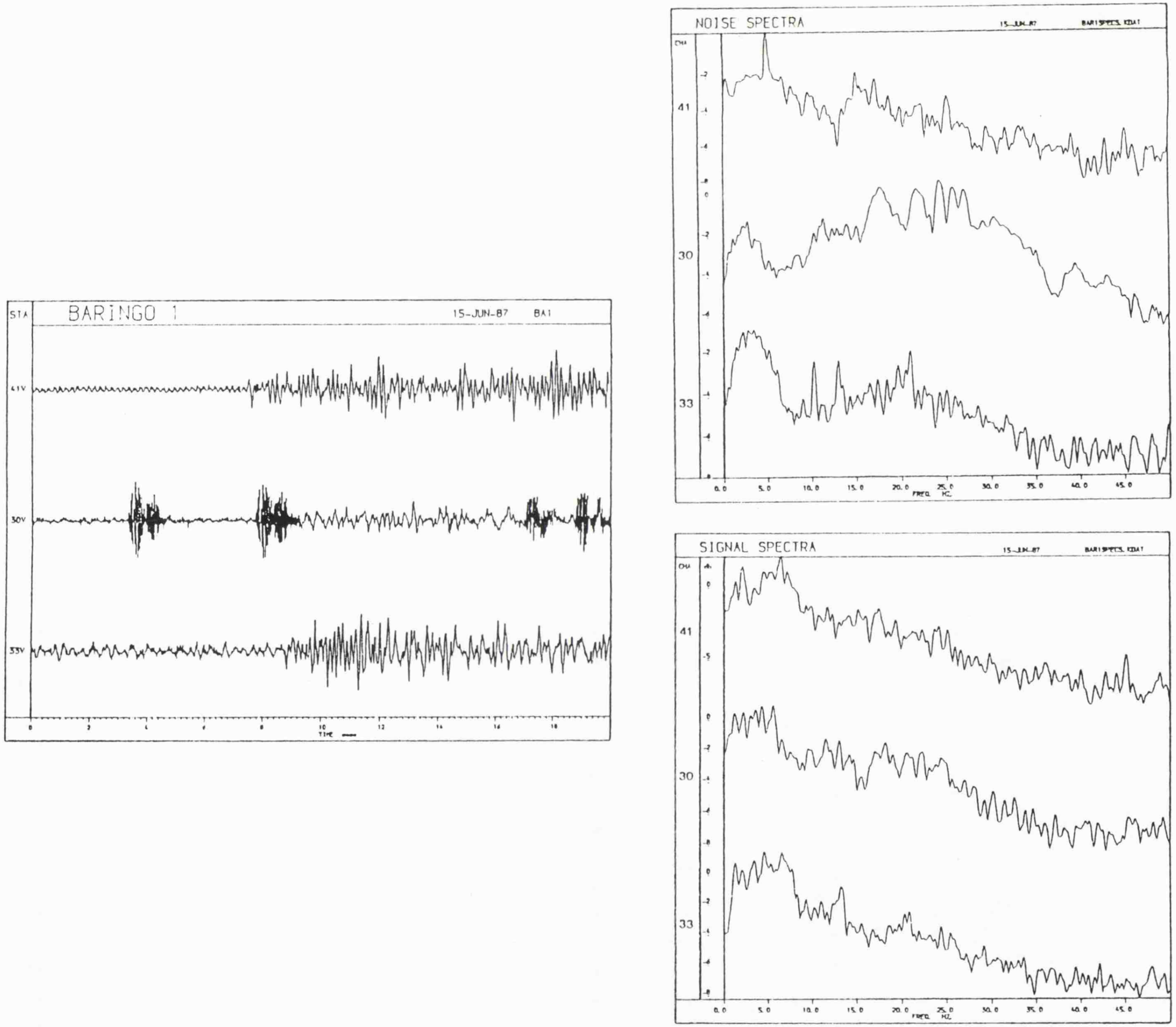

Figure 3.1(a) : Three vertical component recordings of the Baringo 1 shot with accompanying energy spectra of noise and seismic signal.

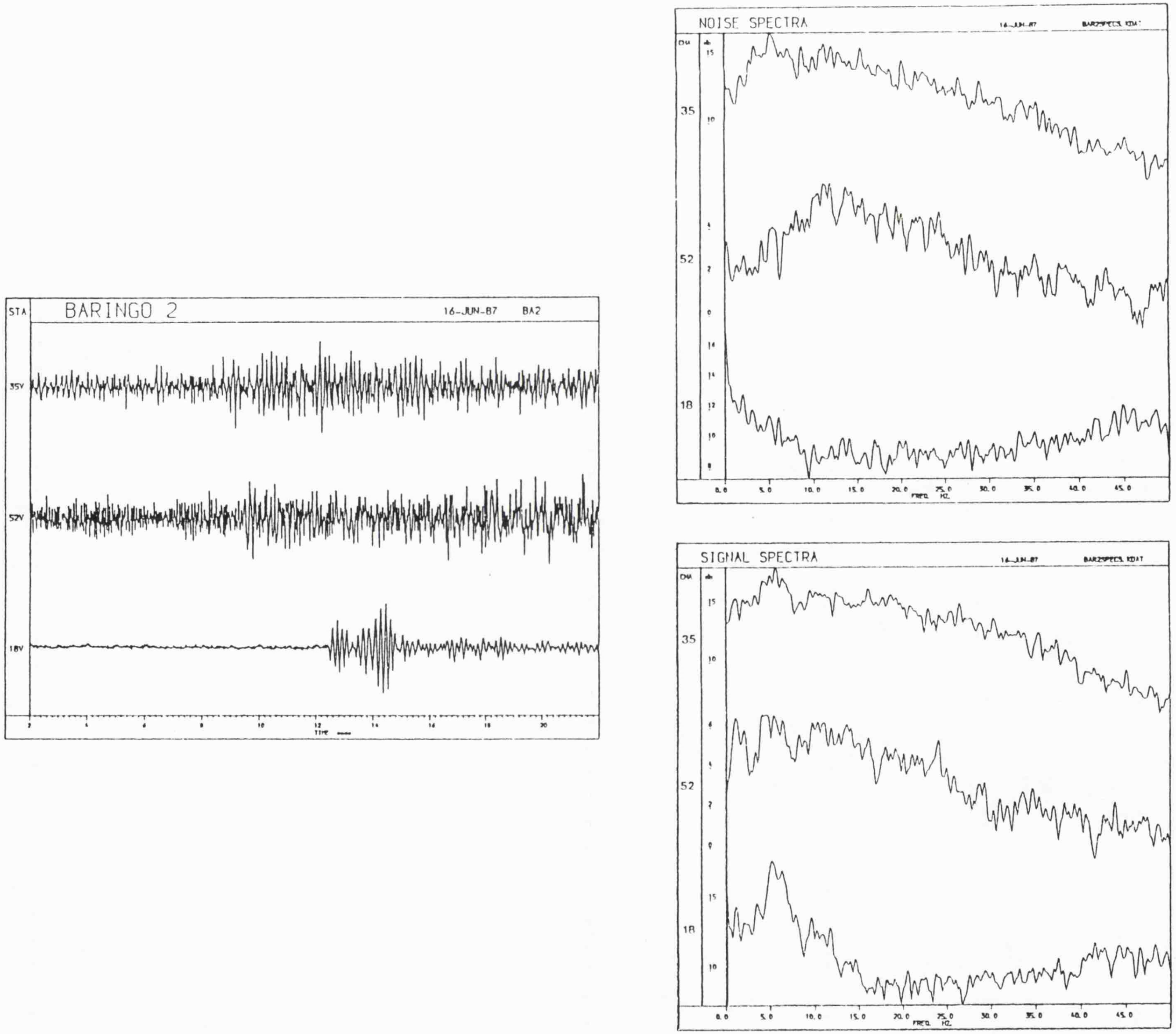

Figure 3.1(b) : Three vertical component recordings of the Baringo 2 shot with accompanying energy spectra of noise and seismic signal.

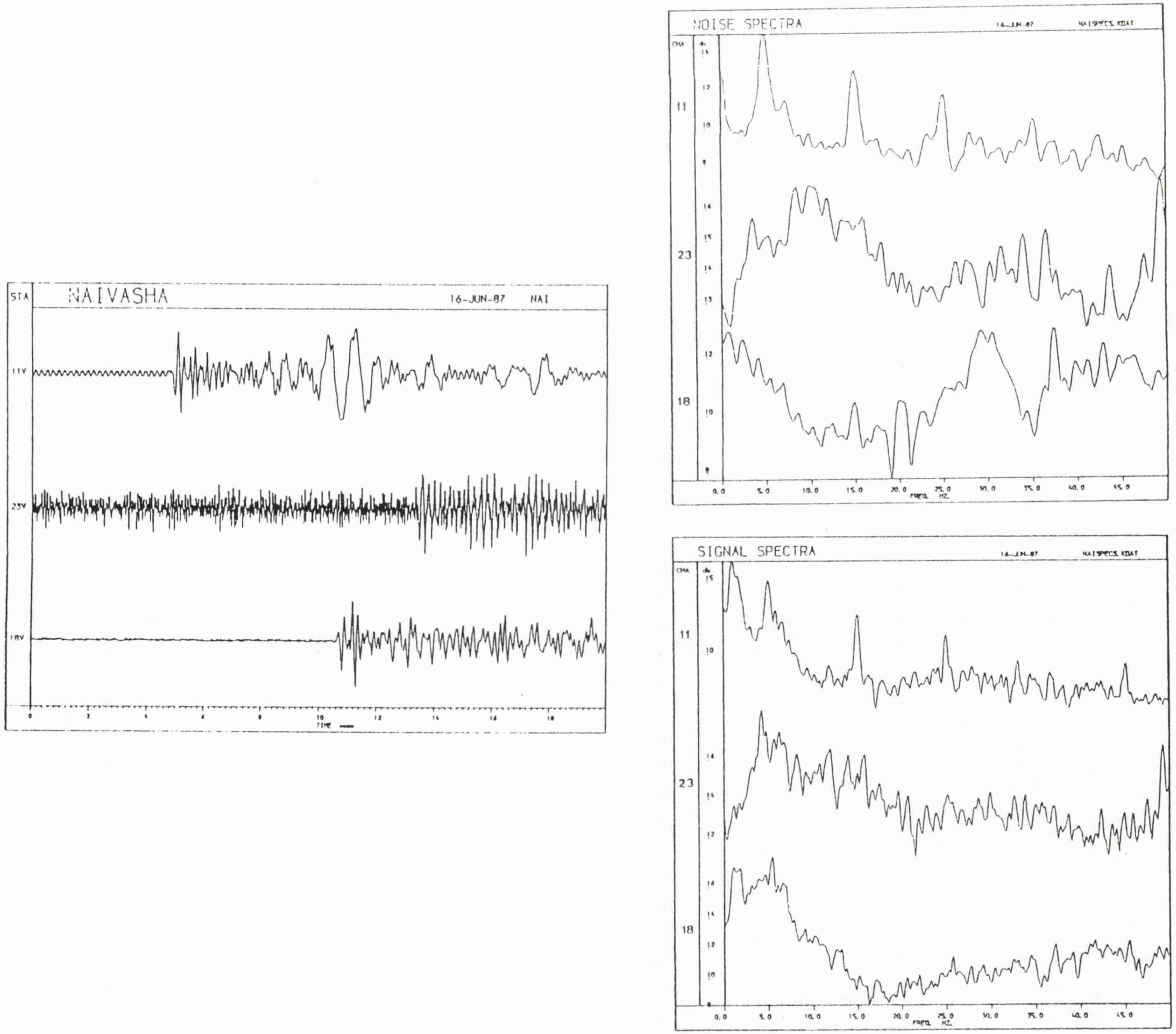

Figure 3.1(c) : Three vertical component recordings of the Naivasha shot with accompanying energy spectra of noise and seismic signal.

caused the 50 Hz mains pick up to appear as 5 Hz on the digitised records. A method of suppressing this spurious A.C. contamination is described in section 3A.4.

3A.3.1.2 Bandpass filtering.

A number of different bandpass filters were tested on a portion of the Baringo record section comprising both BA1 and BA2 traces (vertical component) in the range 45 km to 80 km. These traces were chosen for the trials because it was known that good seismic energy had been generated by the Baringo shots at this range and the poorer quality traces were mainly caused by high background noise levels.

Trials were carried out to ascertain optimum filter parameters. The following parameters resulted in < 10% deviation in the passband and < 1% deviation in the stopbands.

(1) Filter length - 32.

(2) Minimum frequency interval between stopband and passband - 1 Hz.

(3) Ripple weights - 10 (stopbands), 1 (passband).

Figure 3.2 (a-d) shows the result of convolving the Baringo data with three different bandpass filters: (1) 0.5 - 10.0 Hz; (2) 0.5 - 15.0 Hz; and (3) 0.5 - 20.0 Hz. The original unfiltered record section is presented along with the 3 filtered record sections for comparison. It is clear that the bandpass filtering has resulted in a marked improvement in the appearance of the record section. The 0.5 - 10.0 Hz filter clearly gave the best S:N improvement but resulted in the suppression of the higher frequency content of the seismic signal.

It has been shown that bandpass filtering can yield considerable improvement in data quality. As regards the best choice of filter, it depended largely on the high frequency content of the signal. In most cases the optimum choice of the upper passband edge was found to be from 10.0 - 15.0 Hz. The only exception to this was the EWA shot which produced signal energy of significantly higher frequency. In later chapters all record sections presented will be accompanied by details of any filtering performed.

3A.3.2 Polarisation filtering.

When signal and noise exhibit similar spectral characteristics, frequency filters are not effective. The availability of 3 component seismograms allows the determination of filter functions which make use of the polarisation properties of seismic signals in improving S:N ratios. In this study the REMODE type of polarisation filter proved effective. As the

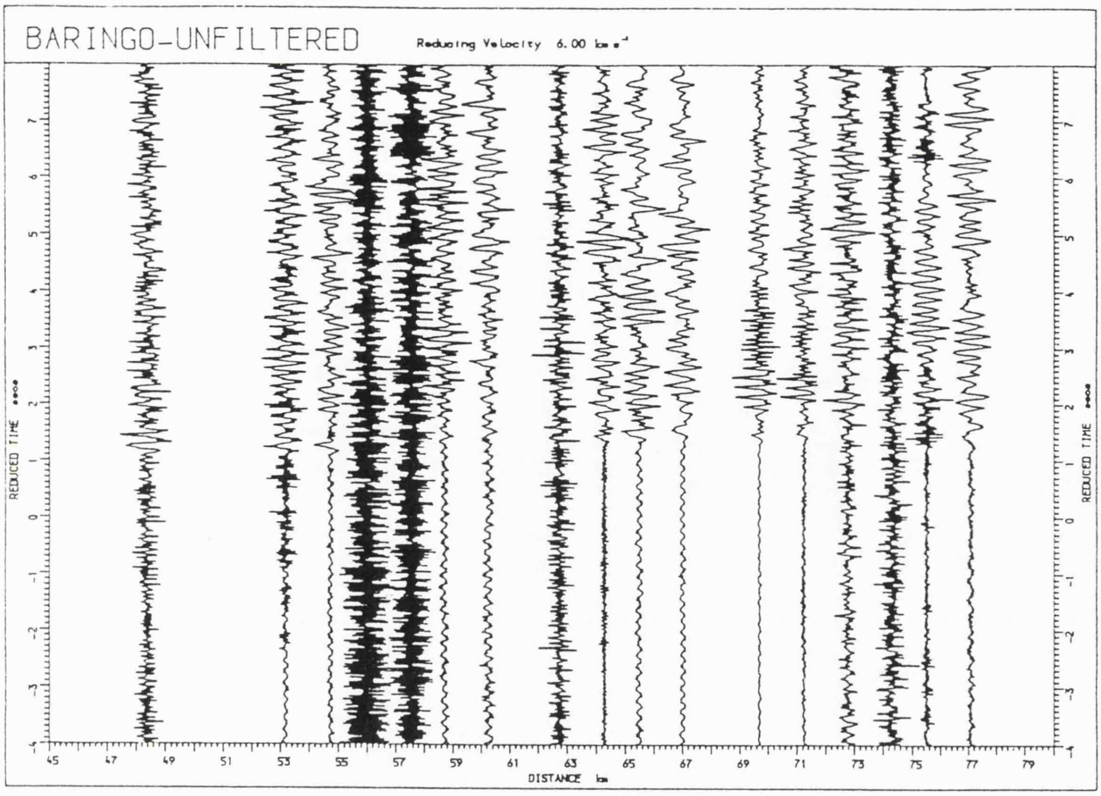

Figure 3.2(a) : Unfiltered portion of the Baringo record section.

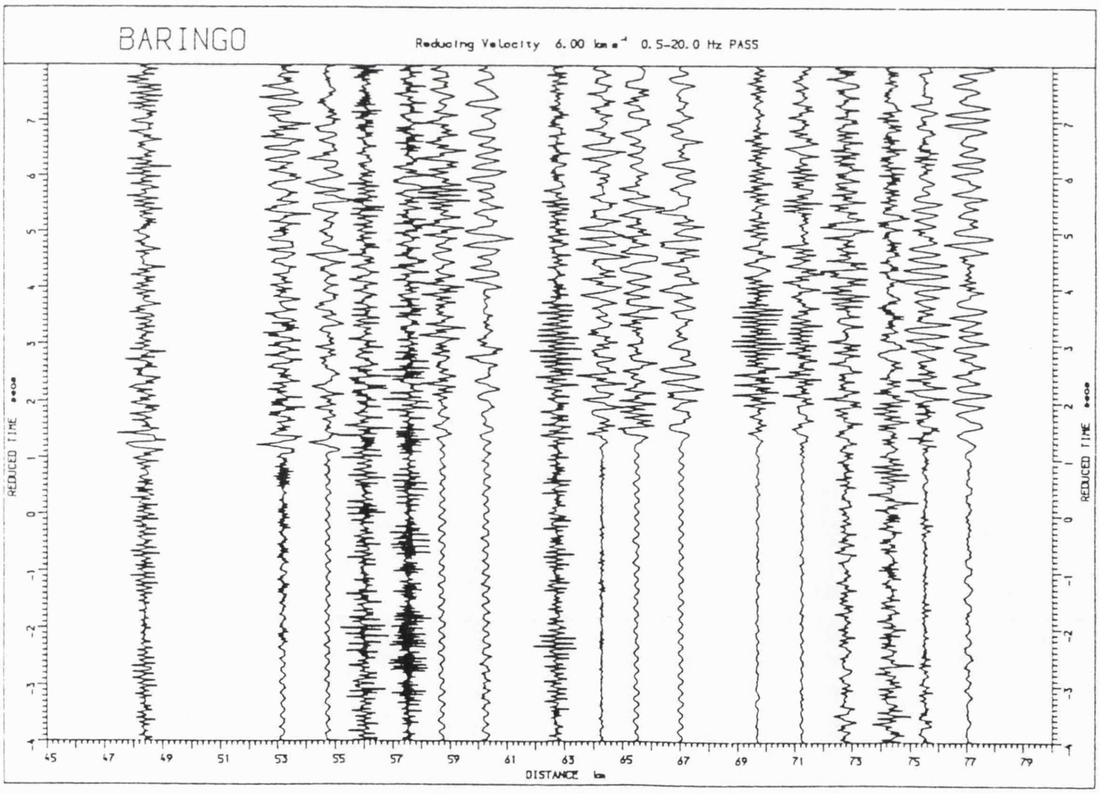

Figure 3.2(b) : Portion of the Baringo record section after the application of a 0.5 - 20.0 Hz bandpass filter.

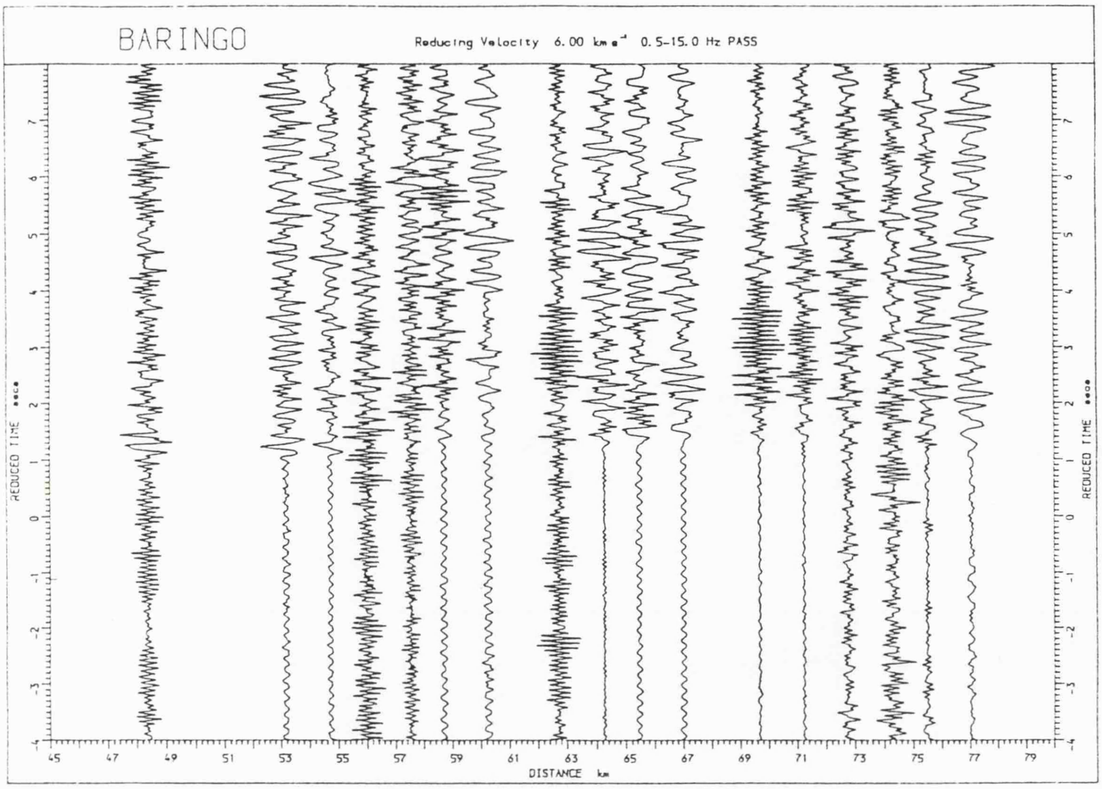

Figure 3.2(c) : Portion of the Baringo record section after the application of a 0.5 - 15.0 Hz bandpass filter.

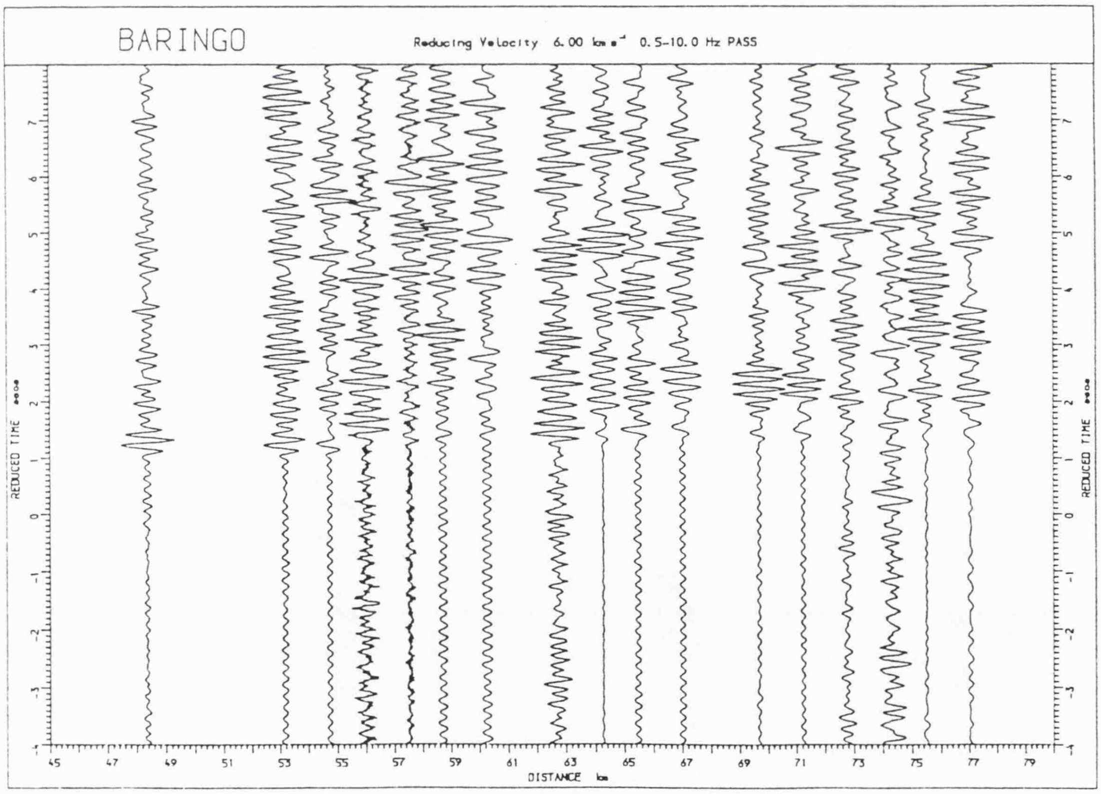

Figure 3.2(d) : Portion of the Baringo record section after the application of a 0.5 - 10.0 Hz bandpass filter.

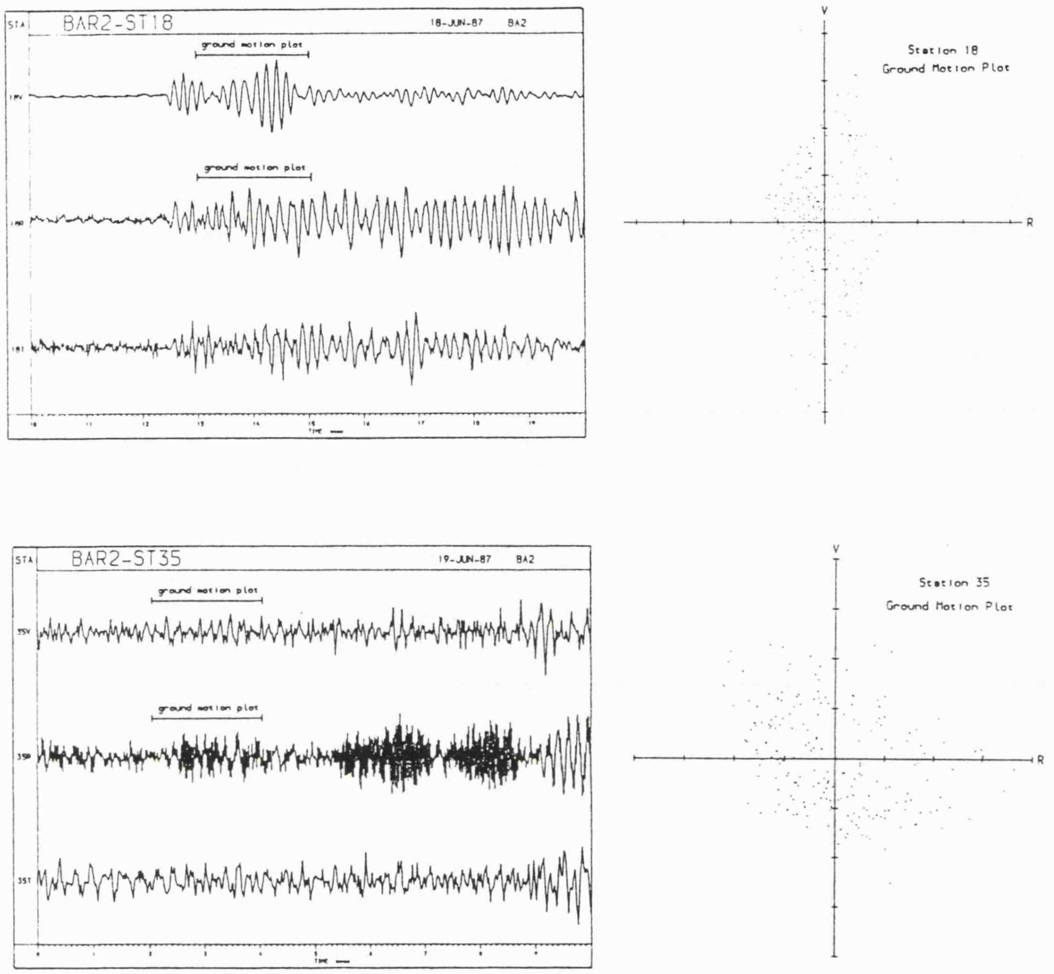

Figure 3.3 : Three component records from stations 18 and 35 of the second Baringo shot with accompanying ground motion plots.

use of this type of filter is not standard, a brief description of its theory is given below.

3A.3.2.1 Theory of REMODE filtering.

Seismic noise consists predominantly of Rayleigh type surface waves of random azimuth (Kanasewich, 1973). It thus exhibits elliptical polarisation with little or no preferred directionality. In contrast, both compressional and shear waves exhibit a high degree of linear polarisation. This is demonstrated in figure 3.3: Programs were written (**HODPLOT** and **HODOGR**, Appendix B) to calculate and plot ground motion from 3 component seismograms. The 2 plots each show ground motion in the vertical-radial plane over a 2 second window. The first is of a compressional wave arrival and shows linear polarisation aligned about 10° from vertical. The second is of background noise and shows no preferred directionality, consisting of randomly aligned ellipses. The REMODE filter (Mims and Sax, 1965; Kanasewich, 1973) makes use of these different polarisation properties. **REMODE** is an acronym for **RE**ctilinear **MO**tion **DE**tector.

The REMODE filter considers only the rectilinearity in the vertical and radial directions. The vertical (z) and radial (r) components are rotated so that the incident body wave bisects the angle between the 2 orthogonal components ($\bar{z}$ and $\bar{r}$ in figure 3.4).

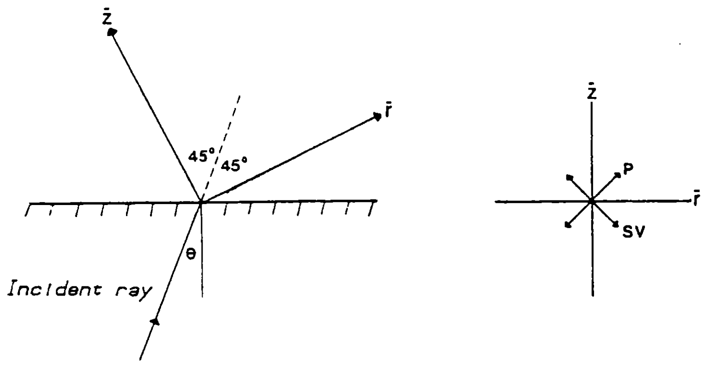

Figure 3.4 : Rotation required to obtain $\bar{z}$ and $\bar{r}$ components. The particle motions of incident P and SV waves are shown along side.

$$\bar{z} = z\cos(\pi/4-\theta) + N\cos\alpha\sin(\pi/4-\theta) + E\sin\alpha\sin(\pi/4-\theta) \qquad 3A.1$$

$$\bar{r} = z\sin(\pi/4-\theta) - N\cos\alpha\cos(\pi/4-\theta) + E\sin\alpha\cos(\pi/4-\theta) \qquad 3A.2$$

where θ is the angle of incidence, α is the azimuth and N and E are the north-south and east-west components respectively. The filter operator is obtained from the cross-correlation function, C(T), of $\bar{z}(t)$ and $\bar{r}(t)$ over a window, W, centred at some time, t, on the time series.

$$C(+T) = \sum_{t-W/2}^{t+W/2} \bar{z}(t)\ \bar{r}(t+T) \qquad 3A.3$$

The negative lags are generated from the positive lags thus insuring that the filter operator is even and introduces no phase distortion. That is

$$C(-T) = C(+T) \qquad 3A.4$$

If the polarisation in the $\bar{z}$-$\bar{r}$ plane is largely rectilinear then C(T) will be large. However, if the motion is elliptical or random it will be small. Thus, by convolving C(T) with the original time series (vertical or radial), rectilinear motion is enhanced and elliptically or randomly polarised motion is attenuated. The filter output is given by:

$$P_Z = K \sum_{T=-L}^{T=+L} \bar{z}(t-T)\ C(T) \qquad 3A.5$$

where K is a normalising factor given by

$$\{K(t)\}^{-2} = \sum_{t-W/2}^{t+W/2} \{\bar{r}(t)\}^2 \sum_{t-W/2}^{t+W/2} \{\bar{z}(t)\}^2 \qquad 3A.6$$

which helps to enhance weak signals of high rectilinearity.

3A.3.2.2 Choice of REMODE filter parameters.

Equations 3A.1 to 3A.6 were coded in FORTRAN (program **REMODE**, Appendix B) and incorporated into the SDPS4 package. Figure 3.5 demonstrates how effective REMODE filtering can be. Each box includes the unfiltered vertical and radial component records along side the vertical component record after the application of the REMODE filter. In all cases a dramatic improvement in S:N ratio is evident. Several parameters must be chosen before applying the filter:

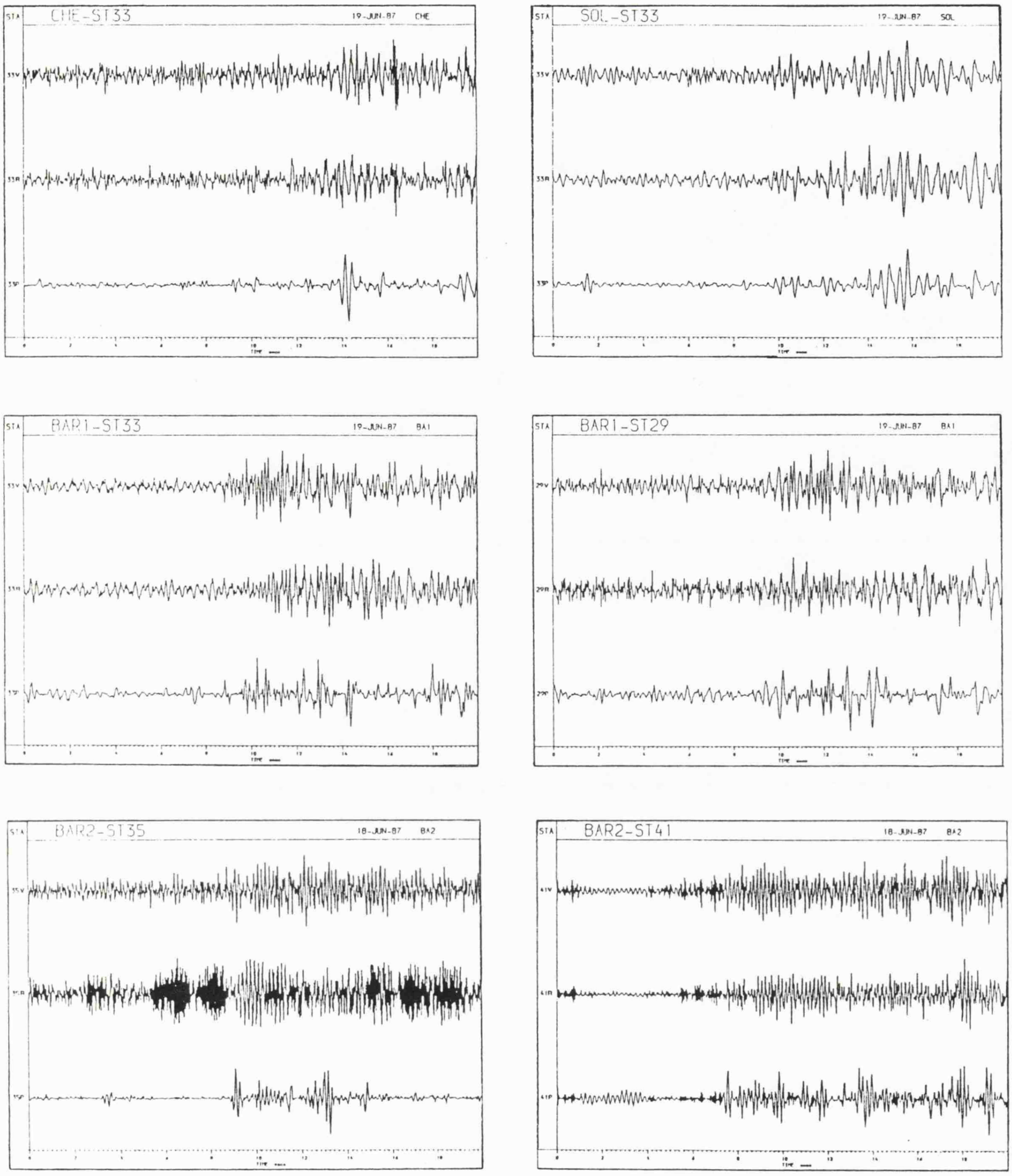

Figure 3.5 : Six examples of the signal enhancement resulting from the application of the REMODE polarisation filter. Each box includes the unfiltered vertical and radial component traces and the vertical component trace after REMODE filtering.

Filter length: This corresponds to (2L+1) in the notation of equation 3A.5. It determines the length of the filter operator to be convolved with the data. The optimum value was found to range from 4 - 8 samples (sample interval = 10ms). Longer values resulted in a smeared output while shorter values gave reduced signal enhancement.

Cross-correlation window length: This parameter corresponds to W in equation 3A.3. It determines the number of samples used in the cross correlation to evaluate the filter operator elements. Maximum enhancement was obtained for a window length of around 50 samples (0.5 secs).

Angle of rotation. This is angle θ, shown in figure 3.4, through which the original axes must be rotated for the incident ray to bisect the new axes ($\bar{z}$ and $\bar{r}$). Of course, this depends on the angle of incidence of the incoming wave. Figure 3.6 shows how the S:N ratio of a REMODE filtered trace (st41, BA2) depends on the angle of rotation chosen. Maximum enhancement was obtained for a rotation of about 35° which corresponds to an angle of incidence of 10° from vertical.

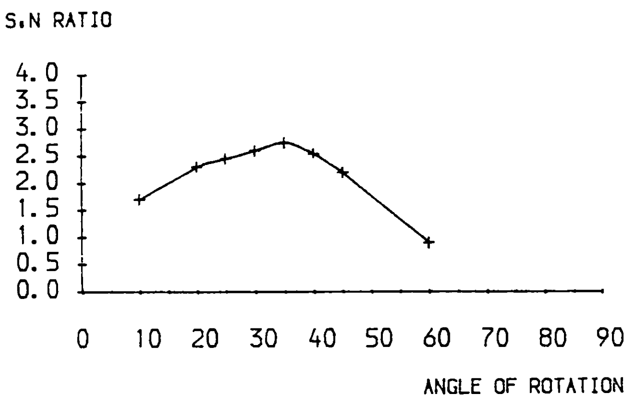

Figure 3.6 : The effect of angle of rotation on signal enhancement resulting from REMODE filtering.

3A.3.2.3 Effectiveness of the REMODE filter.

As will be discussed in the next section, the REMODE filter proved to be effective as an aid to picking first arrival times. It had been hoped that it would also help with the correlation of later phases. However, when complete record sections were REMODE filtered it proved impossible to make reliable correlations other than of first arrivals. Later bursts of energy produced by the filter appeared quite random and could not be correlated confidently from trace to trace.

3A.4 Picking of first arrival times.

3A.4.1 Sources of observational errors.

(1) Signal rounding: As a seismic wave travels from source to receiving station its higher frequencies are attenuated more severely than its lower frequency content. This loss of high frequencies increases with range causing progressive rounding of the first break. Thus the uncertainty in onset times tends to increase with range. However, given the absence of significant background noise, it was estimated that all onset times are accurate to within about 2 samples ($\pm$0.02 secs).

(2) Background noise: It was found that in the presence of moderate background noise (S:N ratio > 2.0) onset times could still be picked quite accurately ($\pm$ 0.05 secs approx). Higher noise levels made the picking of onset times considerably more subjective. A later cycle could be mistaken for a first arrival leading to a substantial error. However, such an error is often obvious from a comparison with onset times from adjacent traces. Various methods designed to make such picks more reliable are discussed in the following section.

(3) A.C. component: The 5 Hz A.C. contamination caused by mains pick up during Geostore tape digitisation (section 3A.3.1.1) led to increased uncertainty in the picking of certain onset times. A method devised to solve this problem is described in the following section.

3A.4.2 Aids to the picking of first arrivals.

First arrival times were measured using program **PICK** (Appendix B) along with the relevant record section. **PICK** enabled any trace to be viewed, sample by sample, on a V.D.U. screen and the first arrival time chosen. Various techniques were used to make "difficult" picks more reliable.

(1) REMODE filter: The use of the REMODE polarisation (section 3A.4.2) often made first breaks significantly more impulsive, thus improving the "pickability" of the trace.

(2) Numerical correlation: Cross-correlation between traces was performed using program **PHASECOR** (Appendix B). A clearly identifiable phase from one trace could be cross-correlated with an adjacent trace of poorer quality. The maximum of the cross-correlation function gives an estimate of the

difference in arrival time between the 2 traces.

(3) Tracing paper correlation: The above process was also carried out by eye with the aid of tracing paper. A clear first arrival wavelet from one trace was copied and superimposed on a poorer quality adjacent trace thus allowing a more confident pick to be made.

(4) A.C. removal: The 5 Hz A.C component could not be removed by normal frequency filtering as 5 Hz occurs within the signal energy spectra of most traces. A method of removing it was devised in which it was averaged over 10 cycles before the arrival of seismic energy and then simply subtracted over the whole trace length (program **ACSHIFT**, Appendix B). This method proved effective as shown in figure 3.7 which shows three traces before and after "A.C. removal".

3A.4.3 Error estimation.

Tables of all the first arrival times picked are presented in Appendix A. Estimates of the observational error associated with each pick were made by assessing the range of time within which the arrival could be said to lie. In general, the lower the S:N ratio the higher the error estimate. It was always assumed, however, that the correct wavelet had been chosen as the first arrival. This could, in a few instances, lead to a gross underestimate of the error but would normally show up in the reduced velocity plot.

The observational error variance, σ_e, is defined by

$$(\sigma_e)^2 = 1/N \sum_{n=1}^{n=N} e_n^2 \qquad \text{3A.7}$$

where e_n are the observational errors for N observations. In practise, the actual observational errors are not available but an approximate error variance, σ_{est}, can be calculated from the error estimates as follows.

$$(\sigma_{est})^2 = 1/N \sum_{n=1}^{n=N} (e_{est})^2 \qquad \text{3A.8}$$

It will later be seen that this estimate of the observational error variance is useful when deciding whether a model shows a "lack of fit" or

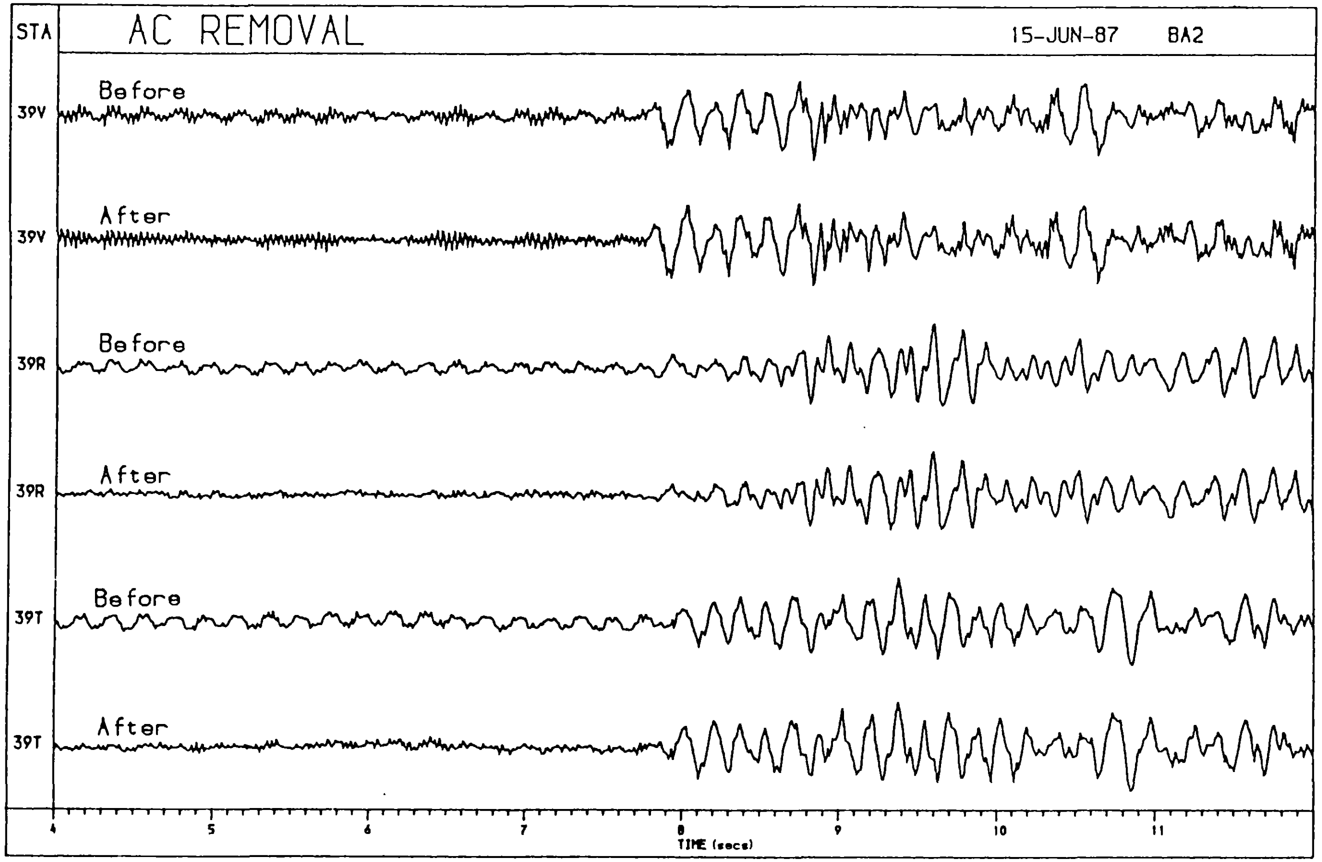

Figure 3.7 : A.C. contaminated traces before and after "A.C. removal".

if the data has been "over modelled".

3A.5 Recovery of amplitude information.

It had originally been intended to normalise the amplitude and phase responses of the various recording systems deployed to those of a reference instrument. This process should improve the lateral coherency of seismic phases and allows modelling of the amplitude-distance variations. Baker et al (1982) presented a suitable method in which the responses of both the actual and reference recording systems are approximated by z polynomial expressions and the normalisation performed by recursive filtering. However, it was decided that KRISP85 refraction data, much of which is very noisy, did not merit such treatment. Instead a simple scaling factor was calculated for each instrument type which allowed the recovery of true amplitude information.

3A.5.1 Determination of scaling factors.

Four huddle tests, as described in section 2.6, allowed the direct comparison of all but one of the recording systems. Unfortunately, the DR100 instruments were not available at the time of these tests. However, DR100 and Wisconcin instruments were situated sufficiently close together on the NS-line for a comparison to be made from the recordings of the BA2 shot.

Figure 3.8 shows a selection of the traces recorded of the second Susua huddle shot. The overloading of some recorders resulted in severe distortion. However, the comparison of individual samples from the first few cycles allowed relative scaling factors to be calculated for the different recording systems. This was carried out on all the available huddle test records. An average scaling factor was then calculated for each system. Similarly, Wisconsin and DR100 recordings of the BA2 shot were used to calculte a scaling factor for the DR100 recorders. The scaling factors derived are shown in table 3.1. Note the factor of 2 difference between digital and analogue Geostore stations. The DR100 scaling factor does not apply to all the DR100 recorders as some had been altered since manufacture. As a result three different scaling factors were needed, the choice of which depended on the individual recorder identification number.

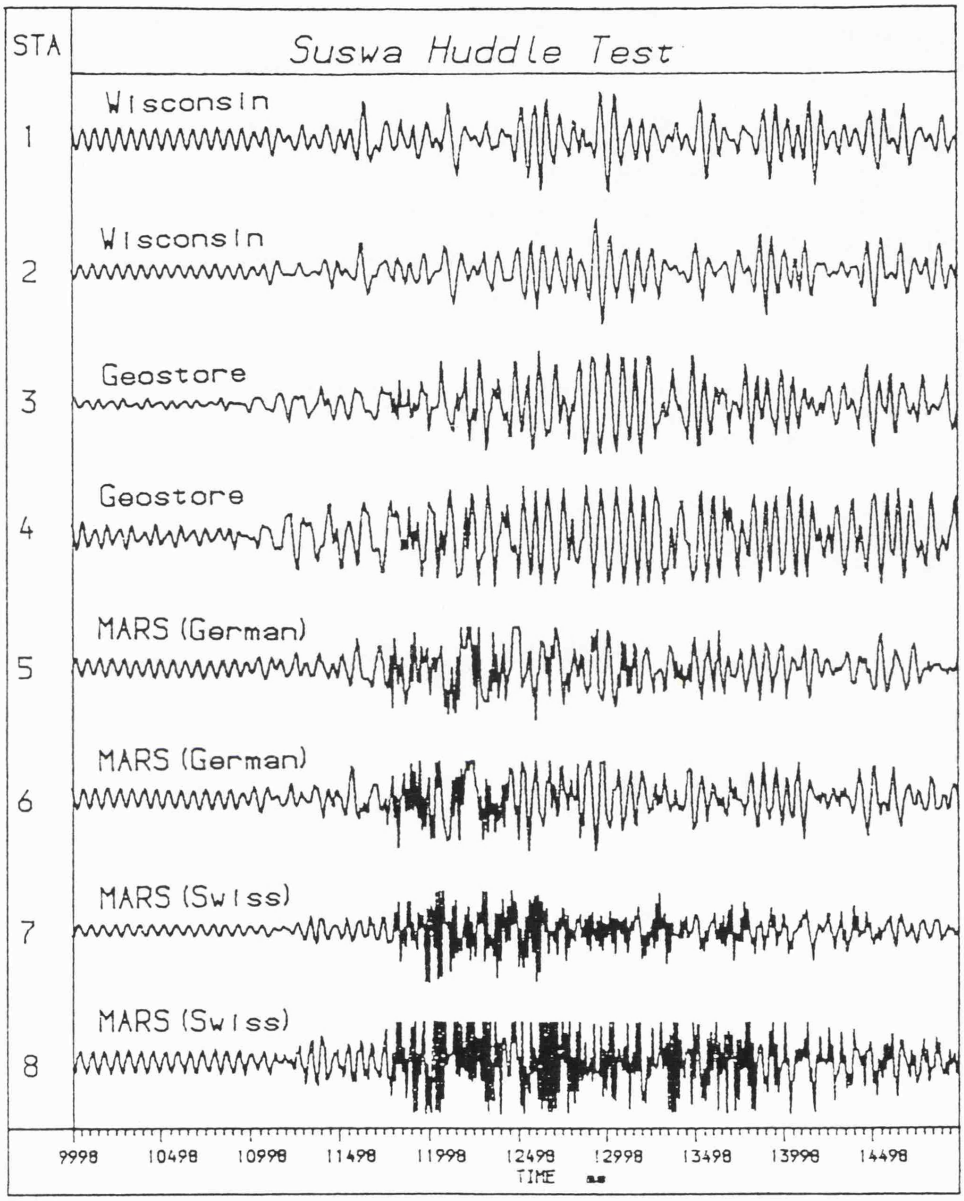

Figure 3.8 : Vertical component recordings of the second Susua huddle test shot.

Table 3.1 : Scaling factors.

Instrument	Gain	Scaling-factor
Wisconsin	24 dB	0.05
Geostore (analogue)	5	0.4
Geostore (digital)	5	0.2
MARS (German)	5	0.11
MARS (Swiss)	6	0.16
DR100	72 dB	2.45

3A.5.2 True amplitude plotting.

The SDPS4 record section plotting routines were modified to allow true amplitude as well as normalised sections to be plotted. This was achieved by calling a subroutine (**TRUE** Appendix B) which performed the required scaling according to the recorder type and gain setting for each trace. A facility was also included to allow range dependent scaling to be performed i.e. for the amplitude of each seismogram to be multiplied by the source-receiver distance raised to a desired power.

B. INTERPRETATION METHODS

3B.1 Least squares analysis.

Apparent velocities and intercept times of refracted phases were calculated by least squares analysis. Program **LINEFIT** (Appendix B) was written for this purpose. It calculates an apparent velocity, intercept time and associated errors for chosen arrival times. The observations were weighted by the reciprocal of the observational error estimate. The arrival time could optionally be corrected for elevation according to the relation

$$\Delta t = \Delta h / (V_1 \cos\theta) \qquad \text{3B.1}$$

where Δt is the time correction, Δh is the elevation difference between stations, V_1 is the velocity of the layer above the refractor and θ is the angle of incidence, assumed critical.

3B.2 Ray tracing using SEIS81.

SEIS81 is a 2-D seismic ray tracing package written by Cerveny, P. and Psenick, I. (Cerveny et al, 1974). It is designed for the computation of seismic rays which arrive at a system of receivers distributed regularly or irregularly along the Earth's surface i.e. "two-point ray tracing". Corresponding travel times, amplitudes and phase shifts are evaluated and synthetic seismograms may be computed if desired. The 2-D model can be laterally inhomogeneous with a combination of curved interfaces, vanishing layers, block structures and isolated bodies. Within an individual layer velocities may vary both vertically and horizontally. The source location is arbitrary and the source radiation pattern may be specified.

A version of **SEIS81** was obtained from the Geophysical Institute at the University of Karlsruhe, West Germany, and implemented on the University of Leicester "VAX cluster". Only the graphics routines were modified significantly, these being converted to use **GHOST80** rather than **CALCOMP** graphical subroutines. This allowed the plotting of ray tracing diagrams etc. on a variety of plotting devices.

No attempt is made to give a rigorous derivation of the mathematics used in 2-point ray tracing. However, an outline of the major computations performed and an example of **SEIS81** in use are included below.

3B.2.1 Theory of 2-point ray tracing.

Treatments of ray tracing theory are given by Cerveny et al (1974), Cerveny et al (1977) and Aki and Richards (1980). This summary deals with 4 aspects of ray tracing; (1) the behaviour of a ray in medium with a continuous velocity function , (2) geometrical spreading, (3) the effect of a first order interface and (4) source characteristics.

3B.2.1.1 Medium with a continuous velocity function.

Notation: x_i - Cartesian coordinates.
v - local velocity which is a continuous function $v(x_i)$ of the coordinates.
t - time.

The wave front of a seismic body wave is described by

$$t = T(x_i) \qquad \text{3B.2}$$

With t held constant this is an implicit equation for a surface i.e. the position of the wave front at a particular time. In an isotropic medium rays are the orthogonal trajectories to the system of wave fronts and are given by the explicit equation

$$x_i = X(t) \qquad \text{3B.3}$$

The direction of the rays are determined by the vector ∇T or alternatively

$$p_i = \partial T/\partial x_i \qquad \text{3B.4}$$

where p_i are the components of the slowness vector, tangential to the ray and of magnitude $1/v$. It can be shown (Aki and Richards, 1980) by considering motions near a wave front that in a general, inhomogeneous medium the function $T(x_i)$ must satisfy the "eikonel equation", which can be written

$$(\nabla T)^2 = 1/v^2 \qquad \text{3B.5}$$

or in terms of slowness vector, p_i, as

$$p_i p_i = 1/v^2 \qquad \text{3B.6}$$

and is a non linear partial differential equation of the first order. Using the ray equation 3B.3 this can be used to give a system of 6 ordinary differential equations of the first order which govern the behaviour of the ray (Aki and Richards, 1980).

$$dx_i/dT = v^2 p_i \quad \text{and} \quad dp_i/dT = -\partial \ln(v)/\partial x_i, \quad i=1,3. \qquad 3B.7$$

These can be solved by standard numerical methods. Thus if a ray is specified by its initial values ($t=t_0$, $x_i=(x_i)_0$, $p_i=(p_i)_0$) the coordinates, x_i, along the ray at any later time can be numerically computed.

If the direction of the ray is specified by azimuth, A, and declination, D then the slowness vector components can be written

$$p_1 = v^{-1}\cos A \sin D, \; p_2 = v^{-1}\sin A \sin D \text{ and } p_3 = v^{-1}\cos D \qquad 3B.8$$

If the velocity depends only on 2 coordinates (say x_1 and x_3) then the system of equations (3B.7) reduces to the following 3 ordinary differential equations

$$dx_1/dT = v(\sin D), \qquad dx_3/dT = v(\cos D)$$

$$\text{and} \quad dD/dT = -v_1(\cos D) + v_3(\sin D) \qquad 3B.9$$

where $v_1 = \partial v/\partial x_1$ and $v_2 = \partial v/\partial x_3$. The system is solved by the Runge-Kutta method enabling the ray coordinates to be ascertained up to the point of intersection of the ray with an interface or boundary.

3B.2.1.2 Geometrical spreading.

The evaluation of geometrical spreading for a ray is simplified if "ray coordinates", q_1, q_2 and T are introduced. The first 2 specify the ray in question (e.g. take off angle at point of source) and T represents the position of the point on the ray. The cross-sectional area of an elementary "ray tube", $d\sigma$, can be evaluated from the relation

$$d\sigma = J\, dq_1\, dq_2 \qquad 3B.10$$

where

$$J = |\partial \mathbf{x}/\partial q_1 \wedge \partial \mathbf{x}/\partial q_2| \quad \text{and} \quad \mathbf{x} = (x_1, x_2, x_3).$$

$||$ denotes the "magnitude of" and Λ denotes the "cross product". The amplitudes of 2 different points on the ray, $A(T_0)$ and $A(T_1)$, are related as follows

$$A(T_1)\surd\{v(T_1)\rho(T_1)J(T_1)\} = A(T_0)\surd\{v(T_0)\rho(T_0)J(T_0)\} \qquad 3B.11$$

where ρ denotes density. Thus the ray amplitudes can be calculated if values of J are known.

If the ray tube spreads only in the (x_1,x_3) plane then it can be shown (Cerveny et al, 1974) that

$$dg_1/dT = g_1v_1\sin D + g_2v_3\sin D + g_3v\cos D$$

$$dg_2/dT = g_1v_1\cos D + g_2v_3\cos D - g_3v\sin D \qquad 3B.12$$

$$dg_3/dT = g_1(v_{13}\sin D - v_{11}\cos D) + g_2(v_{33}\sin D - v_{13}\cos D)$$
$$+ g_3(v_1\sin D + v_3\cos D)$$

where $g_1=\partial x_1/\partial D_0$, $g_2=\partial x_3/\partial D_0$, $g_3=\partial D/\partial D_0$ and $v_{ij}=\partial^2 v/\partial x_i\partial x_j$. D_0 denotes the declination of the ray at the source. Now, g_1 and g_2 are related to the function J by

$$J = \surd(g_1^{\ 2} + g_2^{\ 2}) \qquad 3B.13$$

so J can be evaluated if the above system of differential equations (3B.12) is solved. Thus, the effect of geometrical spreading on the amplitudes of body waves can be calculated.

3B.2.1.3 First order interface.

Consider an interface corresponding to the surface where the velocity function $v(x_i)$ is discontinuous. It can be described by

$$f(x_i) = 0. \qquad 3B.14$$

The components N_i of the normal to the interface are given by

$$N_i = \pm\, \partial f/\partial x_i \;/\; \surd\{\partial f/\partial x_j\ \partial f/\partial x_j\}. \qquad 3B.15$$

The sign depends on the desired orientation of the normal. Let $T=T_r$ denote the point of intersection of the ray with the interface. It is necessary at this stage to introduce some new notation. Let capital letters refer to the point of incidence and barred letters to the medium beyond the interface. Thus at the point of incidence we have X_i, $\bar{X}_i$, P_i, $\bar{P}_i$, V and $\bar{V}$. Of these, X_i, P_i, V and $\bar{V}$ are known quantities and $\bar{X}_i$ and $\bar{P}_i$ are to be determined. Obviously, the continuity of the ray dictates that

$$\bar{X}_i = X_i \qquad \text{3B.16}$$

and it can be shown that $\bar{P}_i$ and P_i are related by

$$\bar{P}_i = P_i - N_i(A \pm B) \qquad \text{3B.17}$$

where

$$A = P_i N_i \quad \text{and} \quad B = \sqrt{\bar{V}^{-2} - V^{-2} + A^2}. \qquad \text{3B.18}$$

The + sign refers to the transmitted wave and the - sign to the reflection. Conversions are handled by giving V and $\bar{V}$ appropriate values (P wave velocity or S wave velocity). The derivatives of X_i and P_i with respect to ray parameters are calculated in similar fashion (Cerveny, 1974) which gives a complete new set of initial values for the continuation of the tracing of the ray beyond the interface.

Reflection/transmission coefficients are calculated using standard formulae (Zoeppritz, 1919) with the relevant values for angle of incidence, V, $\bar{V}$, ρ and ρ. Thus, the amplitude variations across the interface can be computed.

<u>3B.2.1.4 Source characteristics</u>.

The source may be situated at any point in the model and may generate both P and S waves. The radiation patterns of the source may be specified independently, either from tables or analytically, for P or S waves. The source time function has the form of a harmonic carrier modulated by a Gaussian envelope i.e.

$$f(T) = \exp[-(2\pi F_m T/\gamma)^2]\cos(2\pi F_m T+v) \qquad \text{3B.19}$$

where F_m, γ and v are free parameters which govern the wavelet characteristics.

3B.2.2 Operation of **SEIS81**.

The first step in the running of the **SEIS81** package is the creation of a model file. This contains all of the input parameters required by the main program (**SRAY**). The 2-D velocity model is bounded by 2 vertical boundaries and 2, possibly curved, boundaries representing the ground surface and the bottom of the model. Each interface crosses the whole model and is specified by a series of points which are approximated by cubic spline interpolation. Within a layer the velocity is specified at the grid of points of a rectangular network which must cover the entire layer. The velocity distribution is then computed by a bicubic spline approximation.

If refractions are desired from below any interface then the underlying layer must be assigned with a vertical velocity gradient (increasing downwards). The pure head waves, that generally do not exist in laterally inhomogeneous media with curved interfaces, are not considered by **SEIS81**. If desired they must be simulated by slightly refracted waves.

Receivers are distributed regularly or irregularly along the Earths's surface.

During the running of **SRAY** the numerical codes of desired seismic body waves are generated (either automatically or as specified in the input file). The "shooting method" is used i.e. rays are "fired" from the source location at a range of initial angles specified in the input file. For each initial angle, the termination point of the resulting ray is found. If the termination point is not close to a receiving position then shooting is continued with a new initial angle. However, if a ray terminates at the surface and a receiver lies between this and the previous termination point then shooting proceeds iteratively. A "successful iteration" occurs when the ray terminates within a pre-set distance from the receiving position, in which case the amplitude of the arrival is computed and all the information on that ray is sent to output files. In the shooting method care is devoted to certain singular situations (e.g. in the neighbourhood of a critical ray) with the aim of receiving possible refracted waves. Subsidiary routines allow the plotting of ray tracing diagrams, travel time plots or synthetic seismograms.

3B.2.3 Example of **SEIS81** in use.

The KRISP68 velocity model (Griffiths et al, 1971) was chosen to demonstrate **SEIS81**. The 1D P-wave velocity model used was as shown in figure 1.6 except that the 6.4 and 7.5 km/s layers were given velocity depth gradients in order to produce refracted arrivals. In line with the original interpretation, no reflections were generated. Receiving

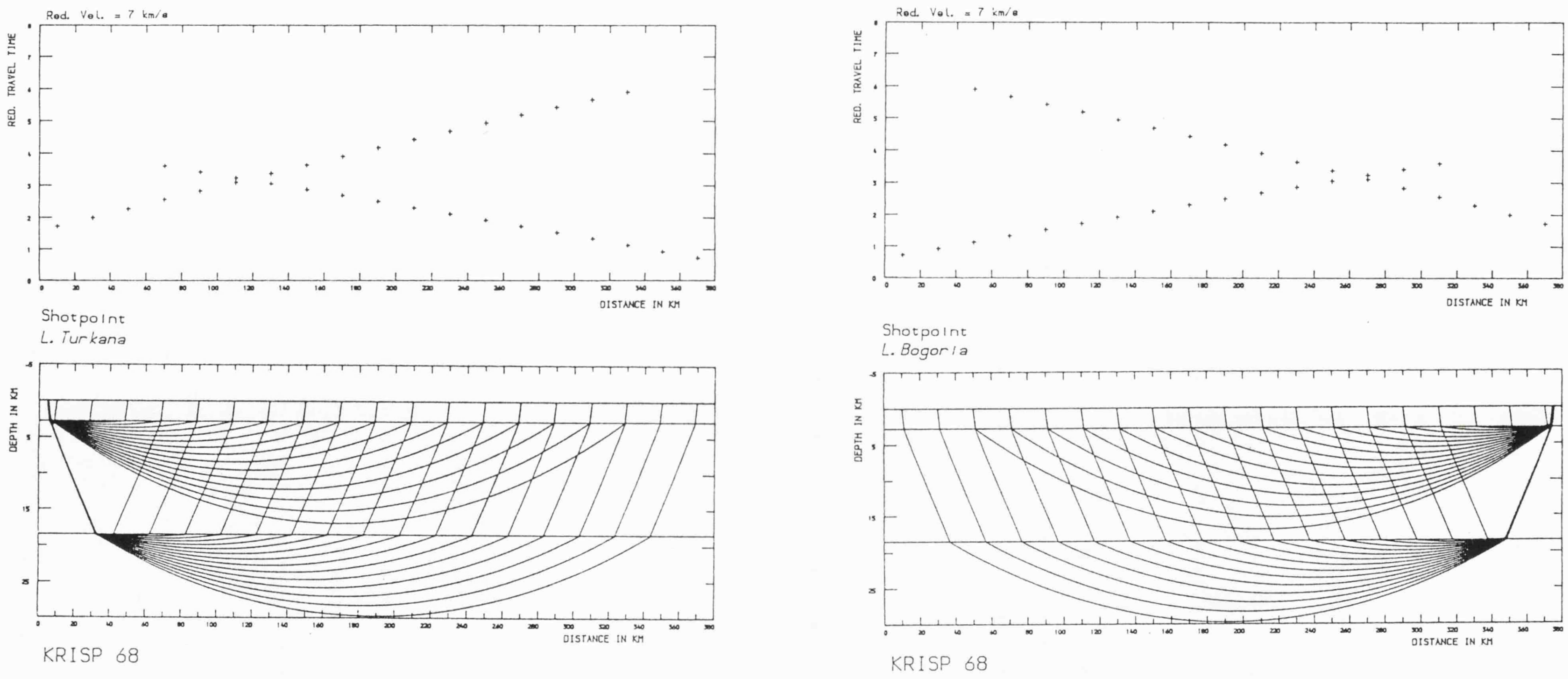

Figure 3.9 : Ray-tracing diagrams and reduced velocity plots obtained from the KRISP68 velocity model.

positions were located at 20 km intervals along the 380 km long model. No account was taken of surface elevation. Figure 3.9 shows the ray tracing diagrams and reduced velocity plots from simulated shots in Lake Turkana and Lake Bogoria (as used in the KRISP68 experiment). Obviously, the plots for the 2 shots are mirror images as the velocity model is 1 dimensional.

3B.3 Time-term analysis.

The time-term method is described in detail by Willmore and Bancroft (1960), Grant and West (1966) and Bamford (1972). A brief outline of the method is included below, followed by an example of its application.

3B.3.1 Theory.

The expression for the travel time of a refracted wave can be written

$$t_{ij} = a_i + a_j + X_{ij}/V \qquad i = 1,N_s \quad j = 1,N_r \qquad \text{3B.20}$$

where: t_{ij} is the travel time between ith shot and jth recorder
a_i is the shot time-term (delay time)
a_j is the receiver time-term (delay time)
X_{ij} is the shot-receiver distance
V is the refractor velocity
N_s is the number of shots
N_r is the number of receivers

Travel times of refracted arrivals can thus be separated into three parts: a down time from the source to the refractor; a time along the refractor; and an up time from the refractor to the receiver (Fig. 3.10). If certain conditions are satisfied then it is possible to determine the values of the unknowns a_i, a_j and V which give the best fit to the observed travel times and distances.

The time-terms are defined as

$$a_i = h_i \cos\theta_i / V_0 \qquad \text{3B.21}$$

where: h_i is the length of the normal
θ_i is the angle of incidence
V_0 is the velocity of the upper layer

If the velocity of the upper layer is known then the depth to the

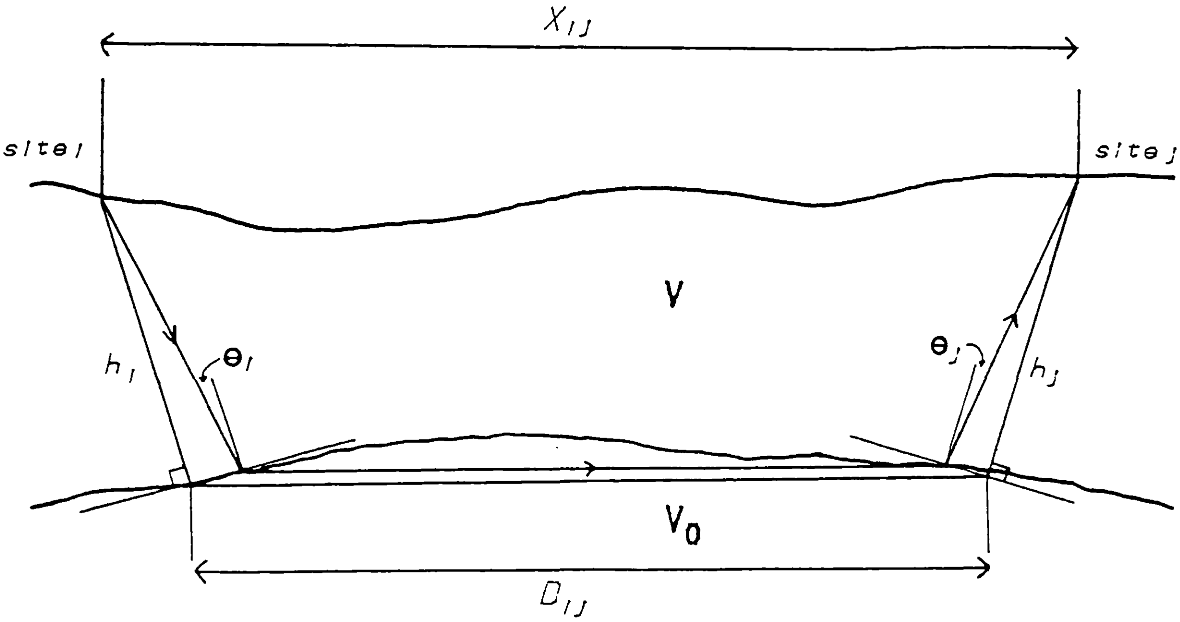

Figure 3.10 : Raypath of a refracted arrival.

refractor can be calculated.

The requirements of the method (as described in the references listed above) are that the velocity of the refractor is uniform and its topography is not too severe. Raitt et al (1969) describe a development of the method which allows for anisotropy of the refractor. Provided there are more knowns than unknowns the system of equations can be solved by least squares. However, the unknowns cannot be determined uniquely unless at least one shot site and receiver site are coincident or one or more stations lie on "outcropping" refractor (Willmore and Bancroft, 1960). The method is most applicable if each receiving station records several shots and if shot points are receiving stations for other shots.

Equation 3B.20 is only exact for a horizontal refractor. In general, a closer approximation to the travel time is written

$$t_{ij} = a_i + a_j + D_{ij}/V \qquad i = 1,N_s \quad j = 1,N_r \qquad \text{3B.22}$$

The distance D_{ij} (Fig. 3.10) is defined by drawing perpendiculars from the sites to the interface tangents at the points of refraction and taking the distance between the points of intersection as the required values of D_{ij}. Of course, the values of D_{ij} are not available so an iterative approach is required. The system of equations is first solved using X_{ij} values as approximations for D_{ij}. The resulting set of time-terms gives a crude indication of the refractor structure from which a set of D_{ij} values can be estimated. These are then used to obtain another solution. This iterative process is repeated until a stable solution is achieved.

The observed travel times are related to the solution values by the relation

$$t_{obs\,l} = a_{si} + a_{sj} + D_{ijl}/V_s + r_l \qquad \text{3B.23}$$

where r_l is the residual associated with observation l. The solution variance is defined by

$$(\sigma_s)^2 = \sum_{l=1}^{l=L} \{r_l^{\,2}/(L-N-1)\} \qquad \text{3B.24}$$

where L is the number of observations and N is the number of time-terms calculated. The ratio of the solution variance to the observational error variance (3A.8) is known as the F ratio (Whitcombe and Maguire, 1979). It is a useful parameter when deciding how "good a fit" has been obtained. If the F ratio is significantly greater than unity then the time-term model shows a "lack of fit". On the other hand, an F ratio significantly less than unity signifies over-modelling of the observed data.

3B.3.2 Example of the time-term method.

In order to test program **TIMTERM** (Appendix B) and as a familiarisation exercise the method was applied to refraction data from a known structure. The 2-D ray tracing package **SEIS81** was used to generate travel times from simulated shots into a simple 2 layer structure involving a syncline and an anticline (Fig. 3.11). The top layer was assigned a velocity of 4.0 km/s and the underlying refractor a velocity of 6.0 km/s. The line included 39 receivers at 2.5 km intervals and "shots" were fired at 0 km, 25 km, 75 km and 100 km. The resulting ray tracing diagrams and reduced velocity plots are shown in figure 3.11. Program **TIMTERM** was run, inputting the shot-receiver distances and the generated travel times. The time-terms obtained were converted to depths using equation 3B.21. Figure 3.12 shows that after 1 iteration the fit between actual and computed refractor depth is reasonable but not perfect. In particular, there are considerable discrepancies at the ends of the model and the anticline is too deep. The structure obtained from the first iteration was used to estimate values for D_{ij} and the inversion process was repeated. It is evident that the new depths obtained (Fig. 3.12) are a better approximation to the actual model, particularly at either end. The refractor velocity was found to be 6.1 $\pm$ 0.04 km/s. This over estimation of the refractor velocity and the remaining misfit in depth, between 45 km and 80 km, are most likely to be a reflection of the velocity depth gradient required by **SEIS81** for the generation of refracted arrivals. Smith et al (1966) and Whitcombe and Maguire (1979) discussed the effect of a refractor velocity gradient on the time-term method. They concluded that if a time-term solution is applied that does not allow for a velocity depth gradient, any real synclinal structure is exaggerated and any real anticlinal behaviour is suppressed. Thus, after the second iteration the syncline was better simulated than the anticline.

After the second iteration the standard errors for the time-terms showed no correlation with distance which suggested that a further iteration would not result in a better solution.

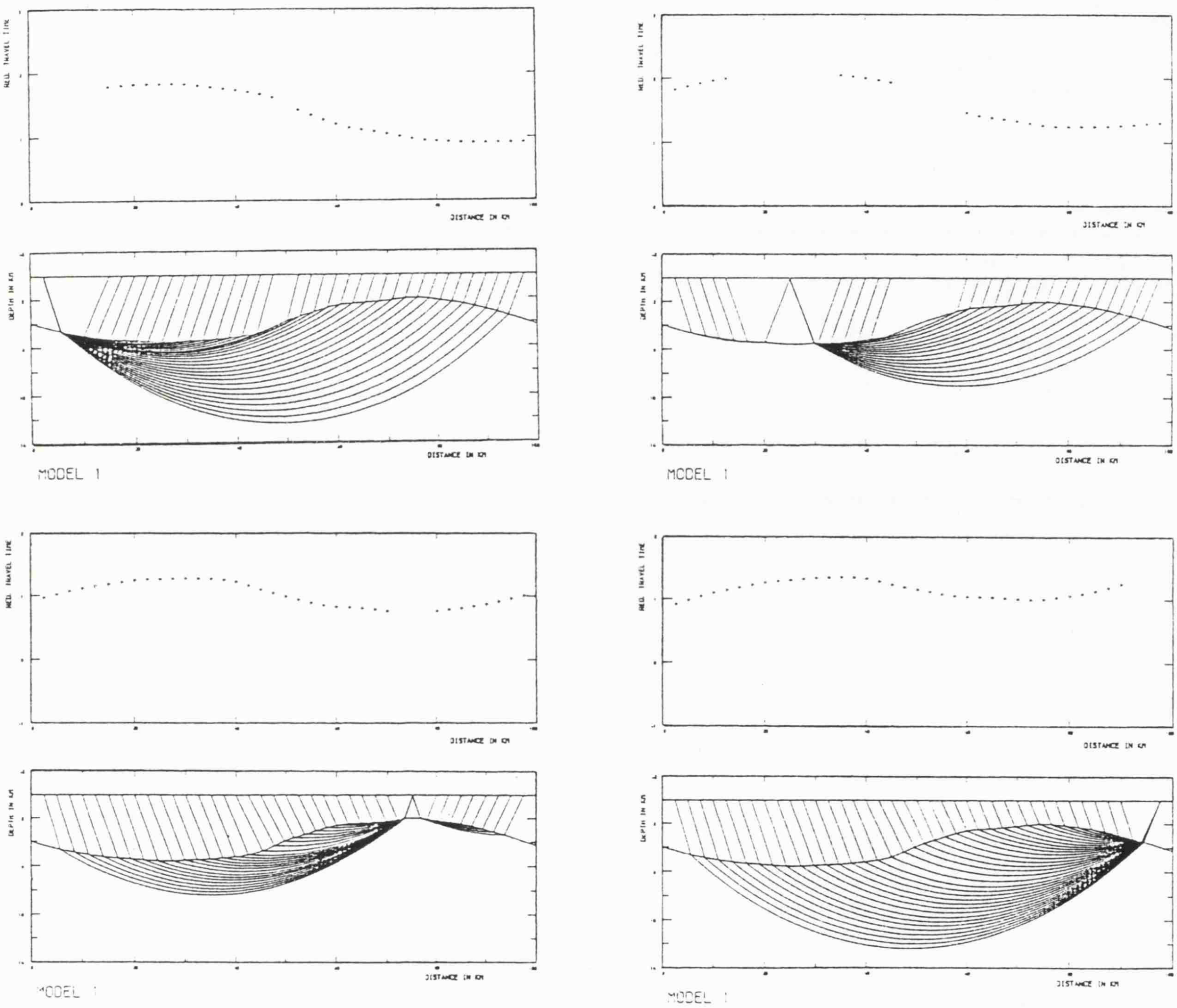

Figure 3.11 : Ray-tracing diagrams and reduced velocity plots for 4 simulated shots into a simple velocity model.

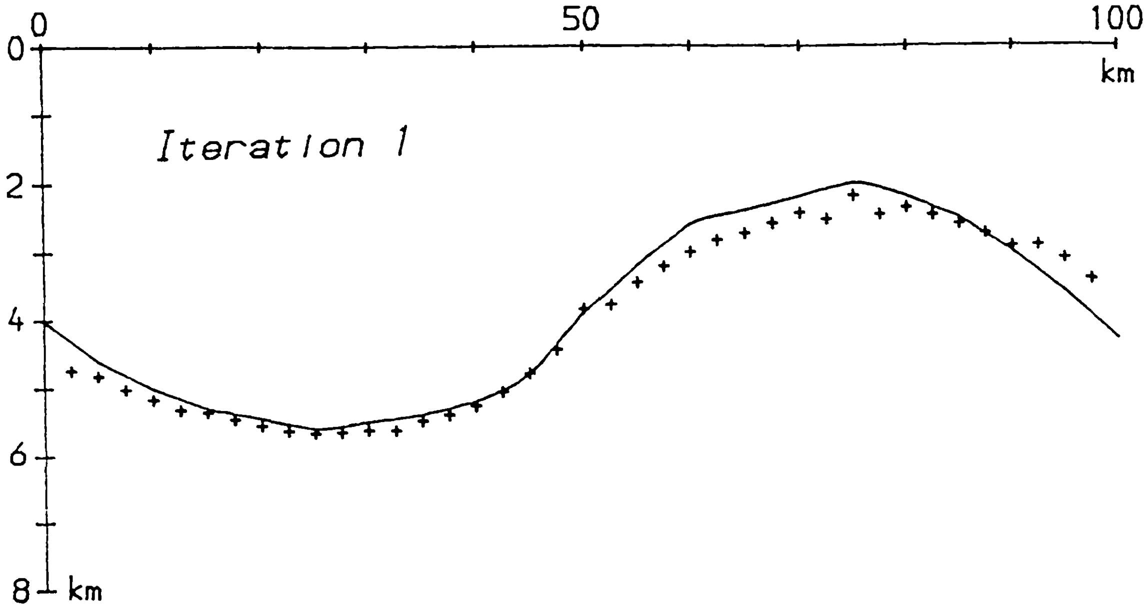

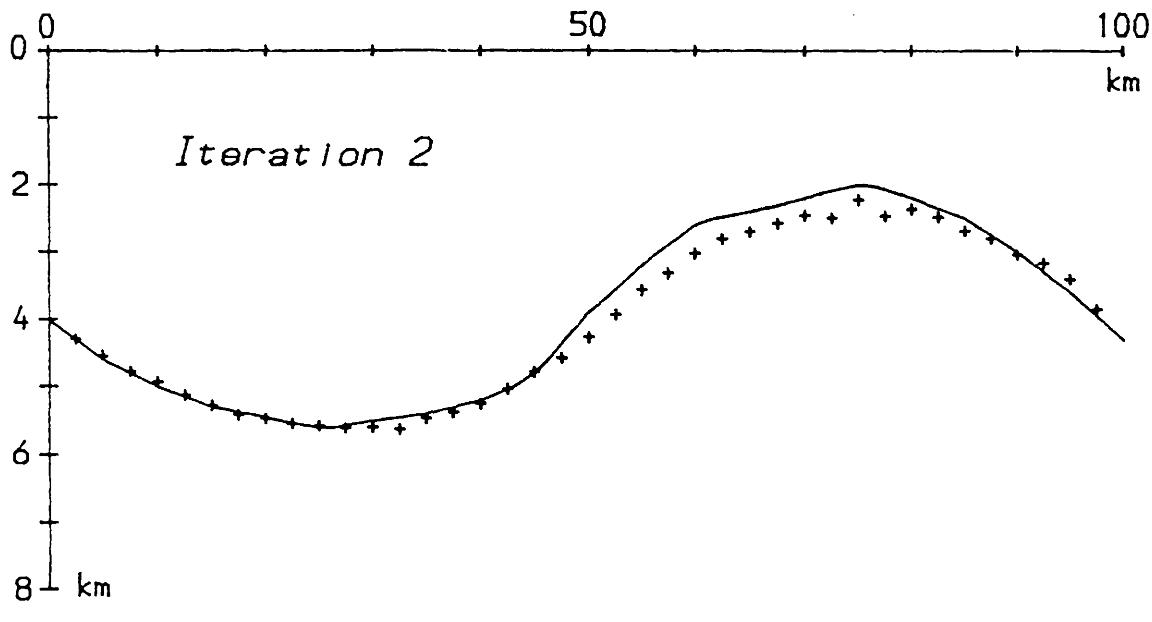

Figure 3.12 : Depths determined by the time-term method after: (a) 1 iteration; and (b) 2 iterations. The continuous curves show the actual structure and the crosses are calculated depths.

CHAPTER (IV)

INTERPRETATION OF REFRACTION DATA

4.0 Introduction.

The interpretation of the refraction data is described in this chapter. Record sections are presented for 11 of the 13 shots fired during KRISP85. All the NS-line record sections have the northern most trace at the left-hand side. Similarly, all the EW-line record sections have the western most trace at the left-hand side. Unless stated otherwise, traces have been normalised and bandpass filtered, the cutoff frequencies being displayed above the section. The P-wave record sections consist of vertical component traces plotted with a reduction velocity of 6.0 km/s. The few S-wave record sections presented comprise radial component traces plotted with a reduction velocity of 3.46 km/s.

Most of the record sections presented have a transparent overlay showing phase correlations identified and pick times of first arrivals. The shot-receiver distances, arrival times and error estimates of all the picks made are listed in Appendix A.

The chapter is divided into 4 sections:

- 4.1 - NS-line Interpretation. This includes the details of 2-D modelling of the shallow P-wave velocity structure (above 10 km depth) and the determination of a deeper 1-D P-wave velocity function.
- 4.2 - Reinterpretation of KRISP75 refraction data. This comprises a brief account of a reinterpretation of KRISP75 refraction data from a line running from Lake Baringo to Lake Bogoria and comparison with the KRISP85 model for that region of the rift.
- 4.3 - EW-line interpretation. Owing to the poor quality of much of the EW-line data this is more qualitative than that of the NS-line.
- 4.4 - S-wave analysis. For the sake of completeness a few S-wave record sections are presented with overlays showing "expected" phase arrival times.

4.1 NS-line interpretation.

4.1.1 Phase correlations.

P-wave record sections for the BA1, BA2, NAI, CHE, SOL, ELM and MAG shots are shown in figures 4.1 - 4.7. No record section is presented for the SU2 shot as poor energy transmission made reliable phase correlations impossible for this shot. The BA1 record section (Fig. 4.1) is divided into 2 parts to enable traces from stations at the southern extremity of the line to be included without reducing the distance scale too much.

Phases A and A', observed over the first 10 - 20 km of the NAI, CHE, SOL, ELM and MAG record sections, are the direct and refracted phases through the Cainozoic volcanics and lake sediments infilling the rift. Phase Pg, the basement refraction, was the best recorded phase of the experiment, identifiable as first arrivals on all of the NS-line record sections shown and out to a range in excess of 140 km in the case of the 2 Baringo shots.

Later phases can only be confidently observed on the BA1, BA2 and NAI record sections. Phase B and C1, which are identifiable on all three, are interpreted as intracrustal reflections. Phase C2, interpreted as the reflected phase from the crust-mantle boundary (PmP), is only observable on the two Baringo record sections. Phase D, on the BA1 record section between 260 and 280 km range, is the only other phase identified. It is interpreted as resulting from refracted or diving waves in the upper mantle i.e. Pn.

4.1.2 Analysis of uppermost crustal phases.

The apparent velocities of the phases denoted A and A' on the record sections were determined by least squares fitting as described in section 3B.1. The travel times were weighted by the reciprocal of the observational error estimate and corrected for elevation. The velocities and intercept times determined are listed along with standard errors and number of data points used, in Table 4.1.

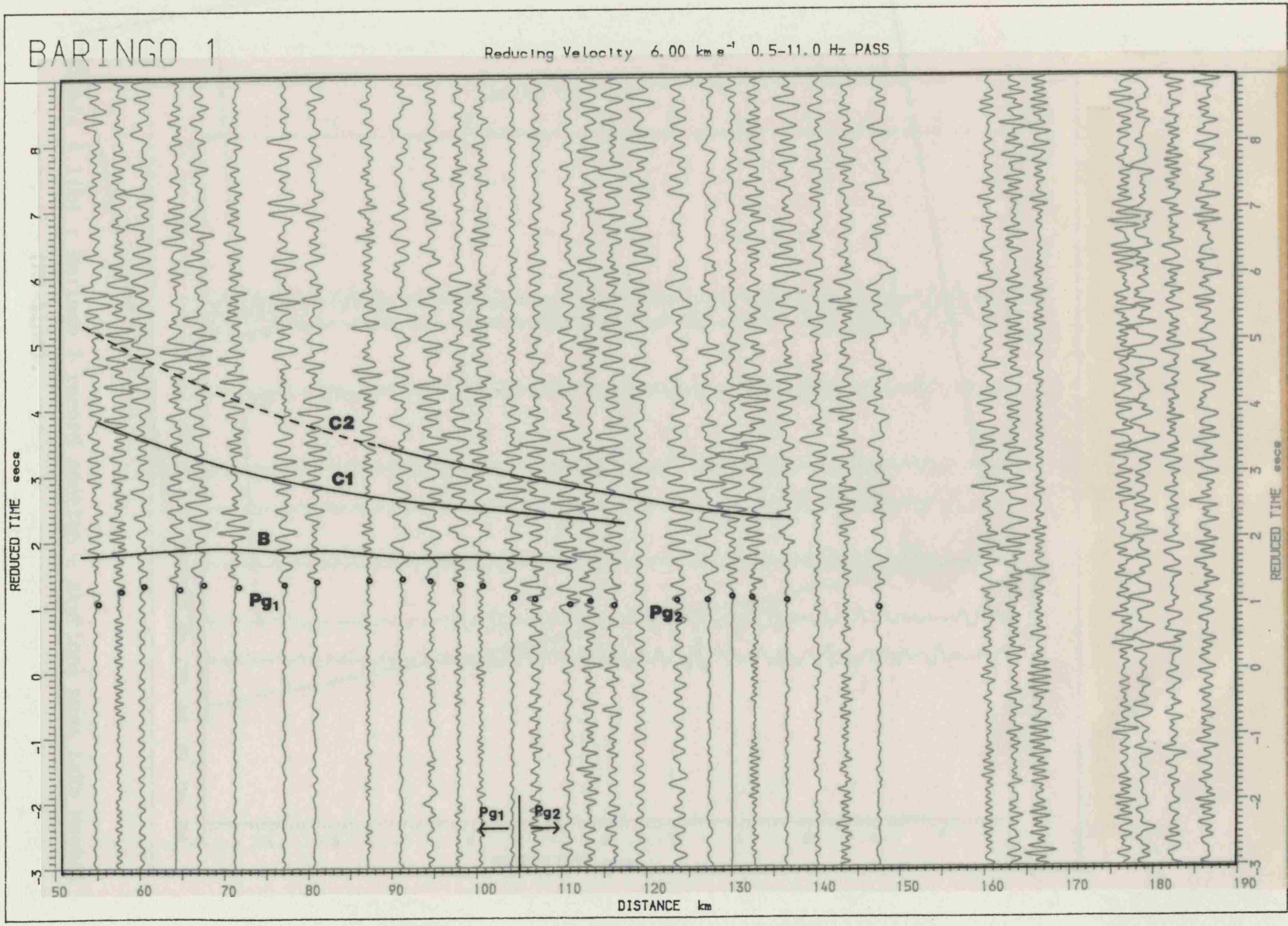

Figure 4.1(a) : Baringo 1 record section (NS-line).

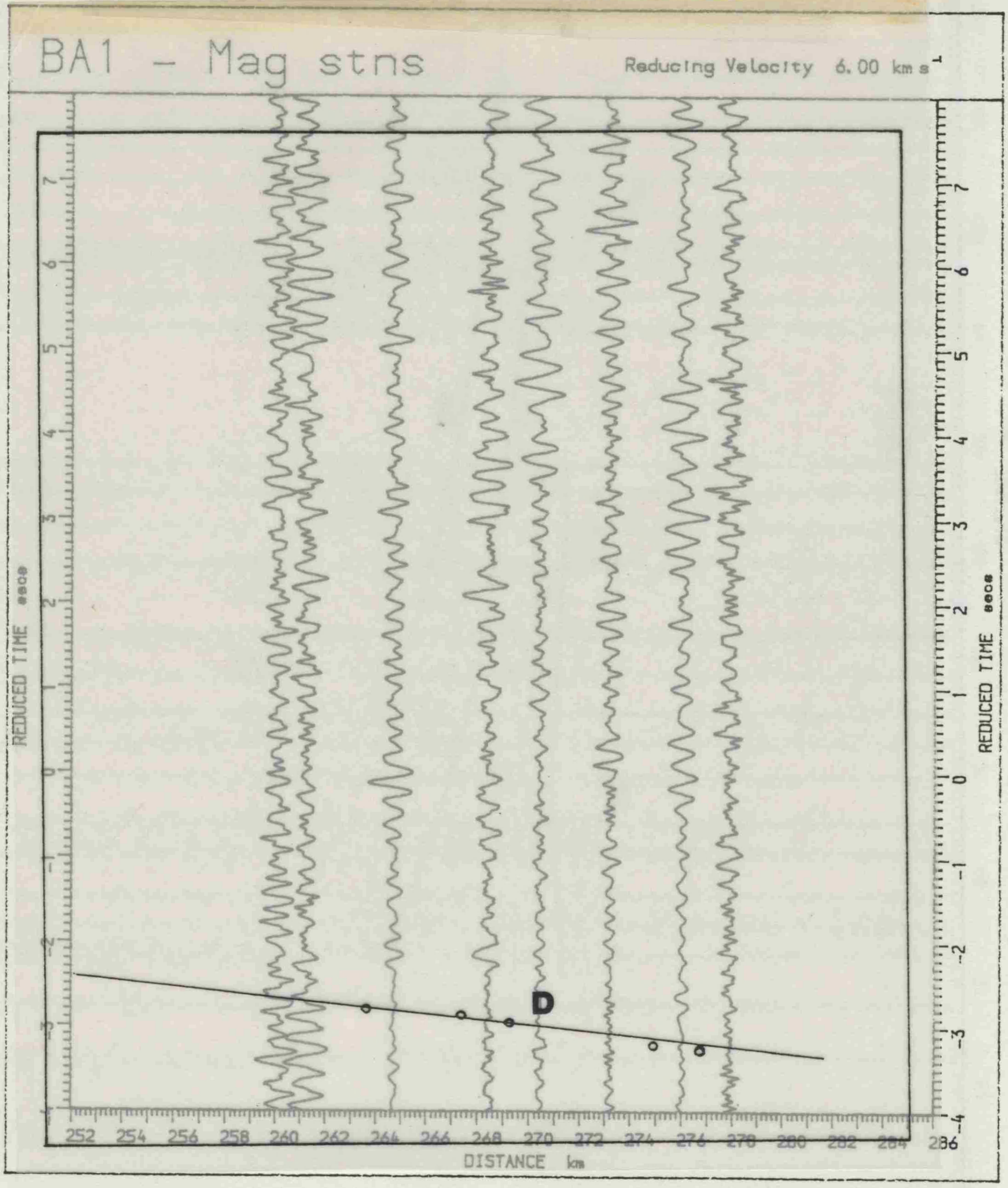

Figure 4.1(b) : Baringo 1 record section - stations near Lake Magadi (NS-line).

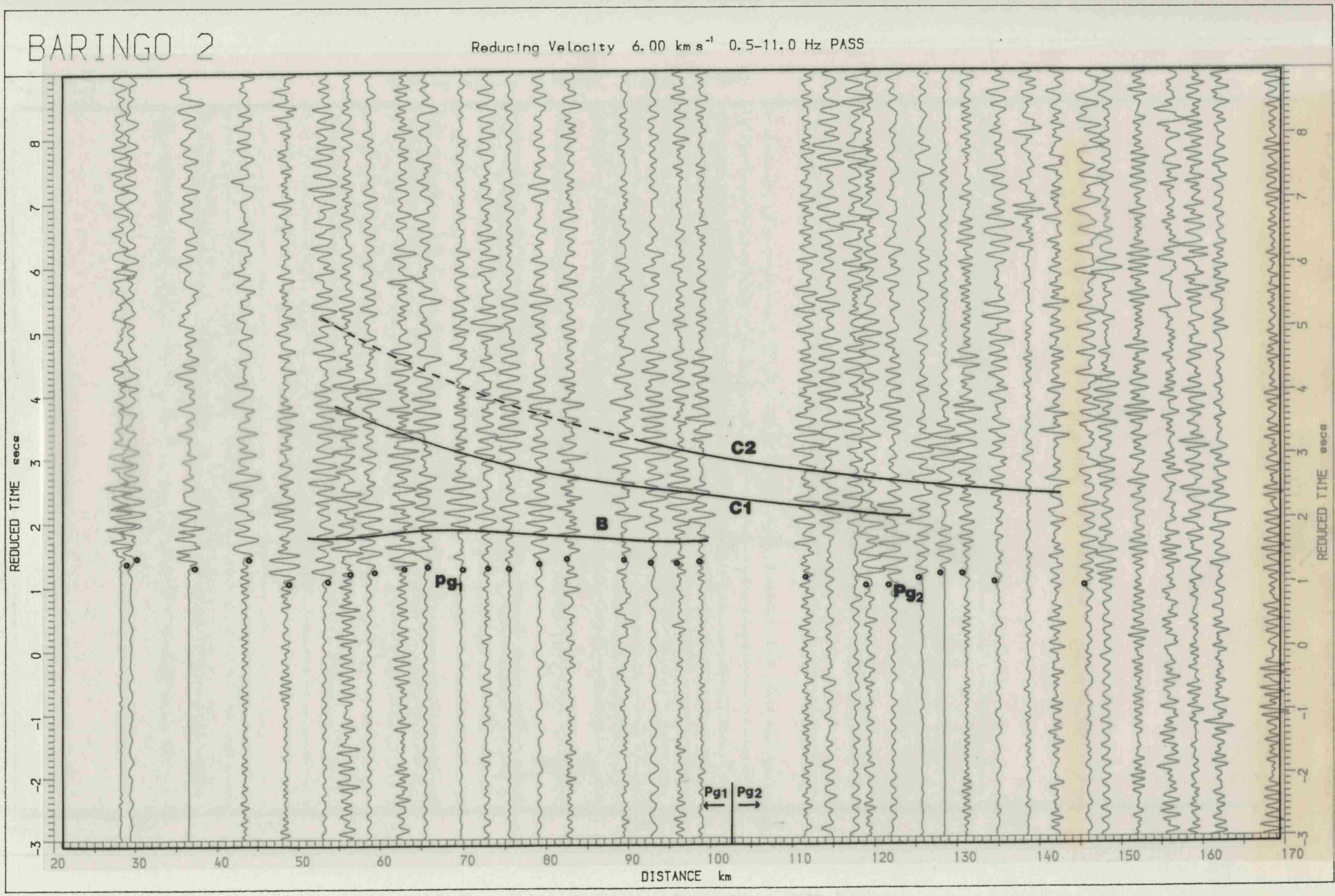

Figure 4.2 : Baringo 2 record section (NS-line).

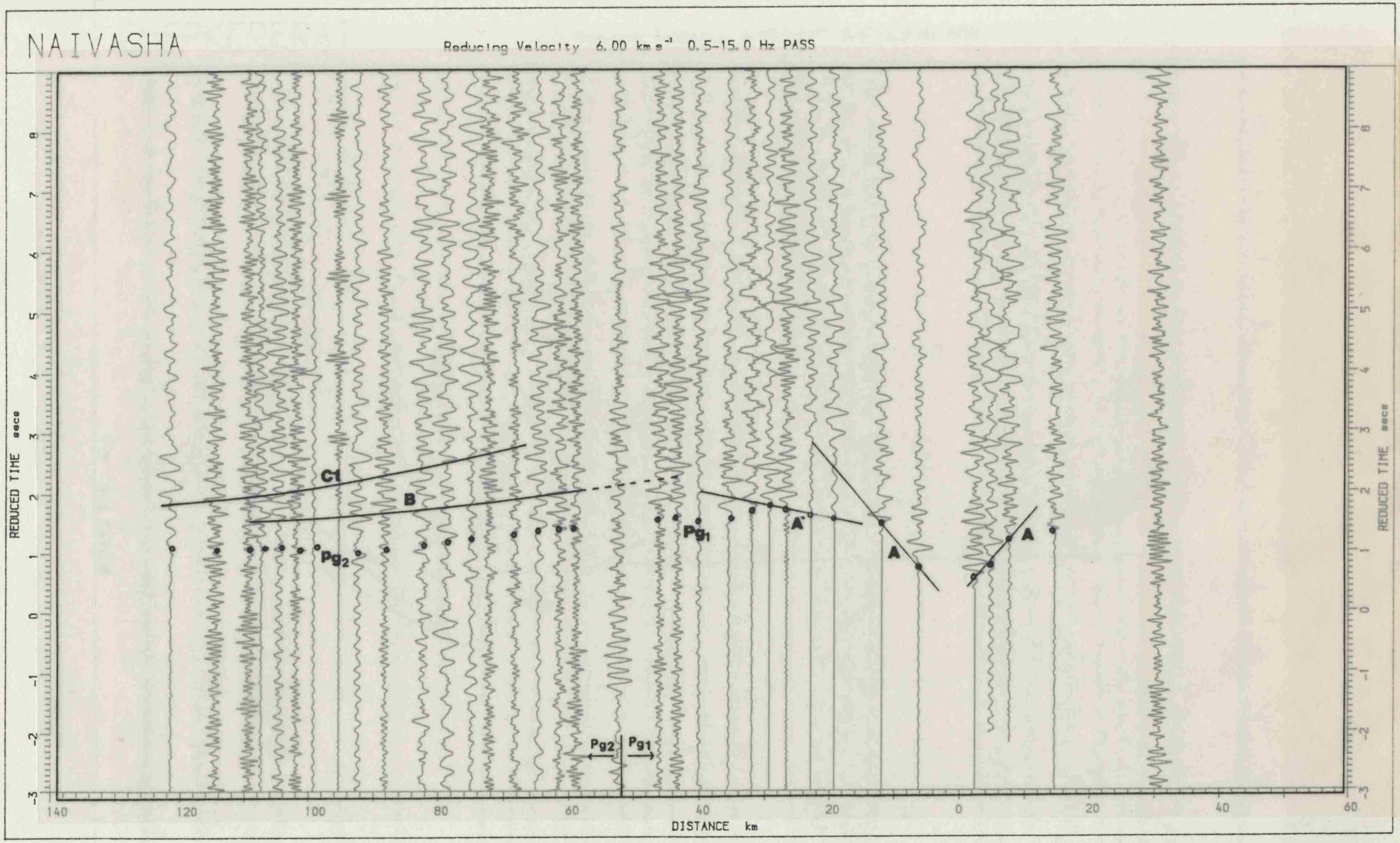

Figure 4.3 : Naivasha record section (NS-line).

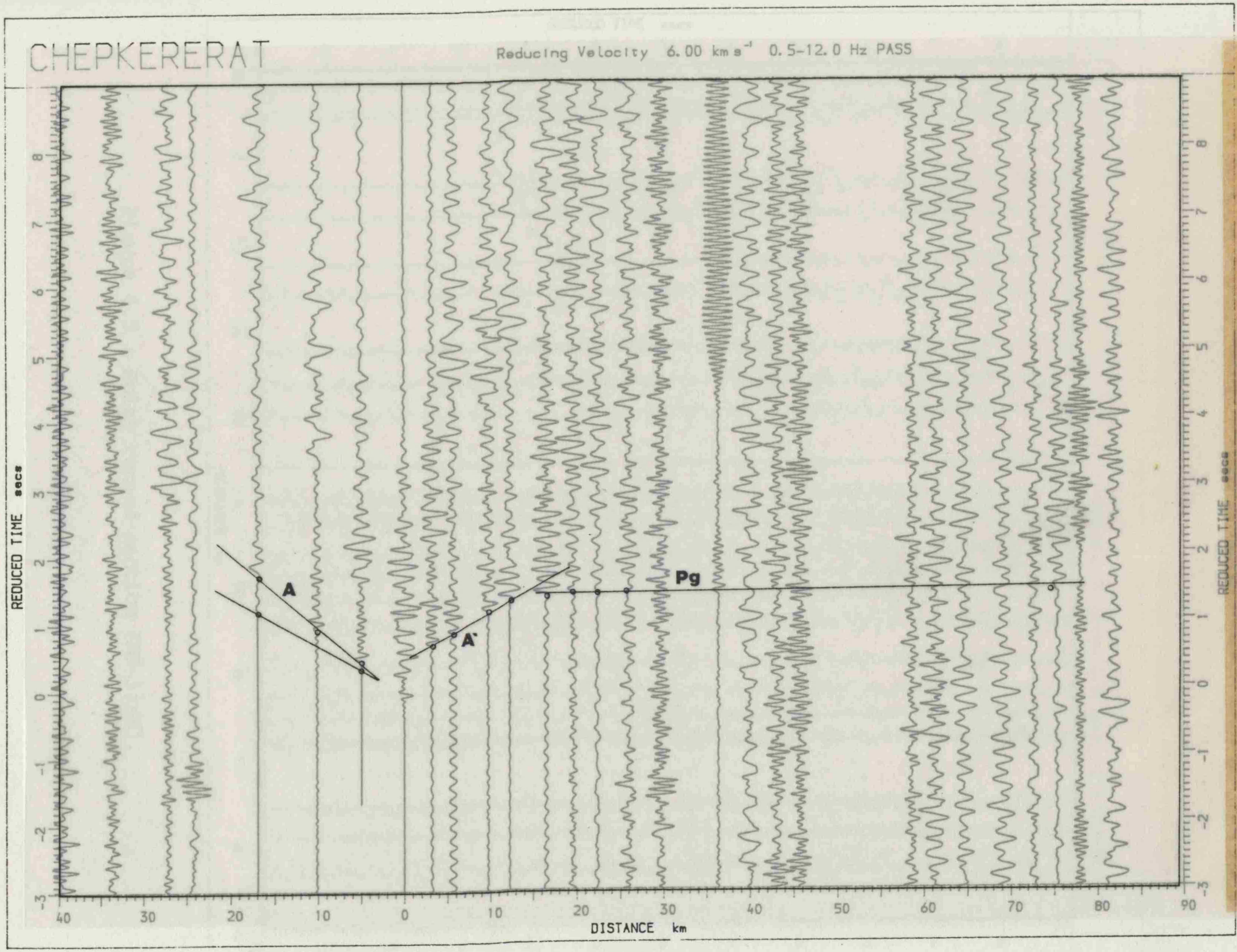

Figure 4.4 : Chepkererat record section (NS-line)

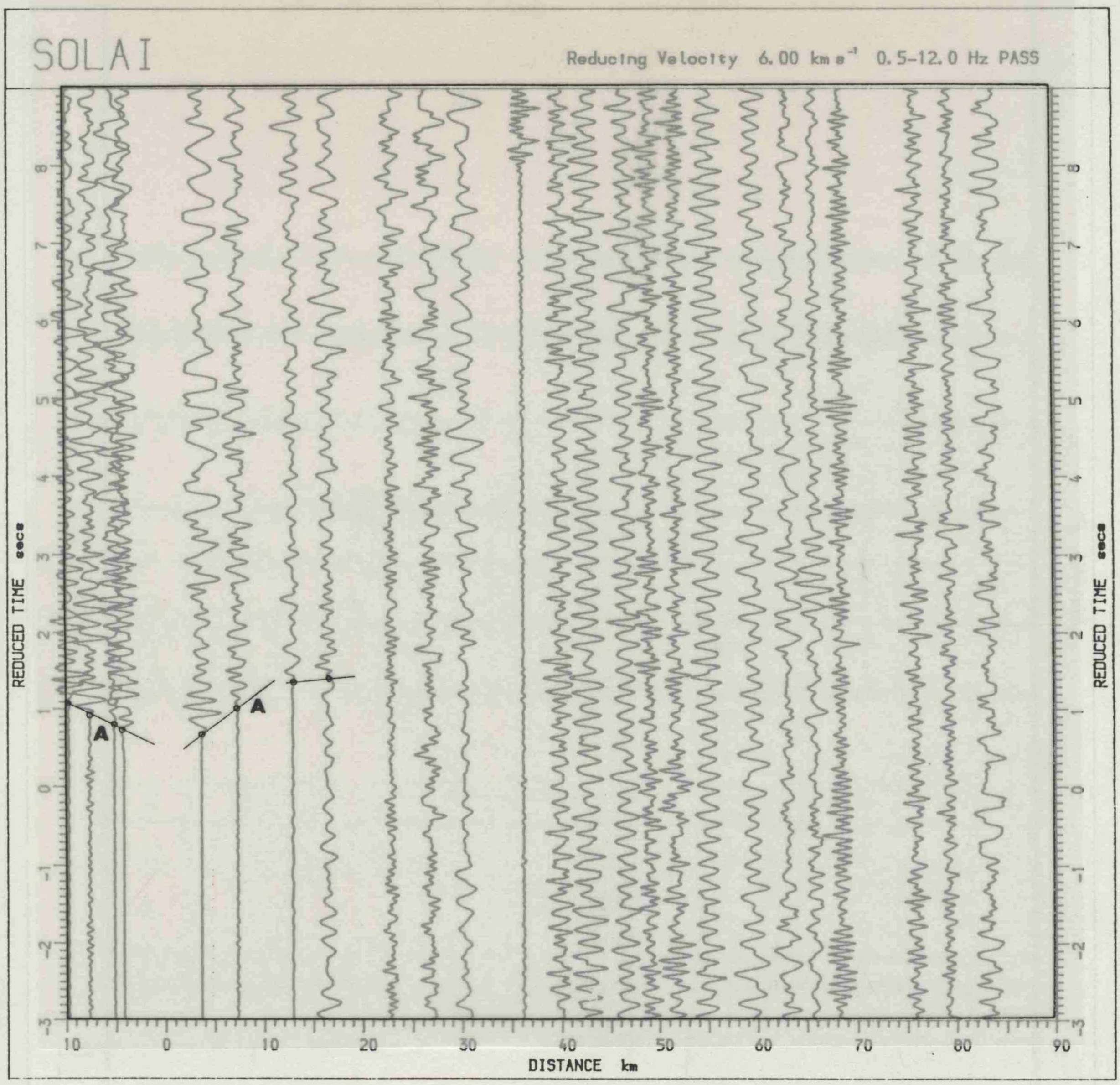

Figure 4.5 : Solai record section (NS-line).

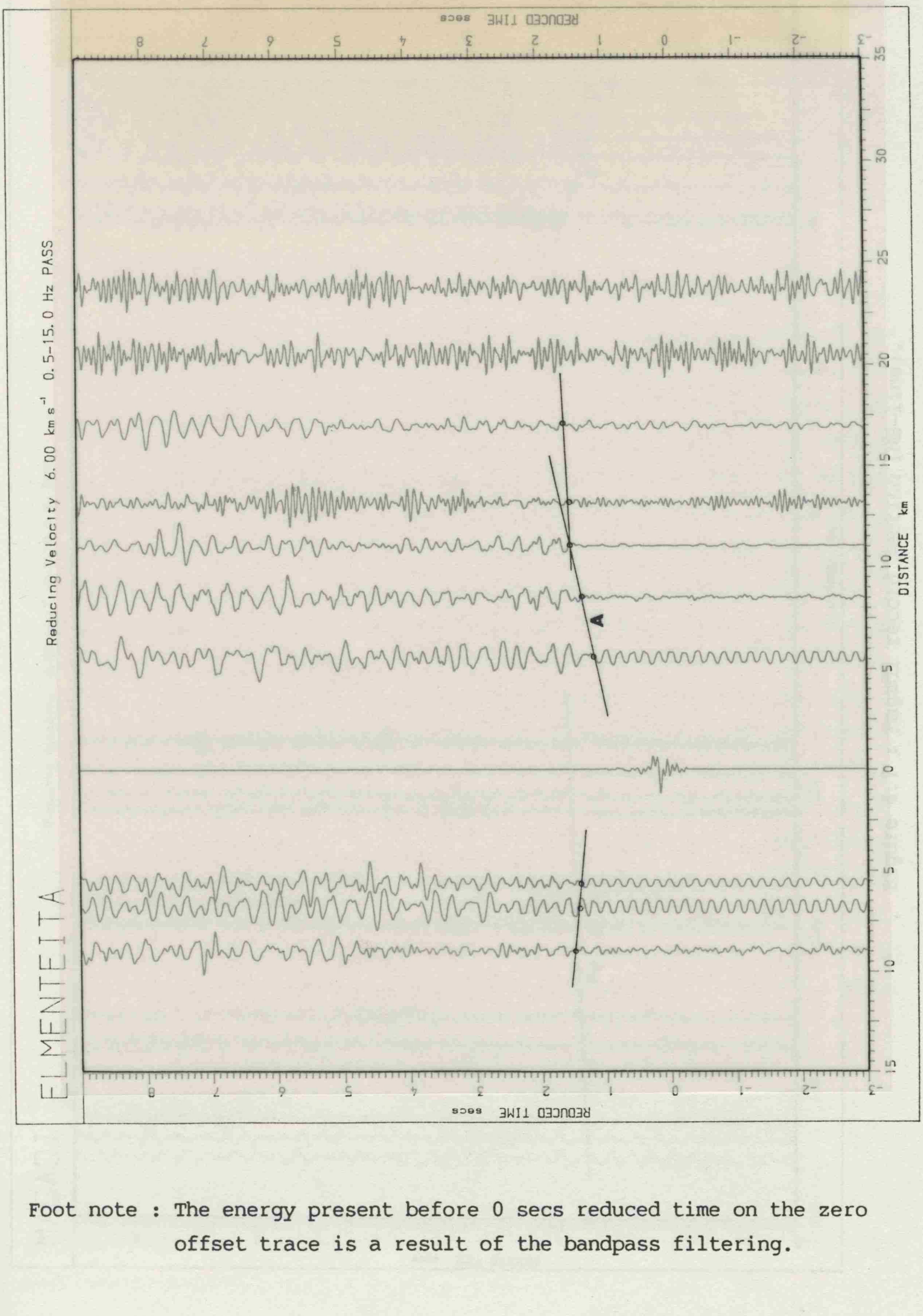

Figure 4.6 : Elmenteita record section (NS-line).

Foot note : The energy present before 0 secs reduced time on the zero offset trace is a result of the bandpass filtering.

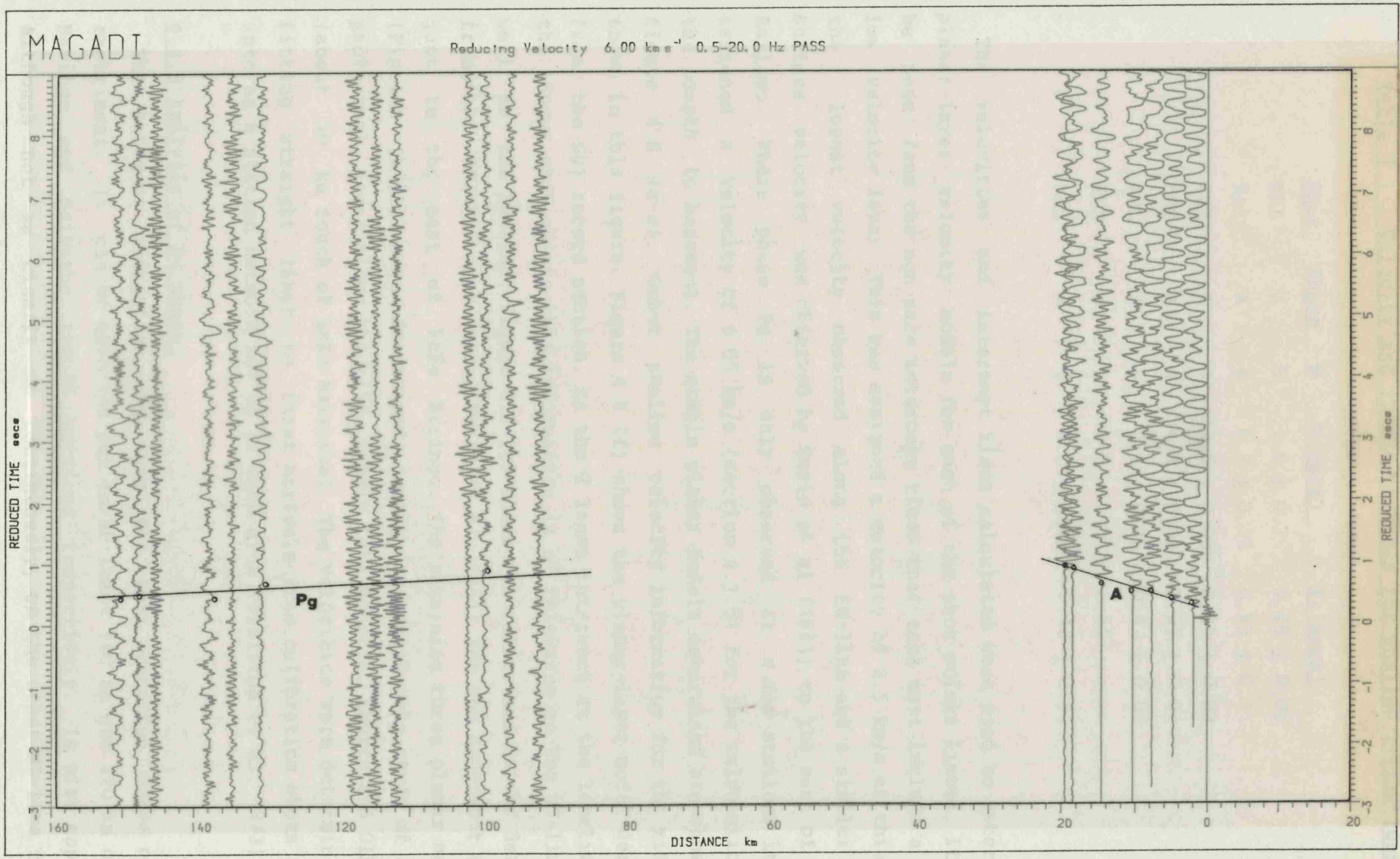

Figure 4.7 : Magadi record section (NS-line).

Table 4.1 : Velocity and intercept times for shallow refractions.

Shot	Phase	N	V(km/s)	T_i(secs)
NAI	A	5	3.6 ± 0.2	0.25 ± 0.05
NAI	A'	4	5.1 ± 0.15	0.93 ± 0.1
CHE	A	3	3.6 ± 0.03	0.29 ± 0.03
CHE	A'	4	4.1 ± 0.04	0.39 ± 0.04
SOL	A	6	4.1 ± 0.13	0.4 ± 0.05
ELM	A	2	4.2	0.62
MAG	A	5	5.0 ± 0.18	0.18 ± 0.06

The velocities and intercept times calculated were used to determine planar-layer velocity models for each of the shot points listed. It can be seen from the non zero intercept times that each must include a thin low velocity layer. This was assigned a velocity of 2.5 km/s as this was the lowest velocity observed along the EW-line and a similar near surface velocity was observed by Swain et al (1981) to the east of Lake Baringo. Where phase Pg is only observed at a few stations it was assigned a velocity of 6.05 km/s (section 4.1.5) for the calculation of the depth to basement. The simple planar models determined are shown in figure 4.8 (a-e). Other shallow velocity information for the rift is shown in this figure. Figure 4.8 (f) shows the planar-layer model derived from the SU1 record section. As the 2 lines intersect at the locality of the Susua shot points this information is of relevance to the NS-line as well as the EW-line. Figure 4.8 (g) shows velocities and depths derived from the KRISP75 experiment (Swain et al, 1981) for the uppermost crust just to the east of Lake Baringo. The remaining three planar models (Fig.4.8 (h-i)) were determined during an earthquake study of three geothermal areas along the rift, namely Lake Bogoria, Eburru and Olkaria (about 10 km south of Lake Naivasha). The velocities were determined by fitting straight lines to first arrivals from calibration shots fired into an 8 station network set up in each area (Hamilton et al, 1973).

4.1.3 Analysis of Pg phase.

The basement refraction, Pg, was the best recorded phase of the experiment. It can be observed out to at least 140 km and 120 km on the Baringo and Naivasha record sections respectively. It also appears, although not as clearly or continuously, on the other NS-line record sections presented.

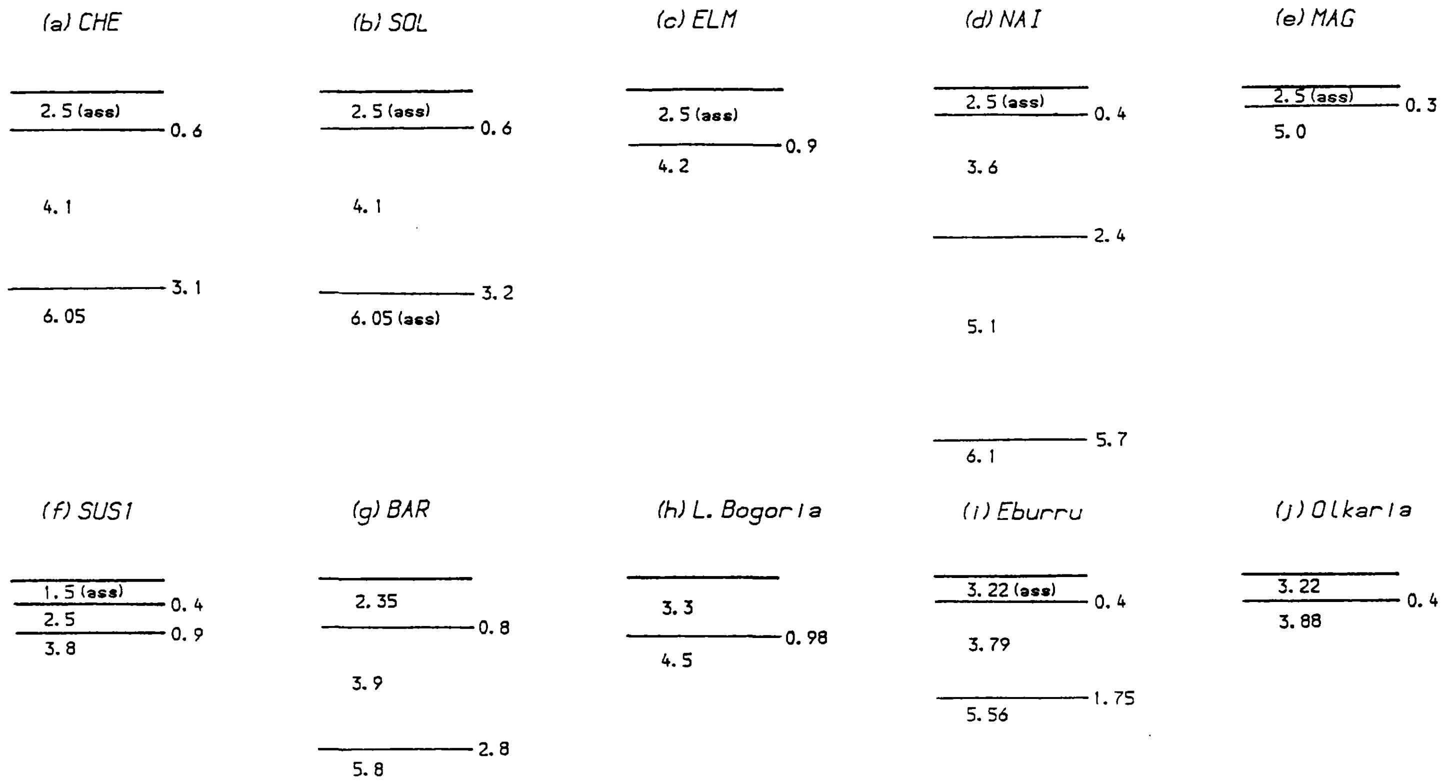

Figure 4.8 : Planar P-wave velocity models for the NS-line.

Apparent velocities for Pg, calculated by least squares fitting of the arrival times listed in appendix A, are listed in table 4.2.

Table 4.2 : Apparent velocities calculated for Pg.

Shot	Phase	N	V(km/s)	T_i(secs)
BA1	Pg	23	6.15 ± 0.08	1.34 ± 0.11
BA2	Pg	28	6.16 ± 0.07	1.44 ± 0.12
NAI	Pg	21	6.24 ± 0.09	1.84 ± 0.14

Close examination of the Baringo and Naivasha record sections revealed definite travel time advances of the Pg phase between stations 24 and 26 i.e. around 105 km range for the BAR shots and 52 km range for the NAI shot. The most likely explanation for such advances in both northward and southward travelling waves is the existence of a narrow "high velocity zone" (HVZ) within the basement (Section 4.1.4). The normal basement velocity can be determined more accurately if the Pg phase is divided into 2 branches, Pg_1 between the shot and the HVZ and Pg_2 beyond the HVZ. The resulting least squares velocities are listed in table 4.3.

Table 4.3 : Apparent velocities calculated for Pg_1 and Pg_2.

Shot	Phase	N	V(km/s)	T_i(secs)
BA1	Pg_1	13	5.94 ± 0.05	1.2 ± 0.1
BA1	Pg_2	8	6.1 ± 0.16	1.3 ± 0.2
BA2	Pg_1	19	5.95 ± 0.05	0.94 ± 0.08
BA2	Pg_2	8	5.96 ± 0.14	0.7 ± 0.15
NAI	Pg_1	5	6.3 ± 0.14	2.0 ± 0.2
NAI	Pg_2	16	5.97 ± 0.04	1.4 ± 0.1

The average of these 6 velocities is 6.04 km/s. Only the Pg_1 branch of the NAI record section has a significantly different apparent velocity. It will be evident later (section 4.1.6) that this is due to deepening of the basement southwards in this region. For all three shots, the total sum of least squares residuals was less once Pg had been divided into 2 branches.

4.1.4 Upper crustal high velocity zone.

The travel time advance, Δt, was estimated from examination of the Baringo and Naivasha record sections to be 0.18 ± 0.03 secs. It is more difficult to estimate the lateral distance over which this advance occurred i.e. the approximate width of the HVZ. Obviously, this distance dictates the increase in velocity necessary to produce the observed travel time advance. If it is assumed that the zone has a uniform velocity of V' then it is easily shown that

$$\Delta t = X/V - X/V' \qquad 4.1$$

where X is the width of the HVZ and V is the velocity of the surrounding medium. Hence

$$V' = (1/V - \Delta t/X)^{-1} \qquad 4.2$$

Figure 4.9 shows a graph of V' plotted against X for Δt = 0.18 secs and V = 6.05 km/s. The lateral extent of the HVZ was estimated from the BA1 record section to be between 8 and 12 km. This suggests the zone has a velocity of between 6.6 and 7.0 km/s. In the final ray tracing model (section 4.1.6) the HVZ was assigned a velocity of 6.8 km/s and a width of 10 km.

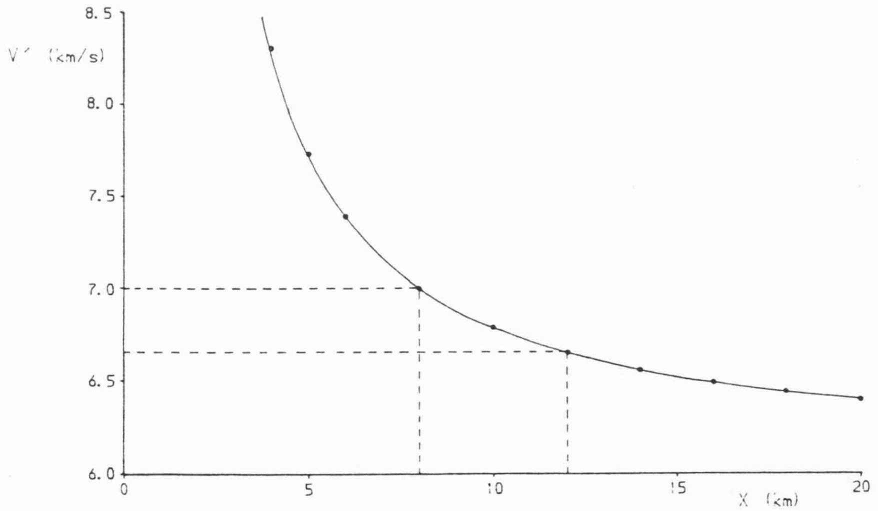

Figure 4.9 : Velocity vs width of the HVZ for a travel time advance of 0.18 secs.

4.1.5 Time-term analysis of basement refraction.

A brief description of the time-term method was given in Chapter 3B. The fact that the Pg phase was well recorded made it a suitable candidate for time-term analysis. The method is most effective if the ratio of the number of observations to the number of time-terms is as high as possible. For this reason only the BA1, BA2, NAI and CHE shots and the 24 recording sites having observed Pg from at least 2 shots were included in the analysis. This gave a total of 68 observations and 27 time-terms as shown by the list of linkages (Table 4.4).

Program **TIMTERM** was first run inputting the station ranges and travel times observed. The resulting time-terms are listed as solution A in table 4.5. The solution velocity is 6.17 $\pm$ 0.018 km/s and solution variance is 0.011 s^2 compared with an observational error variance of 0.0017 s^2. Thus the F ratio (Chapter 3B) has a value of about 6.5 which is high and indicates that the solution is inadequate. This "lack of fit" is easily explained if the requirements of the method are considered. One of the assumptions of the time-term method, as used in this study, is a constant refractor velocity which is not satisfied owing to the occurrence of the HVZ. Examination of the solution residuals (not listed here) gave support to this explanation. The mean residual for observations made between shot and HVZ was found to be +0.03 s while the mean residual for observations made beyond the HVZ was -0.03 s. This definite correlation of solution residuals with position of observation w.r.t. shot and HVZ locality implies that the HVZ was the cause of the high solution variance.

A very simple method was employed to overcome the problem presented by the occurrence of the HVZ. Its effect was corrected for and time-term analysis then performed as if it was not present. The correction consisted of simply adding 0.18 s (as estimated in the previous section) to all the travel times observed beyond the HVZ i.e. stations 13 - 23 for the Baringo shots and stations 27 - 45 for the Naivasha shot. The resulting time-terms and solution velocity and variance are listed as solution B in table 4.5. The solution velocity of 6.07 $\pm$ 0.01 km/s is now in better agreement with the least squares estimates and the solution variance of 0.0051 s^2 is less than half its previous value. The time-terms calculated were converted to depths using equation 3B.21, assuming an average velocity of 4.0 km/s for the rift infill. In the light of the planar velocity models shown in figure 4.8, this is undoubtedly a gross over simplification. However, knowing that ray-tracing forward modelling would be used to determine the final shallow velocity model, it was decided to keep the time-term analysis as simple as possible. The depths calculated are plotted against

Table 4.4 : Time-term linkages.

STATION	BA1	BA2	NAI	CHE	N
NS13	*	*			2
NS16	*	*			2
NS17	*	*	*		3
NS18	*	*	*	*	4
NS19	*	*	*		3
NS20	*	*	*		3
NS23	*	*	*		3
NS27	*	*	*		3
NS28	*	*	*		3
NS29	*	*	*		3
NS30	*	*	*		3
NS32		*	*		2
NS33	*	*	*	*	4
NS34	*	*	*	*	4
NS35		*		*	2
NS36	*	*	*	*	4
NS37	*	*	*		3
NS38	*	*			2
NS39	*	*	*		3
NS40	*	*	*		3
NS41	*	*	*		3
NS43		*	*		2
NS44		*	*		2
NS45		*	*		2

No. of observations = 68

No. of time-terms = 27

Table 4.5 : Time-term solutions.

Site	N	Solution A Time-Term	S.E.	Solution B Time-Term	S.E.	Solution C Time-Term	S.E.
BA1	19	0.786 s	0.013 s	0.637 s	0.009 s	0.842 s	0.010 s
BA2	24	0.753	0.013	0.619	0.008	0.823	0.009
NAI	20	0.787	0.028	0.749	0.019	0.925	0.015
CHE	8	0.627	0.032	0.622	0.029	0.635	0.015
NS13	2	0.921	0.038	0.878	0.033	0.866	0.046
NS16	2	0.857	0.046	0.845	0.040	0.664	0.054
NS17	3	1.026	0.035	1.009	0.031	1.136	0.065
NS18	4	1.079	0.022	1.067	0.020	1.192	0.028
NS19	3	0.930	0.057	0.925	0.042	1.036	0.037
NS20	3	0.882	0.035	0.878	0.033	0.917	0.034
NS23	3	0.954	0.058	0.920	0.040	1.056	0.044
NS27	3	0.996	0.076	0.953	0.010	1.079	0.029
NS28	3	0.984	0.060	0.942	0.020	1.049	0.028
NS29	3	0.991	0.050	0.960	0.010	1.081	0.014
NS30	3	1.019	0.091	0.976	0.039	1.086	0.028
NS32	2	0.959	0.137	0.938	0.074	1.050	0.076
NS33	4	0.914	0.047	0.879	0.031	0.958	0.041
NS34	4	0.866	0.043	0.824	0.024	0.853	0.005
NS35	2	0.882	0.007	0.829	0.013	0.937	0.008
NS36	4	0.827	0.039	0.788	0.026	0.850	0.010
NS37	3	0.851	0.064	0.821	0.053	0.902	0.051
NS38	2	0.822	0.002	0.799	0.004	0.895	0.012
NS39	3	0.810	0.020	0.793	0.024	0.929	0.018
NS40	3	0.755	0.010	0.743	0.014	0.844	0.047
NS41	8	0.627	0.032	0.622	0.029	0.635	0.015
NS43	2	0.605	0.142	0.604	0.108	0.523	0.079
NS44	2	0.915	0.070	0.912	0.114	1.133	0.010
NS45	2	0.807	0.096	0.806	0.034	0.890	0.109

Solution A: Velocity = 6.17 $\pm$ 0.018 km/s Variance = 0.0111 s^2

Solution B: Velocity = 6.07 $\pm$ 0.012 km/s Variance = 0.0051 s^2

Solution C: Velocity = 6.04 $\pm$ 0.011 km/s Variance = 0.0047 s^2

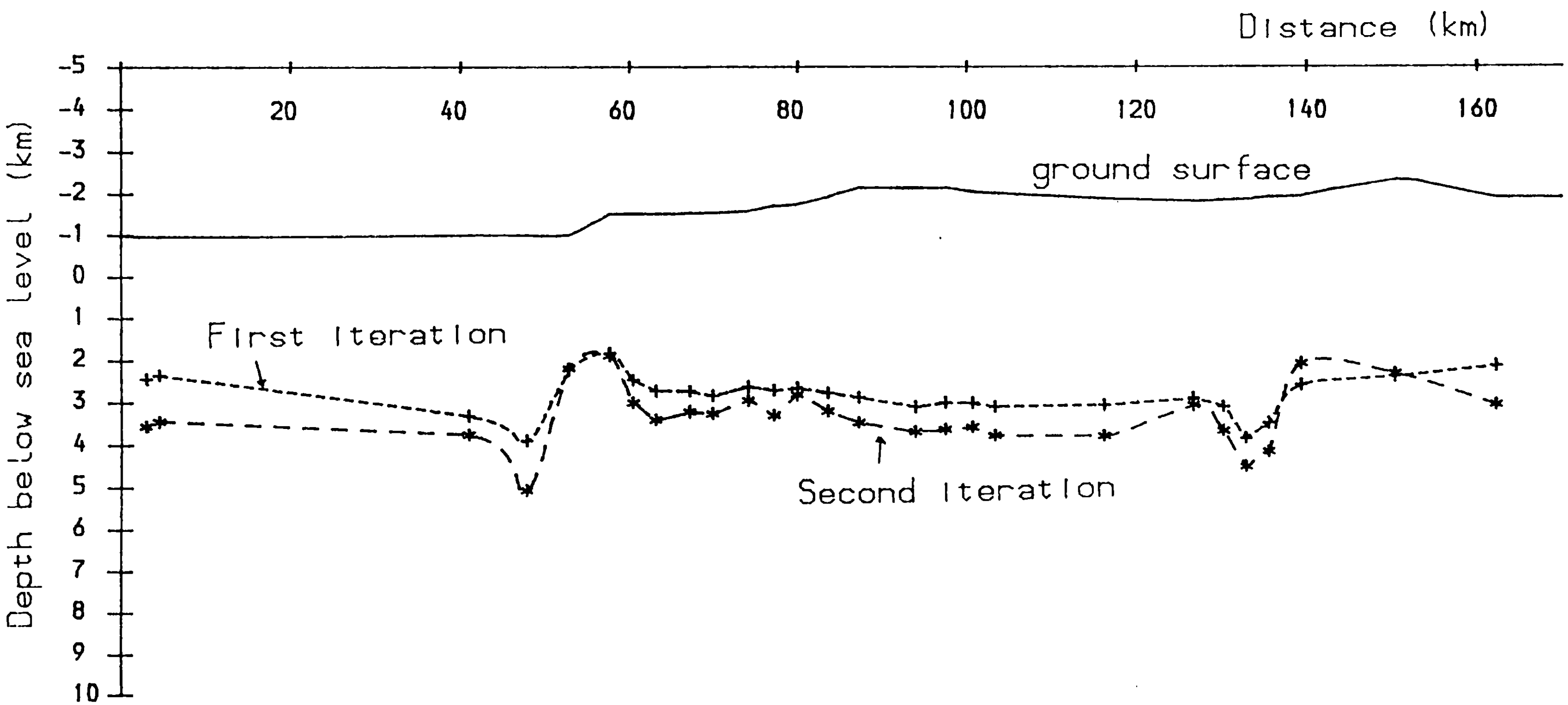

Figure 4.10 : Time-term depths determined for the NS-line.

distance (relative to a reference point 3 km north of BA1) in figure 4.10 (labelled "first iteration") and vary from about 2.7 km below CHE to over 5 km at about 130 km distance. Quite severe basement topography is apparent in places.

A second iteration was performed, distances D_{ij} being determined by the graphical method described in section 3B.3. These replaced the station ranges in the final run of **TIMTERM** resulting in "Solution C" of table 4.5. It can be seen that the solution velocity and variance are little changed. The time-terms were converted to depths and are plotted in figure 4.10 (labelled as "second iteration"). The main differences between the solutions are an overall slight increase in the time-term values and an increase in the severity of the basement topography. The basement topography deduced from ray-tracing modelling (section 4.1.6) is in places different from that deduced from the time-term analysis. This is a result of the assumption made of a uniform rift infill velocity. For example, if the 5.1 km/s layer below NAI had been taken into account during the conversion from time-terms to depths, a significantly greater depth to basement would have been obtained in this region.

4.1.6 Modelling of shallow velocity structure by ray tracing.

Two dimensional modelling of the shallow velocity structure was carried out using the **SEIS81** ray tracing package as described in Chapter 3B. A starting model was devised using the results of the previous 4 sections. This included:

(1) A thin low velocity layer (V = 2.5 km/s).

(2) A layer having velocity around 4.0 km/s thinning southwards.

() A deeper layer of about 5.1 km/s velocity below NAI, the top of which shallowing southwards towards MAG.

(4) A basement velocity of 6.05 km/s.

(5) A 10 km wide zone of 6.8 km/s velocity material in the basement between SOL and ELM.

In order that refracted phases would be generated layers were assigned with positive velocity depth gradients, typically of around 0.01 s^{-1}. The HVZ was simulated by giving the basement layer a fine velocity grid and assigning higher velocities to grid points lying within the zone. For this reason it does not appear on the ray tracing diagrams.

The starting model was adjusted by manual iteration until the observed travel times closely matched the calculated (ray tracing) travel times. This was carried out for all the shots except SU2. Obviously the Baringo and Naivasha travel times provided the most rigorous constraints on the

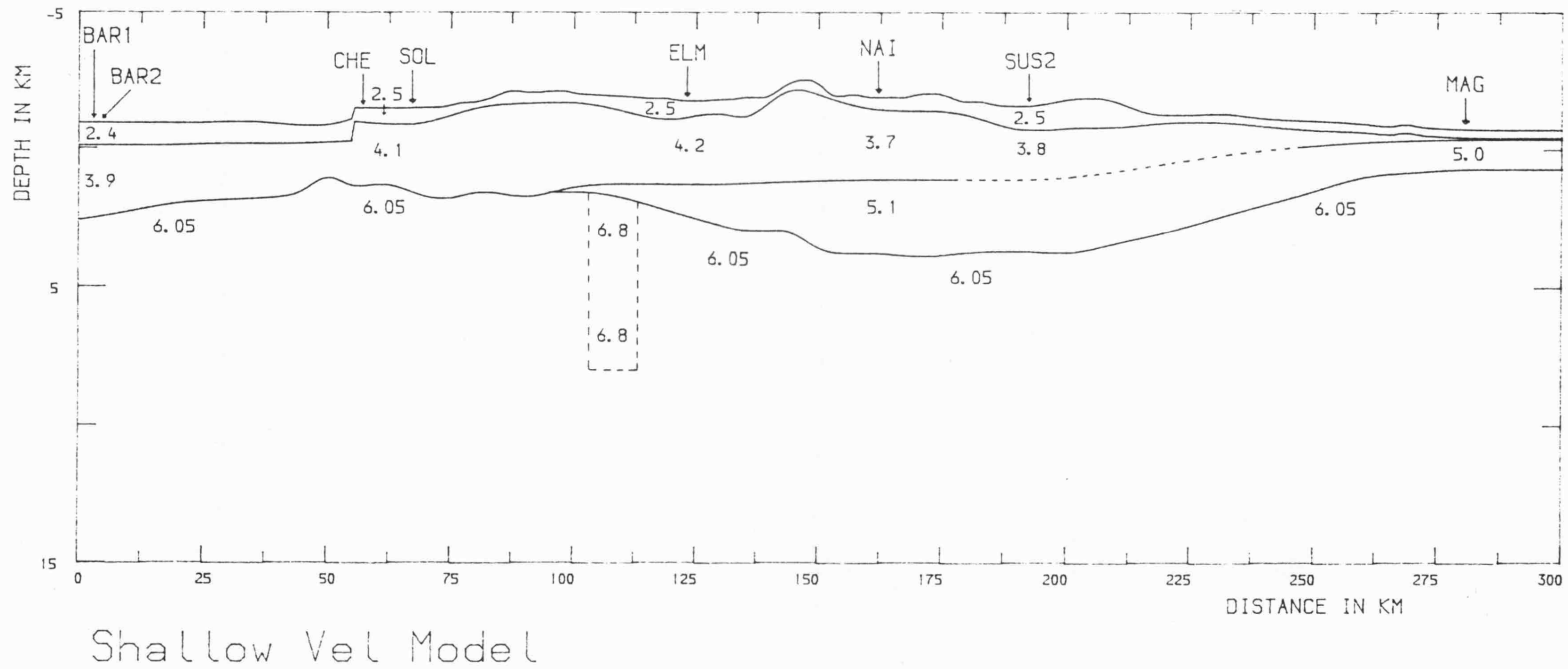

Figure 4.11 : Shallow P-wave velocity model determined from ray-tracing for the NS-line.

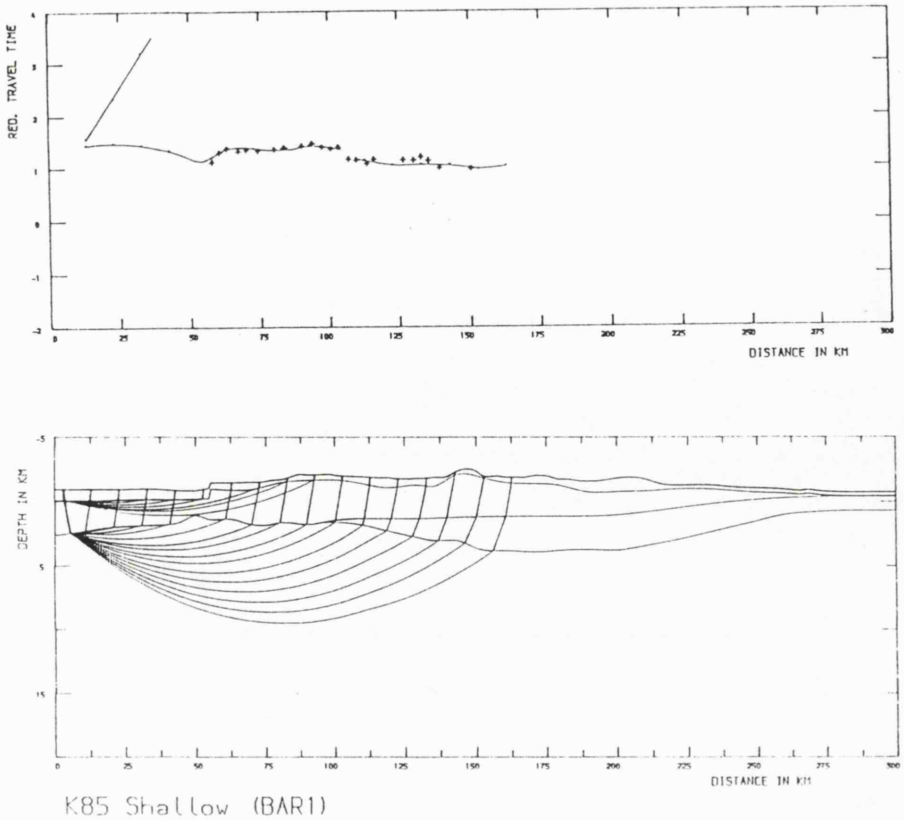

Figure 4.12(a) : Observed and synthetic travel times for the Baringo 1 shot and accompanying ray tracing diagram (Vr = 6 km/s).

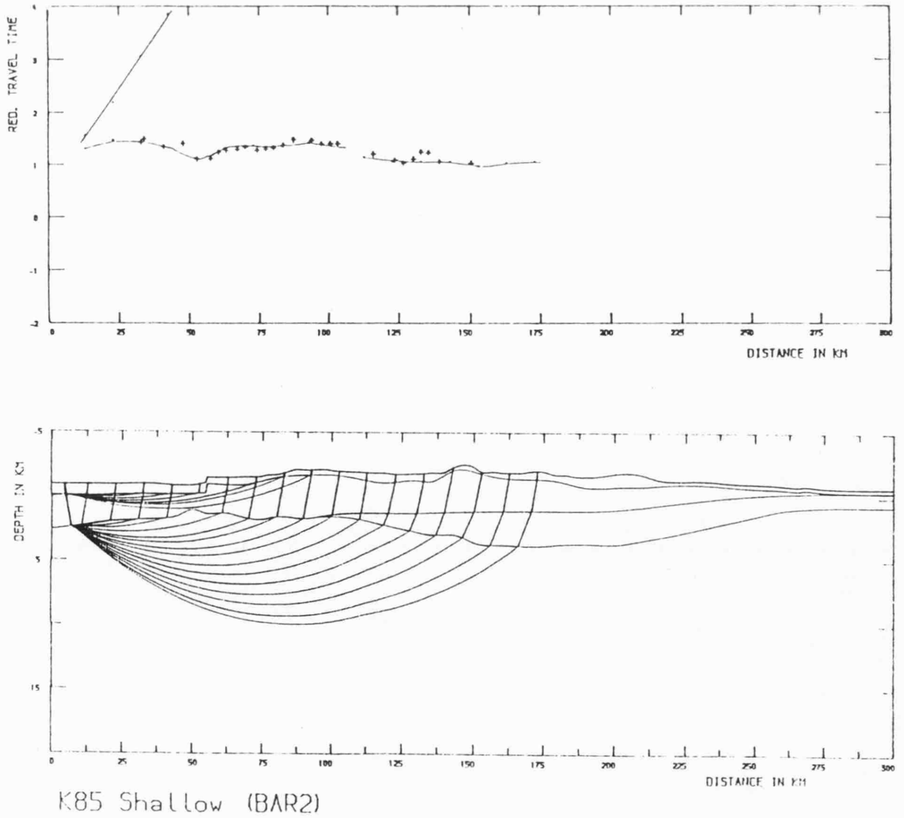

Figure 4.12(b) : Observed and synthetic travel times for the Baringo 2 shot and accompanying ray tracing diagram (Vr = 6 km/s).

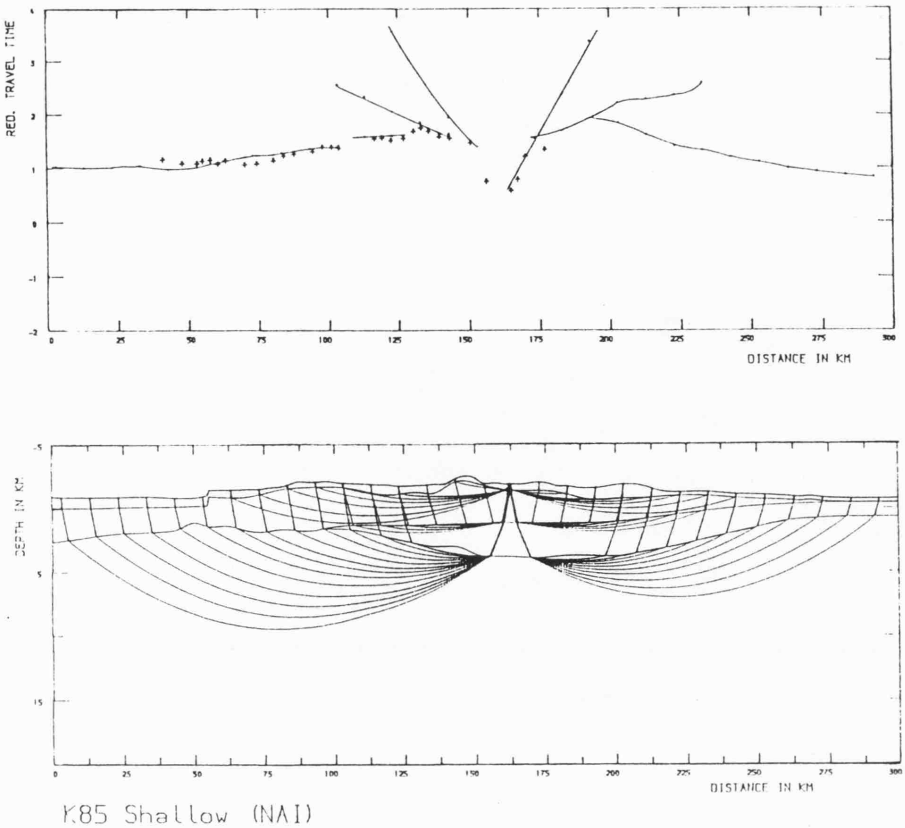

Figure 4.12(c) : Observed and synthetic travel times for the Naivasha shot and accompanying ray tracing diagram (Vr = 6 km/s).

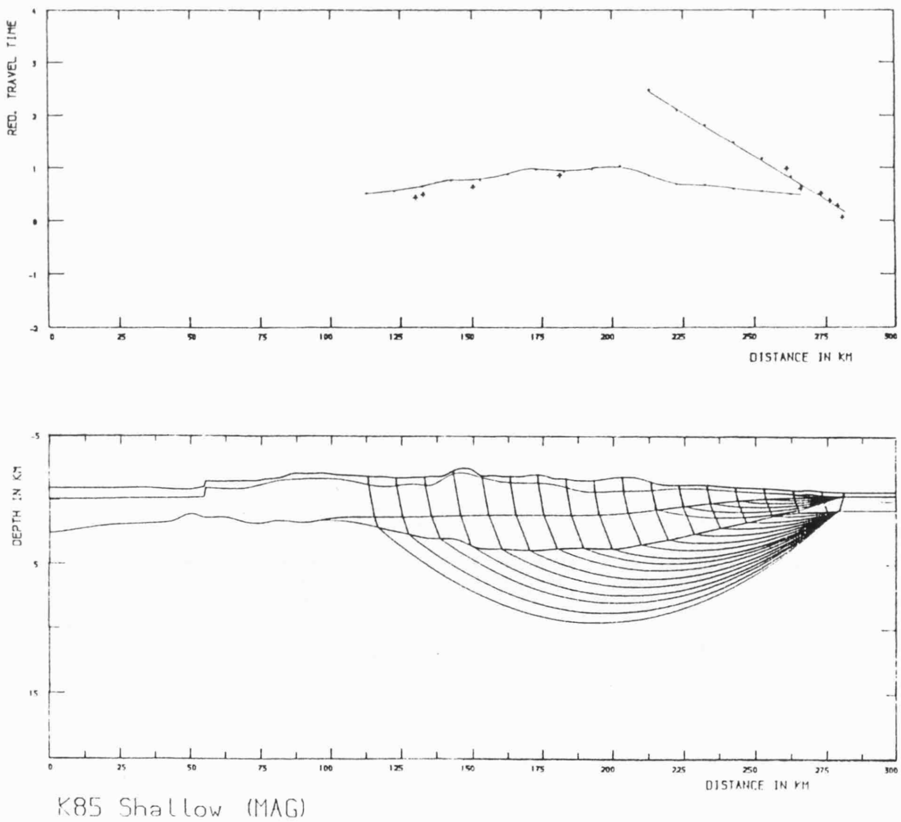

Figure 4.12(d) : Observed and synthetic travel times for the Magadi shot and accompanying ray tracing diagram (Vr = 6 km/s).

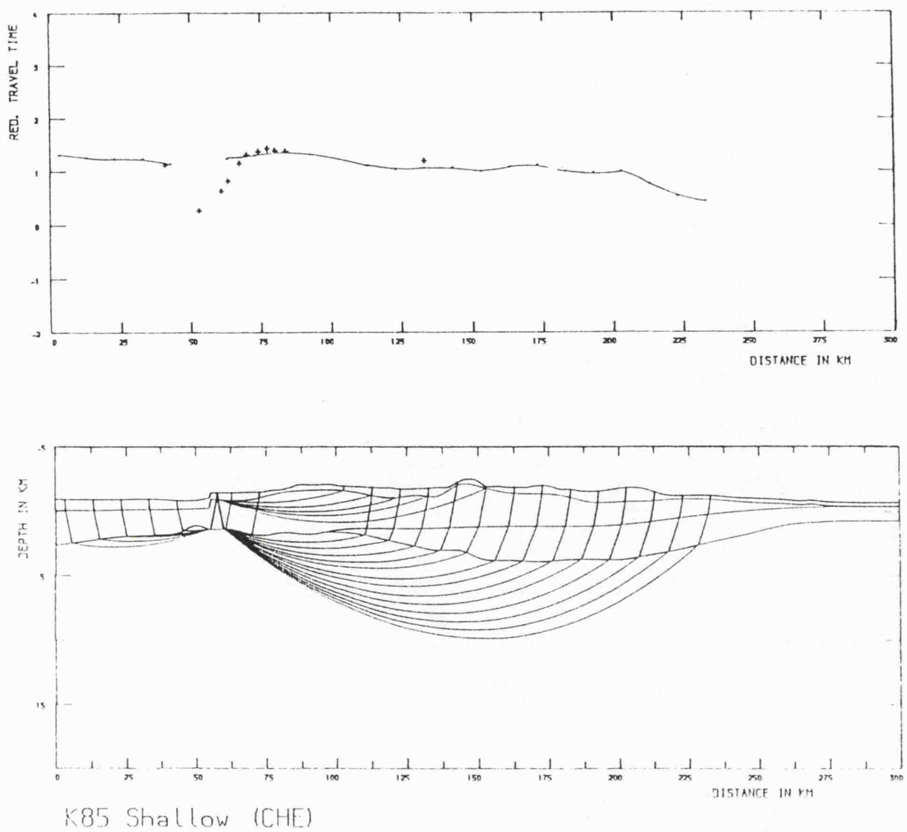

Figure 4.12(e) : Observed and synthetic travel times for the Chepkererat shot and accompanying ray tracing diagram (Vr = 6 km/s).

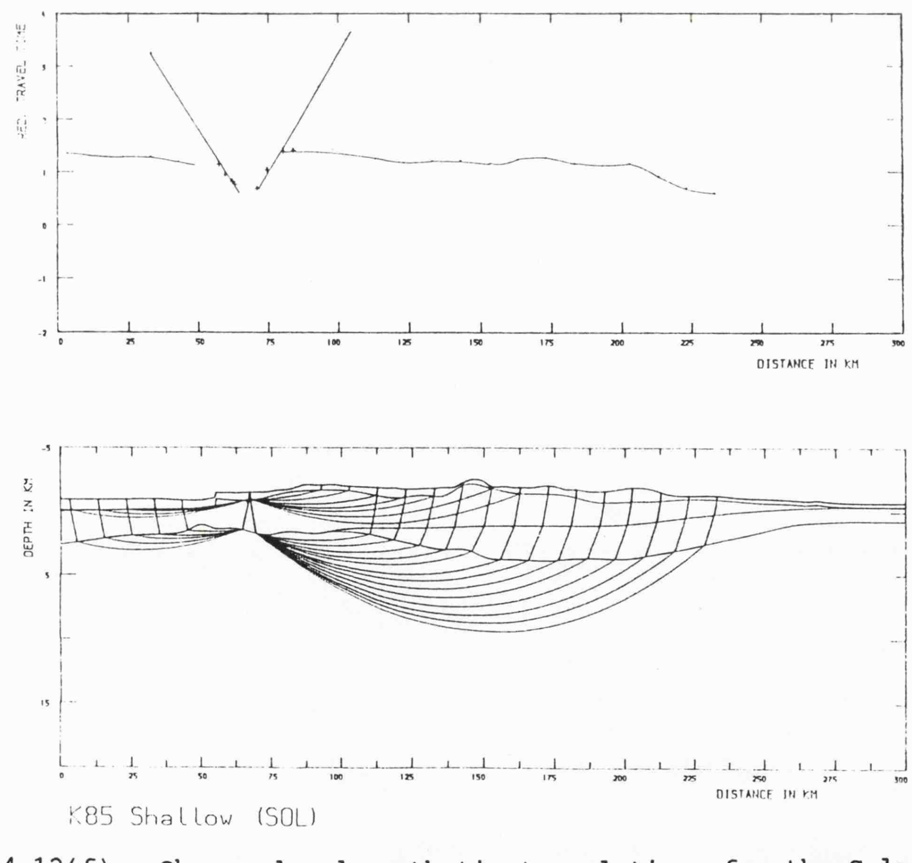

Figure 4.12(f) : Observed and synthetic travel times for the Solai shot and accompanying ray tracing diagram (Vr = 6 km/s).

velocity model. However, the other less well recorded shots also constrained the model. Of course, just because a model gave a good fit for one shot did not mean that it would provide reasonable travel times for the other shots. The shallow velocity model determined is shown in figure 4.11. The horizontal scale on this diagram is the distance from a reference point, 3 km north of BA1. The final ray-tracing diagrams along with reduced velocity plots of actual and synthetic travel times are plotted in figure 4.12. The average absolute difference between observed and synthetic travel time is 0.05 secs. Although the fit is not perfect, it is doubtful that further adjustment of the model could lead to any significant improvement.

The ray tracing modelling of the shallow velocity structure indicated:

(1) The depth to basement varies from less than 2 km below Lake Bogoria and Lake Magadi to about 6 km below Lake Naivasha. North of Lake Bogoria there is a definite deepening of the basement towards Lake Baringo.

(2) The velocity of the rift infill varies from about 2.5 km/s to 5.1 km/s.

(3) A basement velocity of 6.05 km/s is consistent with the observed arrival times.

(4) An approximately 10 km wide zone, of about 6.8 km/s velocity, centred approximately beneath station NS25 produces travel time advances consistent with those observed.

A discussion of the geological implications of the shallow velocity model is reserved until Chapter 7.

4.1.7 Description of later phases.

Phase B is a reflection from a mid-upper crustal transition which is observable on the BA1, BA2 and NAI record sections. It is most pronounced on the two Baringo sections where it is evident from 50 to 100 km range. It has highest amplitude at about 70 km indicating a critical distance of 60 - 70 km. Wide angle reflections have maximum amplitude just beyond the critical distance (Cerveny, 1966).

Phase C1 is also visible on the BA1, BA2 and NAI record sections, but is much more prominent on the two Baringo sections. It can be observed at offsets between 50 and 130 km, having maximum amplitude at 90 - 100 km. In a preliminary interpretation of the KRISP85 data (KRISP working group, 1987) an intra-crustal reflection, labelled C1, was identified, particularly on a polarisation filtered record section of the Baringo data. More detailed study of the properties of the polarisation filter have led to the conclusion that bursts of energy produced by the filter after the first arrival cannot, in general, be reliably correlated from trace to trace (Chapter 3). The preliminary interpretation was made on an incomplete data set and it is now considered that the original correlation (KRISP working group, 1987) of phase C1 is in error.

Phase C2 is interpreted as PmP, the reflected phase from the crust-mantle boundary. It is only well observed on the 2 Baringo record sections on which it can be confidently correlated beyond about 90 km range. Bursts of energy seen on traces recorded at shorter offset distance may also correspond to phase C2 but the correlation is more tentative (hence the dotted line on the record sections). The NAI record section does show energy present in the correct region for the phase (assuming the deep structure is laterally homogeneous). However, the number of "good" traces at the necessary offset is small which makes a confident correlation impossible.

On the BA1 record section a few first arrivals (labelled D) occur in the 260 - 280 km range, in the vicinity of Lake Magadi, at between -2.0 to -3.0 secs reduced time. Least squares analysis gave an apparent velocity of 7.5 $\pm$ 0.2 km/s. The relatively high amplitude of these arrivals suggests they are diving waves in the upper mantle (Pn).

4.1.8 Modelling of deep velocity structure by ray tracing.

As second arrival information from the NS-line is limited to the BA1, BA2 and NAI record sections, it was necessary to assume a 1-D deep velocity model i.e. that velocity varies only with depth. The relative amplitudes of the various phases were used as further constraints on the modelling. Of course, the densities and S-wave velocities assigned to the model layers affect the amplitude variation with range of the phases generated by ray-tracing so further assumptions had to be made. As the S-wave information obtained during the experiment is negligible (Section 4.4) a value of 0.25 was assumed for Poisson's ratio for all layers i.e.

$$V_s = 1/\sqrt{3}\ V_p. \qquad 4.3$$

Densities were calculated using a linear approximation to the Nafe-Drake curve which empirically relates seismic P-wave velocity to density (Nafe and Drake, 1957) i.e.

$$\rho = 0.252 + 0.3788\ V_p. \qquad 4.4$$

This is an assumption commonly made in explosion seismology interpretation.

As the later phases are appreciably more prominent on the Baringo record sections it was these that were initially compared with the ray theoretical synthetic seismograms.

Three classes of velocity depth functions were found to be capable of generating arrival times consistent with those observed. These are shown in figure 4.13. Features common to all three, which were considered to be constrained before forward modelling began, are:

(1) A basement velocity of 6.05 km/s with a positive gradient of about 0.01 s^{-1}. This was well constrained by the analysis of phase Pg described above.

(2) An upper mantle velocity of 7.5 km/s, the apparent velocity measured for phase D. Although unreversed, this agrees with the highest velocity measured during the KRISP68 experiment (Griffiths et al, 1971) conducted along the northern part of the rift (Fig. 1.6).

The three models differ in the velocity variation with depth in the lower crust. Synthetic seismograms obtained for the models are shown in figure 4.14. Amplitudes have been scaled by shot-receiver distance to the power 1.3.

Model(1): The velocity increases in three positive steps from the 6.05 km/s observed at the top of the crust to 7.5 km/s in the upper mantle. Although giving arrival times in agreement with those observed it was found that such a model could not give sufficiently high amplitude arrivals for both the C1 and C2 phases. For example, synthetic seismogram (a) shown in figure 4.14 shows that phase C1 is too weak and has its maximum amplitude at too great a range.

Model(2): This velocity depth function includes a high velocity layer (7.1 km/s) at about 22 km depth, the upper boundary of which gives rise to phase C1. Below this the velocity reverts to a value of about 6.7 km/s for the lower crust. Synthetic seismogram (b) of figure 4.14 shows that the resulting amplitudes are in good agreement with those observed. Of the models considered, this type was found to give the closest overall agreement of travel times and amplitudes.

Model(3): This model includes a low velocity layer at about 22 km depth. It was found that a sufficiently high amplitude C1 phase could not be generated without necessitating an unreasonably low velocity at such a depth within the crust. For example synthetic

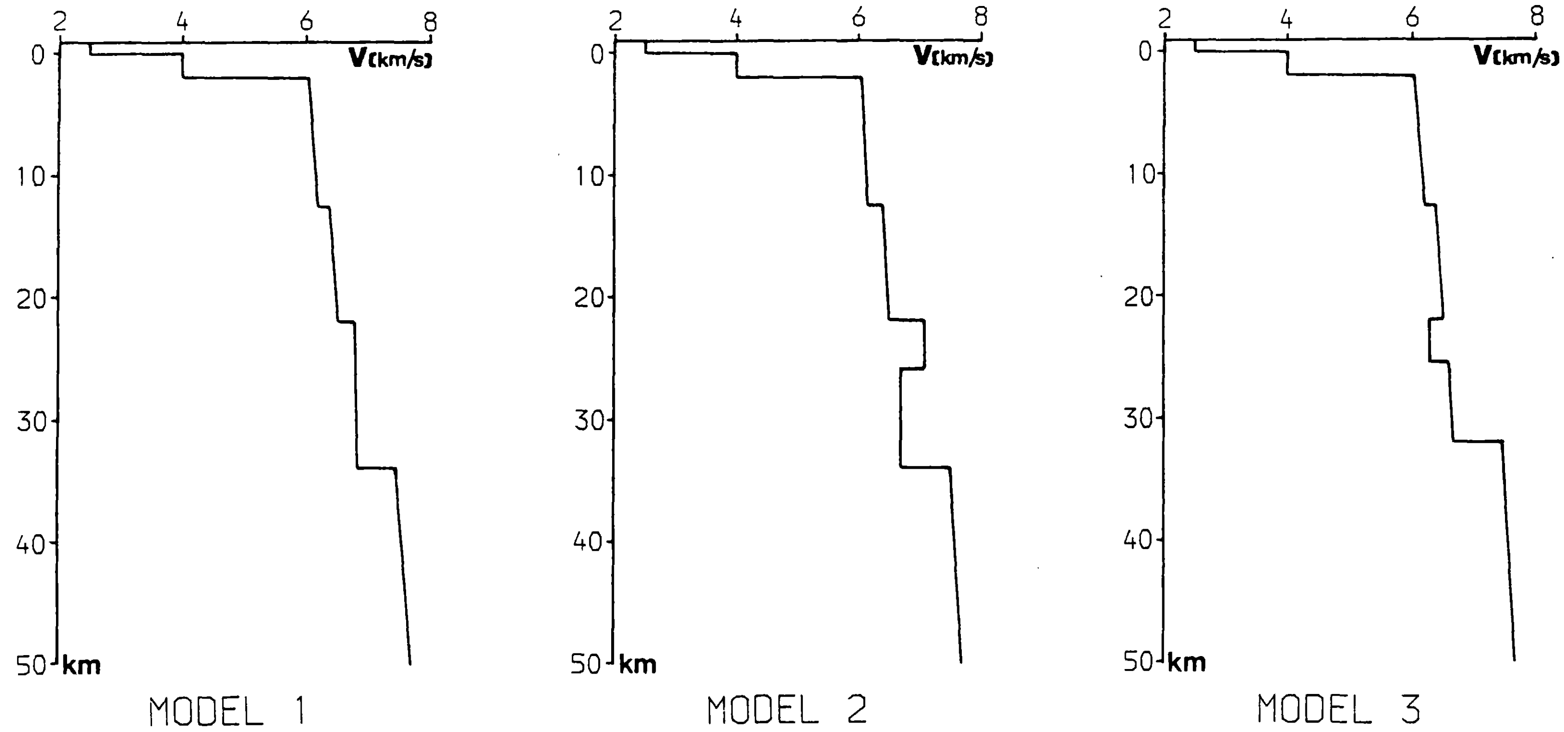

Figure 4.13 : Three classes of velocity-depth functions which gave arrival times consistent with those observed.

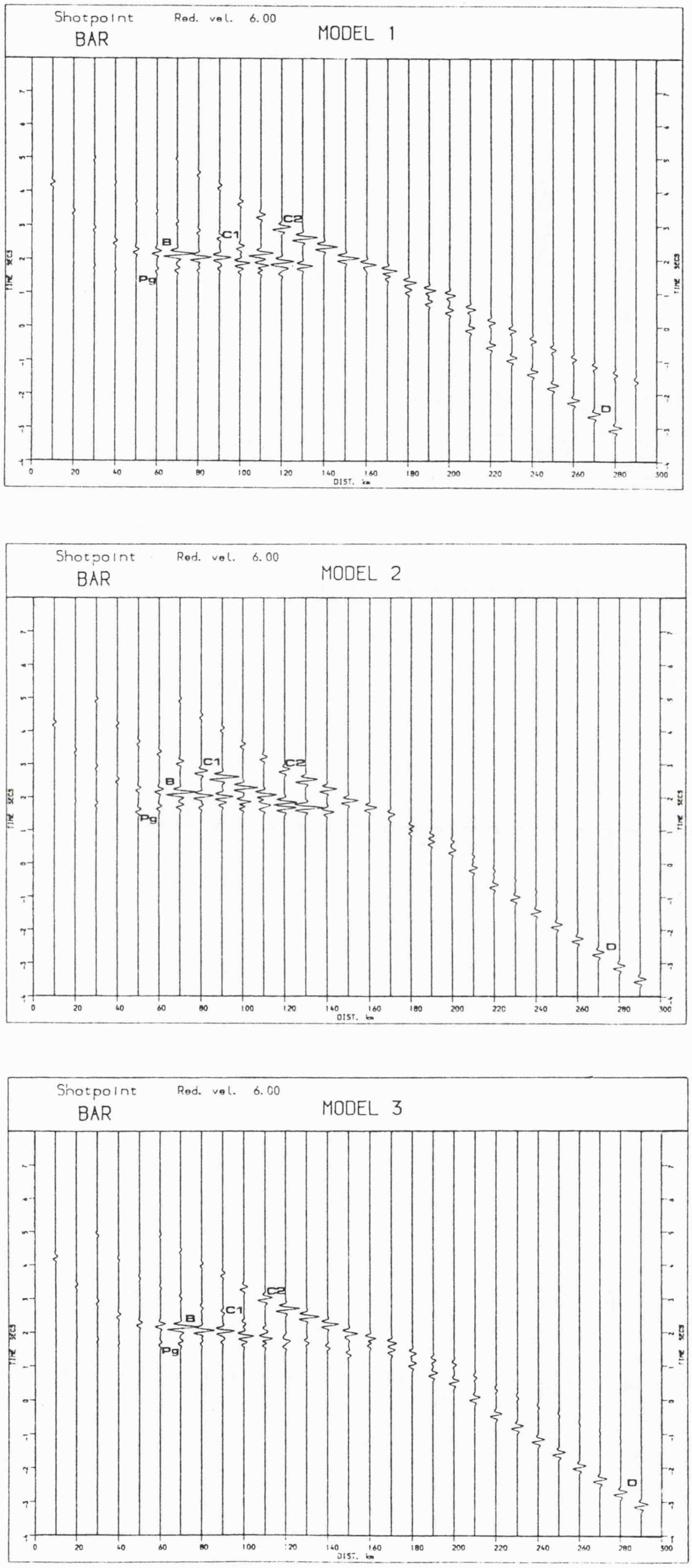

Figure 4.14 : Synthetic seismograms generated for models 1, 2 and 3 of figure 4.13.

seismogram (c) of figure 4.14 shows that a low velocity layer of 6.2 km/s results in phase C1 having too low an amplitude.

The preferred velocity-depth function is shown in figure 4.15 together with the synthetic record section for the Baringo shots and the associated ray tracing diagram. Figure 4.16 shows the same for the Naivasha shot. Figure 4.17 shows amplitude-ratio against distance plots for shot BA2. These include both observed and synthetic amplitude ratios for phases B, C1 and C2, all normalised by Pg. The agreement is satisfactory, the only major discrepancy being that the measured amplitude-ratios of C2 at shorter ranges are significantly higher than those computed. A possible explanation for this is offered below. Amplitude ratios measured for shot BA1 were similar to those of shot BA2 so are not presented here. No amplitude ratios were measured for shot NAI.

The main features of the favoured deep P-wave velocity depth function together with an indication of the uncertainties are summarised below. All depths quoted are relative to sea level. The upper crustal velocity of 6.05 $\pm$ 0.03 km/s increases steadily with depth to a value between 6.15 and 6.20 km/s at 12.5 $\pm$ 1.0 km depth where the velocity increases discontinuously to 6.45 km/s $\pm$ 0.1 km/s. This discontinuity gives rise to phase B. Below this interface it is assumed that the velocity continues to increase gradually with depth to a value of 6.6 $\pm$ 0.1 km/s at 22 $\pm$ 2.0 km depth where it increases discontinuously to 7.1 $\pm$ 0.15 km/s. This is the top surface of the high velocity layer and causes intra-crustal reflection C1. The thickness of this layer is estimated to be about 4 km but neither its thickness nor the velocity behaviour at its base are well constrained. However, the velocity must decrease to a value in the region of 6.7 km/s in order to produce a sufficiently high amplitude C2 (PmP) phase. The crust mantle boundary occurs at 34 $\pm$ 2 km where the velocity increases discontinuously to 7.5 $\pm$ 0.2 km/s. As mentioned above, there is some discrepancy in the amplitude-distance behaviour of this phase. In particular, the synthetic amplitudes calculated for shorter offsets are too low. This is remedied if the upper mantle material is assigned a slightly higher than normal Poisson's ratio (for example 0.28). It is thus possible that the upper mantle has a lower than normal S-wave:P-wave velocity ratio. However, given the limitations of the data, this cannot be stated with much confidence.

The significance of the above velocity depth function will be discussed in Chapter 7.

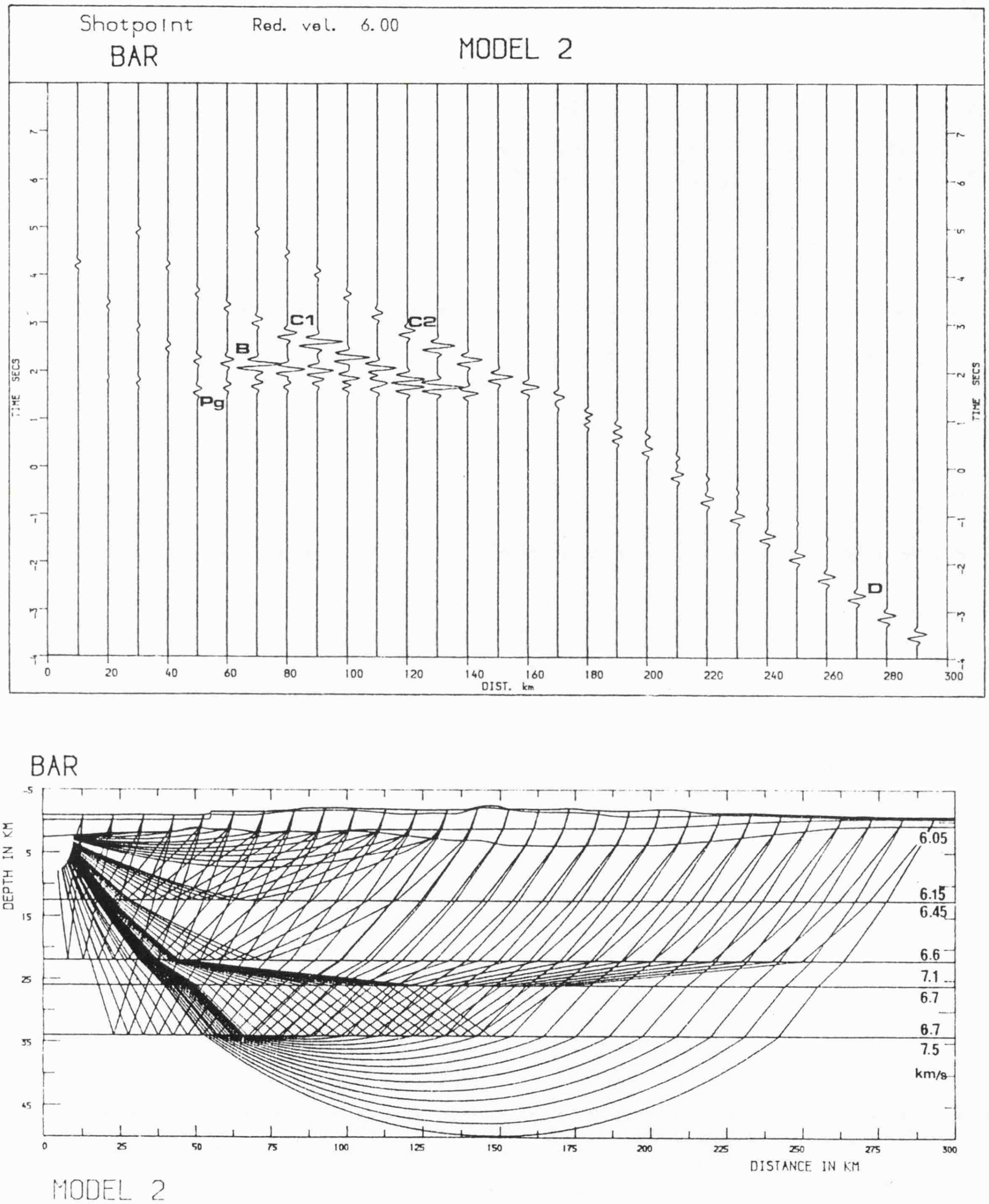

Figure 4.15 : Synthetic seismogram and ray tracing diagram for the Baringo shots.

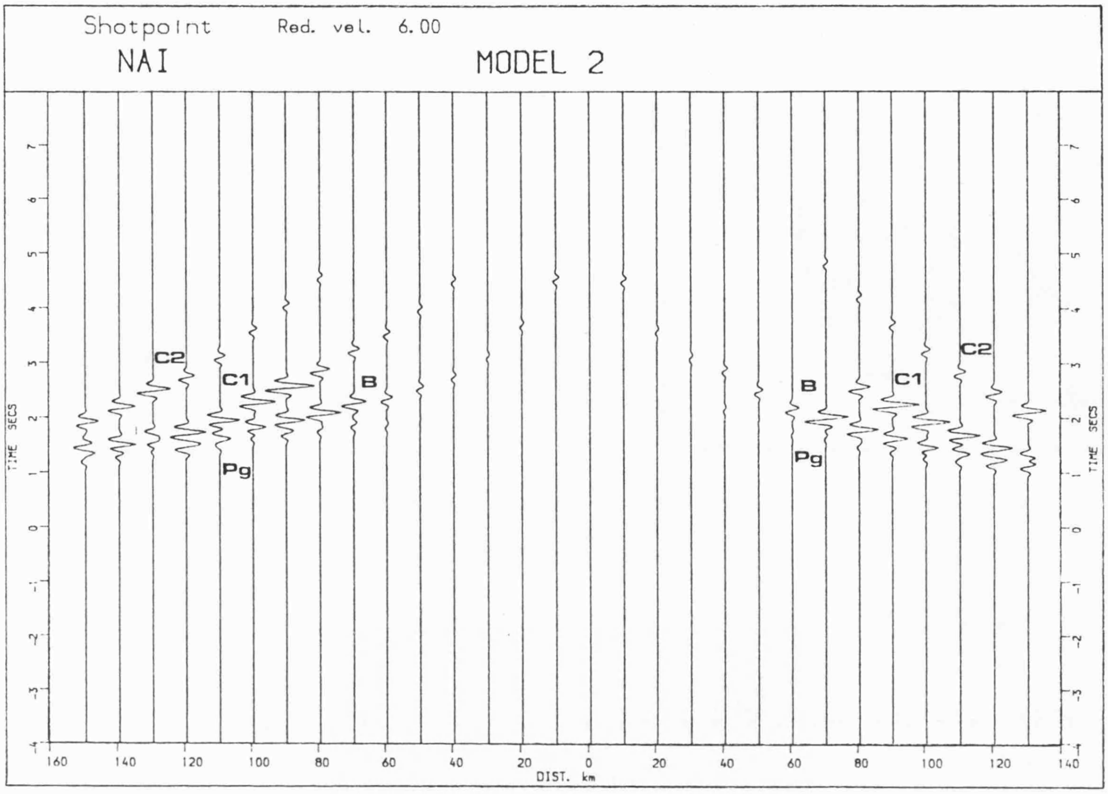

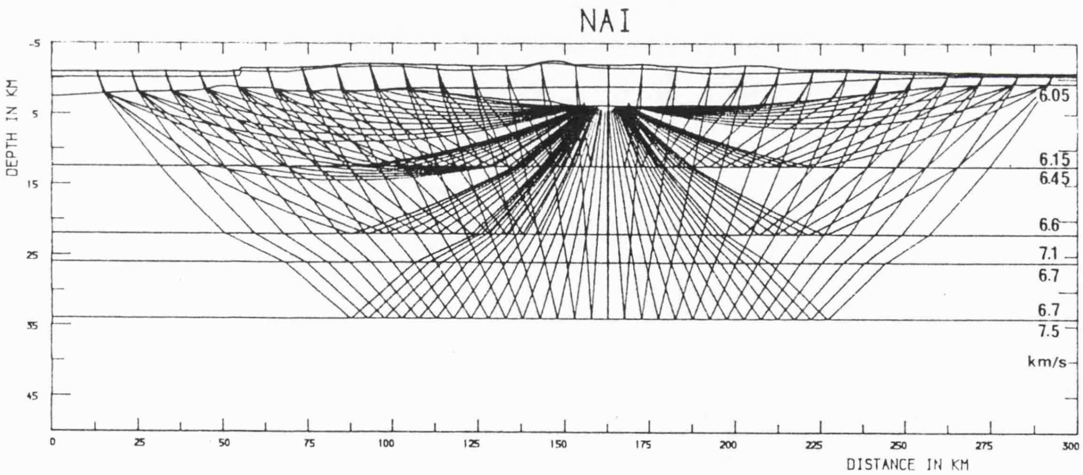

MODEL 2

Figure 4.16 : Synthetic seismogram and ray tracing diagram for the Naivasha shot.

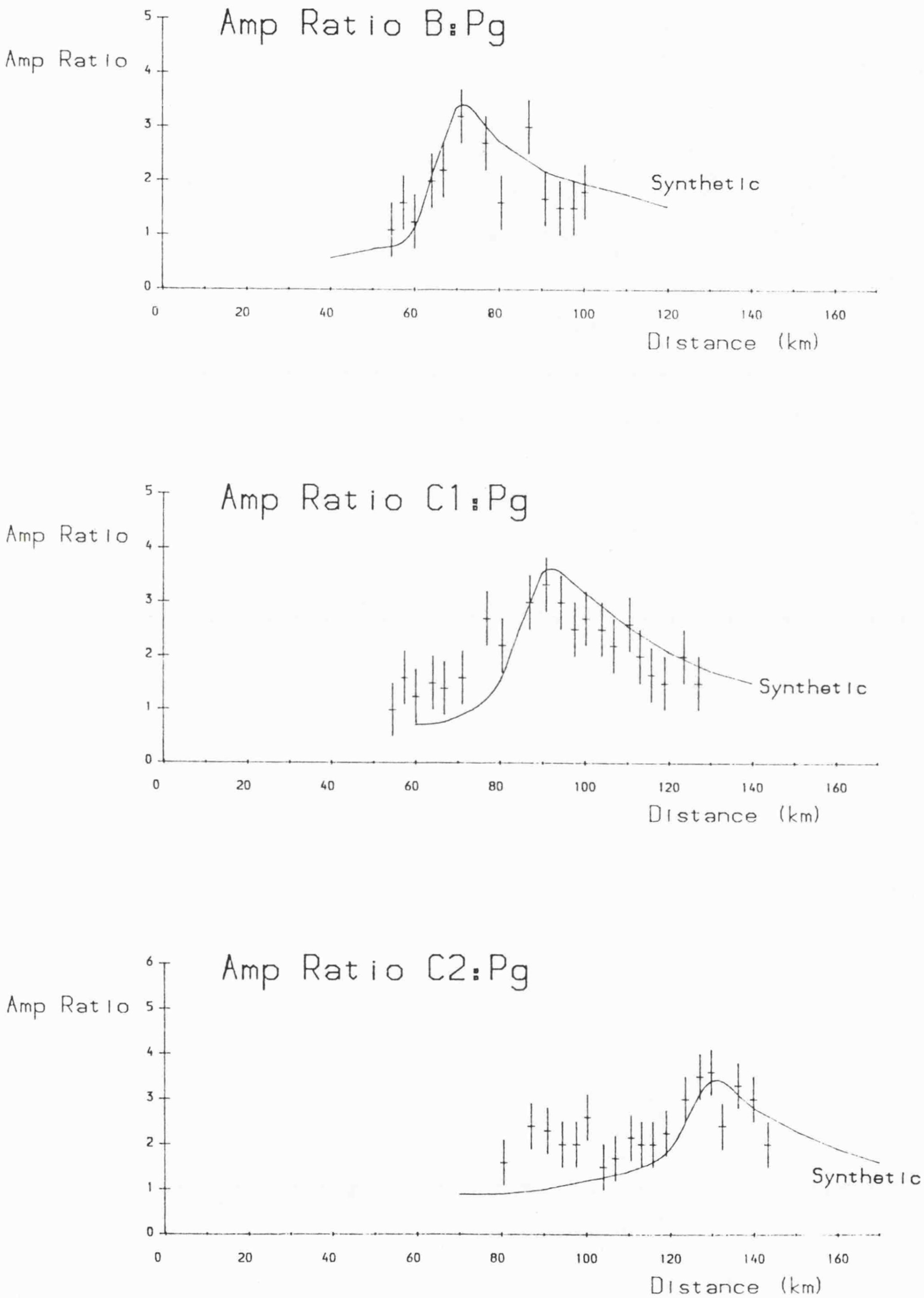

Figure 4.17 : Synthetic and observed amplitude ratios for the Baringo 2 shot.

4.2 Reinterpretation of some KRISP75 data.

The KRISP75 explosion programme included a short line along the rift between Lake Baringo and Lake Bogoria (Fig. 2.1). It is not mentioned in the main publication arising from the project (Swain et al, 1981) but is described briefly by Swain (1979). Owing to poor first arrival energy from shots fired in Lake Bogoria, the only result mentioned is a refractor velocity of 5.75 $\pm$ 0.27 km/s. This is sufficiently different from the 6.05 $\pm$ 0.05 km/s refractor velocity determined from the KRISP85 data to merit further investigation.

Fortunately, a set of first arrival times for the line was obtained. These were checked against paper records where possible and are listed along with ranges in Appendix A.

There were 4 shot points in total, 2 in Lake Baringo (BAN and BAS) and 2 in Lake Bogoria, formerly Lake Hannington (HAN and HAS, using the original nomenclature). Thirty receiving stations were located along the 30 km line between shot points BAS and HAN (Fig. 4.18). Stations 11 to 20 were offset about 2 km to the east where noise levels were more tolerable. This took them close to bedrock at the edge of the alluvial deposits (Fig. 4.18).

Reduced velocity plots of the first arrival times from the 4 shots are shown in figure 4.19. All the first arrivals beyond about 10 km offset are interpreted as the basement refraction, Pg. A time-term interpretation was thought most appropriate as it would yield an estimate of the basement velocity as well as an indication of the variation in depth to basement. In line with the requirements of the method only stations having recorded Pg from at least 2 shots were included in the interpretation. Fortuitously, this removed some of the more doubtful observations (e.g. stations 21 - 24, shot HAN). The proximity of recording station 1 to the HAN shot point allowed them to be treated as one station thus permitting a unique time-term solution to be found. The time-term linkages shown in table 4.6 show that 56 observations were used to calculate 21 time-terms.

Program **TIMTERM** was run, inputting the shot-receiver distances and travel times along with error estimates. The resulting solution is shown in table 4.7. The refractor velocity of 5.95 $\pm$ 0.16 km/s is consistent with the KRISP85 value of 6.05 $\pm$ 0.05 km/s. The time-terms, although quite scattered, are also in general agreement with the northern end of the KRISP85 shallow velocity model (Fig. 4.11) in that they show a general increase from south to north. Lower values obtained for stations 11 - 17 are probably due to their proximity to bedrock. An appreciable thickness of low velocity alluvium below a station will result in a significantly higher delay time. The solution variance of 0.022 s^2 compares with the

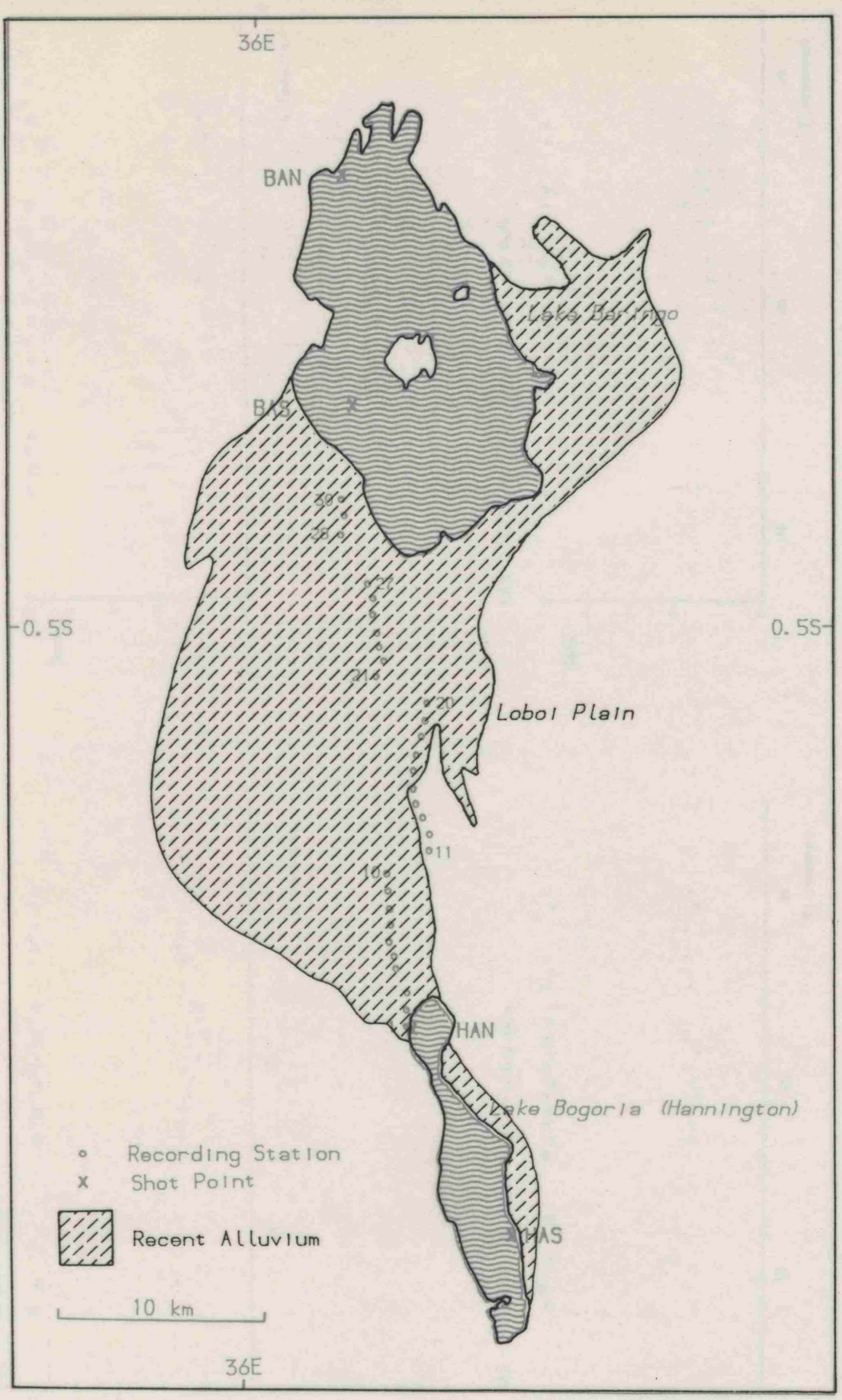

Figure 4.18 : Map showing location of KRISP75 NS-line with overlay showing extent of alluvial deposits.

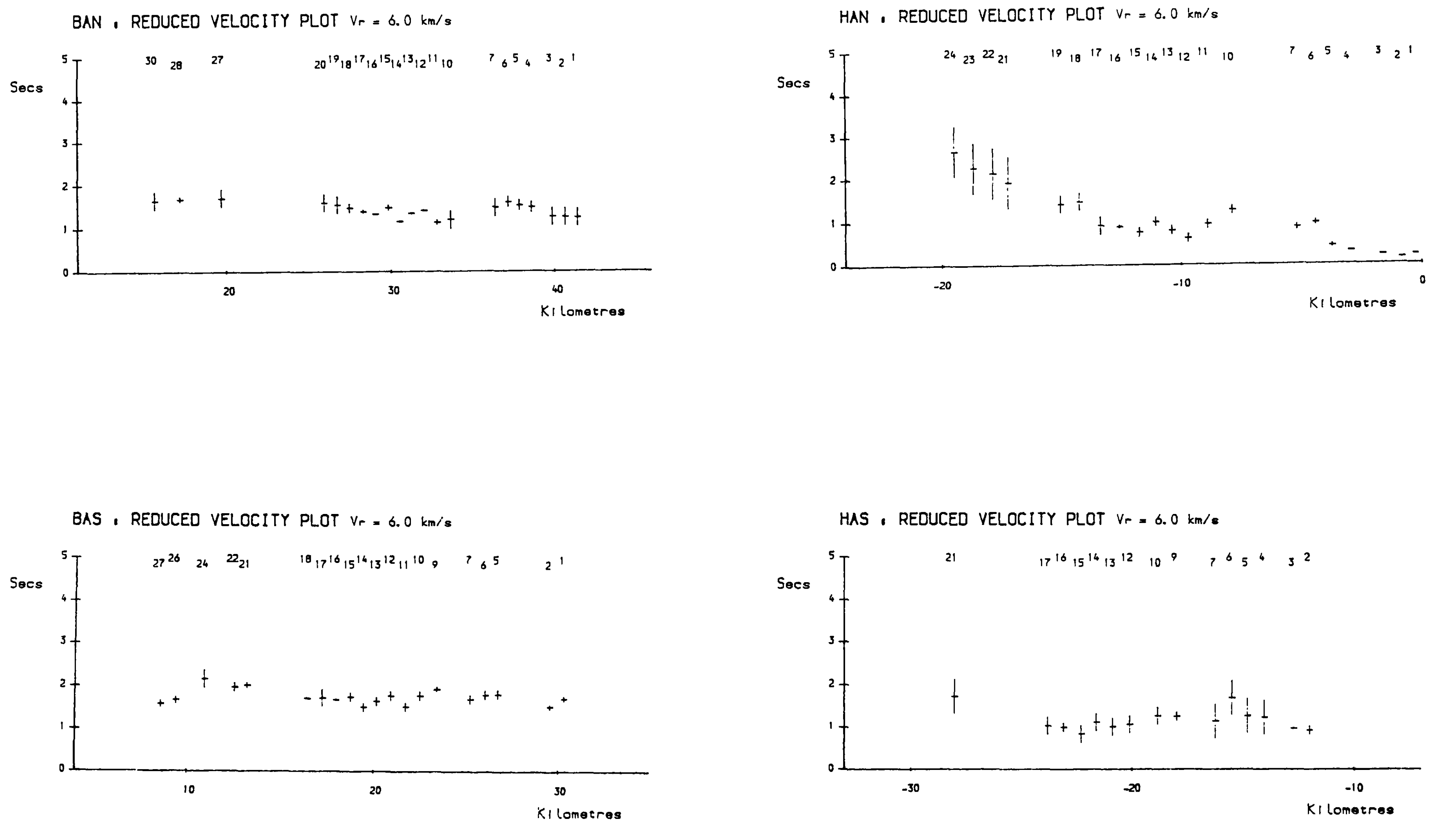

Figure 4.19 : Reduced velocity plots of the shots fired into the KRISP75 NS-line.

Table 4.6 : Time-term linkages and solution for KRISP75 data.

STATION	N	BAN	BAS	HAN	HAS
1(HAN)	3	*	*		*
2	3	*	*		*
3	2	*			*
4	2	*			*
5	3	*	*		*
6	2	*	*		
7	3	*	*		*
9	2		*		*
10	4	*	*	*	*
11	3	*	*	*	
12	4	*	*	*	*
13	4	*	*	*	*
14	4	*	*	*	*
15	4	*	*	*	*
16	4	*	*	*	*
17	4	*	*	*	*
18	3	*	*	*	
19	2	*		*	

SITE	N	T.T.	S.E.
HAS	14	0.44	0.02
HAN(1)	10	0.46	0.05
2	3	0.43	0.02
3	3	0.41	0.01
4	2	0.51	0.04
5	3	0.64	0.03
6	2	0.55	0.06
7	3	0.63	0.03
9	2	0.65	0.02
10	4	0.65	0.1
11	3	0.42	0.06
12	4	0.48	0.1
13	4	0.55	0.02
14	4	0.53	0.08
15	4	0.57	0.09
16	4	0.56	0.02
17	4	0.50	0.02
18	3	0.77	0.17
19	2	0.80	0.13
BAS	15	1.09	0.01
BAN	17	0.94	0.02

No. observations = 56

No. time-terms = 21

Solution velocity = 5.95 ± 0.16 km/s

Solution variance = $0.022\ s^2$

observational error estimate of 0.025 s^2, giving an F ratio of about 1 which makes a second iteration unnecessary.

4.3 EW-line Interpretation.

Record sections are presented for 4 of the 5 EW-line shots in figures 4.20 - 4.23. The 1.14 Tonne, off-end shot at Makuyu (MAK) is not included because it did not provide detectable energy at any of the recording sites. Of the others, the Ewaso Ngiro shot (EWA) was the most successful, providing useful energy out to over 60 km range. The Ntulelei shot (NTU) was observed by stations on the western flank of the rift but was not detected by stations within the rift. The 2 shots fired within the rift, SU1 and MAR, were both only detectable out to about 10 km range. Only a limited interpretation has been possible, the information available not meriting either time-term analysis or ray-tracing modelling. However, shallow velocity-depth functions have been derived for all shots except MAK and additional, more qualitative, conclusions have been made. The velocities and depths determined are shown in form of a schematic cross-section in figure 4.24.

4.3.1 Interpretation of shots EWA and NTU.

The EWA record section (Fig. 4.20) shows reasonable seismic energy out to a range of over 60 km. The basement refraction, Pg, is observable, as a strong first arrival, out to about 60 km. Close examination showed that it consists of 3 branches (<38 km, 38 km - 50 km and >50 km). The most likely explanation for this step like appearance is successive down faulting of the basement. This is supported by the location of major boundary faults between the branches, at about 39 km and 49 km on the record section (Fig. 4.24) Estimates of the time offsets indicate downthrows of the basement of 0.9 $\pm$ 0.4 km and 1.5 $\pm$ 0.5 km for the 2 faults. The average apparent velocity of the 3 branches was found by least squares to be 5.95 $\pm$ 0.15 km/s.

Beyond about 55 km range there is a definite travel time advance of the first arrivals. Possible explanations are: (1) a shallowing of the basement, (2) onset of a refraction from a deeper, higher velocity layer; or (3) a lateral increase in the basement velocity similar to the high velocity zone inferred from the NS-line data. (1) and (3) are more feasible explanations given the similarity of the wave-form before and after the advance. The scale of the advance suggests a combination of the two might be responsible.

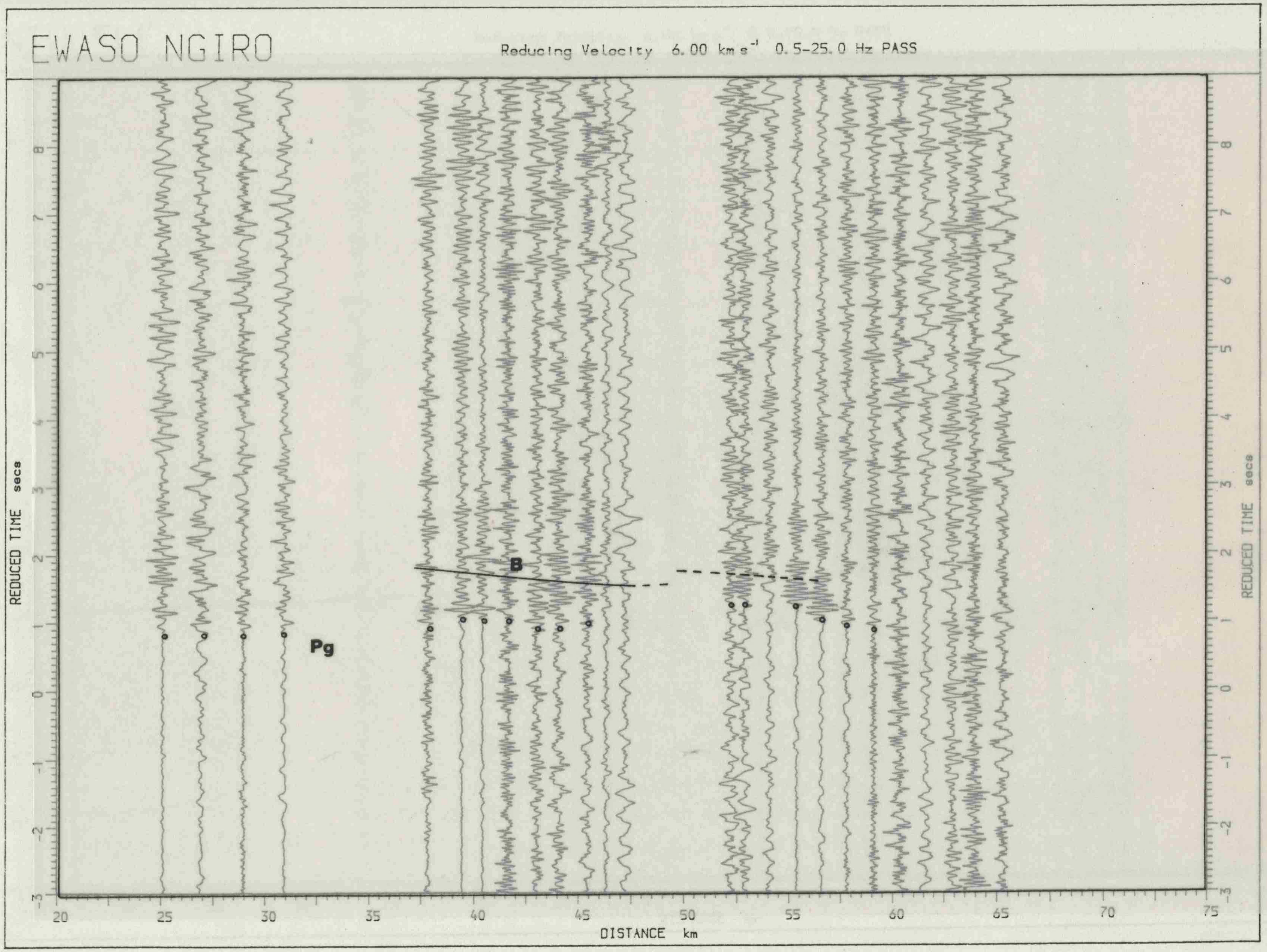

Figure 4.20 : Ewaso Ngiro record section (EW-line).

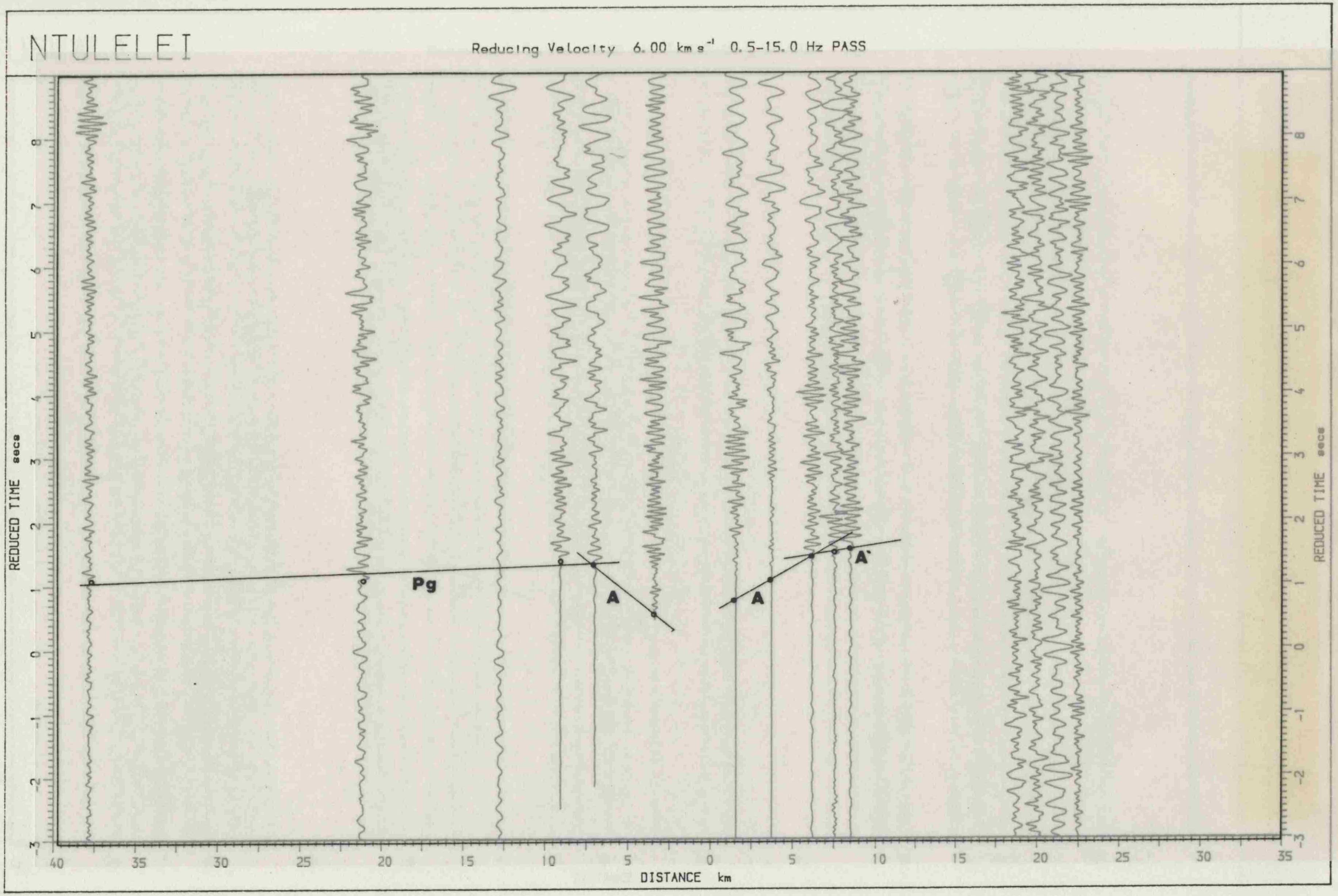

Figure 4.21 : Ntulelei record section (EW-line).

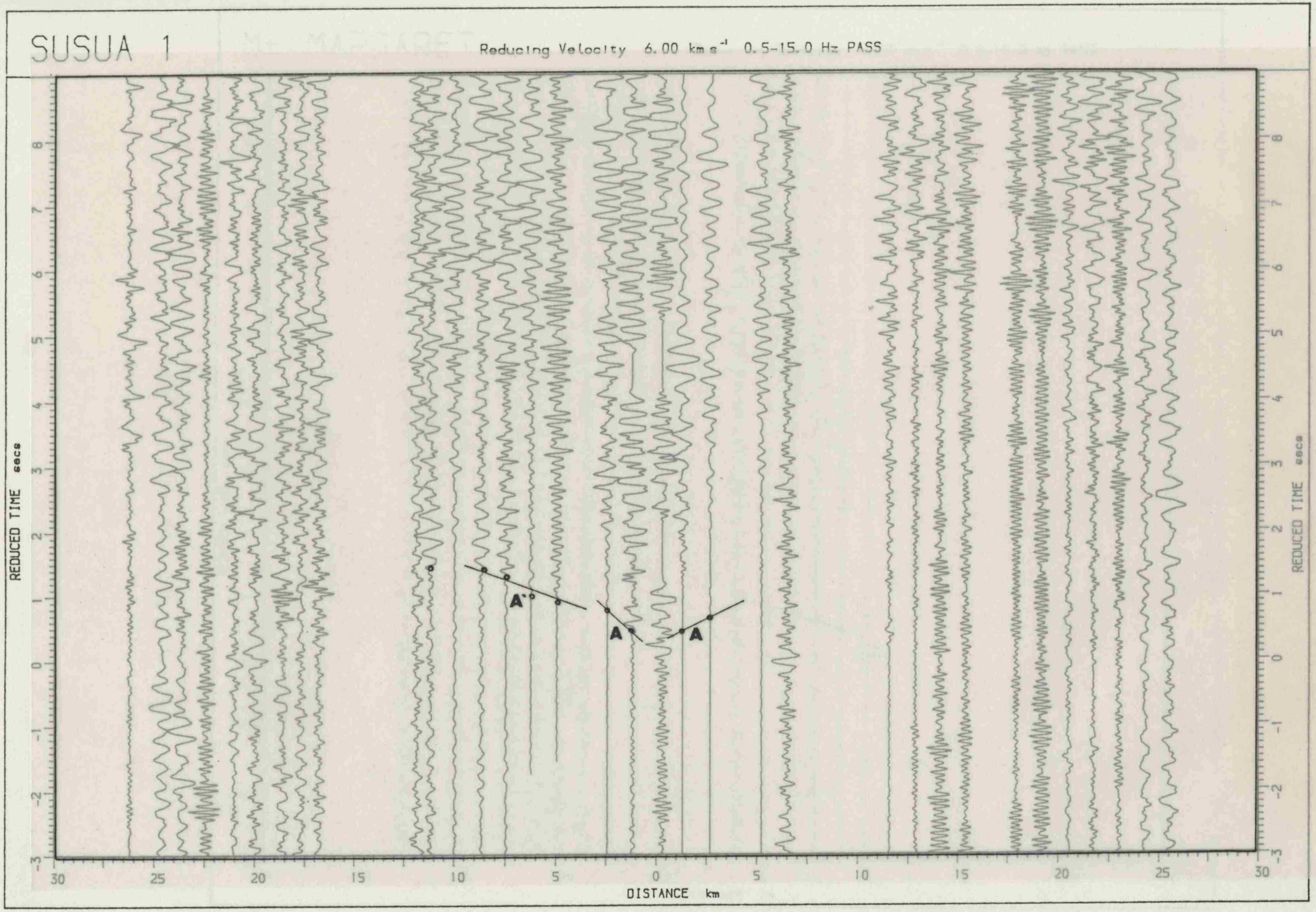

Figure 4.22 : Susua 1 record section (EW-line).

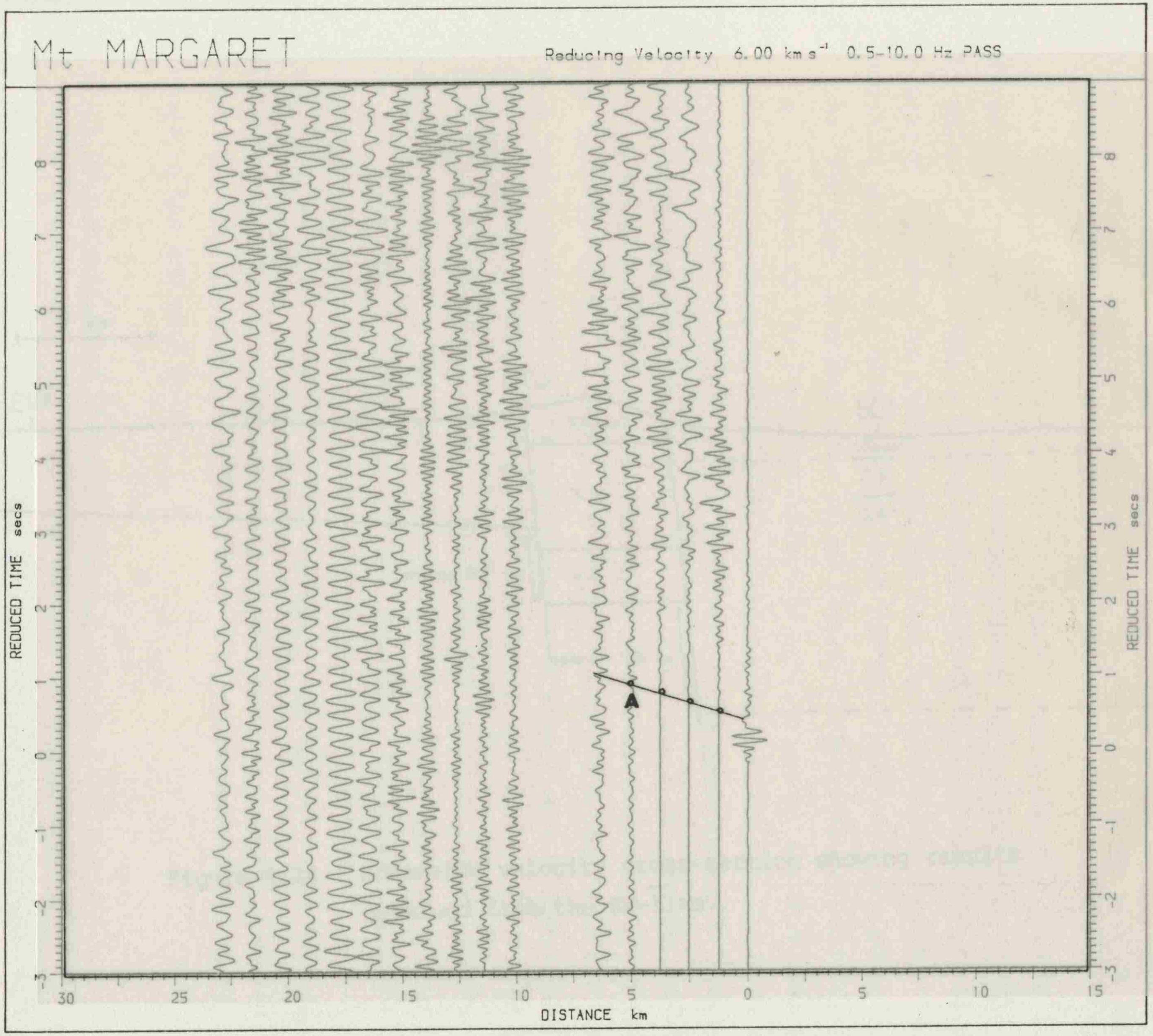

Figure 4.23 : Mt Margaret record section (EW-line).

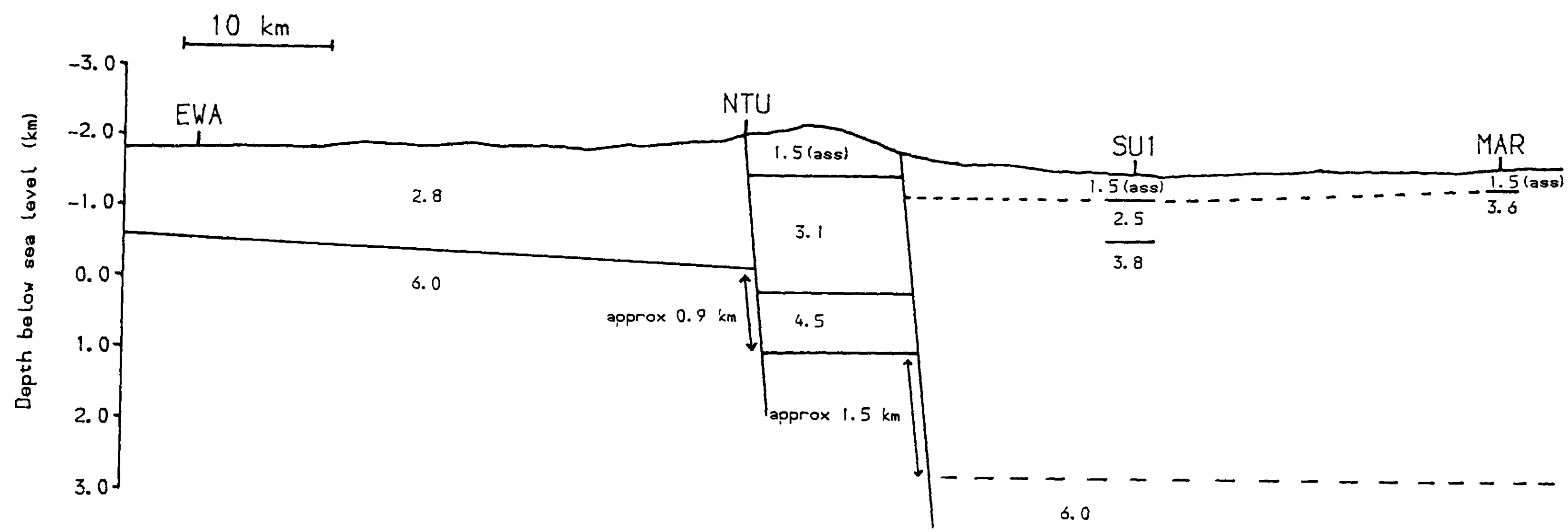

Figure 4.24 : Schematic velocity cross-section showing results obtained from the EW-line.

A later phase, labelled B on the record section, was identified at about 0.9 secs after the first arrival between about 37 km and 47 km range. Whether the correlation can be continued as far as the traces beyond 50 km range is doubtful, hence the dotted line on the record section. This phase appears at about the same time as the intracrustal reflection, phase B on the Baringo and Naivasha record sections from the NS-line. It is probable that it is caused by the same crustal transition at about 12.5 km depth (below sea level).

The most striking feature of the EWA record section is the high frequency content. The seismic energy present is predominantly of 10 - 15 Hz which is significantly higher than observed from the other shots of the experiment. A possible explanation for this is that EWA was the only "wet" borehole shot of the project other than MAK which was not observed at all.

The NTU shot, situated about 10 km west of the western rift margin, was well observed on the flank but failed to provide useful energy within the rift. The most obvious feature of the record section (Fig 4.21) is the asymmetry about the shot point. For this reason velocity depth functions were calculated for west and east of NTU (Fig. 4.24). To the west the first arrival data was combined with that of the EWA shot obtained between EWA and NTU to give a simple 2-D velocity model. A velocity of 6.1 $\pm$ 0.2 km/s was calculated for the basement which underlies a volcanic pile of 2.8 $\pm$ 0.1 km/s velocity (derived from NTU only). The volcanic pile was found to thicken from about 1.2 km below EWA to about 1.9 km immediately west of NTU (Fig 4.24). East of shot NTU, Pg was not observed within the 10 km over which good energy was observed. The planar model derived consists of 1.5 km/s (assumed) and a 2.8 $\pm$ 0.2 km/s layers underlain by 4.5 $\pm$ 0.1 km/s material. The asymmetry of the NTU record section is consistent with the down faulting of the basement inferred from the EWA shot and with the surface expression of a north-south striking fault seen close to the NTU shot point.

4.3.2 Interpretation of shots SU1 and MAR.

There is little to say about the SU1 and MAR shots other than that they provided little information. The record sections (Fig.4.22 and Fig 4.23) show that neither was observed at sufficient range for the thickness of the rift infill to be derived. Planar velocity models calculated for the near surface material are included in figure 4.24.

4.4 S-wave analysis.

S-wave sections are presented for 4 of the more successful shots, namely BA2, NAI, CHE of the NS-line and EWA of the EW-line. These comprise radial traces which should show the predominantly horizontal ground motion of steeply emerging S-waves. A reducing velocity of 3.46 km/s and time scale of $\sqrt{3}$ times that used for the P-wave sections were selected. The choice of these parameters means that if P and S wave record sections are superimposed the S-wave phases should directly overlie the corresponding P-wave phases, assuming a universal value of 0.25 for Poisson's ratio. Any major departures from this rule may then be interpreted in terms of abnormal P-wave:S-wave velocity ratios. The S-wave record sections presented each have an overlay showing expected S-wave phase arrival times predicted from the corresponding P-wave record section.

Close examination of the S-wave record sections (Fig. 4.25 - 4.28) shows that S-wave energy present is generally not of sufficient amplitude for any confident interpretation to be possible. The record sections show that the 2 bore-hole shots have given a slightly higher ratio of S-wave:P-wave energy than the lake shots.

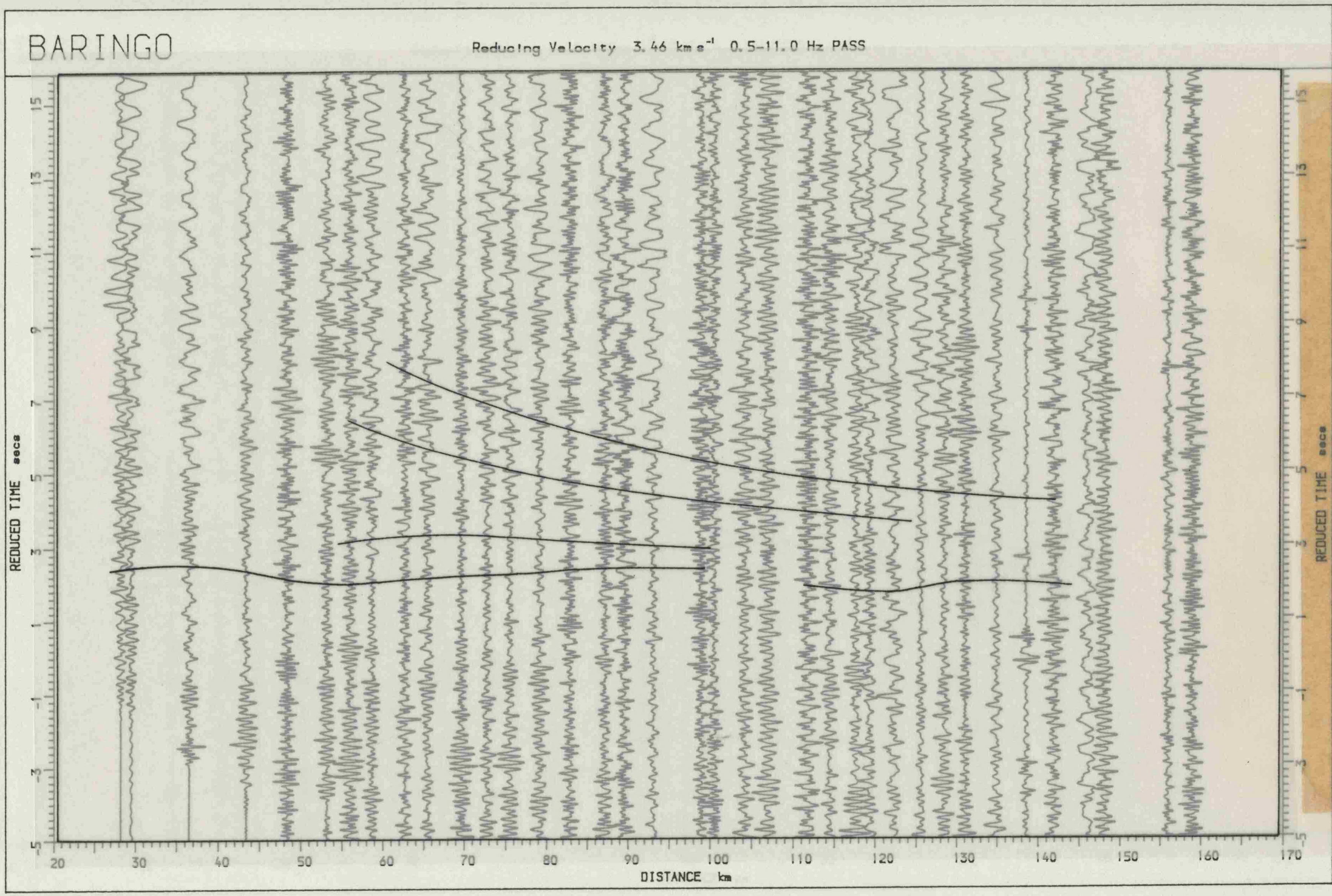

Figure 4.25 : Baringo 2 S-wave record section (NS-line).

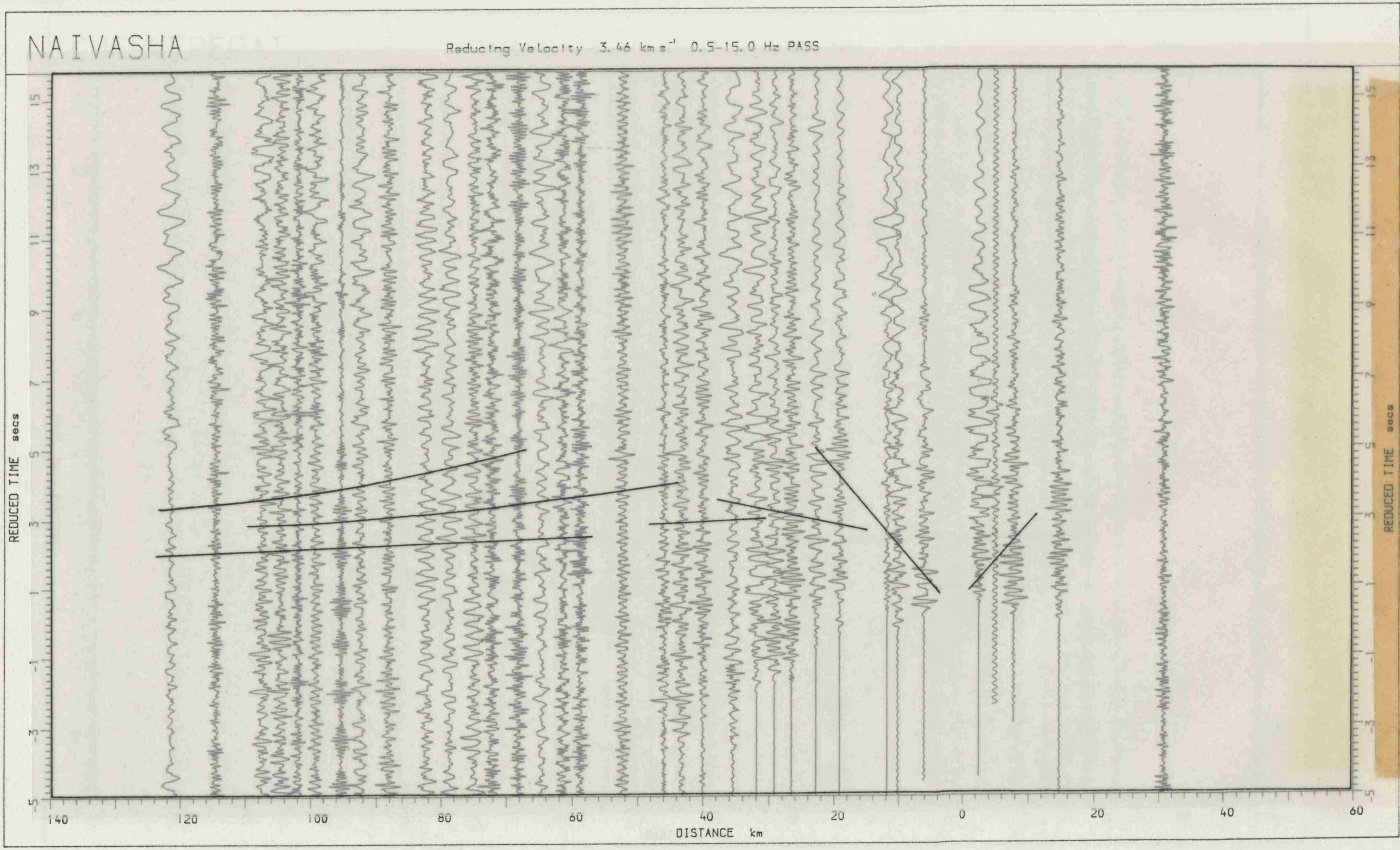

Figure 4.26 : Naivasha S-wave record section (NS-line).

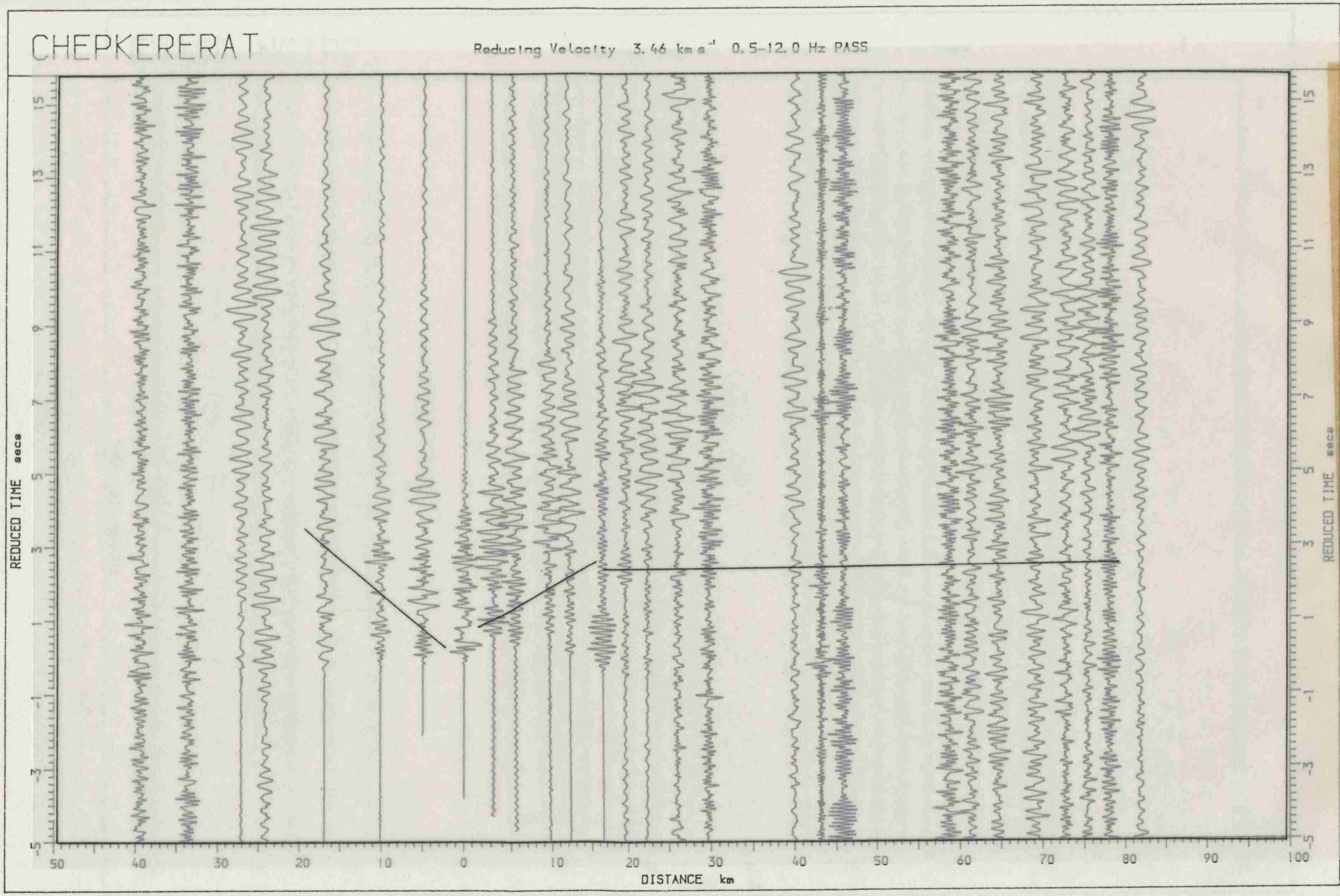

Figure 4.27 : Chepkererat S-wave record section (NS-line).

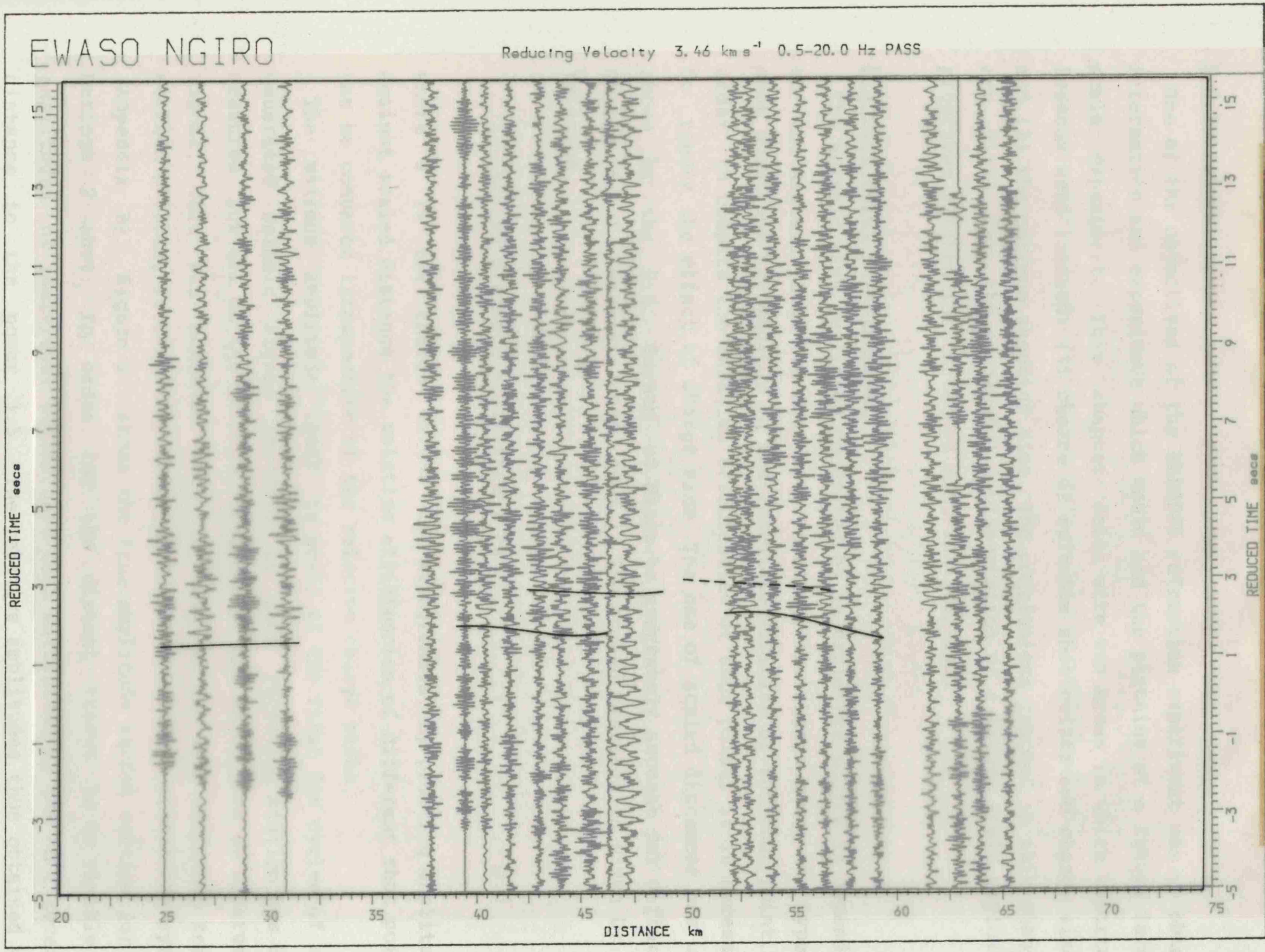

Figure 4.28 : Ewaso Ngiro S-wave record section (EW-line).

CHAPTER (V)

SHOT EFFICIENCIES AND DIURNAL NOISE VARIATION STUDY

5.0 Introduction.

One of the objectives of the KRISP85 refraction experiment was to obtain information and experience which would aid the planning of a future larger scale experiment. This chapter deals with two areas in which important lessons were learned: (1) choice of suitable shot points and charge sizes; and (2) the optimum shooting time. The conclusions reached in this chapter are vital for the successful implementation of a larger scale explosion programme planned for the Kenya rift in 1988/1989.

5.1 Shot point efficiencies.

The seismic wave amplitude generated by an explosive source is dependent on the distance from the source to receiver, the charge size, the type of shot point and the geology in the immediate vicinity of the shot point. In order to compare the relative efficiencies of shot points it is necessary to remove the effect of charge size. The use of scaled distances has been shown by the U.S. Bureau of Mines to accurately account for differing charge sizes (Braile, pers. comm.). The scaled distance is given by the relation

$$\text{scaled distance} = \text{distance} / \sqrt{W} \qquad 5.1$$

where W is the charge weight in kilogrammes. By plotting amplitudes against scaled distance the relative efficiencies of different shot points can be compared irrespective of the relative charge sizes.

The maximum amplitude (peak to peak) of the first few cycles of shot generated seismic signal recorded at each receiving station has been measured for all of the KRISP85 shots except MAK which gave no observable signal. This was achieved with the aid of the true amplitude record section plotting routines incorporated in the SDPS4 data processing system (Appendix B). Figure 5.1 shows the true amplitude record section for the Baringo 2 shot. In order for the distant traces to be visible the amplitudes of individual traces have been multiplied by the shot receiver distance to the power 1.5. The relative amplitudes thus obtained were converted to ground velocities (cm/s) using the known instrument responses. Additional amplitudes were measured from existing paper records of seismograms from four of the KRISP75 shot points (Swain et al, 1981).

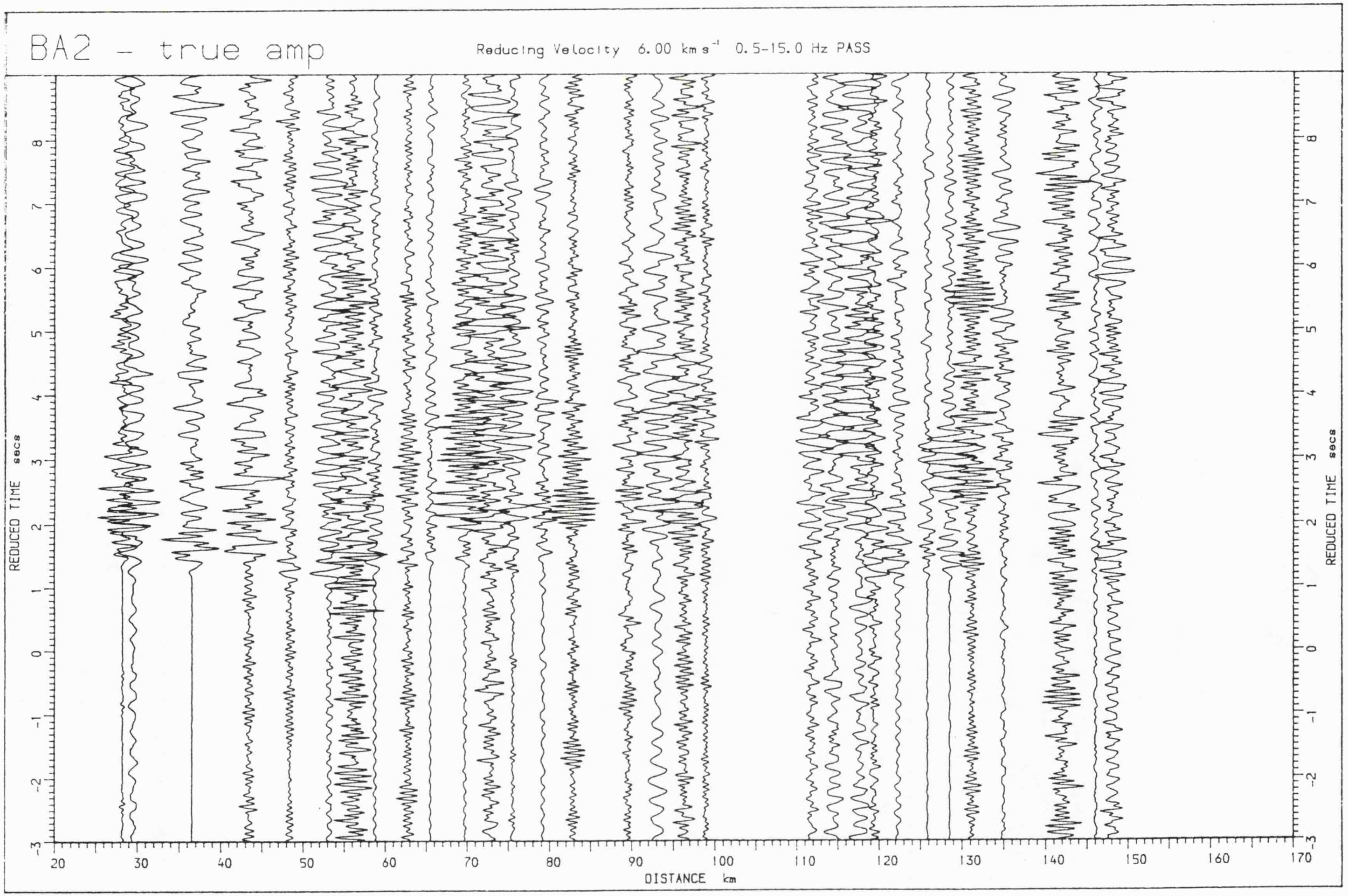

Figure 5.1 : True amplitude record section for the Baringo 2 shot. The amplitudes of each trace have been scaled by the shot-receiver distance to the power 1.5.

These records include calibration signals which allowed the determination of ground velocities in cm/s. The locations of all the shot points used in this analysis, as well as those of the KRISP68 experiment, are shown in figure 5.2.

Figure 5.3 (a-p) consists of 16 amplitude vs scaled distance plots, 12 of them for KRISP85 shots (a-l) and the remaining 4 for KRISP75 shots (m-p). In general, the data for individual shot points plot approximately along straight lines given by

$$\log A = a + b(\log X') \qquad 5.2$$

where A is the amplitude of the ground velocity, X' is scaled distance, **a** is the coupling parameter and **b** is the gradient. The coupling parameter is a rough measure of the efficiency of the shot and the gradient depends primarily on the attenuating properties (Q) and the velocity-depth gradient of the medium along the ray path. The details of each shot together with least squares estimates of **a** and **b** are listed along side each amplitude vs scaled distance plot and are summarised in table 5.1.

Table 5.1 : Coupling parameters and gradients.

Shot	Type	a	b	
BA2	Lake	-3.3	-1.6	
BA1	Lake	-3.9	-1.7	
NAI	Lake	-4.1	-1.6	
EWA	Wet bore-hole	-4.3	-1.7	(assumed)
CHE	Dry bore-hole	-4.65	-1.7	
NTU	Dry bore-hole	-4.6	-1.7	
MAG	Dry bore-hole	-4.4	-1.3	
SOL	Surface	-4.6	-1.7	
ELM	Dry bore-hole (diatomite)	-5.2	-2.0	
MAR	Dry bore-hole (volcanic soil)	-5.0	-1.5	
SU1	Dry bore-hole (volcanic soil)	-4.8	-1.6	
SU2	Dry bore-hole (volcanic soil)	-4.7	-1.9	
BA75	Lake	-4.1	-1.5	
CG75	Shallow water	-4.5	-1.6	
NA75	Rock pool	-4.3	-1.7	
KA75	Dry bore-hole	-4.7	-1.9	

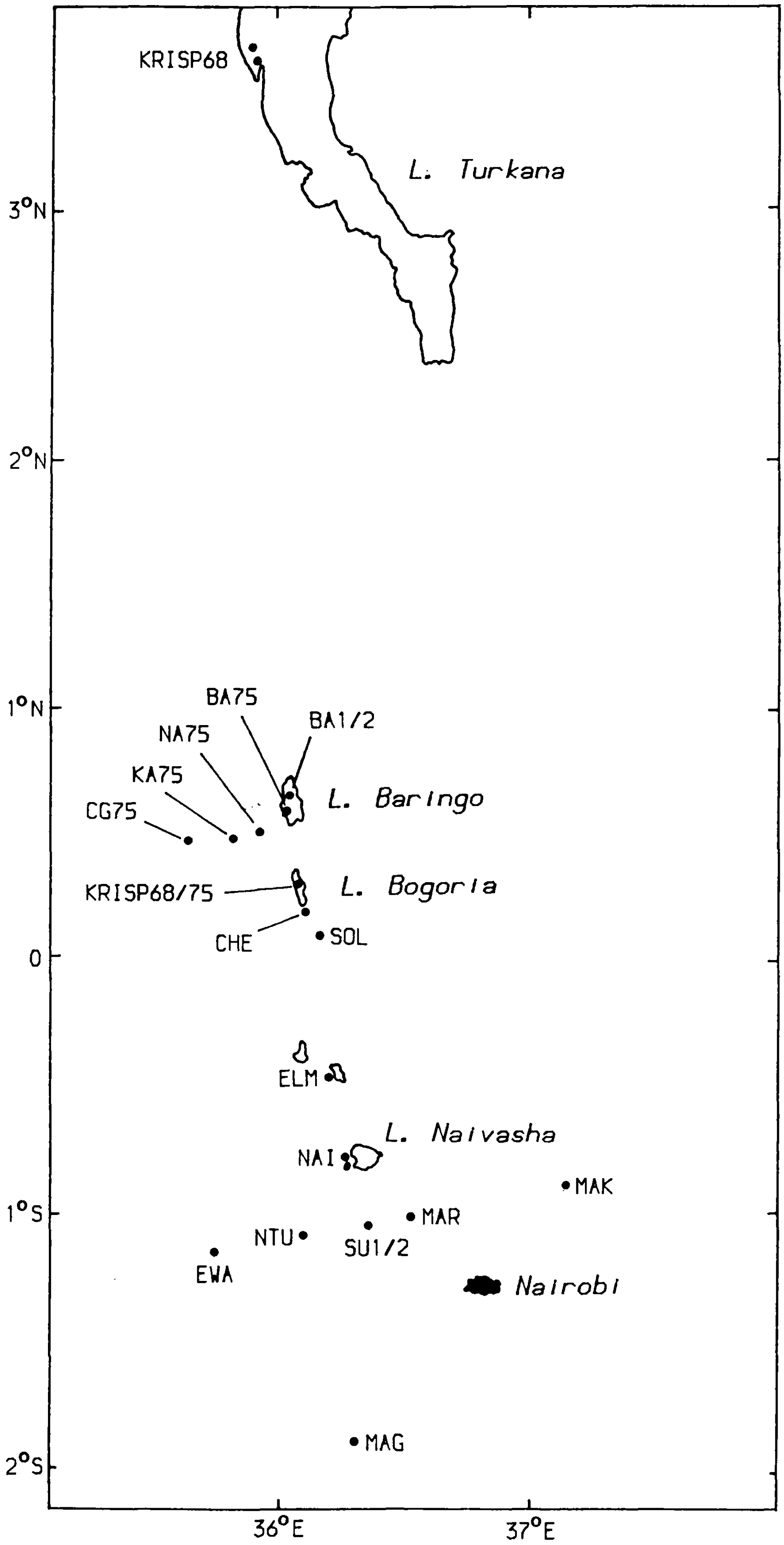

Figure 5.2 : Map showing the locations of shot points used in the KRISP68, KRISP75 and KRISP85 experiments.

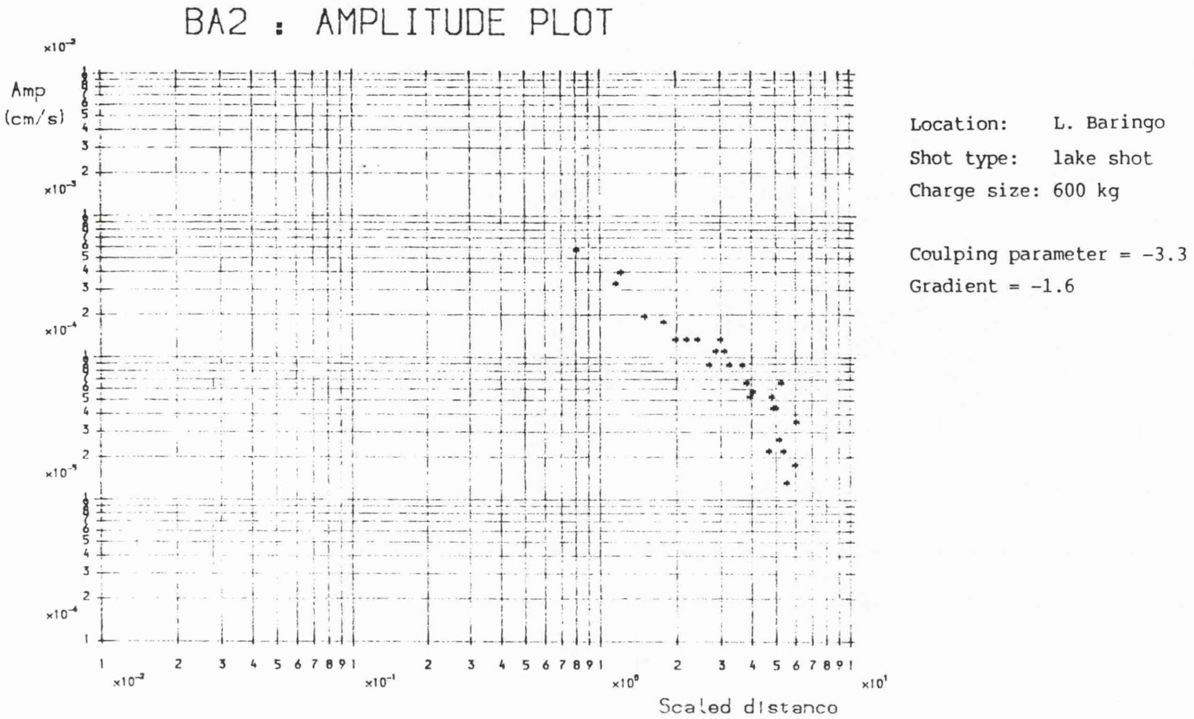

Figure 5.3(a) : Amplitude vs scaled distance plot for the Baringo 2 shot.

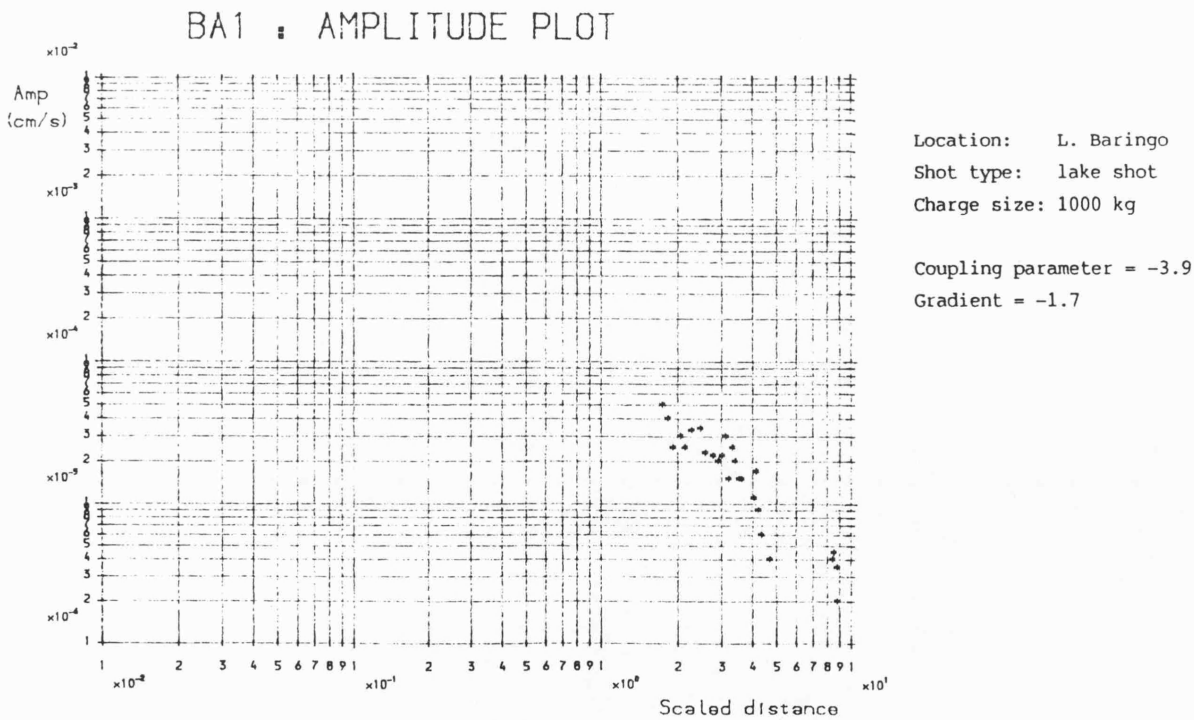

Figure 5.3(b) : Amplitude vs scaled distance plot for the Baringo 1 shot.

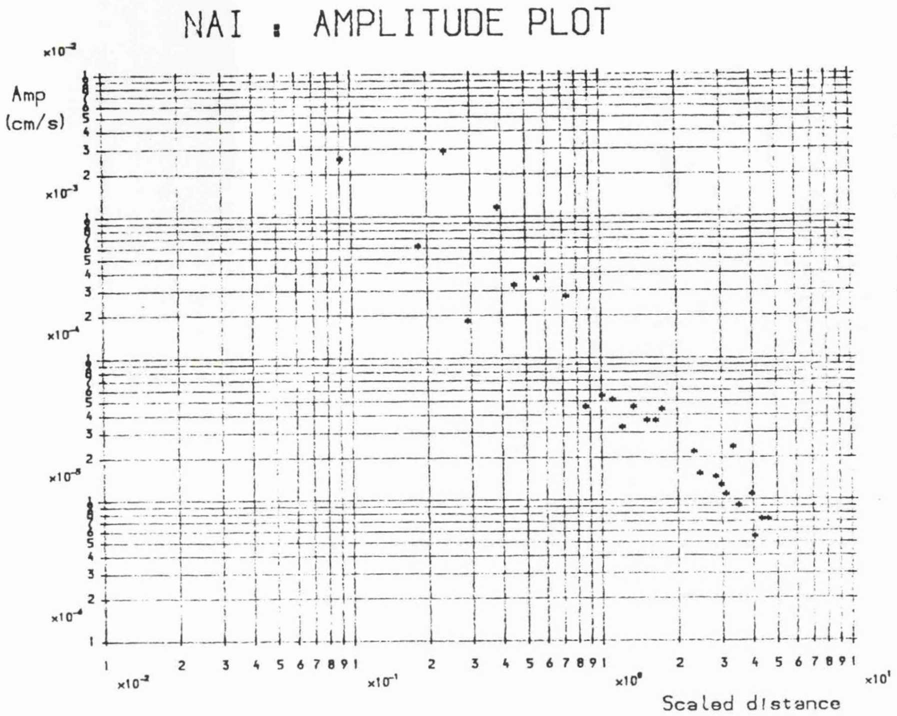

Location: Crater lake
Shot type: lake shot
Charge size: 700 kg

Coupling parameter = -4.1
Gradient = -1.6

Figure 5.3(c) : Amplitude vs scaled distance plot for the Naivasha shot.

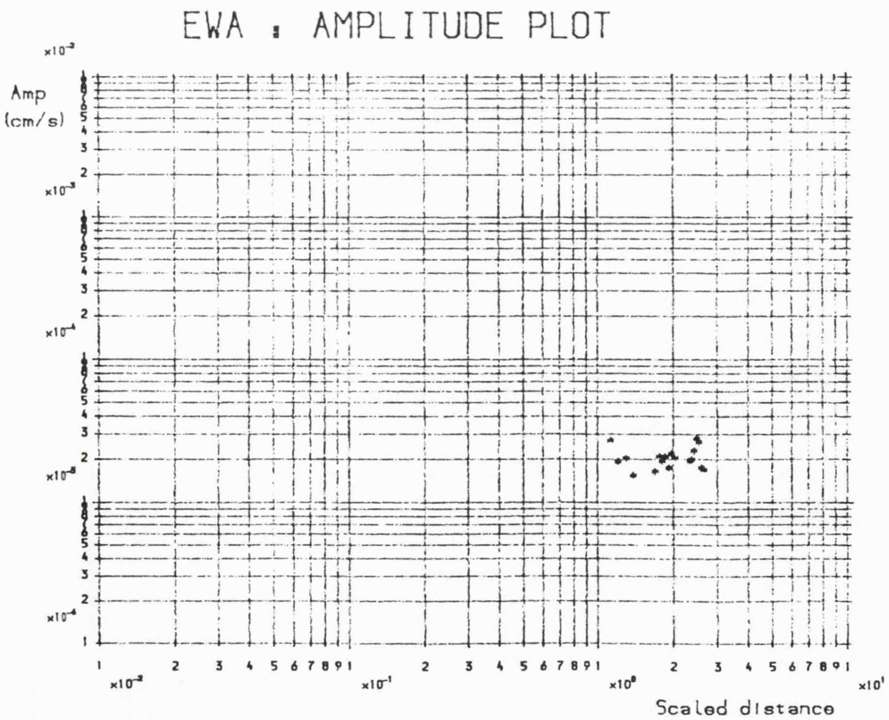

Location: Ewaso Ngiro
Shot type: wet bore-holes
Charge size: 500 kg

Figure 5.3(d) : Amplitude vs scaled distance plot for the Ewaso Ngiro shot.

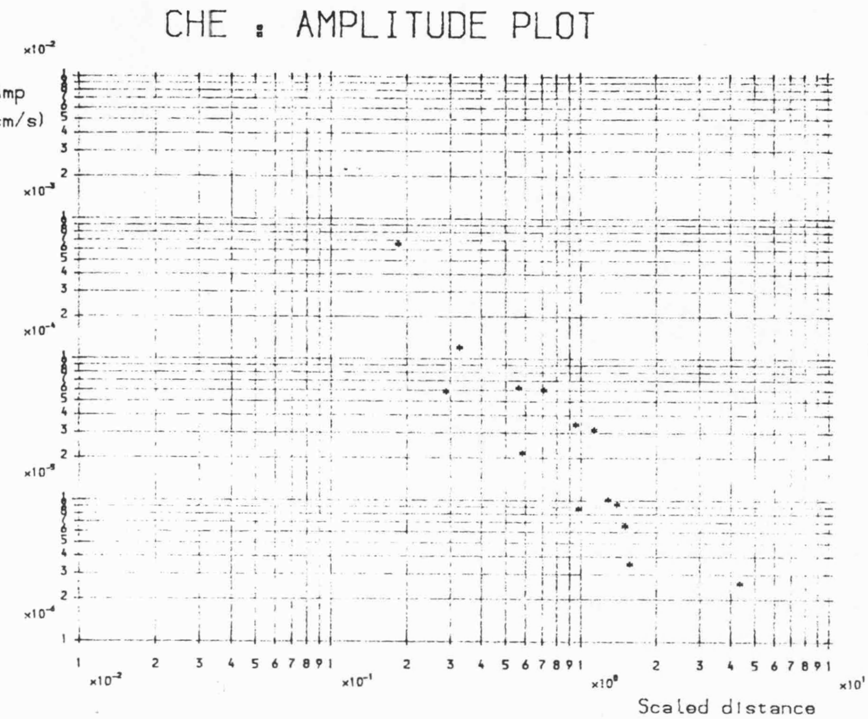

Location: Chepkererat
Shot type: dry bore-holes
Charge size: 300 kg

Coupling parameter = -4.65
Gradient = -1.7

Figure 5.3(e) : Amplitude vs scaled distance plot for the Chepkererat shot.

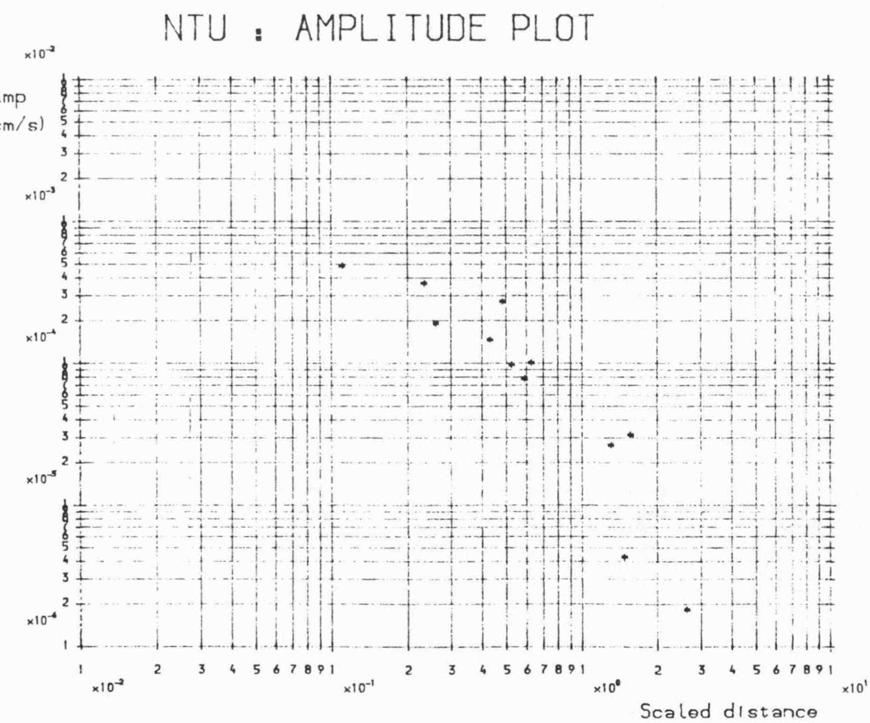

Location: Ntulelei
Shot type: dry bore-hole
Charge size: 210 kg

Coupling parameter = -4.6
Gradient = -1.7

Figure 5.3(f) : Amplitude vs scaled distance plot for the Ntulelei shot.

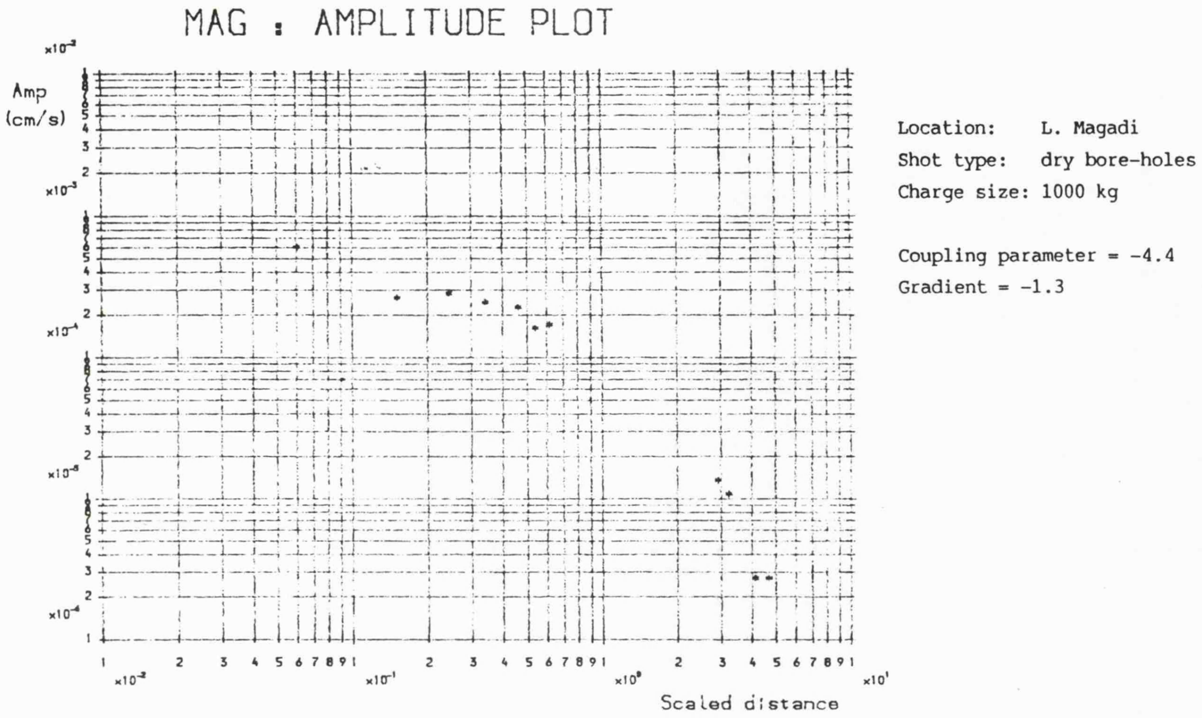

Figure 5.3(g) : Amplitude vs scaled distance plot for the Magadi shot.

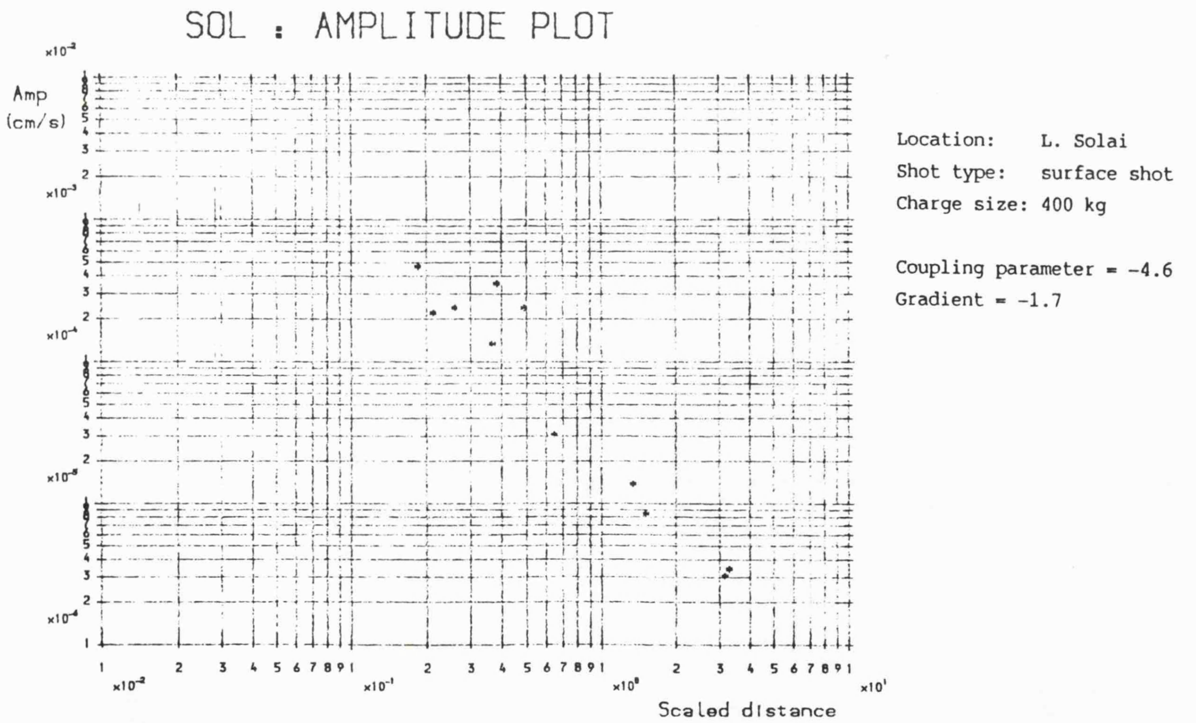

Figure 5.3(h) : Amplitude vs scaled distance plot for the Solai shot.

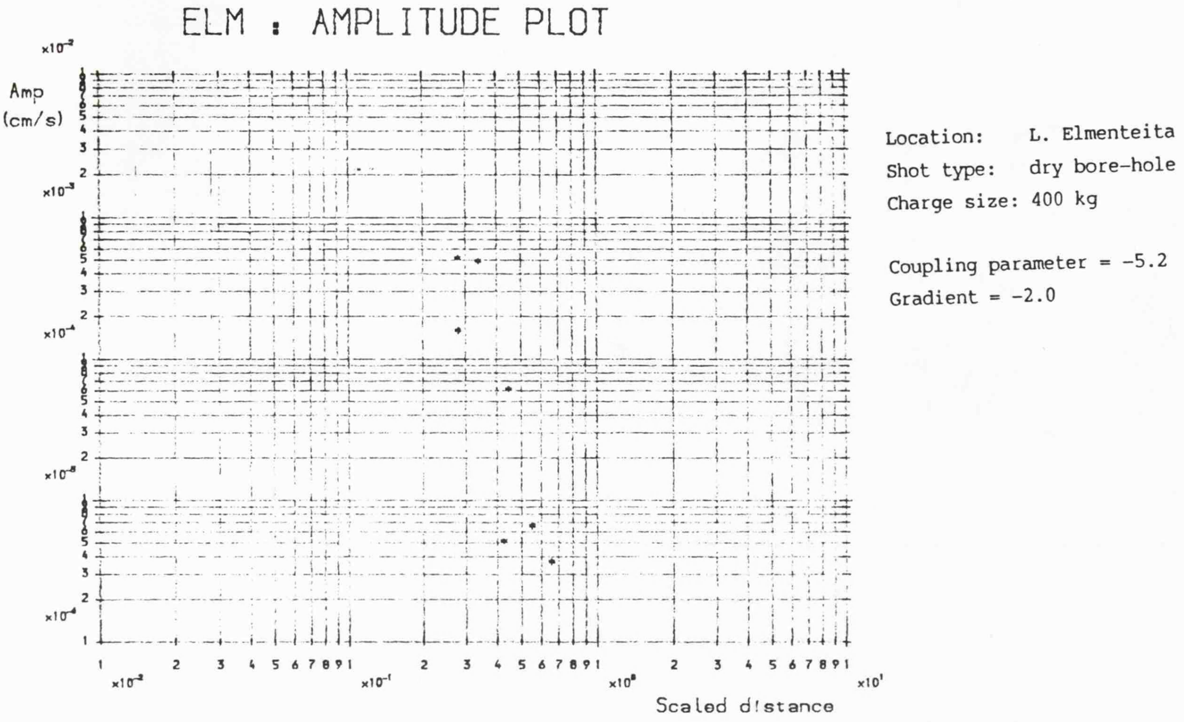

Figure 5.3(i) : Amplitude vs scaled distance plot for the Elmenteita shot.

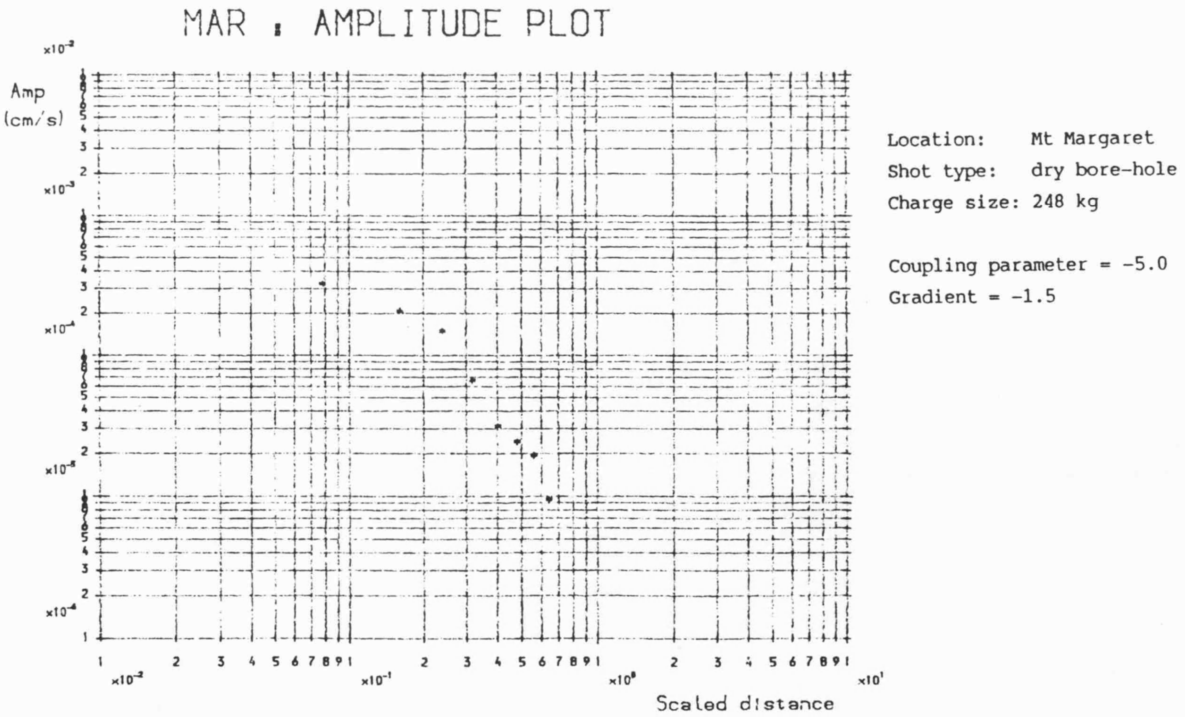

Figure 5.3(j) : Amplitude vs scaled distance plot for the Mt Margaret shot.

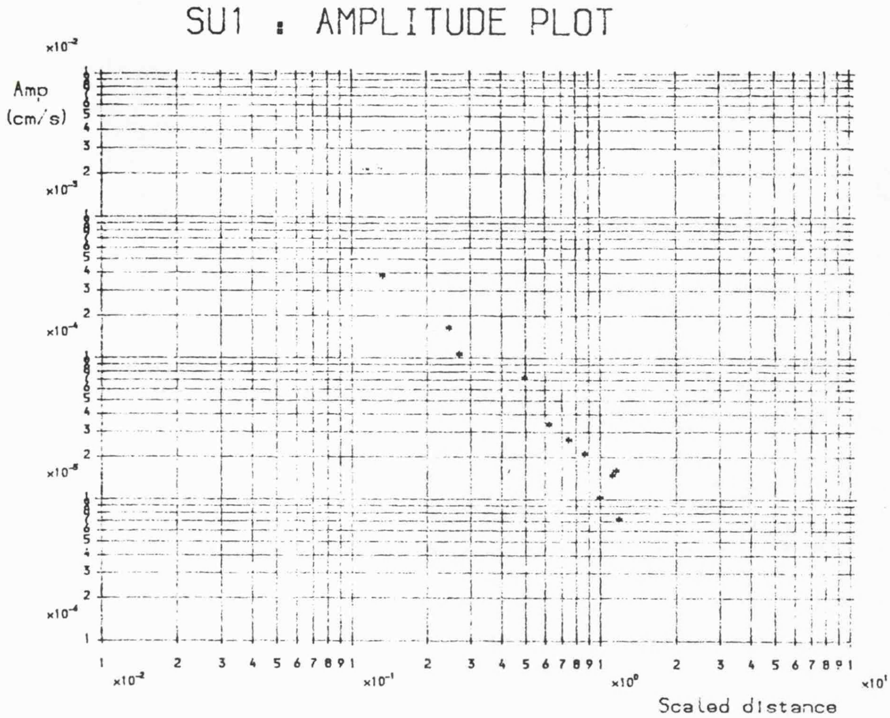

Location: Susua
Shot type: dry bore-hole
Charge size: 100 kg

Coupling parameter = -4.8
Gradient = -1.6

Figure 5.3(k) : Amplitude vs scaled distance plot for the Susua 1 shot.

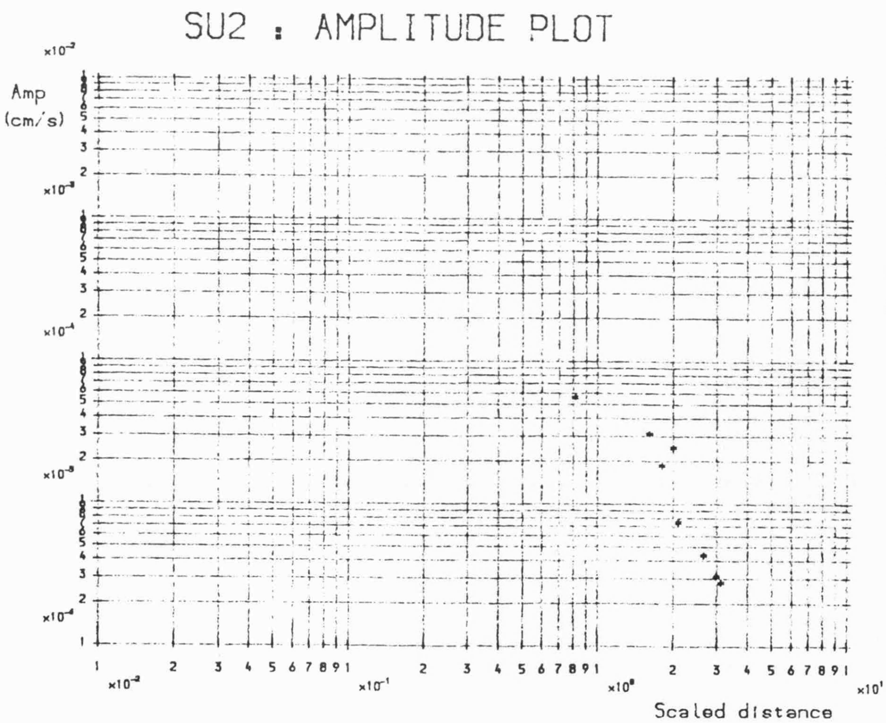

Location: Susua
Shot type: dry bore-holes
Charge size: 400 kg

Coupling parameter = -4.7
Gradient = -1.9

Figure 5.3(l) : Amplitude vs scaled distance plot for the Susua 2 shot.

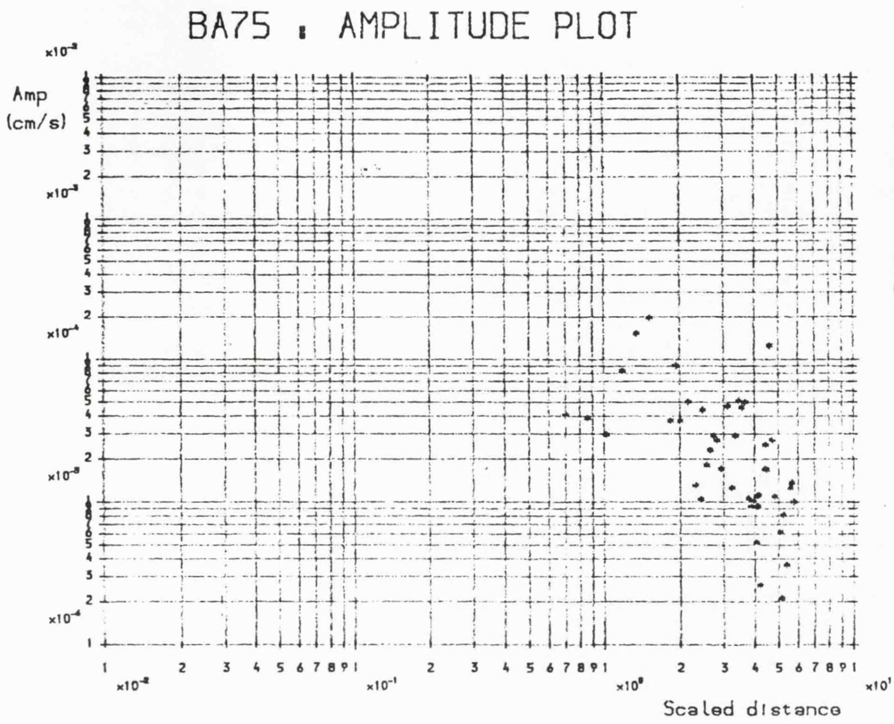

Location: L. Baringo
Shot type: lake shots
Charge size: 23 - 68 kg

Coupling parameter = -4.1
Gradient = -1.5

Figure 5.3(m) : Amplitude vs scaled distance plot for the BA75 shot (KRISP75).

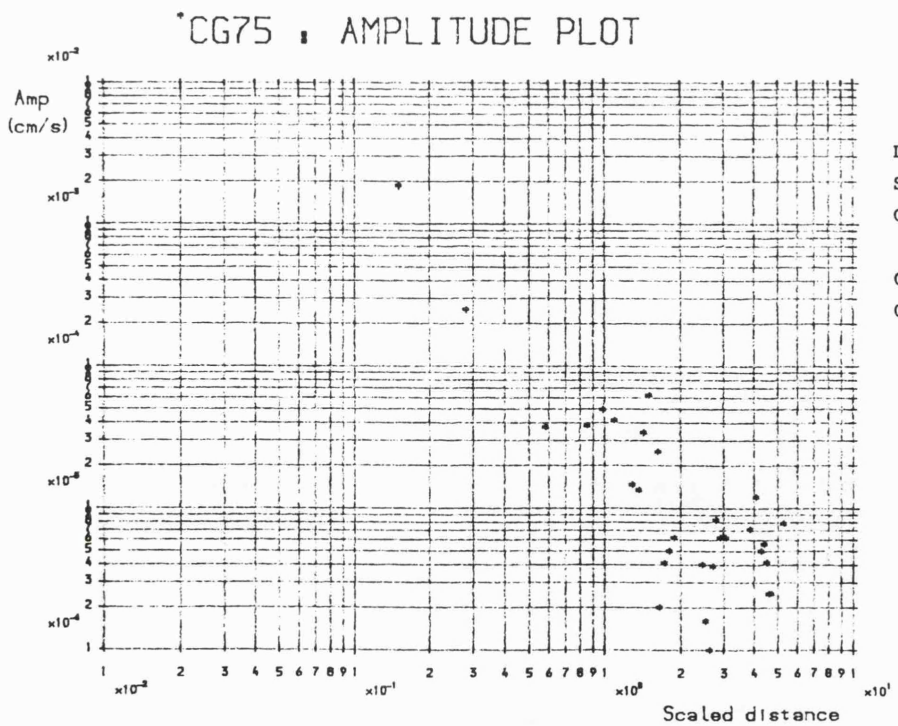

Location: Chebloch Gorge
Shot type: shallow water
Charge size: 29 - 68 kg

Coupling parameter = -4.5
Gradient = -1.6

Figure 5.3(n) : Amplitude vs scaled distance plot for the CG75 shot (KRISP75).

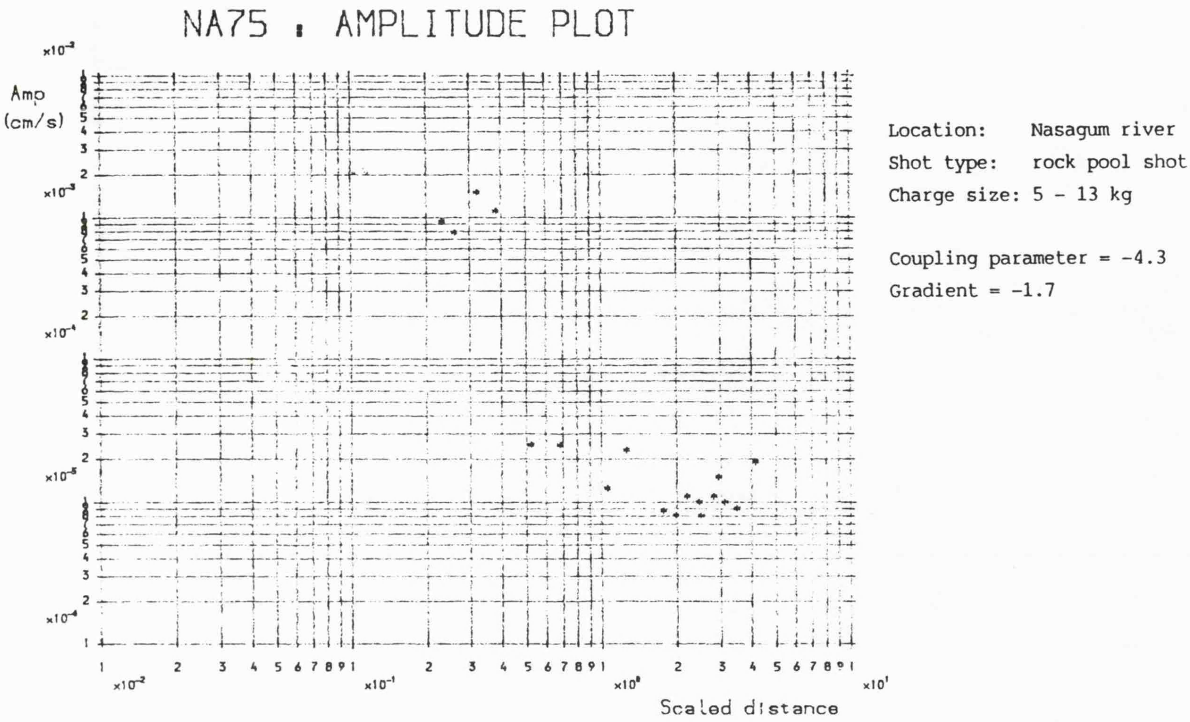

Figure 5.3(o) : Amplitude vs scaled distance plot for the NA75 shot (KRISP75).

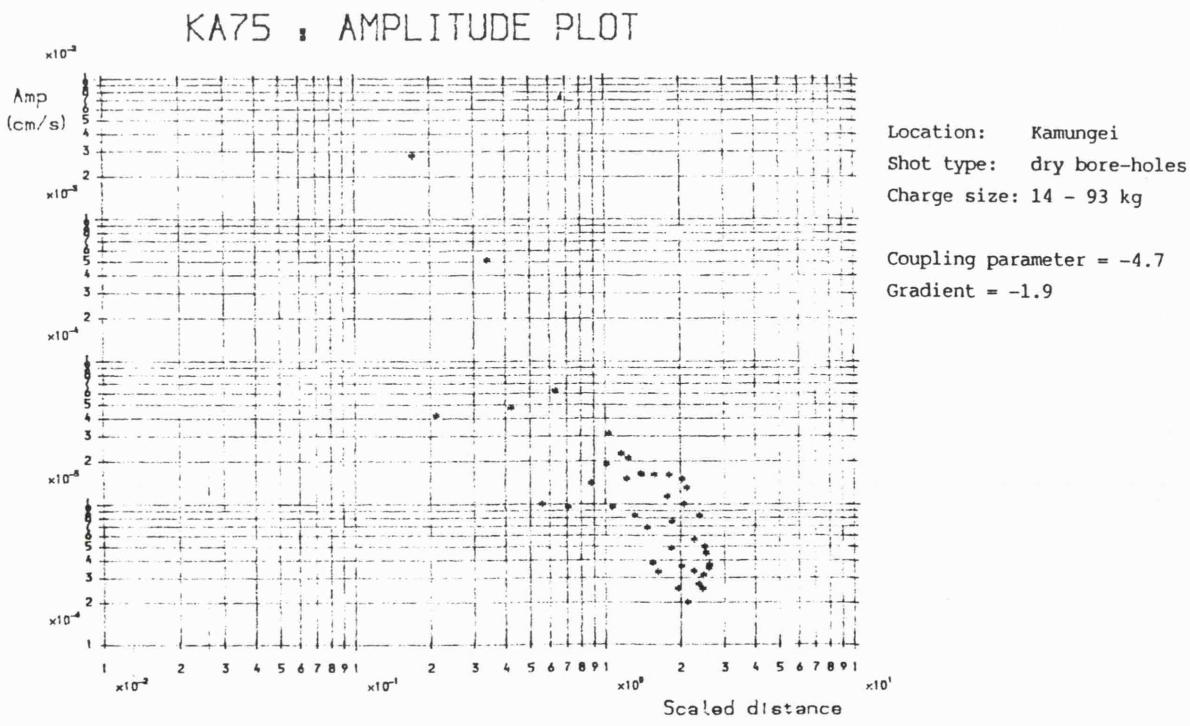

Figure 5.3(p) : Amplitude vs scaled distance plot for the KA75 shot (KRISP75).

Considering the KRISP85 shots first, it can be seen that the lake shots were the most efficient with coupling factors of -3.9, -3.3 and -4.1 for BA1, BA2 and NAI respectively. With the exception of EWA, the BA2 shot was at least an order of magnitude more efficient than any of the bore-hole shots or the one surface shot (SOL). This finding is in accordance with other studies on the relative efficiencies of water shots and bore-hole shots e.g. O'Brien (1960). An interesting observation is that the BA2 shot was between 3 and 4 times more efficient than the BA1 shot. This is a surprising result as the two shots were fired in the same lake and in about the same depth of water. Possible explanations are:

(1) The BA1 charges were laid out along 2 lines parallel to the NS-line (section 2.4) whereas the BA2 charges were distributed along a line perpendicular to it. More energy is propagated in the direction perpendicular to the alignment of a linear distribution of charges than parallel to it (Jacob, 1975).

(2) The material immediately below the BA1 shot was much more attenuating than that below the BA2 shot.

(3) Part of the BA1 shot was not detonated. This explanation is unlikely as the charges were well connected by Cordtex and the shooting party observed the correct number of water jets.

The radiation pattern from a linear array of charges is governed by

$$A = A_0 \sin(N\psi/2)/\sin(\psi/2) \qquad 5.3$$

where $\psi = 2\Pi d\sin\theta/\lambda$, A_0 is the amplitude that would have been obtained from a single charge, N is the number of charges, d is the spacing between charges, θ is the angle subtended from the array perpendicular and λ is the wavelength of the seismic signal (Jacob, 1975). This is analagous to the equation governing the interference pattern of a diffraction grating as can be found in any elementary text book on optics (e.g. Jenkins and White, 1976). Given the charge spacing of approximately 20 m which was employed for the BA1 shot and the dominant seismic frequencies generated, equation 5.3 cannot completely account for the reduced amplitudes so it is likely that a combination of the first 2 effects was responsible.

Of the bore-hole shots, EWA was the most efficient. This can be attributed to the fact that the charges were below the water table. It can be seen from figure 5.3 (d) that the amplitudes observed do not conform to equation 5.2 so values for a and b could not be calculated by least squares. However, assuming a value of -1.7 for **b** gave an approximate value of -4.3 for the coupling parameter. The occurrence of higher amplitudes at increasing distances for this shot must be related to the underlying geology. This will be discussed in Chapter 7. The coupling parameters determined for the remaining bore-hole shots were found to be dependent on the nature of the material surrounding the charge. The bore-holes shots of CHE, NTU and MAG, which have coupling parameters of between -4.4 and -4.6, were drilled into firm material. On the other hand, MAR, ELM and the two Susua shots were fired into very loosely consolidated material and have correspondingly low coupling parameters in the range from -5.2 to -4.8. SOL, although fired in a shallow swamp, was effectively a surface shot. Its coupling parameter of -4.6 compares favourably with those calculated for the dry bore-hole shots. This finding is in agreement with that of Braile (pers. comm.) who has carried out an analysis on over 1100 seismic wave amplitudes measured for different shot types used in refraction profiles in the U.S..

The amplitude vs distance plots for the four KRISP75 shots examined show considerably more scatter than those of the KRISP85 shots. This is because only 11 recording stations were employed on the KRISP75 experiment and each "shot" actually consisted of a number of individual detonations. The observed scatter can be attributed to slight differences in the conditions of each detonation and the failure of the scaling relation, 5.1, to properly account for the individual charge sizes. However, the coupling parameters calculated show agreement with those of the KRISP85 shots. The BA75 shot, fired in about 3.5 metres of water in Lake Baringo, gave the highest coupling parameter (-4.1) while KA75, fired in dry bore-holes, gave the lowest (-4.7). CG75, fired in a deep rock pool and NA75, fired in about 2 metres of water, gave coupling parameters of -4.5 and -4.3 respectively.

Since the 1140 kg MAK shot was not observed by any of the EW-line recording stations it has been impossible to determine a coupling parameter for it. However, if a value of -4.4 is assumed for its coupling parameter and a value of -1.7 is assumed for **b** in equation 5.2 then a seismic amplitude of about 1×10^{-5} cm/s is predicted for the nearest recording station on the EW-line, which has a scaled distance of about 1.9 $km/kg^{0.5}$. As the ambient background noise level on the EW-line at the time of shooting was of the same order of magnitude, it is not surprising that MAK was not observed. Similarly, the poor observation of many of the bore-hole shots was primarily the result of insufficient charge sizes for the given coupling parameters and ambient noise levels.

5.2 Study of diurnal noise variation.

The first three shots of the KRISP85 explosion programme (SU1, EWA and MAR) were fired at around 13:00 hours local time. Initial play backs of recordings made of these shots showed that background seismic noise levels were high at this time of day. Subsequent analysis of the recordings made on the EW-line at this time have shown that the ambient noise levels were typically 10^{-5} - 10^{-4} cm/s. The main sources of this noise are believed to have been wind, people, livestock and traffic on the Narok road which runs along side the EW line (Fig. 2.3). The remaining KRISP85 shots were fired in the early morning (06:00 - 09:00 hours local time) when noise levels were found to be significantly lower (subsequent analysis has shown them to have been typically between 10^{-6} and 10^{-5} cm/s).

In order to establish the optimum time of day for shooting a quantitative study of the diurnal variation of background noise levels has been carried out. During the refraction part of KRISP85 most recording stations only recorded during shooting windows so this data set is not suitable for such a study. The data set used is described fully in the following chapter. It comprises the recordings by a 15 station array, in the vicinity of Lake Bogoria, of about 70 teleseismic events. At this stage suffice it to say that each of the digital records includes a period of 15 - 20 seconds of "quiet" time, before the onset time of the teleseismic event, from which the level of background noise could be determined. The events were recorded during the three month period from September to December of 1985.

A program was written to calculate the route mean square (r.m.s.) noise level for all the available records. The r.m.s. noise levels for 11 of the stations are plotted against local time in figure 5.4 (a-c). As only the diurnal variation of background noise is being examined the unit used is arbitrary. However, the recording stations all had similar instrumentation, so the r.m.s. noise values determined can be compared between stations.

Examination of figure 5.4 shows that the r.m.s. noise level for most of the stations exhibits some kind of diurnal variation. In general, the noise level tends to be lowest between midnight and early morning. Of course, each station shows a different pattern. For example, station 6 shows an abrupt increase in noise level at between 07:00 and 08:00 hours. This is thought to have been the result of noise from a nearby sisal factory. On the other hand, the noise level at station 3, situated along side Lake Bogoria, remains low until mid-afternoon. The higher noise level observed between 15:00 and 22:00 hours can probably be attributed to wind generated waves on the lake (winds tended to be strongest in the evening). Stations 4 and 14 are anomalous in that they do not exhibit any obvious diurnal variation. Noise levels at station 4 are high and widely scattered which can almost certainly be attributed to its location near some hot springs. Conditions at station 14 were quiet most of the time but some quite high r.m.s. noise values determined show no obvious temporal pattern. These were almost certainly caused by electrical noise rather than seismic noise.

It can be seen from the plots of r.m.s. noise that the optimum shooting time is some time between 24:00 and 09:00 hours. It is not obvious from the plots (Fig. 5.4) whether or not noise levels are significantly lower before sun rise (about 06:00 hours). This is an important question because shooting at night would obviously impose considerable logistical problems for both shooting parties and recording parties. To help resolve this question histograms of noise levels have been plotted for between 03:00 and 06:00 hours and also between 06:00 and 09:00 hours, for which similar numbers of r.m.s. values were available. Stations 4 and 14 were excluded as they were considered anomalous. The resulting histograms are shown in figure 5.5. It can be seen that the two periods show quite similar distributions. The mean r.m.s. noise level for the earlier period is 6.6 (units arbitrary) compared to 7.7 for the later period. It is doubtful that the marginally lower noise levels observed before sun rise would merit the considerable difficulties associated with shooting in darkness.

It is important to note that the above conclusions are based on data collected from a small area of the rift, during a three month period (September to December) of one year. It may be that other regions of the rift and surrounding areas show significantly different diurnal variations in background noise level. It is also possible that the diurnal pattern is dependent on the time of year.

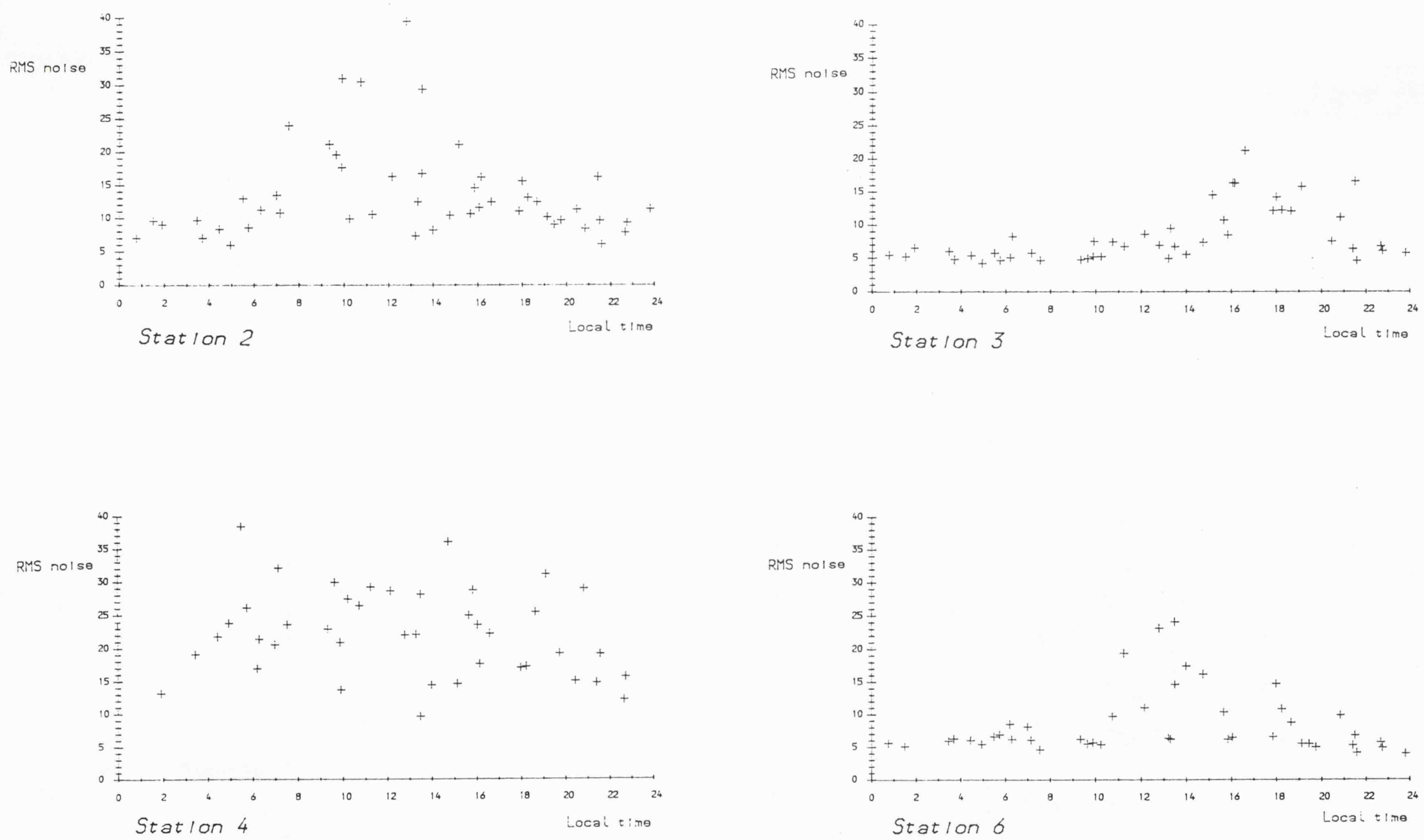

Figure 5.4(a) : Diurnal variation of r.m.s. noise for stations 2, 3, 4 and 6 of the Lake Bogoria network.

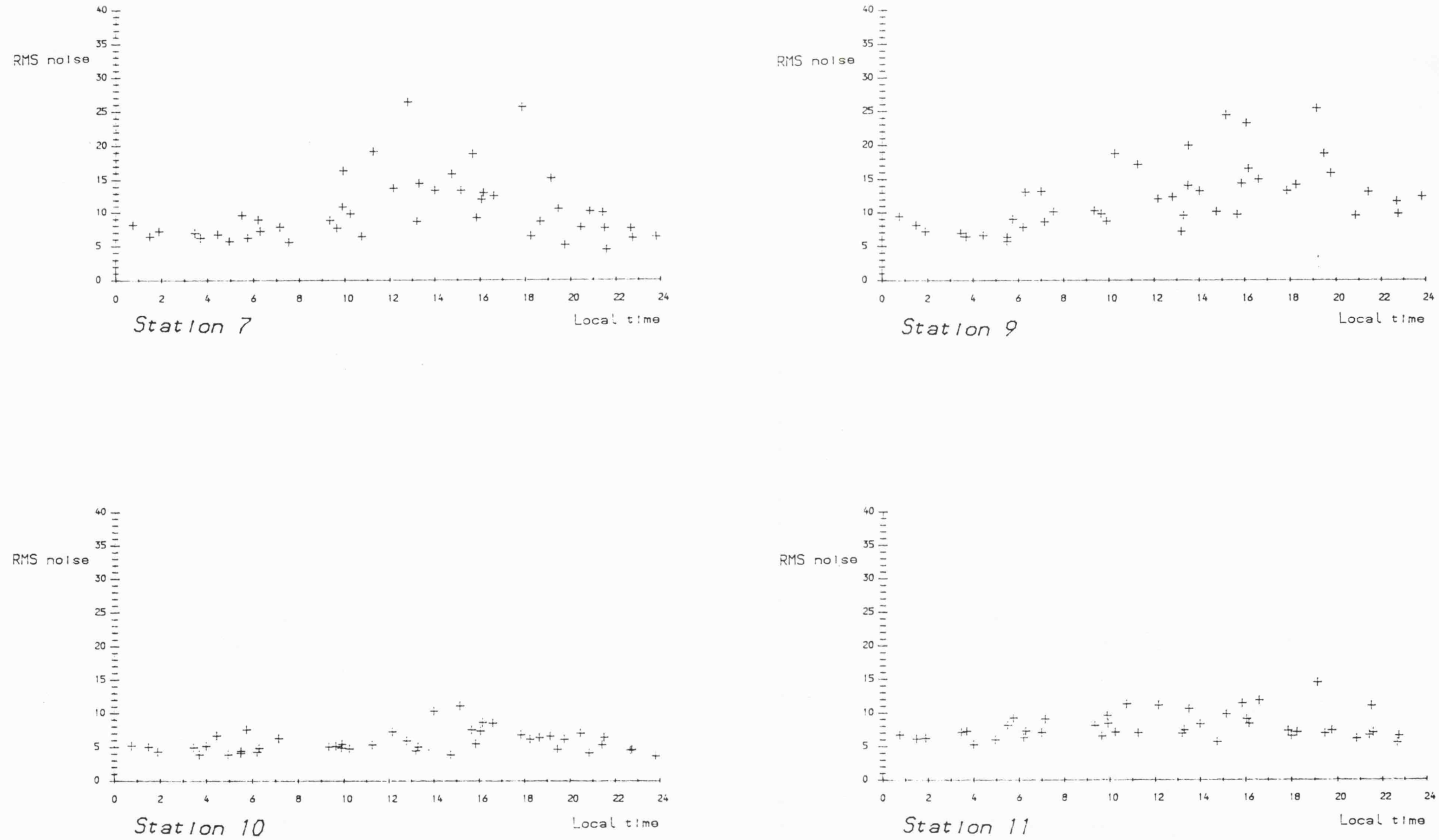

Figure 5.4(b) : Diurnal variation of r.m.s. noise for stations 7, 9, 10 and 11 of the Lake Bogoria network.

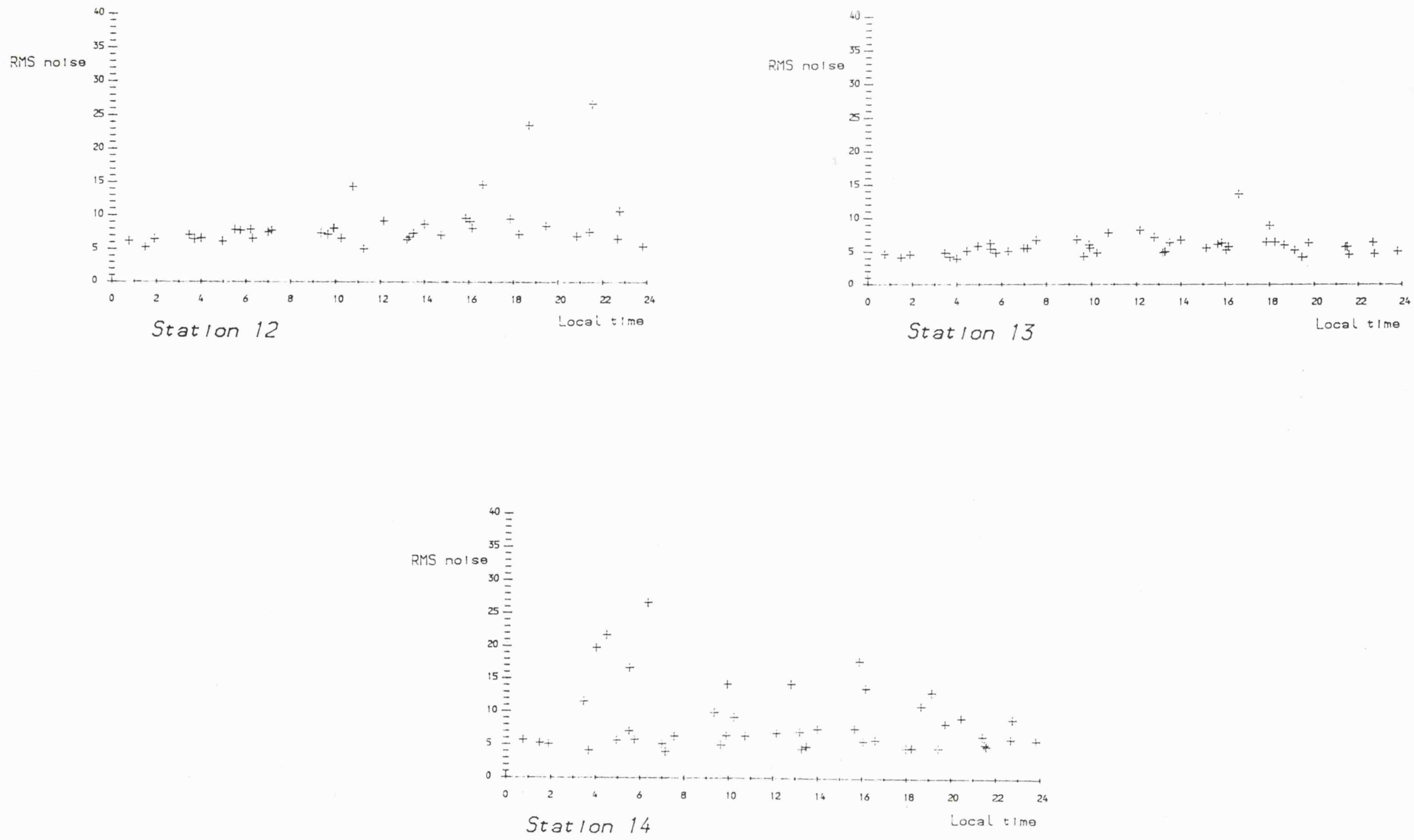

Figure 5.4(c) : Diurnal variation of r.m.s. noise for stations 12, 13 and 14 of the Lake Bogoria network.

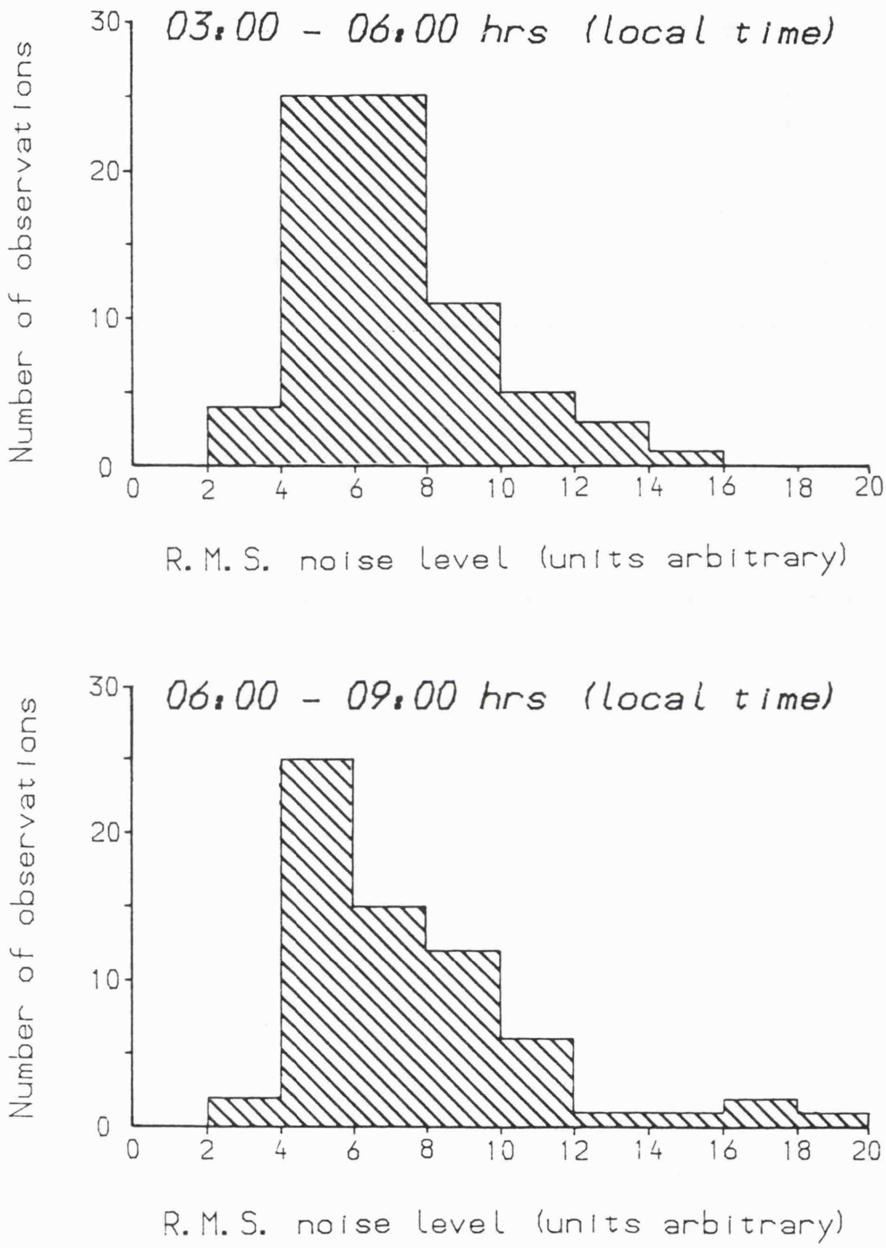

Figure 5.5 : Histograms of r.m.s. noise levels for 03:00 - 06:00 hours and 06:00 - 09:00 hours.

5.3 Recommendations for future refraction experiments in the area.

This analysis has shown that dry bore-hole shots should, if possible, be avoided. If they are employed then they should be in well consolidated material and the charge sizes should be several times larger than those employed during KRISP85. Surface shots, although not always a feasible alternative, are likely to be at least as efficient as dry bore-hole shots. However, the most obvious conclusion to be made from section 5.1 is that lake shots should be utilised as much as possible. If linear arrays of charges are employed then they should always be aligned perpendicular to the desired propagation direction.

Every effort should be made to ensure that station noise levels are as low as possible during shooting windows. A noise test should be carried out at every prospective recording station. If the seismic line passes through highly populated areas, as the KRISP85 NS-line did, then stations should be offset from the line where necessary. It is much preferable to obtain a good record from a station several km from the line than a noisy record from a station directly on it. Even better, such highly populated areas should be avoided at the time of planning of the experiment. At least in the region of the rift between Lake Baringo and Lake Magadi, shots should be fired either at night or just after sun rise. The same may apply to other regions but a study of the diurnal variation of noise levels peculiar to the area in question would be prudent before deciding on shooting windows.

CHAPTER (VI)

INTERPRETATION OF TELESEISMIC EVENTS RECORDED BY THE LAKE BOGORIA ARRAY

6.0 Introduction.

A fifteen station seismic network was operational in the vicinity of Lake Bogoria (Fig. 2.2) for a period of about three months in 1985. This chapter deals with the analysis of 46 teleseismic events recorded by the array.

The chapter is divided into two main sections. The first part describes the determination of absolute and relative travel time residuals from recordings of the P-wave arrivals of the teleseismic events recorded at each station. The second part deals with the inversion of these residuals for three dimensional P-wave velocity structure below the array.

6.1 Local geology and description of the seismic network.

The area of the array (Fig. 6.1) has been mapped, as part of the Geological Survey of Kenya, by Walsh (1960) and McCall (1967) and by Griffiths (1977) within a study by the East African Geological Research Unit (E.A.G.R.U.). It has also been the subject of two United Nations projects. The first was a local earthquake study by Hamilton et al (1973) who attempted to use hypocentre locations to delineate zones of high fracture permeability that may channel hot water from a deep heat source. More recently, the U.N. have carried out a geothermal reconnaissance survey of the Menengai-Bogoria area, the results of which have not yet been published.

The area of the network is covered by an extensive formation of trachyphonolitic lavas, known as the Hannington (now Bogoria) suite. The formation includes 2 basic shield volcanoes (Fig. 6.1): Kwaibus and Goituimet which are located NW and SW of Lake Bogoria respectively. Most of the formation is Pleistocene in age but some activity has continued until recent times (Griffiths, 1977). The lava pile has a visible thickness of 250 m but its actual thickness is probably much greater.

The oldest and most major fault of the area is the 4.5 - 6.0 Ma fault bounding Lake Bogoria to the East (McCall, 1967). The entire surface of the Hannington suite is cut by a dense series of NS trending faults, separating tilted blocks, which are all younger than 2 Ma (Griffiths, 1977). Only the more prominent of these faults are shown in figure 6.1.

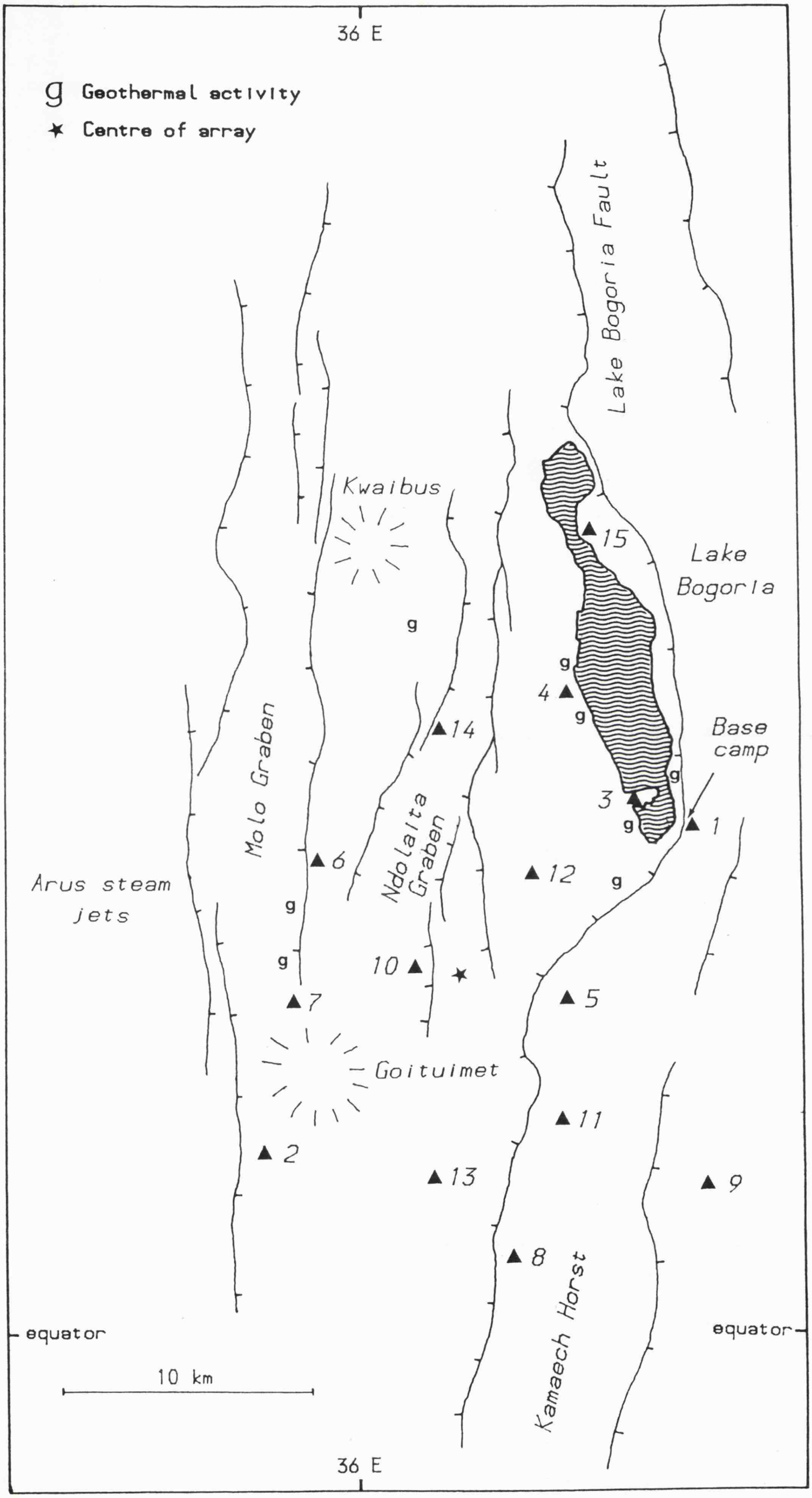

Figure 6.1 : Map showing locations of the Lake Bogoria network.

Several manifestations of geothermal activity are present in the area. Around the shores of Lake Bogoria there are an abundance of fumaroles, steam jets and geysers. Another, less well known, area of geothermal activity, called the Arus steam jets, occurs about 5 km north of Goituimet, on the eastern side of the Molo Graben (Fig. 6.1).

The Lake Bogoria seismic network consisted of 15 recording stations deployed over an area approximately 30 km in diameter (Fig. 6.1). Three component recordings were made at stations 1 - 14 while only the vertical component of motion was recorded at station 15. With the exception of the station 1, all data was telemetered to the base station which was located at the top of the Lake Bogoria fault scarp, at the southern end of Lake Bogoria (station 1 was within a few hundred metres of the base station). In order to satisfy the line of sight requirement of the telemetry linkages, most of the stations were positioned on the top of rocky hills on, or as close as possible to, outcrop. All data was recorded on 5 of the continuously recording Geostore tape recorders described in Chapter 2. In addition a DEC LSI 11/23 minicomputer was used to record data from 13 of the 3 component sets using an event triggered system. This allowed the immediate inspection of events recorded and was an important aid in the maintenance of the network.

Each Geostore recorded three time signals as well as the seismic data. These were: (a) that Geostore's internal clock signal; (b) one Geostore's internal clock signal which was recorded by all the Geostores; (c) an Omega time signal that was recorded by all the Geostores. Absolute timing was provided by the Omega time signal (Chapter 2). However, the Geostore internal clock signal that was recorded by all the Geostores could be used for the relative timing of arrivals across the array in the event of a failure of the Omega system.

The network was operational from the 3rd of September until the 5th of December, 1985. Obviously, not all the stations functioned properly for the whole period. In particular, during the installation and dismantling of the network, only a proportion of the recording stations were operational.

Station locations, which were determined by resection as described in Chapter 2, are listed in Table 6.1.

Table 6.1 : Lake Bogoria network station locations.

Station	Latitude deg min(N)		Longitude deg min(E)		Elevation (metres)
1	0	11.693	36	8.067	1600
2	0	3.365	35	58.389	1570
3	0	12.057	36	6.597	1000
4	0	14.318	36	5.424	1000
5	0	7.480	36	4.738	1700
6	0	10.641	35	58.986	1520
7	0	7.394	35	58.468	1490
8	0	1.303	36	3.381	1860
9	0	4.437	36	7.917	1610
10	0	7.817	36	1.935	1500
11	0	4.651	36	4.719	1700
12	0	10.134	36	4.516	1360
13	0	2.972	36	2.179	1670
14	0	13.075	36	2.690	1310
15	0	18.126	36	5.211	1000

6.2 Teleseismic events.

A list of arrival times of possible teleseismic events was produced from the inspection of a continuous paper playout of the recordings made by a single Geostore. A listing of predicted onset times of teleseismic events at the network for the duration of its operation was made available by the Atomic Weapons Research Establishment (A.W.R.E.) Seismology Unit. The listings are in the form of a printout produced by the unit's computer program, GEDESS (Young and Gibbs, 1968) which uses the preliminary determination of epicentre locations determined by the United States Geological Survey (U.S.G.S.) to calculate expected onset times at selected stations. Comparison of the 2 lists showed that about 90 of the predicted onset times coincided with observed teleseismic events.

These events were digitised at the Global Seismology Unit of the British Geological Survey (B.G.S.), Edinburgh. Generally, a window of 2 or 3 minutes, starting about 20 secs before the predicted onset time, was digitised at a sampling rate of 50 samples/sec. The files created at Edinburgh were converted to SDPS4 format and processed in a similar manner to that described in section 3A.2 except that in this case the appropriate files were merged to create individual event files. Each event file consisted of all the seismic recordings made of the particular event as well as the Omega time signal recorded by each Geostore. These were retained in case any mistakes had been made during decoding and/or gating. At this stage corrections were made for time delays introduced by the 9690 digital system and the misalignment of odd and even recording heads of the Geostores (as described in section 3A.2).

Unfortunately, as a result of either an operator error or a bug in the B.G.S. digitising system (probably the former), 14 of the original events digitised were lost. Of the events successfully digitised, 46 were considered to be of sufficient quality to be worthy of analysis. Many of the remaining events were clearly identifiable at about the predicted onset time but their signal to noise ratio was too low for the reliable measurement of relative arrival times across the array.

The hypocentre locations, origin times, epicentral distances, back bearings and body wave magnitudes of the 46 teleseismic events used in this study are listed in Table 6.2. Figure 6.2 shows the distribution of the events plotted on a zenithal equidistant map of the world, centred on the Lake Bogoria network. It can be seen that of the events used in this study, 20 are P phases (epicentral distance $< 100^{\circ}$) and 26 are core phases (epicentral distance $> 110^{\circ}$).

6.3 Measurement of absolute and relative arrival times.

All the seismograms used in this study were given a weight of from 1 (for a relatively poor recording) to 3 (for a good recording). Figure 6.3 shows the vertical component records of three events of varying quality: (a) and (b) are PKIKP arrivals from hypocentres near Vanuatu Islands (New Hebrides) in the S.W. Pacific Ocean and (c) is a P phase from near Java in Indonesia (after the application of a 5 Hz lowpass filter). The seismograms of (a), (b) and (c) are typical of those weighted 3, 2 and 1 respectively.

It can be seen that even for event (a) of figure 6.3, which is one of the best events recorded, the first-break time is not distinct for every station. For events of lower S:N ratio the position of the first break is often not identifiable at all. Considerable effort was put into ascertaining the most accurate method of measuring the "relative" arrival times of events across the array. Three earthquakes with hypocentres very close together, near Vanuatu Islands, were recorded by all the stations of the network (events 39 - 41 in table 6.2). These events are called VAN1, VAN2 and VAN3 in the following discussion. Two of the events (VAN1 and VAN3) are shown in figure 6.3. The three earthquakes all occurred within a

Table 6.2 : Hypocentre data for teleseismic events.

Ev no	Location	Date	Origin time	Distance	B.B.	Mb
1	S.Greece	07/09/85	10 20 50.2	39.5 deg	341 deg	5.3
2	Mexico	15/09/85	07 57 53.5	130.5	294	5.9
3	Tonga	15/09/85	11 25 04.3	143.7	123	5.7
4	Tonga	15/09/85	17 31 00.8	146.2	121	5.8
5	Tonga	16/09/85	02 54 02.0	146.6	118	4.9
6	Madagascar	17/09/85	10 57 10.7	11.8	155	5.0
7	Fiji region	18/09/85	19 20 41.4	141.8	119	5.0
8	Mexico	19/09/85	13 17 47.3	135.3	296	6.8
9	Taiwan region	20/09/85	15 01 23.5	86.5	65	5.3
10	Mexico	21/09/85	01 37 13.4	134.7	295	6.3
11	N.A.R.	22/09/85	18 23 12.2	80.5	282	5.7
12	Tonga	26/09/85	04 16 21.1	147.2	120	4.8
13	Kermadec Is.	26/09/85	07 27 51.1	132.5	140	6.3
14	Solomon Is.	27/09/85	03 39 08.5	123.3	102	6.2
15	Tonga	27/09/85	10 10 18.9	143.0	128	5.8
16	Crete	27/09/85	16 39 48.7	35.3	346	5.6
17	Yugoslavia	28/09/85	14 50 15.2	43.1	345	5.0
18	Canada	05/10/85	15 24 02.2	116.0	350	6.5
19	Vanuatu	06/10/85	12 00 49.2	130.7	115	5.7
20	Java	09/10/85	01 15 04.6	71.2	97	5.9
21	S Alaska	09/10/85	09 33 32.4	123.7	11	6.2
22	Fiji	12/10/85	02 12 57.9	141.9	126	5.9
23	El Salvador	12/10/85	20 29 20.8	124.6	286	5.4
24	M.A.R.	12/10/85	22 31 10.0	65.9	271	5.4
25	Tajik	13/10/85	15 59 51.2	50.4	33	5.8
26	Timor Sea	23/10/85	00 49 11.1	89.2	101	6.0
27	Fox Is.	25/10/85	02 09 04.3	123.1	20	5.6
28	Banda Sea	25/10/85	18 12 19.5	88.3	97	5.9
29	Algeria	27/10/85	19 34 57.1	45.1	326	5.5
30	Fiji	27/10/85	22 35 18.0	141.6	118	5.4
31	Tonga	28/10/85	12 52 31.2	145.0	117	5.5
32	M.A.R.	10/11/85	12 39 50.9	68.5	274	5.2
33	S.A.R.	18/11/85	18 18 34.7	56.6	230	5.4
34	S. Sandwich	24/11/85	21 32 41.8	75.7	207	5.3
35	Java	25/11/85	16 26 30.4	72.7	99	5.1
35	Taiwan	26/11/85	00 27 04.2	86.2	67	5.0
37	Tonga	26/11/85	06 18 59.3	142.8	128	5.4
38	Ryukyu Is.	26/11/85	10 05 03.5	89.2	66	5.5
39	Vanuatu	28/11/85	02 25 42.3	128.9	108	6.0
40	Vanuatu	28/11/85	03 49 54.1	128.9	108	6.3
41	Vanuatu	28/11 85	06 37 47.2	128.9	108	5.6
42	Tonga	30/11/85	03 04 18.8	146.1	120	5.7
43	N.E. China	30/11/85	14 38 25.4	81.1	52	4.9
44	Indian Ocean	01/12/85	06 16 39.7	34.5	120	5.2
45	Tonga	01/12/85	06 56 02.6	145.4	122	4.8
46	Bonin Is.	03/12/85	00 12 13.9	102.8	62	5.9

A.R. = Atlantic Ridge

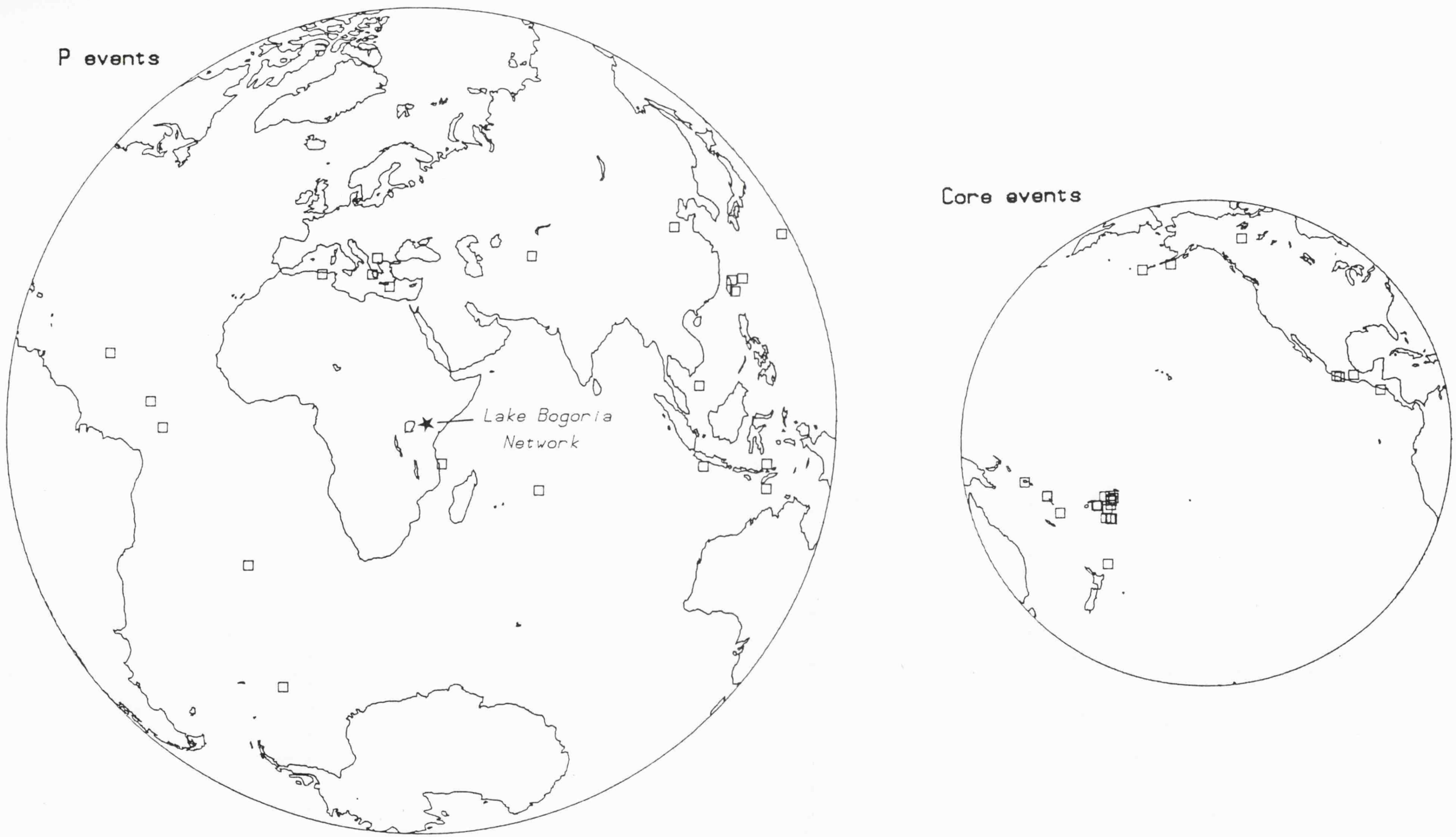

Figure 6.2 : Epicentres of the 46 teleseismic events used in this study on a zenithal equidistant map of the world.

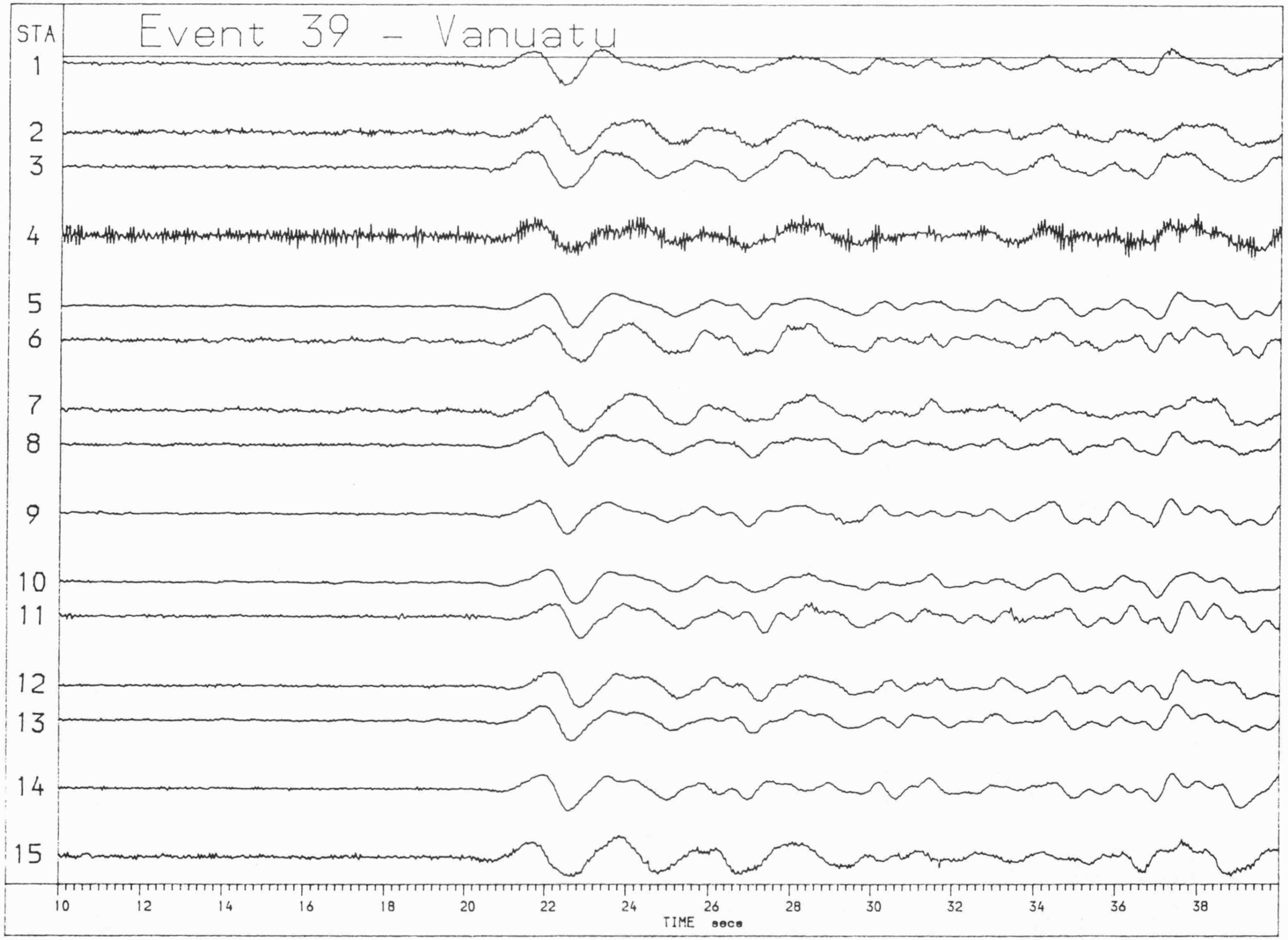

Figure 6.3(a) : Vertical component records of event 39.

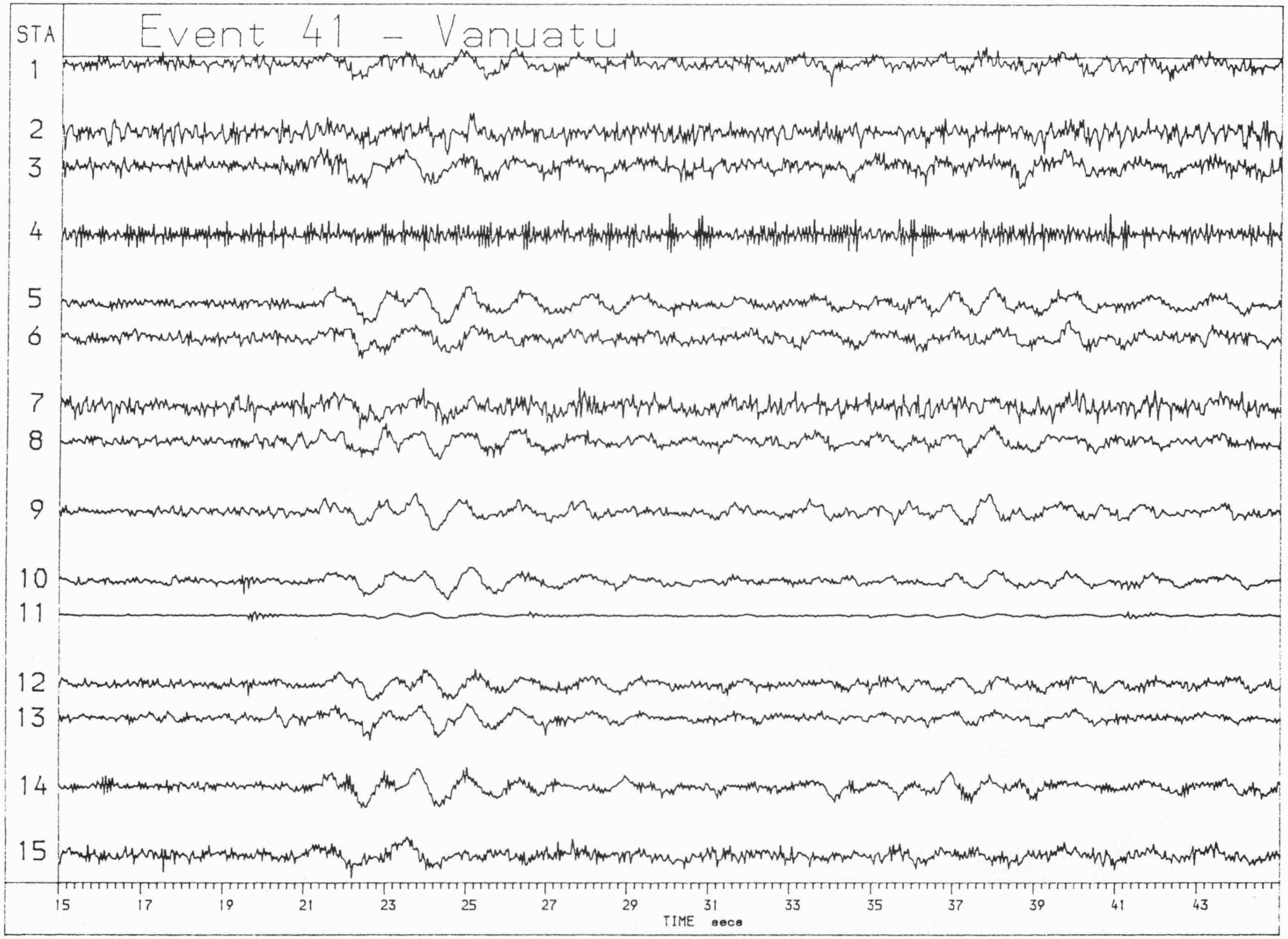

Figure 6.3(b) : Vertical component records of event 41.

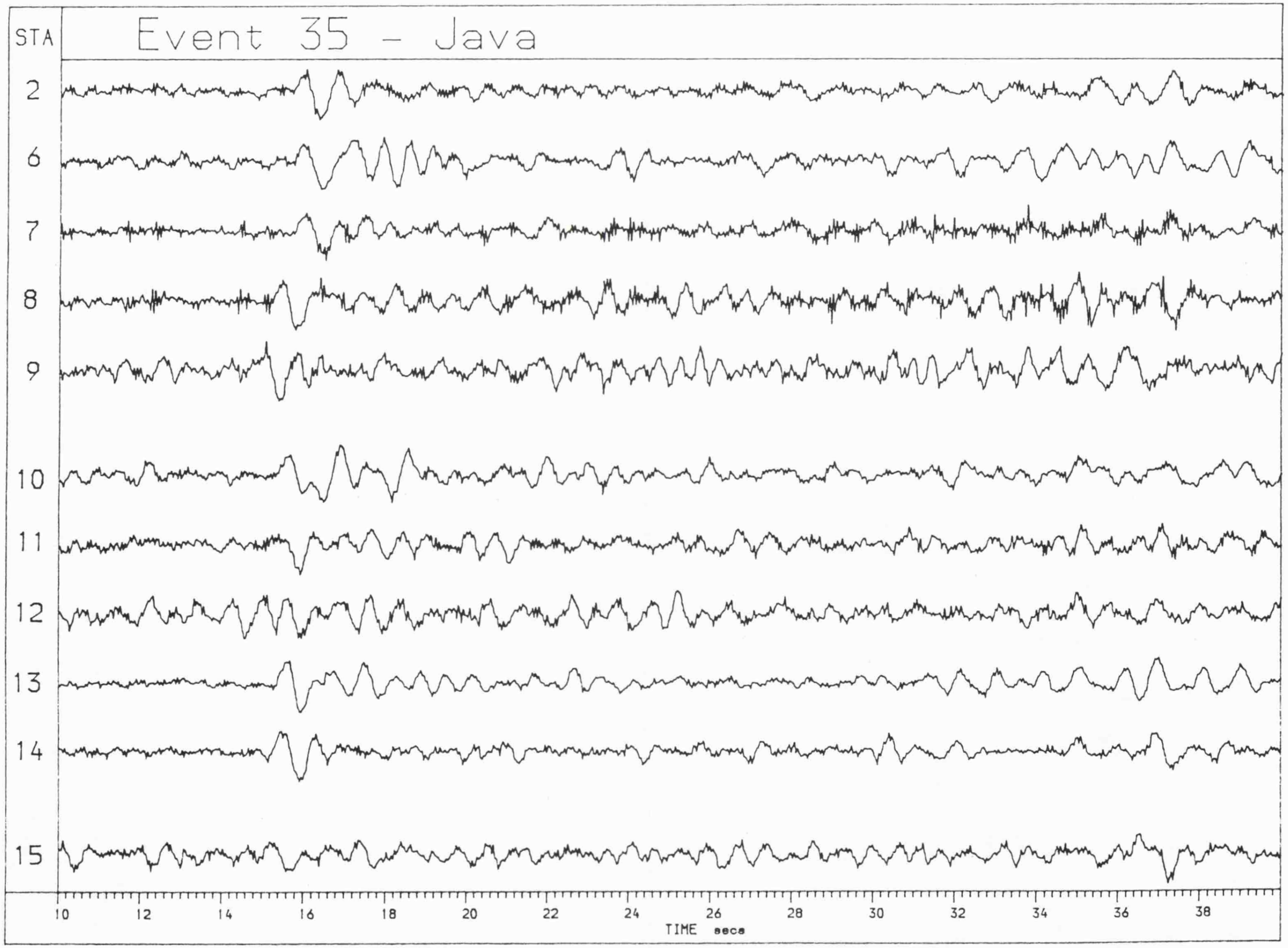

Figure 6.3(c) : Vertical component records of event 35.

period of 4 hours and the epicentre locations listed agree to within 0.1° of latitude and longitude. These events provided a convenient method of testing the accuracy of various methods of measuring relative arrival times. As they all originated from effectively the same hypocentre, the same pattern of relative arrival times across the array should be observed for each one. The following three methods of measuring relative arrival times were tested on the vertical component seismograms.

(1) The time of arrival of some distinctive feature of the waveform, normally the first distinct peak or trough, was measured. This was carried out using program **PIK4A** of the SDPS4 system (Appendix B) which uses interactive graphics to allow the display of a number of seismograms on a V.D.U. and the timing of any feature on the seismograms by means of a user controlled cursor.

(2) The cross-correlation method described in section 3A.4.1 was tested using program **PHASECOR** (Appendix B). A window containing the first few cycles of a selected seismogram was cross-correlated with all the other seismograms recorded of that event. The relative positions of the maxima of the cross-correlation functions determined gave the relative arrival times across the array.

(3) A waveform matching technique was performed as follows. A plot of all of the seismograms was made and a tracing drawn of the first few cycles of the seismogram selected as being most "representative". In general, the coherency of waveforms observed across the array was high (Fig. 6.3). The tracing was then laid on top of the other vertical traces and slid backwards and forwards until the best fit was obtained. This procedure was carried out in combination with method (1) i.e. it was used to "correct" picks made using program **PIK4A**.

Figure 6.4 shows plots of the relative arrival times of the three events determined using the above methods. The times plotted are the observed times minus the average arrival time for the event across the array. It is evident that the third method (waveform matching) gave the most consistent relative arrival times for the three events. The first method gave good agreement between events VAN1 and VAN2, both of which had been assigned with a weight of 3. However, some of the relative arrival times measured for VAN3 are not consistent with those of VAN1 and VAN2. This is because the S:N ratios of the VAN3 seismograms are typically 4 or 5 times lower than those of VAN1 and VAN2. The higher noise level has had the effect of altering the form of the first prominent peak (the distinct feature made use of) on several of the traces. The results obtained from the second

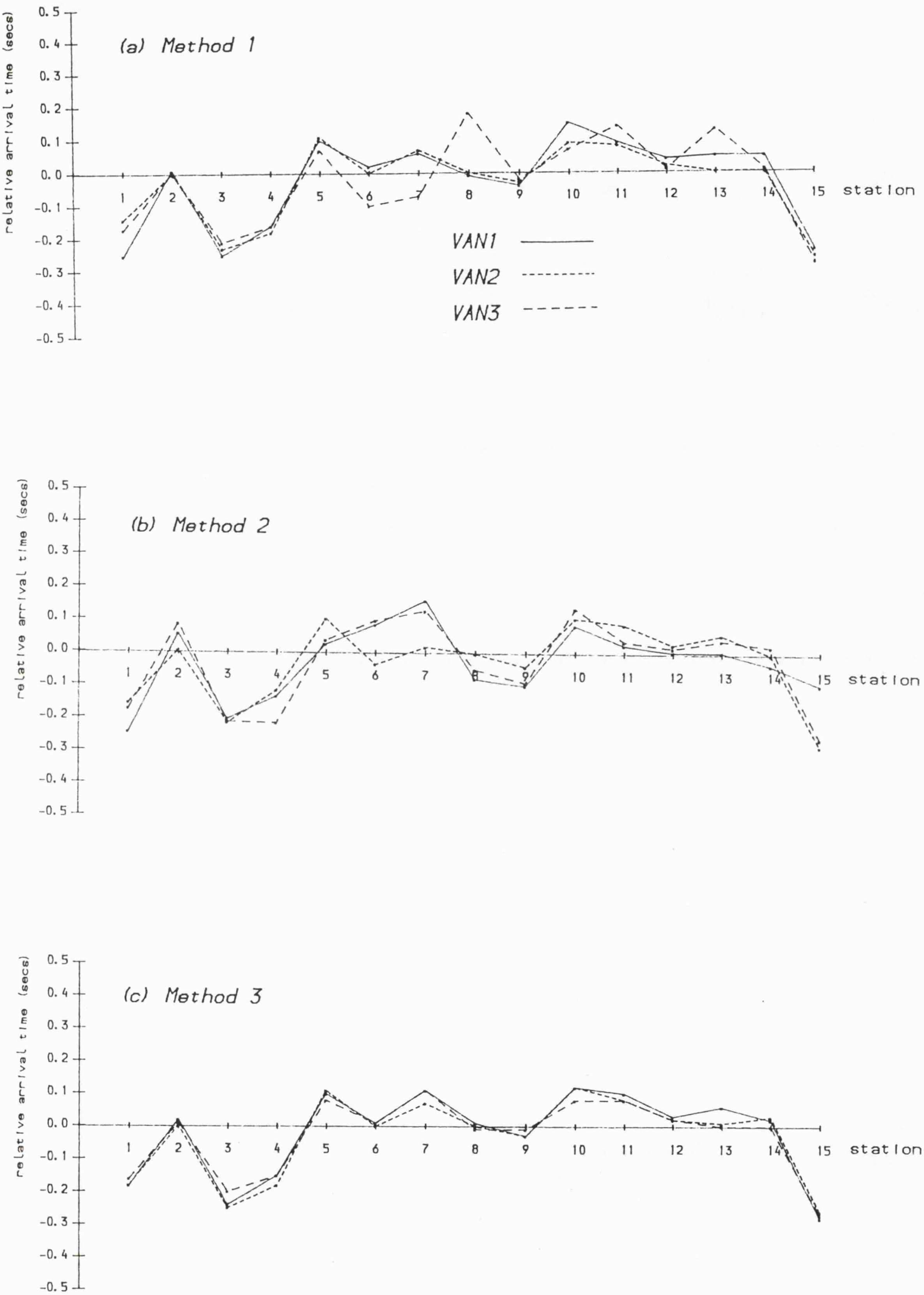

Figure 6.4 : Diagram showing the relative arrival times measured for events VAN1, VAN2 and VAN3 using methods (1), (2) and (3).

method were disappointing, showing the most scatter of the three. This is probably a reflection of the form of the cross-correlation functions calculated which had very broad peaks making the precise location of the maxima difficult.

The above results suggested the following scheme for the measurement of relative arrival times.

(A) Choose a prominent feature of the event (within the first few cycles) common to all seismograms observed.

(B) Measure the arrival times of that feature using program **PIK4A**.

(C) Correct these times using the waveform matching technique on paper plots of the event.

It is estimated that the accuracy of the above method varied from about ± 0.06 secs for observations of weight 1 to ± 0.03 secs for observations of weight 3.

If an event did have a distinct first-break then that time was also measured with an estimated accuracy of between 0.1 to 0.2 secs depending on how impulsive the onset was.

6.4 Calculation of absolute and relative residuals.

The absolute residual (R_{ij}) at station i of event j is obtained by subtracting the theoretical onset-time (T_{tij}) from the observed onset-time (T_{oij}).

$$R_{ij} = T_{oij} - T_{tij} \qquad 6.1$$

The theoretical onset-time is obtained from the predetermined hypocentral coordinates, origin time and a set of recognised travel time tables.

Programs **DELAYP** and **DELAYPKP**, written and described by Pointing (1985), were used for the calculation of the theoretical onset-time, as well as other useful parameters, of P and core phases. The computations involved are outlined below. The term azimuth is used to denote the eastward angle, from the meridian through the epicentre, to the shorter segment of the great circle through both the epicentre and the station. The back bearing denotes the corresponding direction from the station to the epicentre.

(1) The epicentral distance (Δ), azimuth (α) and back bearing (β) were calculated using the standard formulae of spherical trigonometry, a full set of which are given by Bullen (1963). These formulae require the use of geocentric coordinates. Geocentric and geographic longitudes are equal and the geocentric latitude is obtained from the geographic latitude by

$$\tan(\theta') = (1 - \varepsilon)^2 \tan(\theta) \qquad 6.2$$

where θ and θ' are the geographic and geocentric latitudes respectively and ε is the Earth's ellipticity factor.

(2) Travel time tables due to Herrin (1968) were used to calculate the theoretical travel times of P and PKP phases. These were preferred to other tables (e.g. Jeffreys-Bullen tables) because of their better determined gradients (Long and Mitchell, 1970). Computer files containing the P and PKP travel time tables in suitable format allowed the interpolation of intermediate travel times for the given focal depths and calculated epicentral distances.

(3) The apparent velocity at the surface (V_s), sometimes referred to as the phase velocity, was determined by calculating the travel times for epicentral distances Δ-k and Δ+k where k is some small angular distance chosen to be 0.5°, following Savage (1979). The velocity, in degrees per second, is then given by the approximate finite difference equation:

$$V_s = 2k \;/\; \{\, t(\Delta+k) - t(\Delta-k) \,\} \qquad 6.3$$

The velocity values were subsequently converted to km/s.

(4) Travel time tables are constructed for a spherical Earth with a radius equal to the Earth's mean radius. To account for the Earth's elliptical shape a correction must be applied. A method attributed to Dziewonski and Gilbert (1976) was used to make this correction. They used the stationarity of the Fermat raypath to develop a theoretical expression for perturbations in travel time of principal seismic phases due to the Earth's ellipticity:

$$\delta t = 1/4(1+3\cos 2\theta_c)\tau_0 + (\surd 3/2)(\sin 2\theta_c \cos\alpha)\tau_1 + (\surd 3/2)(\sin^2\theta_c \cos 2\alpha)\tau_2 \qquad 6.4$$

where θ_c is the epicentral co-latitude and α is the azimuth from the epicentre to the receiver station. τ_0, τ_1 and τ_2 are functions of epicentral distance and focal depth for the particular seismic phase. Values for these functions are tabulated by Dziewonski and Gilbert. An interpolation method identical to that of (2) was used to obtain intermediate values from the tables.

The calculation of relative residuals (RR_{ij}) for each event isolates the effect of local structure from the often larger effects of errors in origin time, epicentre location and focal depth as well as velocity anomalies occurring along the ray path, not immediately below the array. Two methods are commonly adopted for the calculation of relative residuals:

(1) One station may be assigned as a reference station and its absolute residual subtracted from the absolute residual of all the other stations:

$$RR_{ij} = R_{ij} - RFR_j \qquad 6.5$$

where RFR_j denotes the absolute residual of the reference station for event j. However, this method suffers from two drawbacks. Firstly, it is not always the case that any one station has observed every event satisfactorily. Secondly, it introduces the requirement of there being no variation in the relative residual of the reference station with the back bearing of the event. It will later be evident that this condition was not satisfied by any of the Lake Bogoria stations.

(2) The preferred method was to use the mean of the absolute residuals of each event as a reference. Relative residuals were calculated by subtracting this mean from the absolute residual of each station:

$$RR_{ij} = R_{ij} - M_j \qquad 6.6$$

where

$$M_j = (1/n_j) \sum_{i=1}^{n_j} R_{ij} \qquad 6.7$$

denotes the mean calculated from the n_j stations that observed event j. This technique suffers from the disadvantage that normally not every station has observed every event so the mean of many of the events are necessarily calculated from different subsets of stations. Reasenberg (1980) stated that the resulting relative residuals are only weakly biased by the specific set of stations with observations. However, for some of the events used in this study observations were available for less than half of the stations. Numerical tests showed that the use of such small subsets can have a significant effect on the relative residuals determined.

For this reason a predictive scheme was devised for the calculation of the mean absolute residual for events not having a full set of observations. It is simplest to demonstrate this with an example. Consider the scenario of having observed two events (A and B), of roughly similar back bearing and epicentral distance, at three receiving stations (1,2 and 3). It is reasonable to expect the 2 events to give a roughly similar pattern of relative residuals. However, say event A was observed by all three stations but event B was only observed by stations 1 and 2.

	R(A)	RR(A)	R(B)	RR(B)	R'(B)	RR'(B)
ST1	2.00	0.17	3.00	-0.2	3.00	0.22
ST2	2.50	0.67	3.40	0.2	3.40	0.62
ST3	1.00	-0.83	*	*	1.95^{p}	*
MEAN	1.83		3.20		2.78	

The relative residuals of event A and B are calculated using equations 6.6 and 6.7. It can be seen that the values for the relative residuals calculated for the stations 1 and 2 are significantly different for the 2 events. This is obviously due to the missing observation of event B at station 3. However, given the similarity in the hypocentre locations of the 2 events, a fictitious residual for event B at station 3 can be estimated from the residuals of event A for the 3 stations i.e. it is estimated as the average of

$$R(B)_{st1} + \{R(A)_{st3} - R(A)_{st1}\} = 2.0$$

and

$$R(B)_{st2} + \{R(A)_{st3} - R(A)_{st2}\} = 1.9.$$

When this estimate (superscripted by p) is included in the calculation of the mean absolute residual for event B, more realistic values are obtained for the relative residuals (denoted RR') of event B.

An interactive program, **RELDEL** (Appendix B), was written to determine the relative residuals for each event. If the event being considered was fully observed then relative residuals were calculated using equations 6.6 and 6.7. However, if the event was not fully observed, events of similar epicentral distances and back bearings were used to calculate fictitious absolute residuals for the missing observations. The relative residuals were then calculated by equation 6.6 but the mean was now calculated using:

$$M_j = 1/(n_j + n_p) \{\sum_{i=1}^{n_j} R_{ij} + \sum_{i=1}^{n_p} R^p_{ij}\} \qquad 6.8$$

where n_p is the number of missing observations and R^p_{ij} are the "predicted" absolute residuals. The relative residuals of the events that were not observed by all 15 stations of the array have had their mean residual calculated using equation 6.8.

Before presenting absolute and relative residuals determined for the network some discussion is necessary on the discrimination between the various core phases (PKP).

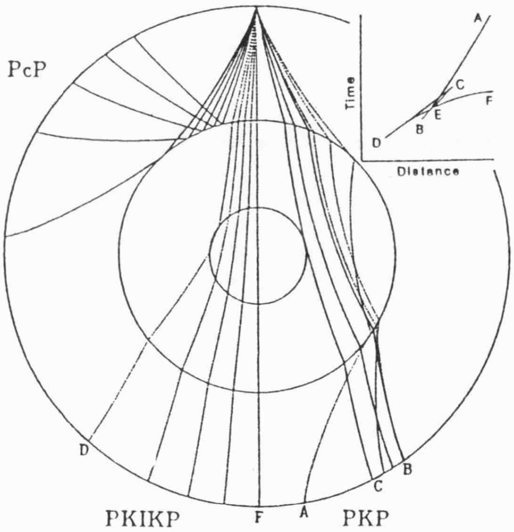

Figure 6.5 : Ray paths of core phases bottoming in the outer core (branches BC and AB) and those passing through the inner core (branch DEF) (after Morrelli and Dziewonski, 1987).

6.5 Discrimination between core phases.

Figure 6.5 shows the PKP ray paths and travel times (inset) of branches AB and BC (outer core transit only) and DF (transit through the inner core), in the original notation of Jeffreys (1939). For epicentral distances less than about 135° or greater than about 150° the correct identification of these phases is relatively straight forward. However, for epicentral distances in the region of 145° it is more difficult because the three branches intersect. As 12 of the 26 core phases used in this study originated from between 141° and 147° (from the Tonga and Fiji islands region of the Pacific) considerable effort was put into the problem of correct identification. Incorrect identification would have lead to substantial errors in the residuals calculated.

The 145° region of the travel time table is shown in figure 6.6. The AB, BC and DEF branches correspond to the PKP_2, PKP_1 and PKIKP phases respectively. Branch GH corresponds to PKHKP arrivals which are generally attributed to the scattering of PKP waves near the core-mantle boundary (Anderssen and Cleary, 1980). The International Seismological Centre (ISC) treats reports of the earliest core phase arrivals from earthquakes as PKIKP observations and provides residuals based on Jeffreys-Bullen PKIKP times. Anderssen and Cleary (1980) analysed some 30000 such residuals from the ISC report of 1967 to show that the data include, in addition to PKIKP, observations of PKP_1, PKP_2 and PKHKP.

The Tonga and Fiji Islands events observed by the network could be divided into two groups; those of $\Delta < 143°$ and those of $\Delta > 143°$ (143° corresponds to B on figure 6.6). The method used to sort out which phases were observed was to calculate sets of relative residuals for each event using all the possible branches of the Herrin tables for the given epicentral distance. These were compared with the patterns of relative residuals obtained for unequivocal PKIKP phases from events of similar back bearing. As all the core phases considered have angles of incidence between about 5° and 11° from vertical they should all give similar patterns of relative residuals (assuming similar back bearings). Such comparisons showed that the Tonga events of $\Delta > 143°$ were PKP_2 arrivals (AB branch) and that the events of $\Delta < 143°$ corresponded to branch GH.

6.6 Absolute residuals.

A single absolute residual is almost worthless since its value is not dependent only on the velocity structure immediately below the station: It is contaminated by other effects such as velocity anomalies anywhere along the ray path and errors in hypocentral location, origin time, travel time tables and onset measurements. For this reason, most of this chapter is devoted to the interpretation of relative residuals which are, for such a small aperture array, not significantly effected by the above (Reasenberg et al, 1980; Long and Mitchell, 1970). However, for the sake of completeness, absolute residuals were calculated for seismograms showing a distinct first-break.

For such a small network it is only pertinent to determine absolute residuals for the network as a whole: It will be seen in the next section that variations in relative residuals across the array are an order of magnitude smaller than the variations in absolute residual from event to

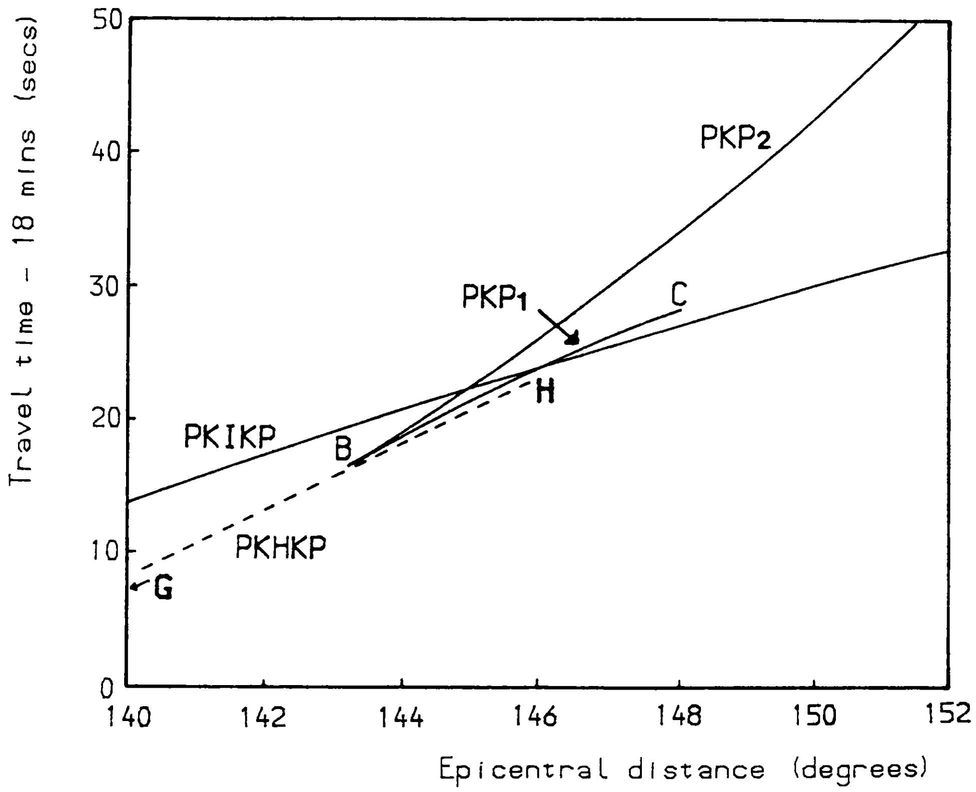

Figure 6.6 : Form of the travel time curves for core phases between epicentral distances 140 and 152 degrees.

event. For each event showing a distinct first-break at any of the stations, onset times were measured and absolute residuals were calculated. Of the 46 events listed in Table 6.2, it was considered that 18 showed first breaks distinct enough for estimates to be made of the onset-time. Elevation corrections were applied to account for the stations height above the Earth's ellipsoidal datum surface, which can be taken as mean sea level. The correction is given by:

$$\delta t = Z(1/V_0^{\,2} - 1/V_s^{\,2})^{1/2} \qquad 6.9$$

where Z is the height above the datum level, V_0 is the velocity of the medium above the datum and V_s is the apparent velocity of the phase at the surface. A value of 4.0 km/s, the velocity of the volcanic infill of the rift in the vicinity of Lake Bogoria determined by the KRISP85 refraction surveys, was used for V_0.

Table 6.3 shows the absolute residuals determined.

Table 6.3 : Absolute Residuals

Event	Location	AR (secs)	Event	Location	AR (secs)
2	Mexico	3.15 ± 0.2	27	Fox Is.	2.83 ± 0.2
3	Tonga	2.94	29	Algeria	2.41
4	Tonga	2.49	33	S.A.R.	1.99
5	Tonga	2.79	36	Taiwan	3.25
9	Taiwan	3.49	39	Vanuatu Is.	2.95
19	Vanuatu Is.	3.58	40	Vanuatu Is.	3.51
23	El Salvador	4.06	41	Vanuatu Is.	3.79
25	Tajik	4.29	42	Tonga	2.44
26	Timor Sea	4.12	44	M.I.R.	2.84

The mean absolute residual for the network is 3.1 secs with a standard deviation of 0.8 secs. The large scatter in the values determined is due to the effects of random errors in location and origin times of the events, velocity anomalies far from the array and picking errors. If these errors are assumed to have a normal distribution then the standard error is 0.2 secs. Because Herrin's tables have been used in the determination of the residuals whereas those due to Jeffreys-Bullen were used in the calculation of hypocentre and origin time, a baseline correction must be applied to the absolute residual determined (Savage and Long, 1985). This was estimated by Savage and Long (1985) and Pointing (1985) to be the subtraction of 2.090 secs and 2.045 secs respectively from the value obtained using Herrin's tables. Thus the absolute residual for the region of the lake Bogoria network is 1.2 $\pm$ 0.2 secs.

6.7 Relative residuals.

The residuals (for the remainder of this chapter relative residuals are referred to simply as "residuals") determined for the 46 events are listed in Appendix C. To show the effect of the underlying velocity structure the events were grouped, according to phase and epicentral back bearing, and the mean residuals were calculated for each station. Because of their relatively steep angle of incidence, all the back bearings of the core events were grouped together. The azimuthal spread of the P events shown on figure 6.2 initially suggested division into three groups: (1) Events from north; (2) Events from west; (3) Events from east. However, examination of the residuals from the eastern events showed that those from the north-east gave quite a different pattern of residuals to those from the east and south-east so a further division was made. The spread of back bearings for each group is shown in Table 6.4 along with the mean residuals calculated and standard deviations.

Figure 6.7 (a-f) shows the patterns of mean residuals for the various phases and back bearings described above. The 0.0 and 0.1 second contours on each of the plots are by no means definitive but are merely intended to draw the readers attention to the main features of each pattern. As expected the residual patterns obtained for the two sets of core phases are broadly similar, owing to the steep angle of incidence of these phases. The patterns obtained from the four different groups of P events are all quite different which is indicative of a high degree of lateral heterogeneity in the upper crust. Most of the stations show a definite variation of residual with event back bearing. For instance, the mean residuals calculated for station 9 (Fig. 6.1) in the SE corner of the network vary from +0.27 secs for events from a NNW direction to 0.0 secs for events from the NE. Similarly, those of station 6 on the western side of the array vary from -0.27 secs for events from the NNW to +0.09 secs for events from the E.

The observation that the highest residuals for the P phases tend to occur at stations most distant from the hypocentres suggested that they may have been caused by errors in the gradients of Herrin's travel time tables. However, tests showed that even a 5% error in the gradient would always lead to an error of less than 0.05 secs across the array. Long and Mitchell (1970) measured relative residuals between stations in Iceland,

Table 6.4 - Average relative residuals.

	PKIKP			Other core phases			P (030° - 070°)			P (090° - 130°)			P (205° - 285°)			P (320° - 350°)		
ST	N	RR	SD	N	RR	SD	N	RR	SD	N	RR	SD	N	RR	SD	N	RR	SD
1	10	-0.05	0.03	10	-0.06	0.03	0			2	-0.11	0.03	3	0.09	0.04	2	0.00	0.02
2	11	-0.10	0.03	7	-0.07	0.03	6	0.00	0.03	4	0.06	0.01	4	-0.09	0.04	4	-0.09	0.04
3	11	0.00	0.04	9	-0.03	0.03	0			3	-0.12	0.03	4	0.11	0.06	2	0.09	0.02
4	11	0.02	0.04	9	0.02	0.02	0			3	0.01	0.04	2	0.12	0.01	3	0.12	0.02
5	8	0.10	0.02	8	0.04	0.03	3	-0.06	0.03	1	0.00		1	0.02		3	0.01	0.02
6	10	-0.15	0.03	8	-0.11	0.04	6	-0.07	0.02	3	0.09	0.02	4	-0.09	0.05	3	-0.27	0.01
7	8	-0.06	0.04	9	-0.02	0.03	5	0.01	0.02	4	0.12	0.03	4	-0.10	0.04	1	-0.14	
8	8	-0.05	0.03	7	-0.05	0.02	5	-0.02	0.03	2	-0.01	0.01	2	-0.11	0.04	2	0.00	0.01
9	10	0.13	0.02	10	0.14	0.04	5	0.00	0.02	4	0.05	0.03	2	0.13	0.05	2	0.27	0.01
10	8	0.05	0.03	9	0.08	0.03	6	0.08	0.03	4	0.03	0.03	4	-0.10	0.06	1	-0.04	
11	8	0.09	0.04	10	0.07	0.03	6	0.06	0.04	4	-0.02	0.01	4	0.08	0.04	3	0.09	0.01
12	9	0.08	0.03	10	0.06	0.03	5	-0.06	0.03	4	-0.05	0.02	5	0.12	0.05	1	0.09	
13	11	-0.01	0.03	9	-0.02	0.03	6	0.13	0.05	5	0.02	0.03	4	-0.07	0.07	3	0.02	0.03
14	11	0.02	0.04	9	0.01	0.02	5	-0.02	0.03	5	-0.03	0.03	4	-0.02	0.02	2	-0.07	0.01
15	3	-0.12	0.02	2	-0.10	0.04	3	-0.02	0.04	2	-0.02	0.03	0			0		

All relative residuals and standard deviations are in seconds

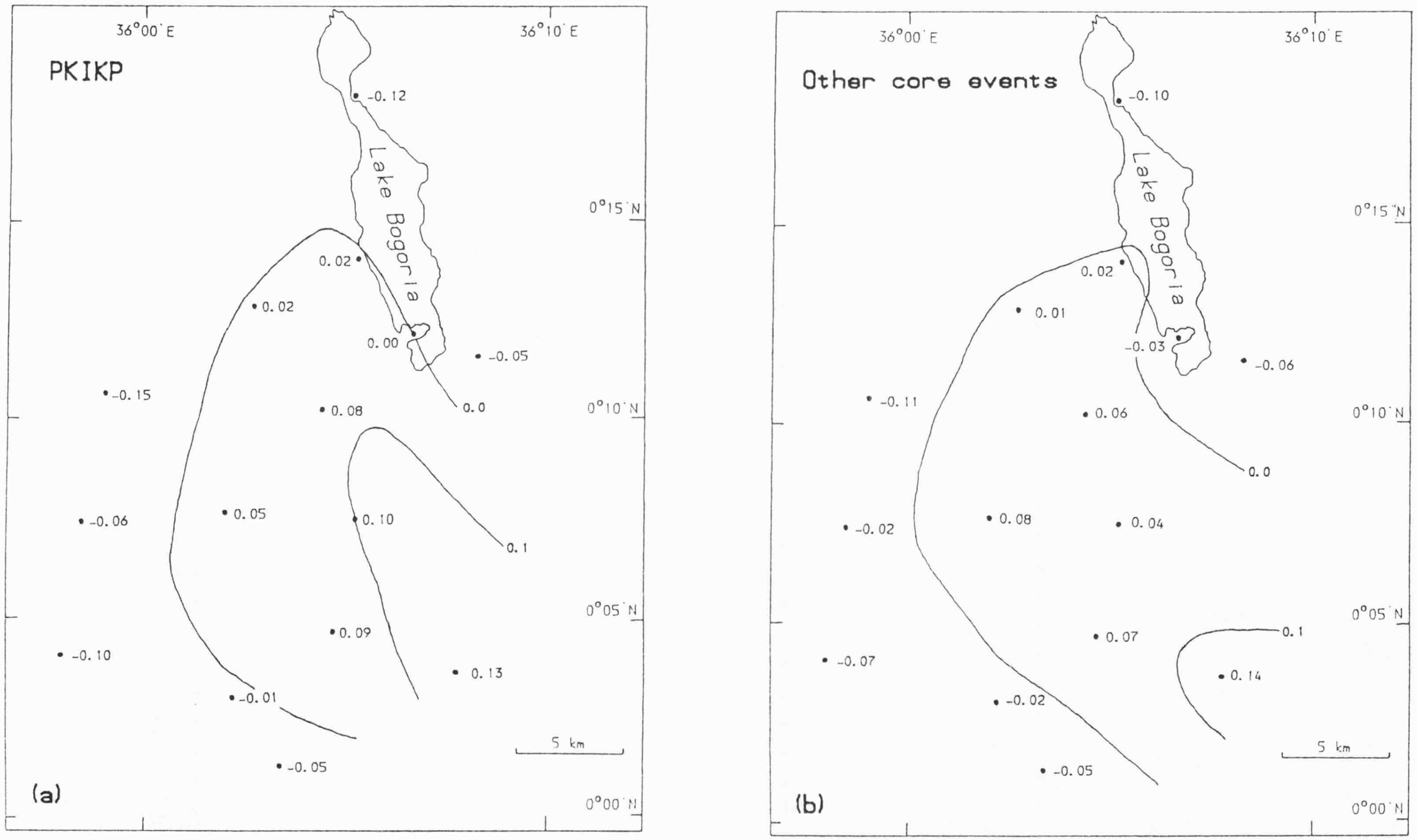

Figure 6.7(a-b) : Mean relative residuals calculated for core phases observed at the Lake Bogoria network.

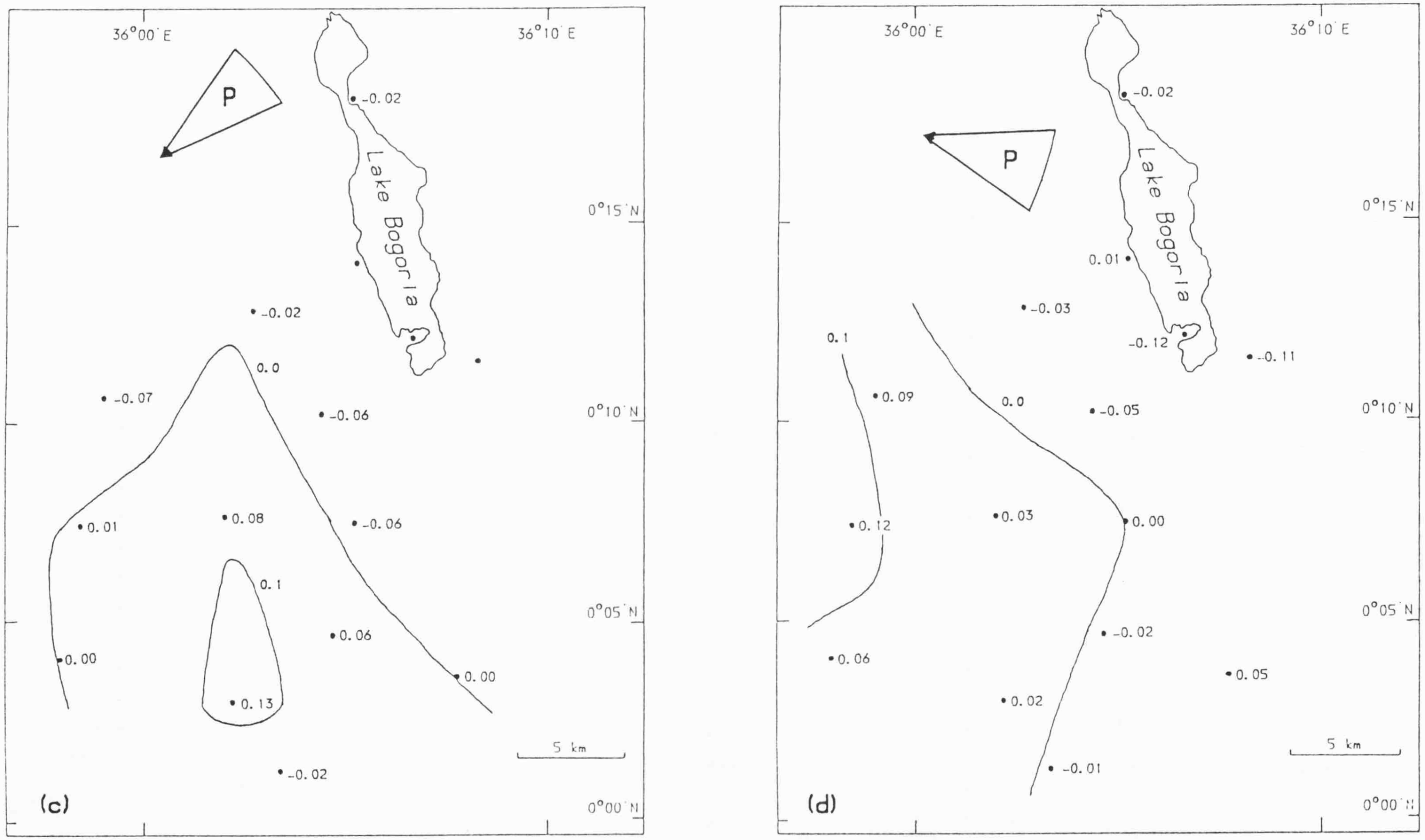

Figure 6.7(c–d) : Mean relative residuals of P phases of back bearing: 030° – 070° (c); and 090° – 130° (d).

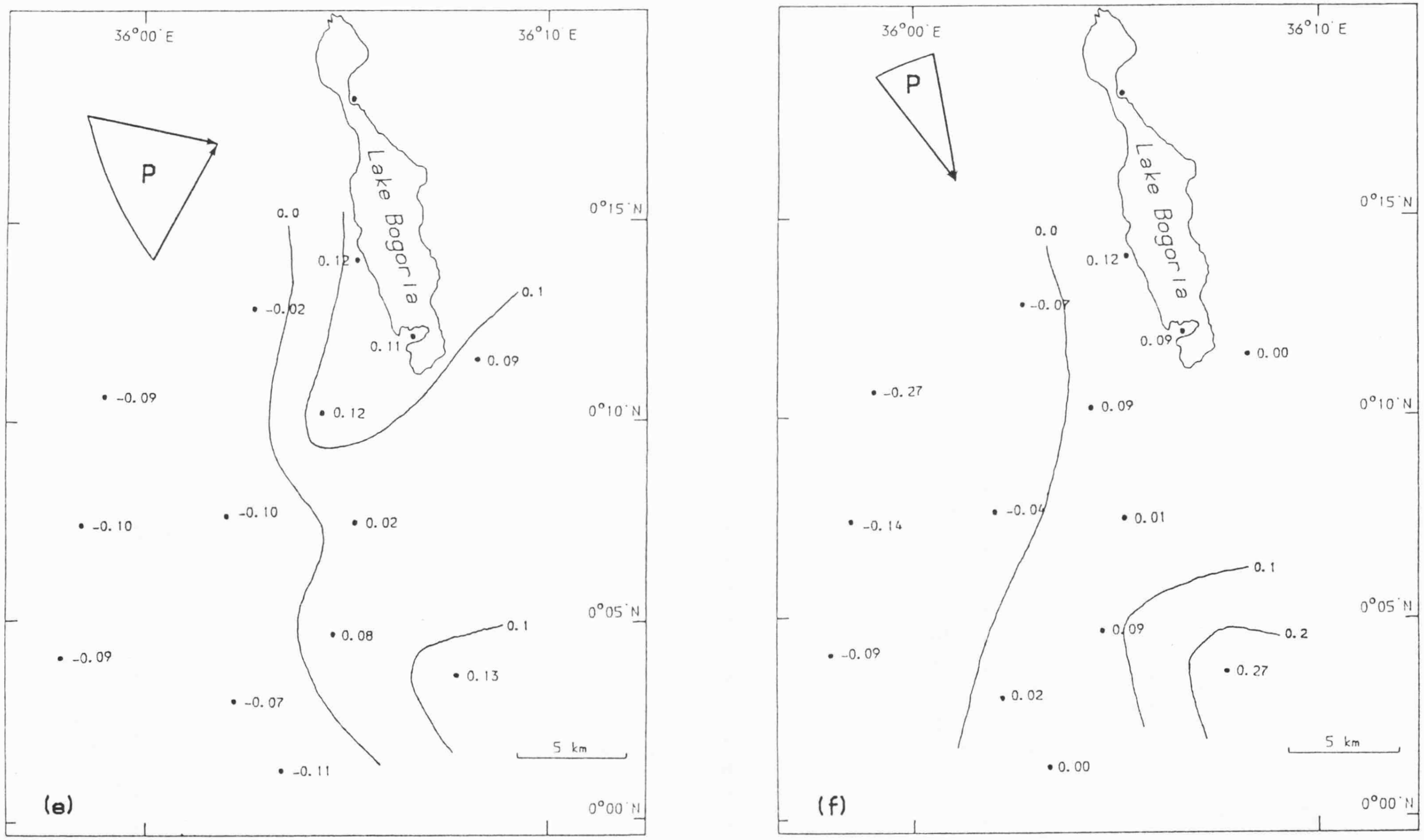

Figure 6.7(e-f) : Mean relative residuals of P phases of back bearing:
205^{o} - 285^{o} (e); and 320^{o} - 350^{o} (f).

Greenland, Sweden and Scotland and considered that even for this experiment, where inter-station distances were up to 15°, errors due to inaccuracies in the gradients of Herrin's tables were negligible. It is thus concluded that the residuals obtained for the Lake Bogoria array are not a result of errors in the travel time tables.

The remainder of this chapter deals with the inversion of the residuals obtained for crustal velocity structure below the network.

6.8 Aki inversion method.

The residuals listed in Appendix C were inverted for P wave velocity structure using the method attributed to Aki et al (1977). Before describing the details of the inversion a brief summary of the theory of the method is necessary.

It is assumed that the velocity structure through the Earth is laterally homogeneous over the cross section encompassed by the wave front between source and receivers in all regions except immediately beneath the network. The three-dimensional velocity structure for the region below the network is obtained by assuming a starting model of plane, horizontal layers, each of constant velocity. Each layer is subdivided into grids of rectangular blocks and rays from each teleseismic event are traced through the initial model to the receiving stations (Fig. 6.8). Each block is assigned a parameter that describes the fractional perturbation of slowness (reciprocal of velocity) relative to the initial value for that layer. Expressing this parameter for block k as m_k, the absolute residual may be written as

$$R_{ij} = T_{oij} - T_{tij} = \sum_k g_{ijk} m_k + e_j \qquad 6.10$$

for station i and event j, where

$$g_{ijk} = d_l/(v_l \cos\theta_l) \; , \qquad 6.11$$

d_l and v_l are the thickness and velocity of layer l and θ_l is the angle between the vertical and the ray path in layer l. The summation with respect to k is made over the block that contains most of the ray path in each layer. Term e_j is a source parameter which is included to absorb errors common to all stations (event origin time etc). It is eliminated by the use of relative residuals rather than absolute residuals. Consideration of all events and stations gives a system of linear

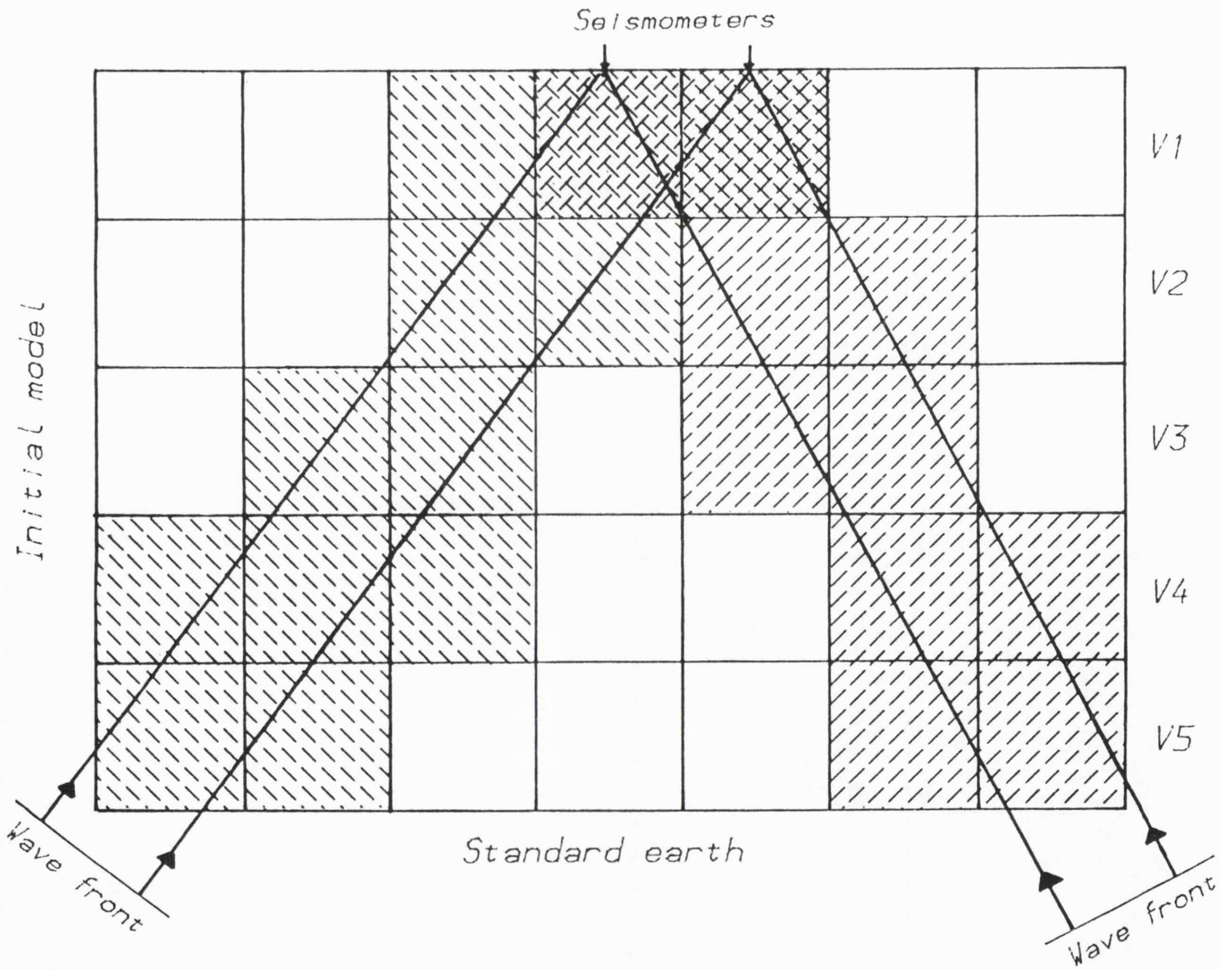

Figure 6.8 : Diagram showing blocks sampled by incident teleseismic waves recorded at two receiving stations (After Aki et al, 1977).

equations which may be expressed in matrix notation (bold symbols are matrices) as

$$\mathbf{r} = \mathbf{G}\mathbf{m} \qquad 6.12$$

where **m** and r are vectors containing the unknown slowness parameters (m_k) and the observed residuals respectively and **G** is a semidefinite matrix consisting of the calculated unperturbed travel times of the ray segments. The method of damped least squares is used to solve 6.12 (Aki et al, 1977; Ellsworth and Koyanagi, 1977) for **m**:

$$\hat{\mathbf{m}} = (\mathbf{G}^T\mathbf{G} + \theta^2\mathbf{I})^{-1}\mathbf{G}^T\mathbf{r} \qquad 6.13$$

where $\hat{\mathbf{m}}$ is the model estimate and θ^2 is the damping parameter (Aki et al, 1977). An image of lateral variations in the velocity of each layer is thus produced. It is important to note that absolute values of velocity variations are not determined by the method. Fortunately, precise knowledge of the vertical velocity profile is not required for the solution to be of quantitative value as it can tolerate substantial errors in layer velocity (Aki et al, 1977).

6.9 Inversion of teleseismic data.

The Aki inversion was carried out using a package of routines obtained from the United States Geological Survey (U.S.G.S.). Program names cited here are as described in the user's manual (Evans, 1986). The programs used in this study include:

(1) **THRDWT**: A weighting pre-processor routine which must be run before carrying out the inversion.

(2) **THRD**: The routine that carries out the damped least squares inversion.

(3) **THRLIST**: A printing routine that converts **THRD** binary output into a readable format.

(4) **AVTHRD**: A pre- and post- processor for **THRDWT** and **THRD** that accomplishes a spatially smooth inversion result by averaging the results from a number of individual inversions.

Additional programs, **REGRID** and **CONTOUR** (Appendix B) were written by the author to produce contour maps of the velocity perturbations obtained.

The chosen starting model , as well as certain parameters controlling the inversion, are listed in Table 6.5. These are the values used in the final inversion from which the velocity perturbations presented later were calculated. The effects of varying the various model parameters are discussed below.

(1) Block size. The choice of lateral block size is controlled primarily by the average station spacing of the network. A block size of 5km x 5km was found to be optimum. Smaller blocks resulted in many blocks not experiencing enough "hits" (rays passing through them) for them to be included in the inversion. In any case, the typical wavelength of teleseismic waves (5 - 10 km) does not warrant smaller blocks. Larger block sizes were found to give inadequate lateral resolution. The block size parameter is not relevant to the top layer which is treated in a different manner to the deeper layers. The normal block stucture is replaced by a separate first layer "block" for each station. The reason for this special treatment is that in the first layer the rays arriving at a given station generally sample a volume through which no rays to any other stations pass.

(2) Initial velocity model. The layer thicknesses and velocities shown in Table 6.5 are a simplified version of the velocity-depth function obtained from the refraction experiment (Chapter 4). The high velocity layer (7.1 km/s) in the lower crust was not included as tests showed that the inclusion of such a thin layer at that depth resulted in unsatisfactory resolution i.e. the diagonal elements in the resolution matrix were all < 0.3. Fortunately, the method can tolerate substantial errors in the velocities assigned to the starting model (Aki et al, 1977). The choice of number of layers to be included in a model depends on; (1) the effect of inhomogeneity below the bottom layer which will be projected on to the solution, and (2) the significance of improving the fit by the addition of an extra layer. Others using the Aki inversion method have used starting models of about the same maximum depth as the diameter of the array (Reasenberg, 1980; Robinson and Iyer, 1981 and Achauer et al, 1986).

(3) Damping parameter. The role of the damping parameter (θ^2) is to suppress the contribution of eigenvectors with eigenvalues smaller than θ^2 from the solution (Aki and Richards, 1980). The effect of varying the damping parameter has been studied by Reasenberg et al (1980) and Achauer et al (1987). Increasing θ^2 tends to reduce the standard errors of the solution but at the same time leads to poorer resolution. On the other hand, decreasing θ^2 has the effect of giving improved resolution at the expense of increased standard errors. A value of θ^2 of about 0.002 $s^2/\%^2$ was found to be a good

compromise, giving acceptable resolution and standard errors (Appendix C).

(4) Minimum number of "hits". A block is only included in the inversion if it is "hit" by a certain number of rays. Some workers have only included blocks having at least 10 hits (e.g. Achauer et al, 1987) whereas others have included all those with at least 5 hits (e.g. Robinson and Iyer, 1981). As a relatively small number of events were used in this inversion, the latter value was adopted. It was found that the peripheral blocks included in the inversion generally experienced less hits than those beneath the central region of the array and thus had correspondingly higher standard errors and were not as well resolved.

Table 6.5 : Aki inversion initial model.

Layer	Thickness	Block size	Velocity	
1	2.5 km	"special"	4.0 km/s	$\theta^2 = 0.0016\ s^2/\%^2$
2	10.0 km	5km x 5km	6.1 km/s	min "hits" = 5
3	10.0 km	5km x 5km	6.5 km/s	
4	10.0 km	5km x 5km	6.7 km/s	

Ray tracing was performed from true elevations so there was no need to correct the residuals for elevation. Station 15 was excluded from the inversion as it observed only a small number of events and it was quite remote from the other stations. Inverting using the above starting model, the variance calculated for the observed residuals of 0.014 s^2 was reduced by 88%, leaving an unmodelled variance of 0.0017 s^2 which is close to that which would be expected from measurement errors. The velocity perturbations, number of hits per block, diagonal elements of the resolution matrix and standard errors calculated for each block are listed in Appendix C. The diagonal elements of the resolution matrices were generally in the range 0.7 - 0.9 which indicates good resolution. The standard errors of the velocity perturbations were mainly between 1% and 1.5% which is acceptable in relation to the magnitude of the velocity perturbations obtained. Higher values obtained were normally associated with blocks which had not experienced many "hits".

The inversion results for a single model depend strongly upon the precise configuration of the block boundaries. The influence of block boundaries is greatly reduced by calculating the average perturbations of several identical models which have been shifted laterally by different distances. Program **AVTHRD** was used to perform 9 separate inversions of the original model, each one with a different lateral offset. The individual results were then averaged to give a spatially smoothed result for each model layer. Obviously, the above only applies to the lower 3 layers as it is meaningless to offset the "special" first layer.

The velocity perturbations determined for the first layer are listed in Table 6.6 and those of the lower layers are shown by contour maps in figure 6.9 (a-c).

Table 6.6 : Layer 1 - velocity perturbations.

Station	Pertub' (%)	SE (%)	Station	Perturb' (%)	SE (%)
1	-8.13	1.25	8	3.46	1.57
2	4.09	1.73	9	-10.45	1.50
3	8.01	1.56	10	12.91	1.63
4	5.13	1.68	11	-2.60	1.47
5	1.40	1.74	12	3.65	1.67
6	13.71	1.32	13	4.20	1.39
7	7.29	1.62	14	9.85	1.49

As a check on the validity of the inversion, it was repeated with a starting model identical to that shown in Table 6.5 except for a 45° rotation. The fact that a similar pattern of velocity perturbations was obtained, apart from the 45° rotation, suggests that the velocity perturbations obtained are real features of the crust and not a fabrication of the method.

6.10 Results of Aki inversion.

The velocity perturbations determined for the first layer vary from +13.7% for station 6 to -10.4% for station 9. Such variations in velocity are not exceptional for the volcanics and sediments infilling the rift. They may, in part, reflect variations in the depth to basement and thicknesses of lower velocity superficial deposits.

The contour maps of velocity perturbations for layers 2, 3 and 4 (Fig. 6.9) were drawn using programs **REGRID** and **CONTOUR** (Appendix B). The contours near the edges of each plot are less reliable owing to the lack of blocks included in the inversion in these areas and the higher standard errors associated with peripheral blocks. Comparison of the contour maps for the three layers shows that the variations in velocity perturbations obtained for layer 2 are more extreme than those obtained

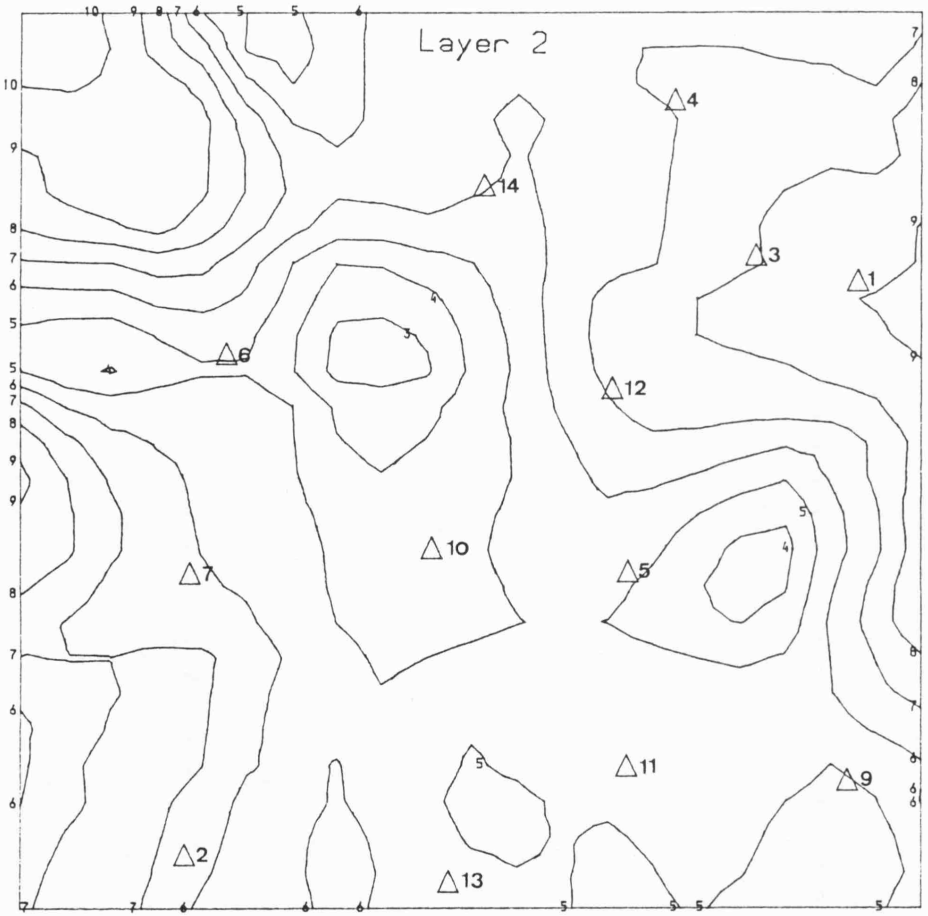

Contour no	V perturbation
1	-10 %
2	-8 %
3	-6 %
4	-4 %
5	-2 %
6	0 %
7	+2 %
8	+4 %
9	+6 %
10	+8 %
11	+10 %

Figure 6.9(a) : Contoured velocity perturbations for layer 2.
Triangles show recording station locations.

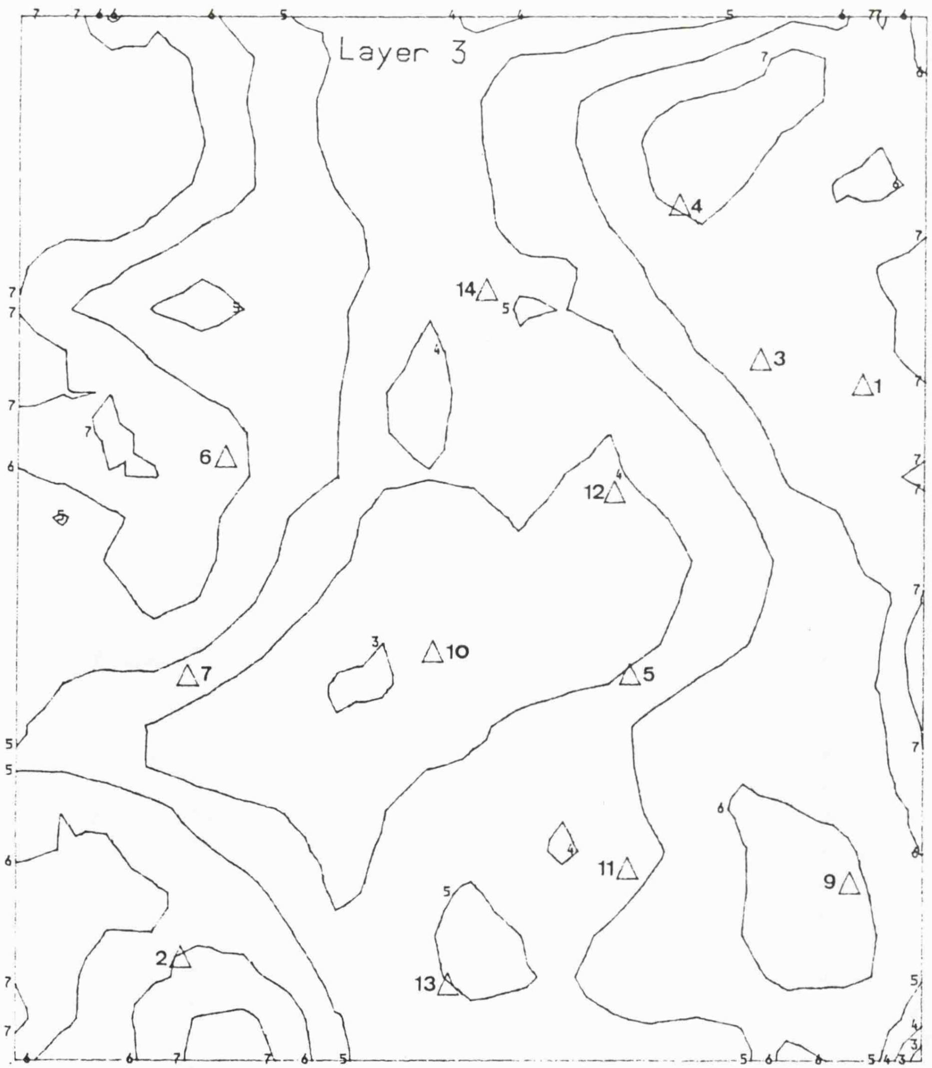

Contour no	V perturbation
1	-10 %
2	-8 %
3	-6 %
4	-4 %
5	-2 %
6	0 %
7	+2 %
8	+4 %
9	+6 %
10	+8 %
11	+10 %

Figure 6.9(b) : Contoured velocity perturbations for layer 3. Triangles show recording station locations.

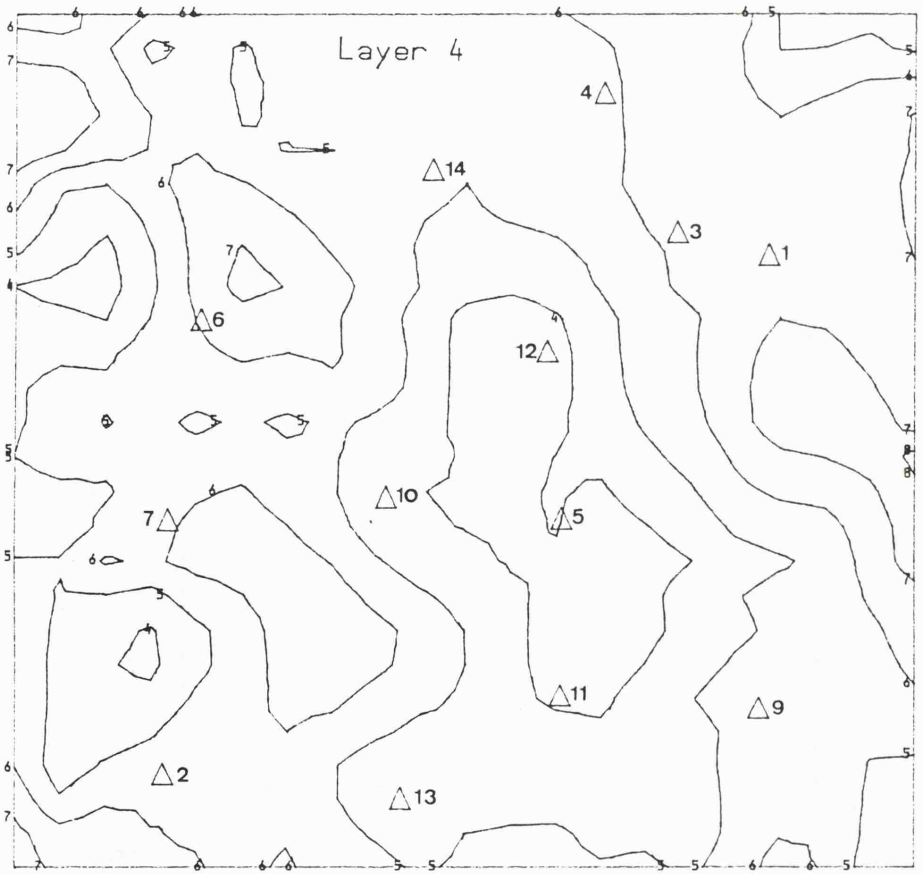

Contour no	V perturbation
1	-10 %
2	-8 %
3	-6 %
4	-4 %
5	-2 %
6	0 %
7	+2 %
8	+4 %
9	+6 %
10	+8 %
11	+10 %

Figure 6.9(c) : Contoured velocity perturbations for layer 4. Triangles show recording station locations.

for layers 3 and 4. Beneath the array (receiving stations are shown by triangles) the perturbations in layer 2 vary from -6% to +4%. The velocity perturbations observed for layers 3 and 4 vary from -4% to +2% and -4% to 0% respectively. Lateral heterogeneity below the Lake Bogoria network is thus most pronounced in the upper crust. For this reason, the following discussion concentrates on the possible geological significance of the velocity perturbations observed in layer 2.

Inspection of the velocity perturbations associated with layer 2 shows the existence of two distinct zones of low velocity, one to the east of station 5 and one to the east of station 6. There are also areas of high velocity: one to the west of station 7 and a more widespread region of higher velocity to the NE of the array. These, however, are not as reliable as the former as they do not lie directly under the array.

The Bouguer gravity anomaly for the Lake Bogoria region was examined to ascertain whether any correlations exist between the velocity perturbations observed and the density of the underlying medium. Unfortunately, with the exception of a narrow strip in the immediate vicinity of Lake Bogoria, there are few gravity measurements available for the region of the network and those that do exist are not regularly spaced. It has thus proved impossible to make any definite correlations between the velocity perturbations and the Bouguer gravity anomaly.

The interpretation of the pattern of velocity perturbations observed in layer 2 in terms of geology is not straight forward. A possible explanation for the areas of higher velocity is that in these areas the upper crust is intruded by basaltic dykes. There is a possible correlation between the occurrence of surface manifestations of geothermal activity (Fig. 6.1) and the zones of higher velocity. However, this is probably fortuitous as the occurrence of hot springs and fumaroles around Lake Bogoria and in the Molo Graben is most likely to be because of the presence of surface water at these localities. Most of the geothermal activity around Lake Bogoria occurs very close, or indeed under, the Lake. Similarly, at Arus (Fig. 6.1) the hot springs are all situated on the eastern bank of the Molo river. The geothermal activity in both areas is thought to result from surface water going down fissures associated with faulting and being returned as steam after coming into contact with hot volatiles (mainly CO_2) (McCall, 1967).

Low velocity zones under other geothermal areas have been interpreted as signifying the presence of magma bodies. Robinson and Iyer (1981) interpreted a maximum velocity contrast -7% relative to the surrounding rock as signifying the presence of partial melt under the Roosevelt hot springs area. Reasenberg et al (1980) suggested that a low velocity body under the Coso Springs geothermal area is caused by the presence of partial melt in the middle crust. More recently, Achauer et al (1986) interpreted a small anomalous volume "with at least 7% low velocity" as a chamber of molten or partially molten rock.

The two low velocity zones observed under the Lake Bogoria array may delineate areas of molten or partially molten rock in the upper crust. Perhaps they have contributed to Hannington Suite of trachyphonolitic lavas. There is no obvious surface manifestation of eruptive centres above the low velocity zones. However, the lava flows are thought to have predominantly been emitted through north-south fissures. Griffiths (1977) suggested that shallow seated magma chambers below the area have rendered the overlying strata abnormally unstable and susceptible to brittle fracture. They would also explain why the area is geothermally active.

Further research is required before the low velocity zones can definitely be attributed to the presence of magma chambers. A study of the amplitudes of the teleseismic rays observed over the array might help to confirm their presence. A region of melt would attenuate the amplitude of seismic waves passing through. If it could be shown that the waves having passed through the a low velocity zone had also been attenuated, this would corroborate the above hypothesis. Unfortunately, there has been insufficient time for such a study.

CHAPTER (VII)

DISCUSSION

7.0 Introduction.

In this chapter the "geophysical" results from previous chapters are put into a geological context. Comparison is made with previous geological and geophysical studies of the Kenya rift. No attempt is made to present a definitive model which explains all the observed features, however, during the course of this chapter existing models of the Kenya rift are critically examined. The main aspects of the rift structure that are dealt with are:

(1) The depth to "basement" within the rift and on the western flank.
(2) The nature of the "basement".
(3) The existence of the axial intrusion.
(4) The origin of reflection B - the brittle-ductile transition zone?
(5) The high velocity material at mid-lower crustal depth.
(6) The crustal thickness.

7.1 The depth to "basement".

At this stage in the discussion the term "basement" refers to the material of P-wave velocity of about 6.05 km/s observed beneath both the axis of the rift and the rift flanks. Velocities for the rift infill vary from about 1.5 km/s inferred for the volcanic soils of the Susua plain to 5.1 km/s observed at about 3 km beneath Lake Naivasha (Figs. 4.11 and 4.24). Velocities in the region of 4 km/s observed along much of the rift correspond to the complex succession of phonolites, trachytes and basalts described in Chapter 1. The higher velocities observed by the NAI and MAG shots might be the result of substantial thicknesses of Pliocene basalts which have a high density (Fairhead, 1976) and are thought to have correspondingly high velocity (Swain, 1979). Alternatively, the 5.1 km/s velocity observed below Lake Naivasha could be the result of high pressure associated with burial at such depth causing compaction.

The rift infill thickness has been shown to vary considerably along the rift. It is has a maximum thickness of about 6 km below Lake Naivasha compared with thicknesses of about 2 km and 1.5 km below Lake Bogoria and Lake Magadi respectively. This is in general agreement with the longitudinal section proposed by King (1978) suggesting that the rift infill is thickest below the Lake Naivasha region (about 4.5 km). However, the analysis of both KRISP75 and KRISP85 refraction data demonstrated thickening northwards from Lake Bogoria towards Lake Baringo which was not predicted by King.

The low angle detachment model of Bosworth et al (1986) and Bosworth (1987) (Chapter 1) is consistent with this observation of a relatively shallow basement below Lake Bogoria and deepening both northwards and southwards. In Bosworth's model the rift is envisaged to consist of a series of sub-basins of half-graben form, separated by accommodation zones. Such a zone is proposed to cross the rift at the southern end of Lake Bogoria, separating the Nakuru-Naivasha sub-basin from the Baringo-Bogoria sub-basin, which implies the basement should be shallowest in this region. Similar shallowing between sub-basins has been been observed in seismic reflection profiles from the water-filled basins of Lake Turkana (Dunkelman, 1986), Lake Tanganyika and Lake Malawi (Rosendahl et al, 1986).

The velocity cross-section determined from the EW-line data (Fig. 4.24) demonstrates that over 1 km of volcanics overlie the basement on the western flank. This volcanic pile consists of a series of tuffs, ashes, basalts, phonolites and trachytes (Wright, 1967). The above value is significantly greater than expected, considering the presence of small outcrops of Precambrian basement about 10 km east of shot point EWA. This may be indicative of a tilted block type structure for the basement below the western flank which is obscured by the volcanic pile.

Travel time offsets measured from the EWA record section indicated throws of about 0.9 km and 1.5 km for the major faults associated with the western rift margin at the latitude of the EW-line (about 1°S).

7.2 The nature of the "basement".

The combined interpretation of Pg arrivals from EWA and NTU, on the western flank of the rift, gave a velocity of 6.0 $\pm$ 0.1 km/s. Several small outcrops of Precambrian metamorphic basement exist between EWA and NTU and it is exposed over a wide area a few kilometres south of EWA. It is thus certain that the 6 km/s observed corresponds to Precambrian basement. Time-term analyses of both the KRISP75 and KRISP85 refraction data sets yielded refractor velocities of about 6.05 km/s for below the rift which are not significantly different from that obtained from the flank. The most obvious deduction to be made is that Precambrian basement immediately underlies the infill of the rift. A value of about 6 km/s for the Precambrian basement agrees with the models determined in and around the rift by Rykounov et al (1972), Bonjer et al (1970) and Maguire and Long (1976) (Fig. 1.6). Mohr (1987) considered that the sub-rift velocities of 6.0 - 6.1 km/s reported by the KRISP working group (1987) represent the partially molten and fractionated uppermost part of an asthenolith, rather than down faulted crust. However, it is difficult to justify such an interpretation: Similar sub-rift velocities have been determined below the Rhinegraben (Prodehl, 1981), the Rio Grande rift (Olsen et al, 1979) and the Baikal rift (Puzirev et al, 1978) and no such asthenolith has been invoked. This problem might have been resolved if it had been possible to determine S-wave velocities for the upper crust. If the 6.05 km/s material does represent partially molten mantle material, as suggested by Mohr (1987), then a higher than normal Poisson's ratio would be expected. Unfortunately, S-waves were not well enough observed during KRISP85 for any deductions to be made on the Poisson's ratio of subrift material.

The interpretation of the 50 km long, KRISP75 refraction line which ran west of Lake Baringo (Fig. 1.7) yielded a refractor velocity of 5.7 $\pm$ 0.025 km/s which was attributed to metamorphic basement (Swain et al, 1981). This is significantly lower than the 6.05 km/s observed along the rift in this study. A possible explanation for this observation is that beneath the rift the Precambrian basement is highly fractured, with microcracks aligned by the regional stress field predominantly along the axis of the rift. This could result in seismic anisotropy, resulting in higher velocities in the NS direction than in the EW direction. P-wave anisotropy of up to 8% have been observed by Crampin et al (1986) for a region of the Cascades Range in the U.S.A.. Unfortunately, Pg was not observed along the portion of the KRISP85 EW-line within the rift so this hypothesis could not be tested further.

The Pg phase was observed out to a distance of around 150 km along the NS-line. This is further than is normal for refraction profiles on continental crust and is indicative of a relatively high velocity-depth gradient and/or high Q. It has been shown by Hill (1971) that the effects of anelasticity (Q^{-1}) and velocity gradients cannot be separated by using the amplitude decay with distance of Pg alone. Braile (1977) has presented a method for determining Q for the upper crust by using the combined interpretation of the amplitudes of both refracted and reflected crustal phases. Although this has not been pursued, the observation of Pg out to such long distances and the assumption that Q is not exceptionally high for the upper crust below the rift implies the presence of a relatively high velocity-depth gradient.

The scaled-distance vs amplitude plots presented in Chapter 5 (Fig. 5.3) suggest variations in the anelasticity of the basement. In particular, the plots for BA1, BA2 and NAI all show an increased rate of amplitude decay with distance which coincides with the location of the intra-rift volcano, Eburru. Although the above ambiguity still applies, such lateral differences in observed amplitudes are more likely to reflect changes in Q than velocity-depth gradients. The basement below Eburru thus appears to be of lower Q than the surrounding basement which might reflect the presence of magma below this region.

A feature of the scaled distance vs amplitude plot of the EW-line shot, EWA, which is more difficult to explain is the observation of the amplitude of Pg increasing out to a distance of about 55 km from the shot. This could be the result of variations in the attenuating properties of the volcanic cover. However, this is unlikely as the thickness of volcanics is greatest within the rift where some of the highest amplitudes were observed. Other possible explanations are an exceptionally high velocity-depth gradient or increasing values of Q with depth.

The observation of travel time advances in the Pg phase from shots BA1, BA2 and NAI implied the existence of a zone of high P-wave velocity (approx 6.8 km/s) in the upper crust roughly adjacent to the northern end of Lake Nakuru (Fig. 2.3). This might reflect the presence of basic intrusive material in the basement. Such a high velocity zone (HVZ) would be expected, from the Nafe-Drake relation (Nafe and Drake, 1957), to have a correspondingly high density. Gravity measurements were made at all the recording sites along the NS and EW line. Figure 7.1 shows the terrain corrected Bouguer anomaly for NS-line stations 20 - 31. It can be seen that there is a distinct positive anomaly between stations 23 and 27 which is in good agreement with the proposed location of the HVZ. The amplitude of the positive anomaly is of the order of 10 mgals. A "very rough" calculation was performed to determine the the gravity anomaly that would be expected to be associated with the HVZ. It was assumed that the body has the shape of a vertical cylinder. Its top was assumed to be 3.5 km below the surface, its diameter was assigned a value of 10 km (section 4.1.4) and it was assumed to extend to a depth of 9 km from the surface (the vertical extent of the HVZ was not constrained by the refraction data). A density of 2.64 g/cm^3 was assigned to the crystalline basement (Fairhead, 1976) and the Nafe-Drake relation gave a value of 2.83 g/cm^3 for the density of the HVZ. Using the analytical expression for the gravitational attraction of a vertical cylinder (Telford et al, 1976), the positive anomaly over the axis of the cylinder was calculated to be 11 mgals. Given the assumptions made, the agreement between the magnitude of the observed and calculated anomalies may well be fortuitous. However, the

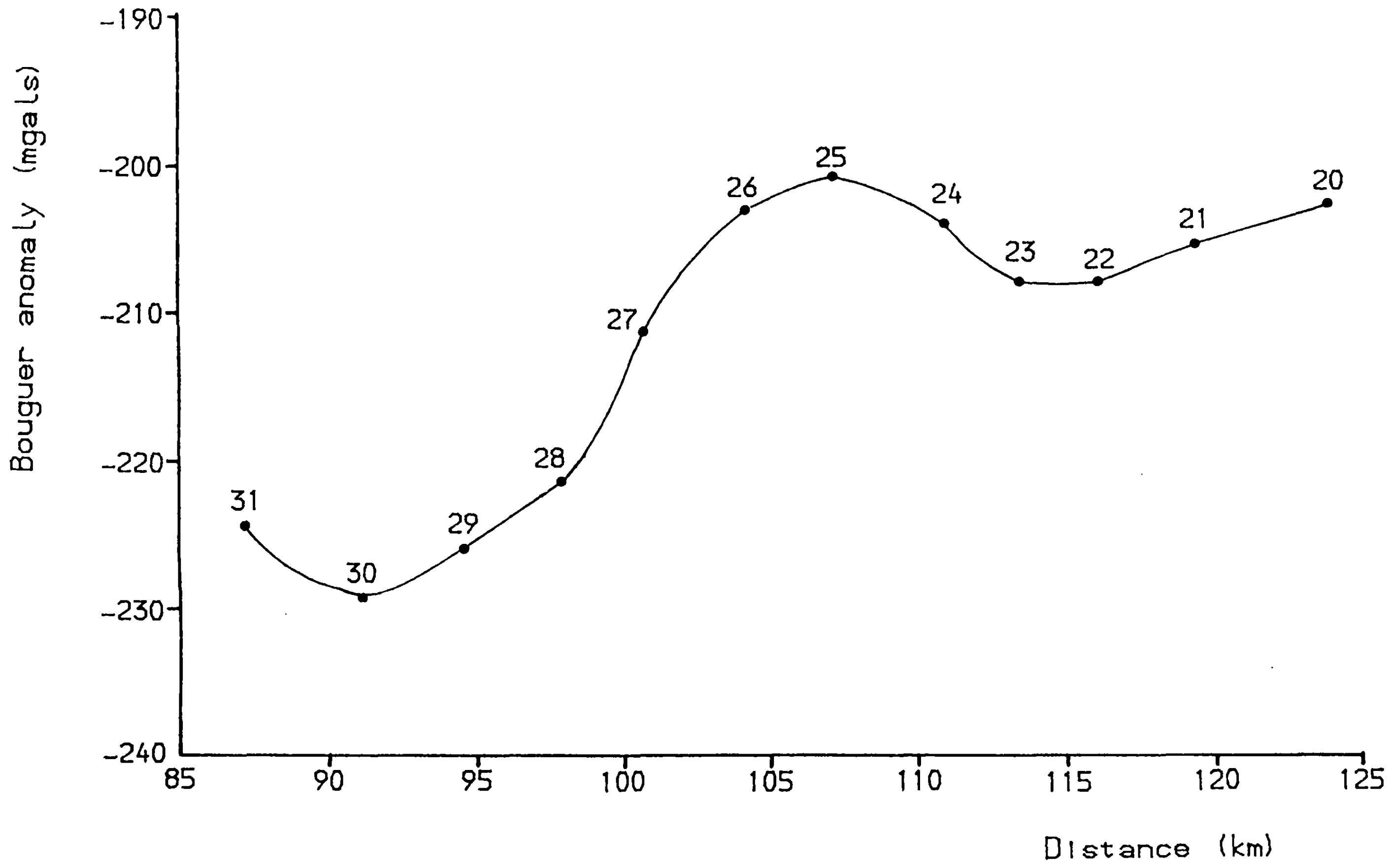

Figure 7.1 : Bouguer gravity anomaly for stations 20 to 31 of the KRISP85 NS-line.

observed positive Bouguer anomaly does corroborate the existence of the HVZ. The most likely explanation for the high velocity, high density zone is the existence of gabbroic or basaltic intrusive material.

The Aki inversion of teleseismic relative residuals described in Chapter 6 showed lateral heterogeneity in the upper crust below the Lake Bogoria array. The preferred interpretation of the two low velocity zones observed is the presence of magma chambers.

7.3 The existence of the axial intrusion.

As already mentioned in Chapter 1, several interpretations of the positive Bouguer anomaly which runs along the axis of the rift have implied the presence of a dense, wedge shaped, ultrabasic, intrusive mass reaching to within a few kilometres of the rift floor (Searle, 1970; Baker and Wohlenberg, 1971; Daracott et al, 1972). Searle (1970) and Baker and Wohlenberg (1971) suggested that this intrusion is composed of upper mantle material which has filled the gap between separating continental blocks. Support for the existence of such an axial intrusion has come from two seismic studies. Firstly, the KRISP68 seismic refraction investigation between Lake Turkana and Lake Bogoria (Griffiths et al, 1971) indicated the presence of high velocity (6.38 km/s) material within 3 km of the rift floor. Secondly, reduced teleseismic delay times measured at the centre of the rift at a latitude of about 0.5°S were said by Savage and Long (1985) to "provide independent confirmation of the existence of the axial intrusion previously inferred from gravity data".

The KRISP85 NS-line was deliberately positioned to follow the axial positive Bouguer anomaly as closely as logistically possible (Fig. 2.1). It had been hoped that it would provide final confirmation of the presence of the axial intrusion. However, the P-wave velocity sections shown in figures 4.11 and 4.15 indicate that, with the exception of a high velocity zone between SOL and ELM, the velocity of the upper crust is about 6.05 km/s immediately below the rift infill, increasing to between 6.15 and 6.2 km/s at about 12.5 km depth. As discussed in the previous section, such P-wave velocities are quite normal for metamorphic basement and certainly do not provide any "confirmation" for the existence of an axial intrusion. That is not to say that the presence of more diffuse zones of intrusive material has been precluded. A low concentration of basaltic dykes in normal Precambrian crust beneath the rift might not significantly alter its bulk seismic velocity. The velocity-depth gradient inferred for the upper crust is consistent with the amounts of such intrusive material increasing with depth. However, it now seems highly improbable that the kind of crustal separation invoked in the models of Searle (1970), Baker and Wohlenberg (1971) and Mohr (1987) has occurred. This finding is in agreement with Swain (1979) who concluded, on the basis of the KRISP75 seismic experiment and 2-D gravity modelling, that "normal crust is continuous across the rift, though there is probably some thinning below the rift". Although the gravity profiles implied the existence of a tabular zone of intrusives in the upper crust this was thought to be more likely of the "layered basic" variety than one associated with crustal separation.

If there is no massive axial intrusion beneath the rift then how can the axial positive Bouguer anomaly be explained? Searle (1970) determined that the positive Bouguer anomaly over the rift floor between 1.25°S and 0.25°N is between 40 and 80 km wide and has an amplitude of between 30 and 60 mgals. Searle (1970) rejected a possible model involving dense basaltic lavas infilling the rift because the density and thicknesses required to explain the anomaly were thought excessive in the light of geological estimates. However, Fairhead (1976) reinterpreted one of the EW gravity profiles (at about 1.1°S) originally investigated by Searle (1970). In particular, he revised the regional Bouguer anomaly used by Searle (1970) in determining the residual Bouguer anomaly. Fairhead (1976) assumed that the regional anomaly follows the observed Bouguer anomaly over exposed sections of the Precambrian basement both to the west and east of the rift. Where the basement material is covered by volcanics, the regional was assumed to be a smooth interpolation of those values on either side of the rift. This more rigorous treatment of the regional had the effect of reducing the amplitude of the positive anomaly determined by Searle (1970) by over 50%, as shown in figure 1.8. The resulting negative lobes are associated with substantial thicknesses of low density Cainozoic volcanics (Wright, 1967; Baker et al, 1972) overlying the rift flanks. The interpretation of the EWA and NTU record sections of the EW-line of KRISP85 demonstrated that the thickness of these volcanics is greater than previously thought. Fairhead (1976) concluded that the reduced positive anomaly might be explained by the presence of substantial thicknesses of dense Pliocene basaltic lavas buried beneath the rift floor (King and Chapman, 1972). He has measured densities of about 2.9 g/cm^3 for the Kaparaina basalts of the Lake Baringo area and the olivine basalts of S. Kenya. Of course, this does not preclude the existence of an axial intrusion but it does provide an alternative explanation for the positive Bouguer anomaly. The upper crustal velocities determined during KRISP85 together with the gravity interpretation just described suggest that the positive axial Bouguer anomaly is the result of the combined gravitational effect of dense basaltic lavas buried beneath the rift floor and zones of basaltic dykes in the Precambrian basement which are most concentrated along the axis of the rift. There is, however, no justification for the models of Baker and Wohlenberg (1970), Searle (1970) or Mohr (1987) which invoke a mantle diapir reaching to shallow levels beneath the rift, causing separation of crustal blocks.

Some comments are required on the above mentioned seismic investigations which offered support for the existence of an axial intrusion. The locations of the recording stations used in the teleseismic investigation reported by Savage and Long (1985) are shown in figure 1.7. The relative delay-times measured for stations in and around the rift were projected on to a line perpendicular to the rift axis at a latitude of about 0.5° (defined by the maximum of the positive Bouguer anomaly). Savage and Long (1985) noted a "pronounced reduction in delay times coincident with the axial gravity high". Their preferred interpretation for this observation was an intrusion of anomalous upper mantle material, of velocity 7.5 km/s, reaching to within 20 km of the surface. A major weakness in their interpretation is that the station locations for which delay times were projected on to a straight line across the rift are separated by distances of up to about 30 km along the rift. It is highly questionable whether the projection of delay time over such distances is justified. The teleseismic relative residuals described in this study and the preliminary PKIKP delay times obtained from the Wisconsin array (14 stations, 35 km spacing) (Green and Meyer, 1986), which was centred over the Lake Naivasha area of the rift, indicate that the variations in delay time can be as high along the rift as across it. In addition, it has been shown that basement topography along the rift can be severe. Long (1987) has since reinterpreted the pattern of delays observed in terms of a 20 km wide region of high velocity in the top 20 km of the crust, and not in the lower crust as previously concluded.

The interpretation of the KRISP68 refraction line (Griffiths et al, 1971) shown in figure 1.6 comprises a planar velocity model with 6.38 km/s material from about 2.8 km depth down to about 18.5 km where the velocity increases to 7.5 km/s. Although the line was reversed, including shots in Lake Turkana and Lake Bogoria (Fig. 1.7), the two velocities determined are apparent because it was thought likely that the first arrivals from Lake Turkana (V_a = 7.5km/s) were from a deeper layer than those from Lake Bogoria (V_a = 6.38 km/s). The 6.38 km/s P-wave velocity obtained for the material below the rift infill is significantly greater than that deduced from this study. The higher velocity might partly be the result of shallowing of the basement towards Lake Turkana. However, this could only account for up to about 0.1 km/s of the difference given the maximum overall dip of about 0.5° allowed on geological grounds. The observations from which the 6.38 km/s velocity was determined were made at between 100 km and 300 km distance from the Lake Bogoria shot point. It is unlikely that "head waves" would be observed at such range. The arrivals are more likely to correspond to refracted (diving) waves which may have penetrated the crust to several kilometres depth. Thus the velocity immediately below the rift infill might be significantly lower than 6.38 km/s.

On the other hand, 6.38 km/s material might actually occur near the surface below the KRISP68 seismic line. This would suggest that the amount of basic intrusive material present in the upper crust is greater below the KRISP68 line than below the KRISP85 NS-line.

7.4 The origin of reflection B. Brittle-ductile transition zone?

Phase B, which is present on the BA1, BA2 and NAI record sections of the NS-line and possibly on the EWA record section of the EW-line, has been interpreted as a reflection from a discontinuity at about 12.5 km depth (below sea level) where the P-wave velocity increases from between 6.15 km/s and 6.2 km/s to about 6.45 km/s (Chapter 4).

The phase is present on the BA1 and BA2 record sections between about 50 km and 100 km range. The ray tracing diagram of figure 4.15 shows that the reflector is definitely present below Lake Bogoria which is about 50 km from the origin. The focal depths of about 300 local earthquakes recorded by the Lake Bogoria seismic network are shown in figure 7.2. These were located using the **HYPOINVERSE** program by Cooke (pers. comm.). It is evident that the hypocentres mainly occur above a depth of about 12 km below sea level. This threshold depth for seismicity coincides with the depth of the reflector which suggests the two are related. Earthquakes are caused by the sudden slippage of rock along a fracture surface so, in general, they are restricted to zones of brittle deformation. The maximum depth at which earthquakes occur in a seismically active area, such as the Lake Bogoria region, thus normally delineates the brittle-ductile transition zone. It is therefore likely that the discontinuity in velocity giving rise to reflection B is also associated with the transition from brittle to ductile behaviour.

Bosworth et al (1986) and Bosworth (1987) have suggested that the normal faults of the Kenya rift, and other continental rifts, may merge into low angle detachment systems in the region of the brittle-ductile transition

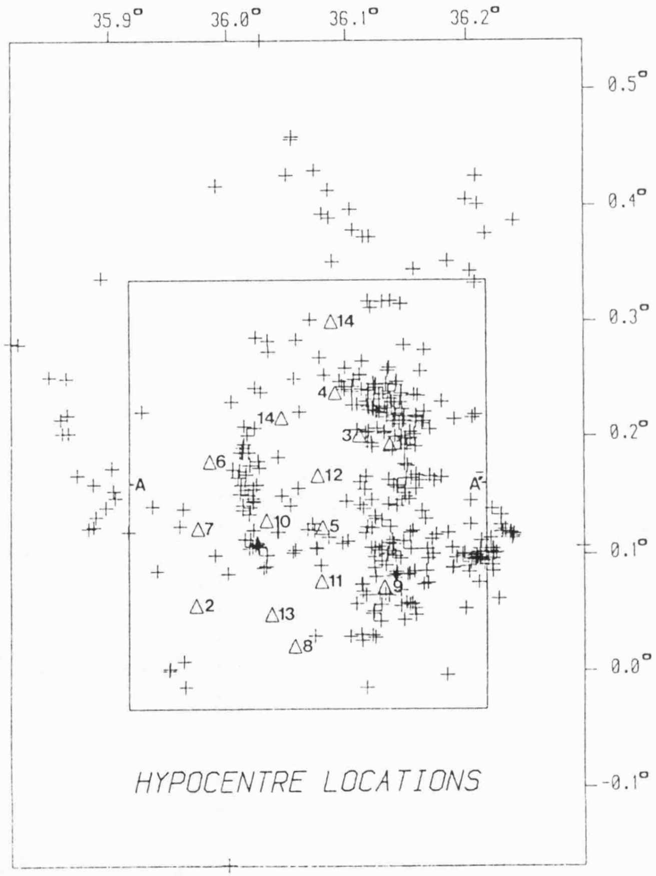

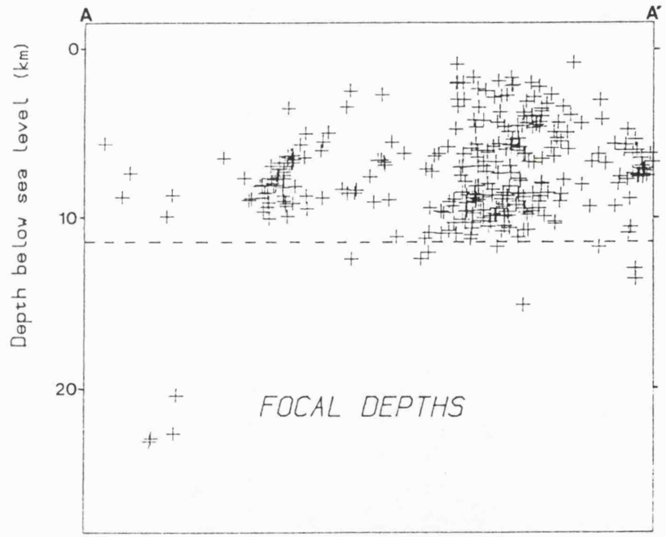

Figure 7.2 : Hypocentre locations and focal depths of local earthquakes recorded by the Lake Bogoria seismic array. Triangles are recording station locations.

for quartz rich crustal rocks (Chapter 1). If such detachment surfaces exist beneath the Kenya rift then they may occur at about the depth of the transition causing reflection B.

A combined reflection and drilling study of the rifting of the northern continental margin of the Bay of Biscay revealed a similar strong reflection associated with a detachment surface at the brittle-ductile transition (Montadert et al, 1979). The strong horizontal reflector was shown by a refraction study of the region to be caused by an increase in velocity from about 5.0 km/s to 6.3 km/s (Avedick et al, 1979). Drilling of the tilted blocks above the detachment surface demonstrated the presence of continental basement as well as sedimentary rocks. The boundary defining the near horizontal base of the listric faults and the reflector was thus interpreted as corresponding to a mechanical discontinuity in the upper continental crust and not as a particular geological horizon in the sedimentary rocks allowing decollement. This discontinuity, which the authors believe to have "clearly existed at the time of rifting" was situated at around 6 to 8 km below sea level in the central part of the rift.

Detachment surfaces, if they exist, would be expected to follow regions of low strength in the lithosphere. The strength of the lithosphere is controlled by the lithospheric rheology and as a consequence is dependent on the geothermal gradient and lithospheric composition. Kusznir and Park (1987) have carried out numerical modelling of the elastic, ductile and brittle response of the lithosphere to lateral stress. Their model predicted low strength regions at the base of the crust due to the contrast in rheologies of plagioclase and olivine across the Moho. Other low strength regions were predicted for the upper and middle crust at major compositional or rheological boundaries. It was shown that in the presence of low-medium thermal gradients deep detachments are likely to form in response to tensile forces. On the other hand, high geothermal gradients favour the development of shallower detachments at the expense of the deeper horizons. The high heat flow of 105 ± 51 mWm^{-2} observed within the Kenya rift (Morgan, 1982) might therefore suggest that any compositional and/or rheological boundary in the upper crust could be the site of a detachment surface.

The increase in velocity responsible for reflection B could be caused by a compositional change but probably merely reflects the transition from brittle to ductile behaviour of quartz and feldspar rich crustal rock. The low strength region associated with the boundary might control the location of detachment surfaces such as proposed by Bosworth (1987).

7.5 Intrusion in the lower crust.

The travel time and amplitude behaviour of phases C1 and C2 are best explained by the occurrence of a high velocity layer (approx 7.1 km/s) at about 22 km depth with lower velocity (approx 6.7 km/s) normal crust below. Neither the thickness nor the lateral extent of this layer can be resolved by the refraction data. The most likely geological explanation for such a layer is the presence of a sill-like intrusive body, presumably of mantle origin, in the lower crust. Little can be said about the nature of this intrusion. It might consist of many thin layers of mafic material separated by normal lower crustal material, the fine structure of which is not resolvable by the seismic data available.

It is of interest to note that a mid-crustal magma body (MCMB) has been inferred to lie below Socorro on the Rio Grande rift (Olsen et al, 1982). The evidence for this feature comes (1) unusual S to S and S to P reflections from microearthquakes occurring over the body; (2) strong P-wave reflections observed on COCORP vertical reflection profiles; and (3) unusually strong wide-angle reflections on refraction profiles that are best explained by anomalously low S-wave velocity just beneath the reflector interface (Olsen et al, 1982). The P-wave velocity inferred for the MCMB is no different from that of the country rock. The low S-wave velocity has been interpreted as indicating the presence of partially molten material (Olsen et al, 1982).

More recent COCORP surveys have suggested that the Socorro MCMB is not unique. Unusually strong mid-crustal reflections have been observed on sections from Death Valley and eastern Nevada (Brown et al, 1987). These "bright spots" all have depths in the range 18 - 20 km which has led Brown et al (1987) to suggest that density or rheology is responsible for entrapping magmas as they migrate through the crust.

The higher velocity observed for the sill-like intrusion below the Kenya rift suggests it is quite different from the Rio Grande rift MCMB, the former being solid. The existence of large volumes of basic intrusive material in the crust is consistent with geological evidence. The Miocene plateau phonolites, because of their huge bulk, restricted time-range and the lack of quantitatively significant associations of related basic and intermediate rocks, pose a considerable petrogenetic problem (Williams, 1970). Isotopic evidence has suggested that they were formed by partial melting followed by fractional crystallisation of mantle derived material (Lippard, 1972). On the basis of evidence from phenocrysts Lippard suggested that the fractionation took place at relatively deep levels. Perhaps the high velocity layer observed in this study is the crystallised basic residue of the fractionation which gave rise to the Miocene plateau phonolites.

7.6 Crustal thickness below the rift.

The KRISP85 explosion data has indicated that the depth of the Moho (assumed here to be where the P-wave velocity increases to about 7.5 km/s) is about 34 km (below sea level) beneath the central sector of the rift. The continental crust is therefore approximately 36 km thick beneath the apex of the Kenya dome. This compares with crustal thicknesses of about 44 km for the western flank below Kaptagat (Maguire and Long, 1976) and 42 km for the eastern flank below Nairobi (Bonjer et al, 1970; Herbert and Langston, 1985) (Fig. 1.6). This implies moderate crustal attenuation (about 6 km) below the rift. This is consistent with Swain (1979) who concluded on the basis of regional gravity data that a crustal thickness of less than 35 km below the apex of the Kenya dome would imply either an unreasonably low density contrast (<0.3 g/cm^3) between upper mantle and lower crustal material or gross over compensation of the rift. Previous estimates for the crustal thickness below the rift are 36 km for Southern Kenya (Rykounov et al, 1972) and 18.5 km for N.Kenya (Griffiths et al, 1971). If the interpretation of Griffiths et al (1971) is correct then the KRISP85 result demonstrates drastic thinning of the crust along the rift axis from the centre of the Kenya dome towards Lake Turkana. This would imply that the isostatic compensation of the Kenya topographic dome may be achieved by crustal thickening as well as low density upper mantle material. Swain (1979) suggested that the upper mantle low density material might contribute as little as 40 mgals to the observed 140 mgals north-south charge in the gravity field of the compensation between the equator and Lake Turkana. He concluded that the remainder could be explained by about 8 km of crustal thinning along the rift axis between the centre of the dome and Lake Turkana.

The apparent velocity of about 7.5 km/s obtained from the BA1 shot of KRISP85 is consistent with asthenospheric upwelling giving rise to a lower than normal upper mantle velocity. However, it should be noted that this is an apparent velocity and an appreciable Moho dip (say > 2°) would result in the actual velocity being at least 0.15 km/s different.

CHAPTER (VIII)

CONCLUSIONS AND RECOMMENDATIONS

The most important conclusions to be made from this study are:

(1) The depth to basement varies substantially along the axis of the rift. The thickness of rift infill varies from about 6 km below Lake Naivasha to about 2 km and 1.5 km below Lake Bogoria and Lake Magadi respectively.

(2) The P-wave velocity of 6.05 km/s obtained from the analysis of the Pg phase suggests that, at least below the KRISP85 NS-line, the rift infill is predominantly underlain by normal Precambrian metamorphic basement. No evidence has been obtained for the existence of an "axial intrusion" reaching to shallow levels below the rift. The localised high velocity zone inferred to underlie the KRISP85 NS-line adjacent to the northern end of Lake Nakuru suggests that in places the crystalline basement is pervaded by dense, high velocity intrusive material. Such zones are probably concentrated along the axis of the rift and contribute to the positive axial Bouguer anomaly observed over the rift. They do not, however, imply that any crustal separation has occurred.

(3) The relative residuals determined for the Lake Bogoria array indicate considerable lateral heterogeneity in the upper crust beneath the array. An Aki inversion has indicated the presence of two distinct low velocity zones which may be associated with magma chambers.

(4) The inferred position of the brittle-ductile transition zone beneath the rift has been shown to be coincident with an increase in P-wave velocity from about 6.2 km/s to about 6.45 km/s.

(5) A high velocity layer inferred for the lower crust (approx 22 km below sea level) may indicate the presence of a sill-like basic intrusion.

(6) The crustal thickness deduced for below the KRISP85 NS-line is about 36 km which implies that only moderate crustal attenuation has occurred beneath the central sector of the rift. If the interpretation of

the KRISP68 refraction data by Griffiths et al (1971) is correct, drastic crustal thickening must occur along the axis of the rift, southwards from Lake Turkana.

Suggestions for further work are:

(1) A study should be carried out on the amplitudes of the teleseismic arrivals recorded by the Lake Bogoria array. If it could be demonstrated that the low velocity zones indicated by the Aki inversion are also zones of higher than normal attenuation this would support the magma chamber hypothesis.
However, given that the typical wavelength of teleseismic waves is of the same order as the widths of the low velocity zones, any attenuation occurring might not be detectable. Such a study would have more chance of success if the seismic signal used was of shorter wavelength. Seismic energy from shots or microseismic activity might be attenuated appreciably by the low velocity zones.

(2) The depth to basement has been found to increase both northwards and southwards from Lake Bogoria. This is in accordance with the low angle detachment model proposed by Bosworth et al (1986) who suggested that the area is the site of an "accommodation zone". If this is true it should have a complex wrench and oblique-slip faulting history. A few seismic reflection lines across this area (NS and EW) might resolve whether or not this type of tectonism exists.

(3) A small scale 2-D gravity survey (measurements on a 2 km grid) over the high velocity zone inferred to lie beneath the NS-line might resolve its lateral and vertical extent. Seismic control from one or more short refraction lines would allow a more unique interpretation.

APPENDIX A

FIRST ARRIVAL TIMES

(1) KRISP85

Line-NS   Shot-BA1

Site	Range(km)	Time(secs)	±	Site	Range(km)	Time(secs)	±
NS41	54.71	10.23	0.01	NS23	113.28	19.96	0.1
NS40	57.53	10.87	0.03	NS20	123.76	21.77	0.04
NS39	60.23	11.40	0.03	NS19	127.31	22.35	0.02
NS38	64.25	12.02	0.03	NS18	129.99	22.86	0.02
NS37	67.00	12.50	0.02	NS17	132.63	23.23	0.04
NS34	77.04	14.18	0.04	NS16	136.44	23.72	0.03
NS33	80.68	14.83	0.03	NS13	147.48	25.56	0.05
NS31	87.11	15.93	0.1	NS55	264.69	41.68	0.05
NS30	91.05	16.63	0.05	NS54	267.89	42.20	0.05
NS29	94.58	17.15	0.05	NS53	270.39	42.15	0.06
NS28	97.79	17.65	0.04	NS51	275.99	43.17	0.03
NS27	100.42	18.12	0.04	NSMAG	277.86	43.45	0.05
NS26	104.14	18.51	0.02				
NS25	106.91	18.95	0.05				
NS24	110.78	19.45	0.1				

Line-NS Shot-BA2

Site	Range(km)	Time(secs)	±	Site	Range(km)	Time(secs)	±
NS47	28.19	6.12	0.01	NS30	89.49	16.38	0.05
NS46	29.47	6.40	0.02	NS29	93.02	16.89	0.04
NS45	36.52	7.42	0.01	NS28	96.24	17.44	0.1
NS44	43.37	8.73	0.02	NS27	98.87	17.87	0.1
NS43	48.35	9.16	0.01	NS23	111.73	19.81	0.05
NS41	53.16	9.97	0.01	NSELM	119.30	20.96	0.03
NS40	55.98	10.56	0.05	NS20	122.21	21.40	0.01
NS39	58.69	11.06	0.01	NS19	125.75	22.00	0.01
NS38	62.71	11.74	0.04	NS18	128.43	22.64	0.01
NS37	65.45	12.24	0.01	NS17	131.08	23.07	0.03
NS36	69.68	12.88	0.01	NS16	134.88	23.52	0.05
NS35	72.75	13.42	0.02	NS13	145.92	25.35	0.02
NS34	75.49	13.89	0.02				
NS33	79.13	14.58	0.02				
NS32	82.81	15.27	0.05				

Line-NS Shot-NAI

Site	Range(km)	Time(secs)	±	Site	Range(km)	Time(secs)	±
NS45	121.52	21.41	0.02	NS23	46.01	9.22	0.02
NS44	114.63	20.18	0.05	NS22	43.32	8.78	0.04
NS43	109.39	19.31	0.06	NS21	40.10	8.20	0.06
NS42	107.44	19.04	0.02	NS20	35.54	7.49	0.02
NS41	104.64	18.59	0.03	NS19	31.98	7.02	0.02
NS40	101.96	18.06	0.04	NS18	29.30	6.64	0.01
NS39	99.23	17.67	0.08	NS17	26.65	6.14	0.02
NS37	92.41	16.46	0.05	NS16	22.87	5.40	0.01
NS36	88.19	15.77	0.06	NS15	19.24	4.77	0.01
NS34	82.35	14.86	0.04	NS13	11.89	3.46	0.01
NS33	78.71	14.34	0.02	NS11	6.21	1.78	0.01
NS32	74.98	13.76	0.05	NS09	2.40	0.97	0.01
NS30	68.29	12.69	0.05	NS08	4.84	1.59	0.01
NS29	64.72	12.18	0.03	NS07	7.66	2.49	0.01
NS28	61.52	11.64	0.05	NS05	14.57	3.78	0.02
NS27	58.89	11.19	0.05				

Line-NS Shot-CHE

Site	Range(km)	Time(secs)	±	Site	Range(km)	Time(secs)	±
NS45	16.93	3.94	0.01	NS36	16.51	4.12	0.01
NS43	4.96	1.09	0.01	NS35	19.59	4.69	0.05
NS40	3.19	1.16	0.01	NS34	22.33	5.11	0.05
NS39	5.64	1.76	0.01	NS33	25.97	5.70	0.05
NS38	9.76	2.77	0.01	NS18	75.37	13.95	0.03
NS37	12.29	3.36	0.02				

Line-NS Shot-SOL

Site	Range(km)	Time(secs)	±	Site	Range(km)	Time(secs)	±
NS41	9.74	2.77	0.01	NS37	3.67	1.29	0.01
NS40	7.61	2.21	0.02	NS36	7.33	2.26	0.02
NS39	5.16	1.68	0.02	NS34	12.91	3.53	0.02
NS38	4.22	1.47	0.02	NS33	16.52	4.16	0.03

Line-NS Shot-ELM

Site	Range(km)	Time(secs)	±	Site	Range(km)	Time(secs)	±
NS23	8.93	2.97	0.1	NS19	8.50	2.75	0.03
NS22	6.77	2.53	0.1	NS18	11.05	3.38	0.01
NS21	5.58	2.31	0.1	NS17	13.16	3.72	0.05
NS20	5.59	2.07	0.05	NS16	16.99	4.43	0.05

Line-NS Shot-MAG

Site	Range(km)	Time(secs)	±	Site	Range(km)	Time(secs)	±
NS19	150.68	25.54	0.05	NS55	14.62	3.03	0.01
NS18	148.05	25.15	0.05	NS53	7.72	1.77	0.01
NS13	130.68	22.40	0.05	NS52	4.79	1.17	0.01
NS03	99.71	17.46	0.05	NS51	1.90	0.59	0.01
NS57	19.49	4.22	0.01				

Line-EW Shot-EWA

Site	Range(km)	Time(secs)	±	Site	Range(km)	Time(secs)	±
EW48	25.08	5.05	0.01	EW36	44.04	5.32	0.05
EW47	26.91	5.32	0.02	EW35	45.41	8.68	0.05
EW46	28.95	5.68	0.03	EW30	52.21	9.99	0.02
EW45	30.91	6.05	0.03	EW29	52.86	10.14	0.02
EW41	37.81	7.28	0.06	EW27	55.37	10.47	0.02
EW40	39.43	7.70	0.02	EW26	56.56	10.50	0.02
EW39	40.40	7.82	0.01	EW25	57.79	10.56	0.02
EW38	41.59	7.99	0.06	EW24	59.08	10.75	0.02
EW37	43.00	8.13	0.04				

Line-EW Shot-NTU

Site	Range(km)	Time(secs)	±	Site	Range(km)	Time(secs)	±
EW41	0.09	0.07	0.01	EW40	1.58	1.07	0.01
EW43	3.35	1.16	0.03	EW38	3.75	1.78	0.01
EW45	6.98	2.50	0.02	EW36	6.21	2.51	0.02
EW46	9.05	2.89	0.01	EW35	7.57	2.79	0.02
EW49	21.24	4.69	0.05	EW34	8.50	3.00	0.02
EWEWA	37.82	7.47	0.03				

Line-EW Shot-SU1

Site	Range(km)	Time(secs)	±	Site	Range(km)	Time(secs)	±
EW21	1.17	0.67	0.02	EW27	8.66	2.90	0.03
EW22	2.43	1.20	0.02	EW29	11.17	3.32	0.02
EW24	4.96	1.73	0.02	EW19	1.31	0.68	0.01
EW25	6.24	2.08	0.02	EW18	2.69	1.21	0.03
EW26	7.47	2.56	0.03				

Line-EW Shot-MAR

Site	Range(km)	Time(secs)	±	Site	Range(km)	Time(secs)	±
EW00	0.04	0.07	0.01	EW03	3.77	1.43	0.03
EW01	1.23	0.71	0.01	EW04	5.01	1.74	0.1
EW02	2.53	1.07	0.04				

(2) KRISP75

Line-HB Shot-BAN

Site	Range(km)	Time(secs)	±	Site	Range(km)	Time(secs)	±
1	41.47	8.16	0.2	14	30.56	6.25	0.02
2	40.69	8.04	0.2	15	29.87	6.46	0.06
3	39.89	7.92	0.2	16	29.05	6.17	0.02
4	38.59	7.92	0.12	17	28.31	6.11	0.04
5	37.84	7.84	0.12	18	27.47	6.06	0.1
6	37.16	7.80	0.12	19	26.73	6.00	0.2
7	36.36	7.54	0.2	20	25.93	5.92	0.2
10	33.67	6.81	0.2	27	19.74	5.00	0.2
11	32.84	6.61	0.06	28	17.25	4.56	0.06
12	32.03	6.75	0.02	30	15.70	4.27	0.2
13	31.27	6.65	0.02				

Line-HB Shot-BAS

Site	Range(km)	Time(secs)	±	Site	Range(km)	Time(secs)	±
1	30.35	6.79	0.06	14	19.48	4.76	0.1
2	29.58	6.46	0.06	15	18.78	4.89	0.1
5	26.73	6.28	0.1	16	17.98	4.69	0.02
6	26.04	6.15	0.1	17	17.25	4.61	0.2
7	25.25	5.91	0.1	18	16.43	4.46	0.02
9	23.45	5.85	0.05	21	13.21	4.23	0.06
10	22.55	5.54	0.1	22	12.56	4.07	0.1
11	21.77	5.15	0.1	24	10.95	4.00	0.2
12	20.97	5.28	0.1	26	9.45	3.25	0.08
13	20.20	5.02	0.1	27	8.63	3.02	0.08

Line-HB Shot-HAN

Site	Range(km)	Time(secs)	±	Site	Range(km)	Time(secs)	±
1	0.26	0.26	0.01	14	11.05	2.84	0.1
2	0.85	0.28	0.01	15	11.74	2.71	0.1
3	1.64	0.49	0.01	16	12.57	2.98	0.04
4	2.96	0.80	0.01	17	13.36	3.14	0.2
5	3.72	1.05	0.04	18	14.24	3.84	0.2
6	4.42	1.70	0.06	19	15.02	3.92	0.2
7	5.20	1.72	0.06	21	17.23	4.80	0.6
10	7.88	2.58	0.1	22	17.87	5.12	0.6
11	8.89	2.42	0.1	23	18.68	5.38	0.6
12	9.69	2.23	0.1	24	19.47	5.91	0.6
13	10.39	2.53	0.1				

Line-HB Shot-HAS

Site	Range(km)	Time(secs)	±	Site	Range(km)	Time(secs)	±
1	11.31	2.90	0.01	10	18.81	4.41	0.2
2	11.96	2.92	0.1	12	20.09	4.41	0.2
3	12.68	3.08	0.01	13	20.86	4.49	0.2
4	14.03	3.57	0.4	14	21.59	4.72	0.2
5	14.79	3.73	0.4	15	22.28	4.55	0.2
6	15.49	4.27	0.4	16	23.07	4.84	0.1
7	16.22	3.84	0.4	17	23.80	5.00	0.2
9	17.95	4.25	0.1	21	28.02	6.40	0.4

APPENDIX B

DESCRIPTIONS OF COMPUTER PROGRAMS

Introduction.

This appendix consists of brief descriptions of the computer programs cited in the text and listed on microfiche in the back pocket of this thesis. These programs have been written in FORTRAN-77 for use on the Leicester University DEC VAXcluster. Many of the programs thus include statements and syntax peculiar to VAX-extended FORTRAN-77. Modifications may thus be necessary for use in other hardware environments.

Seismic Data Processing System.

SDPS4 is version 4 of the seismic data processing systems developed at Leicester University for the handling and processing of long range seismic refraction and earthquake data. Several programs written by the author have been incorporated into this system. A broad outline of the programs available within the SDPS4 system is as follows:

(1) Programs for conversion from other formats to SDPS4 format.

(2) Editing programs used for the input of header information, trace deletion, file merging, resampling of traces, etc.

(3) Time signal analysis programs used for the decoding of time signals.

(4) Filtering programs including frequency, polarisation and velocity filtering algorithms.

(5) Data dumping programs allowing header information and trace data to be dumped to a output file which can be examined at the terminal or printed.

(6) Plotting programs, using GHOST80 graphical subroutines, which enable seismograms to be plotted at various plotting devices. These include several routines for the plotting of record sections.

(7) Picking programs designed to aid the picking of phase arrivals times.

A detailed description of these programs is given in the system's User Manual (Higham, 1987).

Program GATOMG (SDPS4).

The wow and flutter associated with analogue recording result from tape transport speed inaccuracies and oscillator instabilities (for frequency-modulated recordings). After digitisation, the recorded time signal must be analysed and the nominal sampling frequency corrected for. The correction factor is described here as the "stretch factor".

Program GATOMG is designed to perform the decoding of the Omega binary coded decimal timing signal (Chapter 2). It is normally used on individual "Geostore files" which, of course, still include the Omega time code. The following operations are performed: (1) the calculation a stretch factor for the time series; (2) the decoding of the B.C.D. signal; (3) the absolute timing of the first sample; (4)the deletion of auxiliary channels and (5) the gating of seismograms to a specified time or a reducing velocity relative to the shot instant.

The above are carried out as follows:

(1) The noise level characteristics of the signal are analysed by subroutine NOISLV.
(2) The start of the first minute code is found by subroutine NOBITS. The Omega time signal comprises a period of 48 seconds of bit repetition every second followed by a period of 12 seconds with "no bits". The start of the first minute is found by looking for the end of the first period with "no bits".
(3) The leading edge of 20 consecutive seconds are stacked (subroutine STACK) assuming 9 different sampling frequencies around the supposed one. Each stack is cross-correlated against an ideal step function (subroutine CRCOR). The stack giving the maximum cross-correlation peak determines the nearest integer sampling frequency to the actual.
(4) The relative timing of the maximum peak obtained in (3) is found by carrying out least squares analysis (subroutine LINFIT) on the cross-correlation function to either side of the peak. The inter- ception point of the 2 lines determines the precise location of the peak in the time series (accurate to about 0.1 times the nominal sampling interval).
(5) The procedures outlined in (2), (3) and (4) are repeated later in the record. The time difference between the cross-corelation peaks is then calculated in terms of samples. The ratio of this time to the actual time (known from the Omega time signal) is the stretch factor.
(6) The B.C.D. Omega time signal is then decoded by determining the logic of the 48 bits (subroutine LOGIC) and converting these to decimals (subroutine BINDEC).
(7) As the stretch factor and time of the first leading edge of the first minute have now been determined, the calculation of the time of the first sample of the time series is straight forward. Gating and trace deletion are then performed (subroutine GATE) as specified by the user.

Program ACSHIFT (SDPS4).

This program was written to remove the spurious, 5 Hz, A.C. component introduced during the digitisation of the KRISP85 refraction experiment Geostore recordings. This was achieved by stacking the first 10 cycles of the contaminated record, which are in the "quiet period" of the seismogram i.e. before the arrival of shot generated signal. The amplitudes of the resulting stacked cycle were then divided by 10 and were subtracted along the whole trace. This procedure was only effective if the amplitude of the seismic noise was small compared with the amplitude of the 5 Hz, A.C. component.

Program PHASECOR (SDPS4).

This program calculates the cross-correlation function between a specified phase from one seismogram and a second seismogram. It was designed to aid the determination of the relative arrival times of a seismic phase occurring on two seismograms when a high level of coherency is observed between the seismograms. The occurrence of the maximum value of the cross-correlation function value should coincide with the difference in the arrival times of the phase at the 2 recording stations.

The program is designed to be used interactively. The user first specifies which seismograms are to be cross-correlated. A specified portion of the seismogram containing the "cleaner" phase is displayed, sample by sample, on the screen so that the user can choose the precise time window during which the phase is observed. The chosen window is then cross-correlated with the second seismogram. The location of the peak of the cross-correlation function is ascertained and displayed. The user may optionally view the cross-correlation function.

Program REMODE (SDPS4).

REMODE polarisation filtering (Kanasewich, 1975) is performed by this program. The vertical and radial component seismograms from one recording station are selected by the user. Various filter parameters are then chosen and the filtering is performed according to the theory presented in Chapter 3. A SDPS4 output file is created which contains the unfiltered vertical and radial component traces of the selected station along with the REMODE filtered vertical and radial component traces.

Program PICK (SDPS4).

Program PICK allows a crude, sample by sample, screen dump of a portion of a chosen seismogram. This can be used to help with the picking of first arrival times. Once the portion of the seismogram has been viewed, the user is prompted for the sample number closest to the first break. The travel time associated with that sample number is then displayed on the screen. This program should, of course, always be used in combination with a record section of the shot in question.

Program TRUE (SDPS4).

The record section plotting routines of the SDPS4 system were modified to permit the plotting of true amplitude record sections. This was achieved by the inclusion of subroutines to calculate the relative amplitudes of seismograms given the scaling factors determined for the various recording systems (Chapter 3) and the gain setting for each seismogram. The gain setting and recording system type is contained in the header information block of each seismogram. Subroutines for each instrument type (GEOS1, GEOS2, MARS1, MARS2, WISC, DR100) calculated a scaling factor for each of the seismograms to be plotted which allowed for both the response of the instrument and the gain setting of the instrument. The amplitudes of the seismograms plotted were then multiplied by the scaling factors calculated. A further option was included in the record section plotting routines to allow the scaling of the "true" amplitudes determined, by the shot-receiver distance to a user specified power. This enabled all the seismograms, recorded over a wide range of distance, to be visible on the record section.

Programs HODOGR (SDPS4) and HODPLOT.

These programs are used in combination to plot hodograms (ground motion plots) from three component seismograms. HODOGR is used to generate ground displacements from ground velocities. This is carried out by the subroutine GNDMOT which calls NAG library routine D01GAF to perform the required numerical integration. Ground displacements for each component are written to an output file. This file is read by program HODPLOT which uses GHOST80 graphics subroutines to plot hodograms. The user has the option of a single plot (one plane of motion) or three plots (three planes of motion).

Program LINEFIT.

This program was written to plot reduced velocity plots, travel time plots or carry out least squares analysis on sections of travel time curves. It reads the necessary travel time information from a file containing all the travel time picks for a particular shot. Shot point and recording station coordinates and elevations are read from a file including all the coordinate and elevation information for the experiment. Shot-receiver distances are then calculated for the receiving stations for which travel times are available. A least squares straight line is fitted to the station coordinates and the perpendicular to this, through the shot point, is used to ascertain which travel times should be plotted to the left of the shot point and which to the right. The user then has the option of; (1) determining the apparent velocity and intercept time of chosen branches of the travel time curve by least squares; (2) producing a travel time plot for chosen receiving stations; or (3) producing a reduced velocity plot for chosen receiving stations. Elevation corrections may be optionally applied.

Program TIMTERM.

This program performs time-term analysis on refraction data. The author did not write the original version of this program but modified it for use in this study. Travel times and receiving station - shot point linkages are read from unit 9. The linkage information is assigned to the "time-term matrix" which is inverted by NAG library routine F01ACF. The refractor velocity may optionally be constrained to a desired value or be included in the inversion. Time-terms, refractor velocity (if required), observation residuals and standard errors are then calculated and output to the screen.

Program AMPLOT.

This program was written for the analysis and plotting of scaled distance vs seismic amplitude information. The scaled distances and amplitudes are read from unit 8. The user has the option of performing least squares analysis (subroutine LESQ) to calculate the shot point coupling parameter and gradient (a and b as described in Chapter 5) or plotting the data on a log - log graticule (subroutine PLOTER which calls GHOST80 graphics routines).

Program RELDEL.

All the absolute residuals measured (Chapter 6) were stored in separate files. Program RELDEL was used to convert the absolute residuals to relative residuals. If the event in question was observed by all the recording stations this simply involves the calculation of the mean absolute residual and subtraction of this value from all the absolute residuals. If the event was not fully observed the user is prompted for other events of similar back bearing and epicentral distance. These are then used to determine "predicted absolute residuals", in the manner described in Chapter 6. These take the place of the missing observations to calculate the mean absolute residual. The relative residuals for the event are then calculated as above.

Programs REGRID and CONTOUR.

These programs were written to allow contour maps to be plotted of any surface. They were used to contour the velocity perturbations calculated in Chapter 6. REGRID interpolates the observed data, read from unit 9, on to a regular grid using the GHOST80 routine REGRID. Program CONTOUR reads the regularly spaced data and draws a contour map using the GHOST80 routine CONTRA. Contour intervals are specified by the user.

APPENDIX C

RELATIVE RESIDUALS AND AKI INVERSION OUTPUT

The first part of this appendix consists of the relative residuals determined for the 46 teleseismic events recorded by the Lake Bogoria seismic network. Below the heading for each of the events a list is given of

(1) Station number

(2) Observation weight (1-3)

(3) Back bearing of event (degrees)

(4) Relative residual (secs)

(5) Slowness of event (secs/degrees)

for each observation of the event.

The second part of the appendix is the output of a single Aki inversion using the starting model of table 6.5. The star in the middle of grids for layers 2, 3 and 4 is the approximate centre of the array as shown in figure 6.1.

*EVENT19	VANUATU	6/10/85	PKIKP	
ST1	1	115.000	-0.071	1.883
ST2	2	115.000	-0.061	1.883
ST3	3	115.000	-0.126	1.883
ST4	2	115.000	-0.116	1.883
ST5	3	115.000	0.194	1.883
ST6	3	115.000	-0.161	1.883
ST7	2	115.000	-0.013	1.883
ST9	3	115.000	0.199	1.883
ST10	3	115.000	0.029	1.883
ST12	1	115.000	0.074	1.883
ST13	3	115.000	0.084	1.883
ST14	3	115.000	0.029	1.883

*EVENT39	VANUATU	28/11/85	PKIKP	
ST1	3	107.900	-0.013	1.888
ST2	3	107.900	-0.063	1.888
ST3	3	107.900	-0.163	1.888
ST4	3	107.900	-0.128	1.888
ST5	3	107.900	0.147	1.888
ST6	3	107.900	-0.123	1.888
ST7	3	107.900	-0.003	1.888
ST8	3	107.900	0.097	1.888
ST9	3	107.900	0.167	1.888
ST10	3	107.900	0.107	1.888
ST11	3	107.900	0.177	1.888
ST12	3	107.900	0.067	1.888
ST13	3	107.900	0.097	1.888
ST14	3	107.900	-0.023	1.888

*EVENT40	VANUATU	28/11/85	PKIKP	
ST1	3	107.800	-0.019	1.888
ST2	3	107.800	-0.071	1.888
ST3	3	107.800	-0.141	1.888
ST4	3	107.800	-0.151	1.888
ST5	3	107.800	0.189	1.888
ST6	3	107.800	0.121	1.888
ST7	3	107.800	-0.041	1.888
ST8	3	107.800	0.099	1.888
ST9	3	107.800	0.179	1.888
ST10	3	107.800	0.109	1.888
ST11	3	107.800	0.169	1.888
ST12	3	107.800	0.049	1.888
ST13	3	107.800	0.059	1.888
ST14	3	107.800	-0.011	1.888

*EVENT41	VANUATU	28/11/85	PKIKP	
ST1	3	107.700	0.035	1.888
ST2	3	107.700	-0.065	1.888
ST3	3	107.700	-0.115	1.888
ST4	1	107.700	-0.120	1.888
ST5	3	107.700	0.150	1.888
ST6	2	107.700	-0.120	1.888
ST7	3	107.700	-0.020	1.888
ST8	3	107.700	0.085	1.888
ST9	3	107.700	0.190	1.888
ST10	3	107.700	0.060	1.888
ST11	3	107.700	0.230	1.888
ST12	3	107.700	0.040	1.888
ST13	3	107.700	0.040	1.888
ST14	3	107.700	-0.040	1.888

*EVENT2	MEXICO	15/09/85	PKIKP	
ST1	3	294.000	0.002	1.888
ST2	3	294.000	-0.025	1.888
ST3	3	294.000	-0.060	1.888
ST4	3	294.000	-0.068	1.888
ST5	3	294.000	0.172	1.888
ST6	3	294.000	-0.140	1.888
ST7	3	294.000	-0.006	1.888
ST8	3	294.000	0.045	1.888
ST9	3	294.000	0.191	1.888
ST10	3	294.000	0.030	1.888
ST11	3	294.000	0.188	1.888
ST12	3	294.000	0.075	1.888

*EVENT10	MEXICO	21/09/85	PKIKP	
ST1	3	295.500	-0.041	1.842
ST2	3	295.500	-0.127	1.842
ST3	3	295.500	-0.084	1.842
ST4	3	295.500	-0.030	1.842
ST6	3	295.500	-0.086	1.842
ST8	3	295.500	0.012	1.842
ST10	3	295.500	0.052	1.842
ST11	3	295.500	0.159	1.842
ST13	3	295.500	0.059	1.842
ST14	3	295.500	0.001	1.842

*EVENT8	MEXICO	19/09/85	PKIKP	
ST1	3	296.300	-0.016	1.811
ST2	3	296.300	-0.013	1.811
ST3	3	296.300	-0.076	1.811
ST4	3	296.300	-0.049	1.811
ST6	3	296.300	-0.068	1.811
ST7	3	296.300	-0.021	1.811
ST8	3	296.300	0.065	1.811
ST9	3	296.300	0.151	1.811
ST10	3	296.300	0.076	1.811
ST11	3	296.300	0.075	1.811
ST12	3	296.300	0.079	1.811
ST13	3	296.300	0.053	1.811
ST14	3	296.300	-0.088	1.811

*EVENT23	EL SALV	12/10/85	PKIKP	
ST1	3	286.100	0.020	1.905
ST2	3	286.100	-0.104	1.905
ST3	3	286.100	-0.065	1.905
ST9	3	286.100	0.177	1.905
ST10	3	286.100	0.020	1.905
ST13	3	286.100	0.020	1.905
ST14	3	286.100	-0.003	1.905

*EVENT21	ALASKA	9/10/85	PKIKP	
ST1	3	10.800	0.025	1.938
ST3	3	10.800	-0.111	1.938
ST4	3	10.800	-0.025	1.938
ST7	3	10.800	-0.123	1.938
ST9	3	10.800	0.139	1.938
ST10	3	10.800	0.061	1.938
ST13	3	10.800	0.040	1.938
ST14	3	10.800	-0.013	1.938

*EVENT18	CANADA	5/10/85	PKIKP	
1ST2	3	349.900	-0.011	1.938
1ST3	3	349.900	-0.136	1.938
1ST4	3	349.900	-0.058	1.938
1ST5	3	349.900	0.192	1.938
1ST6	3	349.900	-0.096	1.938
1ST7	3	349.900	-0.054	1.938
1ST9	3	349.900	0.258	1.938
3ST10	1	349.900	0.053	1.938
1ST12	3	349.900	0.025	1.938
1ST13	3	349.900	0.016	1.938
1ST14	3	349.900	-0.023	1.938

*EVENT14	SOL IS	27/09/85	PKIKP	
ST1	3	123.200	-0.056	1.972
ST2	3	123.200	-0.065	1.972
ST4	3	123.200	-0.100	1.972
ST5	3	123.200	0.155	1.972
ST6	3	123.200	-0.185	1.972
ST8	3	123.200	0.053	1.972
ST9	3	123.200	0.199	1.972
ST11	3	123.200	0.184	1.972
ST12	3	123.200	0.079	1.972
ST13	3	123.200	0.082	1.972
ST14	3	123.200	0.069	1.972

*EVENT13	KER IS	26/09/85	PKIKP	
ST1	3	140.300	-0.042	1.872
ST2	3	140.300	-0.028	1.872
ST3	3	140.300	-0.170	1.872
ST4	3	140.300	-0.110	1.872
ST5	3	140.300	0.136	1.872
ST6	1	140.300	-0.104	1.872
ST8	3	140.300	0.041	1.872
ST11	3	140.300	0.115	1.872
ST12	3	140.300	0.105	1.872
ST13	3	140.300	0.136	1.872
ST14	3	140.300	-0.073	1.872

*EVENT27	FOX IS	25/10/85	PKIKP	
ST10	3	19.820	0.091	1.938
ST11	3	19.820	0.155	1.938
ST12	3	19.820	0.092	1.938
ST13	3	19.820	0.024	1.938
ST14	3	19.820	0.012	1.938

*EVENT42	TONGA	30/11/85	PKP2	
ST1	3	119.900	-0.011	3.610
ST2	3	119.900	-0.053	3.610
ST3	3	119.900	-0.129	3.610
ST4	3	119.900	-0.109	3.610
ST5	3	119.900	0.123	3.610
ST6	3	119.900	-0.104	3.610
ST7	3	119.900	-0.022	3.610
ST8	3	119.900	0.071	3.610
ST9	3	119.900	0.211	3.610
ST10	3	119.900	0.117	3.610
ST11	3	119.900	0.158	3.610
ST12	3	119.900	0.040	3.610
ST13	3	119.900	0.087	3.610
ST14	3	119.900	-0.015	3.610

*EVENT3	TONGA	15/09/85	PKP2	
ST1	3	123.300	-0.030	3.184
ST2	3	123.300	-0.027	3.184
ST3	3	123.300	-0.168	3.184
ST4	3	123.300	-0.113	3.184
ST5	3	123.300	0.145	3.184
ST6	3	123.300	-0.043	3.184
ST7	3	123.300	0.027	3.184
ST8	3	123.300	0.024	3.184
ST9	3	123.300	0.156	3.184
ST10	3	123.300	0.141	3.184
ST11	3	123.300	0.135	3.184
ST12	3	123.300	0.049	3.184

*EVENT4		15/09/85	PKP2	
ST1	3	120.800	-0.014	3.610
ST2	3	120.800	-0.069	3.610
ST3	3	120.800	-0.155	3.610
ST4	3	120.800	-0.073	3.610
ST5	3	120.800	0.103	3.610
ST6	3	120.800	-0.097	3.610
ST7	3	120.800	-0.007	3.610
ST8	3	120.800	0.075	3.610
ST9	3	120.800	0.231	3.610
ST10	3	120.800	0.075	3.610
ST11	3	120.800	0.140	3.610
ST12	3	120.800	0.027	3.610

*EVENT5	TONGA	16/09/85	PKP2	
ST1	3	118.200	-0.033	3.68
ST3	3	118.200	-0.173	3.68
ST4	3	118.200	-0.084	3.68
ST5	3	118.200	0.090	3.68
ST6	3	118.200	-0.127	3.68
ST7	3	118.200	-0.030	3.68
ST8	3	118.200	0.079	3.68
ST9	3	118.200	0.253	3.68
ST10	3	118.200	0.078	3.68
ST11	3	118.200	0.152	3.68
ST12	3	118.200	0.030	3.68

*EVENT31	TONGA	28/10/85	PKP2	
ST1	3	117.100	0.021	3.36
ST2	3	117.100	-0.042	3.36
ST3	3	117.100	-0.104	3.36
ST4	3	117.100	-0.112	3.36
ST7	3	117.100	-0.014	3.36
ST9	3	117.100	0.177	3.36
ST10	3	117.100	0.122	3.36
ST11	3	117.100	0.116	3.36
ST12	3	117.100	0.053	3.36
ST13	3	117.100	0.017	3.36
ST14	3	117.100	-0.026	3.36

*EVENT37	TONGA	26/11/85	PKHKP	
ST3	3	127.700	-0.085	2.69
ST5	3	127.700	0.134	2.69
ST6	3	127.700	-0.071	2.69
ST7	3	127.700	-0.020	2.69
ST8	3	127.700	0.074	2.69
ST9	2	127.700	0.171	2.69
ST10	3	127.700	0.106	2.69
ST11	3	127.700	0.152	2.69
ST12	3	127.700	0.073	2.69
ST13	3	127.700	0.044	2.69
ST14	3	127.700	-0.020	2.69

*EVENT45	TONGA	01/12/85	PKP2	
ST2	2	122.400	-0.052	3.44
ST3	2	122.400	-0.137	3.44
ST5	2	122.400	0.085	3.44
ST6	3	122.400	-0.062	3.44
ST7	3	122.400	0.034	3.44
ST8	3	122.400	0.051	3.44
ST10	3	122.400	0.088	3.44
ST11	3	122.400	0.102	3.44
ST12	3	122.400	-0.017	3.44
ST13	3	122.400	0.073	3.44
ST14	3	122.400	-0.019	3.44

*EVENT12	TONGA	26/09/85	PKP2	
ST1	1	119.900	-0.030	3.74
ST3	1	119.900	-0.175	3.74
ST4	2	119.900	-0.060	3.74
ST5	2	119.900	0.087	3.74
ST6	2	119.900	-0.155	3.74
ST8	2	119.900	0.089	3.74
ST9	2	119.900	0.216	3.74
ST13	2	119.900	0.061	3.74
ST14	2	119.900	-0.060	3.74

*EVENT15	TONGA	27/09/85	PKHKP	
ST1	3	128.300	0.005	2.69
ST2	3	128.300	0.007	2.69
ST4	2	128.300	-0.103	2.69
ST5	1	128.300	0.105	2.69
ST8	3	128.300	0.041	2.69
ST9	3	128.300	0.142	2.69
ST11	3	128.300	0.113	2.69
ST12	3	128.300	0.049	2.69
ST13	3	128.300	0.011	2.69
ST14	3	128.300	-0.005	2.69

*EVENT22	FIJI	12/10/85	PKHKP	
ST1	3	126.200	-0.062	2.76
ST2	3	126.200	0.006	2.76
ST3	3	126.200	-0.136	2.76
ST4	3	126.200	-0.118	2.76
ST6	3	126.200	-0.036	2.76
ST7	3	126.200	0.032	2.76
ST9	3	126.200	0.142	2.76
ST10	3	126.200	0.078	2.76
ST13	3	126.200	0.044	2.76
ST14	3	126.200	-0.015	2.76

*EVENT7	FIJI	18/09/85	PKHKP	
ST2	3	119.600	0.002	2.77
ST6	3	119.600	-0.042	2.77
ST7	3	119.600	0.004	2.77
ST9	3	119.600	0.176	2.77
ST10	3	119.600	0.106	2.77
ST11	3	119.600	0.111	2.77
ST12	3	119.600	0.048	2.77
ST13	3	119.600	0.090	2.77
ST14	3	119.600	0.012	2.77

*EVENT30	FIJI	27/10/85	PKHKP	
ST1	1	118.700	0.000	2.80
ST4	1	118.700	-0.107	2.80
ST7	1	118.700	0.042	2.80
ST9	1	118.700	0.221	2.80
ST11	1	118.700	0.180	2.80
ST12	1	118.700	0.031	2.80
ST13	1	118.700	0.026	2.80
ST14	1	118.700	-0.036	2.80

*EVENT20 JAVA 09/10/85 P

ST1	3	97.200	-0.094	6.005
ST2	3	97.200	0.112	6.005
ST3	3	97.200	-0.255	6.005
ST4	3	97.200	-0.052	6.005
ST6	3	97.200	0.100	6.005
ST7	3	97.200	0.178	6.005
ST9	3	97.200	0.063	6.005
ST10	3	97.200	0.081	6.005
ST13	3	97.200	0.066	6.005
ST14	3	97.200	-0.070	6.005

*EVENT35 JAVA 25/11/85 P

ST2	3	99.100	0.112	5.903
ST6	3	99.100	0.112	5.903
ST7	3	99.100	0.140	5.903
ST8	3	99.100	0.096	5.903
ST9	3	99.100	0.085	5.903
ST10	2	99.100	0.081	5.903
ST11	3	99.100	0.055	5.903
ST12	3	99.100	-0.100	5.903
ST13	3	99.100	0.073	5.903
ST14	3	99.100	-0.095	5.903

*EVENT44 INDIAN OCEAN 01/12/85 P

ST1	3	120.200	-0.041	8.606
ST2	3	120.200	0.093	8.606
ST3	3	120.200	-0.228	8.606
ST4	3	120.200	-0.150	8.606
ST5	3	120.200	0.069	8.606
ST6	3	120.200	0.153	8.606
ST7	3	120.700	0.102	8.606
ST8	3	120.700	0.096	8.606
ST9	3	120.700	0.159	8.606
ST10	3	120.700	-0.015	8.606
ST11	3	120.700	0.072	8.606
ST12	3	120.700	-0.040	8.606
ST13	3	120.700	0.136	8.606
ST14	3	120.700	-0.111	8.606

*EVENT28 BANDA SEA 25/10/85 P

ST2	3	97.000	0.093	4.652
ST3	3	97.000	-0.196	4.652
ST4	3	97.000	-0.078	4.652
ST7	3	97.000	0.148	4.652
ST9	3	97.000	0.083	4.652
ST11	3	97.000	0.044	4.652
ST12	3	97.000	-0.066	4.652
ST13	3	97.000	0.086	4.652
ST14	3	97.000	-0.032	4.652

*EVENT26 TIMOR 23/10/85 P

ST10	3	101.000	0.043	4.702
ST11	3	101.000	0.046	4.702
ST12	3	101.000	-0.043	4.702
ST13	3	101.000	0.054	4.702
ST14	3	101.000	-0.038	4.702

*EVENT38 RYUKYU 26/11/85 P

ST2	3	66.000	0.015	4.702
ST6	3	66.000	-0.040	4.702
ST7	3	66.000	0.023	4.702
ST8	3	66.000	0.050	4.702
ST9	1	66.000	0.019	4.702
ST10	3	66.000	0.093	4.702
ST11	1	66.000	0.142	4.702
ST12	2	66.000	-0.069	4.702
ST13	3	66.000	0.117	4.702
ST14	3	66.000	-0.063	4.702

*EVENT36 TAIWAN 26/11/85 P

ST2	3	67.500	-0.008	4.868
ST5	3	67.500	-0.042	4.868
ST6	3	67.500	-0.068	4.868
ST7	3	67.500	-0.017	4.868
ST8	3	67.500	0.074	4.868
ST9	3	67.500	0.013	4.868
ST10	3	67.500	0.087	4.868
ST11	3	67.500	0.079	4.868
ST12	3	67.500	-0.137	4.868
ST13	3	67.500	0.275	4.868
ST14	3	67.500	-0.084	4.868

*EVENT40 BONIN IS 03/12/85 P

ST2	2	62.400	-0.032	4.528
ST5	2	62.400	0.020	4.528
ST6	3	62.400	-0.037	4.528
ST7	3	62.400	0.034	4.528
ST8	3	62.400	0.113	4.528
ST9	3	62.400	0.029	4.528
ST10	3	62.400	0.103	4.528
ST11	2	62.400	0.110	4.528
ST12	3	62.400	-0.112	4.528
ST13	3	62.400	0.160	4.528
ST14	2	62.400	-0.073	4.528

*EVENT9 TAIWAN 20/09/85 P

ST2	3	65.500	0.017	4.846
ST6	3	65.500	-0.046	4.846
ST8	3	65.500	0.036	4.846
ST10	3	65.500	0.110	4.846
ST11	3	65.500	0.097	4.846
ST12	3	65.500	-0.083	4.846
ST13	3	65.500	0.165	4.846
ST14	3	65.500	-0.101	4.846

*EVENT43 CHINA 30/11/85 P

ST2	3	52.500	0.067	5.287
ST5	3	52.500	0.004	5.287
ST6	3	52.500	-0.093	5.287
ST7	2	52.500	-0.003	5.287
ST8	3	52.500	0.067	5.287
ST9	3	52.500	0.055	5.287
ST10	3	52.500	0.047	5.287
ST11	3	52.500	0.057	5.287
ST12	3	52.500	-0.049	5.287
ST13	3	52.500	0.141	5.287

*EVENT16	CRETE	27/09/85	P	
ST2	3	346.500	-0.100	8.84
ST4	3	346.500	0.033	8.84
ST5	3	346.500	0.080	8.84
ST6	3	346.500	-0.280	8.84
ST8	3	346.500	0.091	8.84
ST9	3	346.500	0.314	8.84
ST11	3	346.500	0.127	8.84
ST13	3	346.500	0.029	8.84

*EVENT29	ALGERIA	27/10/85	P	
ST1	3	326.200	0.000	7.89
ST2	3	326.200	-0.036	7.89
ST3	3	326.200	-0.013	7.89
ST4	3	326.200	-0.017	7.89
ST7	3	326.200	-0.145	7.89
ST9	3	326.200	0.315	7.89
ST10	3	326.200	-0.036	7.89
ST11	3	326.200	0.156	7.89
ST12	3	326.200	0.063	7.89
ST13	3	326.200	0.097	7.89
ST14	3	326.200	-0.106	7.89

*EVENT1	GREECE	07/09/85	P	
ST1	3	341.300	0.032	8.27
ST2	3	341.300	-0.140	8.27
ST3	3	341.300	-0.058	8.27
ST4	3	341.300	-0.000	8.27
ST5	3	341.300	0.067	8.27
ST6	3	341.300	-0.265	8.27

*EVENT17	YUGOSLAVIA	28/09/85	P	
ST2	3	344.900	-0.039	8.065
ST4	3	344.900	-0.011	8.065
ST5	3	344.900	0.039	8.065
ST6	3	344.900	-0.300	8.065
ST8	3	344.900	0.090	8.065
ST11	3	344.900	0.142	8.065
ST13	3	344.900	0.047	8.065
ST14	3	344.900	-0.125	8.065

*EVENT34	S SANDWICH	24/11/85	P	
ST2	3	207.400	-0.132	5.687
ST5	3	207.400	0.071	5.687
ST6	3	207.400	-0.030	5.687
ST7	3	207.400	-0.085	5.687
ST8	3	207.400	-0.070	5.687
ST10	3	207.400	-0.007	5.687
ST11	3	207.400	0.105	5.687
ST12	3	207.400	0.065	5.687
ST13	3	207.400	-0.038	5.687
ST14	2	207.400	-0.054	5.680

*EVENT33	S.A.R.	18/11/85	P	
ST1	3	230.300	0.151	4.382
ST2	3	230.300	-0.091	4.382
ST3	3	230.300	0.058	4.382
ST6	3	230.300	0.042	4.382
ST7	3	230.300	-0.083	4.382
ST10	3	230.300	0.081	4.382
ST11	3	230.300	0.117	4.382
ST12	3	230.300	0.102	4.382
ST13	3	230.300	-0.161	4.382
ST14	3	230.300	-0.122	4.382

*EVENT11	N.A.R.	22/09/85	P	
ST1	3	282.600	0.124	5.338
ST2	3	282.600	-0.022	5.338
ST3	3	282.600	-0.023	5.338
ST4	3	282.600	0.001	5.338
ST6	3	282.600	-0.132	5.338
ST8	3	282.600	0.017	5.338
ST11	3	282.600	0.113	5.338
ST12	3	282.600	0.059	5.338
ST13	3	282.600	0.040	5.338
ST14	3	282.600	-0.062	5.338

*EVENT32	M.A.R.	10/11/85	P	
ST3	2	274.400	0.056	6.243
ST4	2	274.400	-0.003	6.243
ST6	1	274.400	-0.120	6.243
ST7	1	274.400	-0.222	6.243
ST9	2	274.400	0.208	6.243
ST10	2	274.400	-0.152	6.234
ST11	2	274.400	0.193	6.234
ST12	2	274.400	0.068	6.234
ST13	2	274.400	-0.046	6.234

*EVENT24	M.A.R.	12/10/85	P	
ST1	3	271.000	0.063	6.424
ST2	3	271.000	-0.044	6.424
ST3	3	271.000	-0.083	6.424
ST7	2	271.000	-0.107	6.424
ST9	2	271.000	0.112	6.424
ST10	2	271.000	-0.113	6.424
ST12	3	271.000	0.187	6.424
ST14	3	271.000	-0.060	6.424

*EVENT25	TAJIK	13/10/85	P	
ST2	3	33.500	0.013	7.517
ST6	3	33.500	-0.096	7.517
ST7	3	33.500	-0.010	7.517
ST9	3	33.500	0.017	7.517
ST10	3	33.500	0.025	7.517
ST11	3	33.500	0.171	7.517
ST13	3	33.500	0.138	7.517
ST14	3	33.500	-0.022	7.517

ST1 1	ST2 2
-7.52	3.03
31	41
0.8097	0.7537
1.25	1.73
ST3 3	ST4 4
7.80	6.43
33	33
0.7254	0.7558
1.56	1.68
ST5 5	ST6 6
1.15	11.12
28	39
0.7471	0.7260
1.74	1.32
ST7 7	ST8 8
4.01	4.86
36	31
0.7125	0.7772
1.62	1.57
ST9 9	ST10 10
-12.68	11.84
38	39
0.7002	0.7284
1.50	1.63
ST11 11	ST12 12
-1.96	2.03
40	39
0.7840	0.7170
1.47	1.67
ST13 13	ST14 14
3.63	8.06
43	41
0.7978	0.7999
1.39	1.49

Layer 1

Legend:

Block number and station name
Velocity perturbation
Number of hits (rays)
Diagonal of the resolution matrix
Standard errors

Layer 2

Legend:

Block number and station name
Velocity perturbation
Number of hits (rays)
Diagonal of the resolution matrix
Standard errors

15 0	16 0	17 0	18 0	19 0	20 0	21 1	22 0	23 0	24 0	25 0
26 0	27 0	28 0	29 0	30 1	31 1	32 -1.61 5 0.8144 1.64	33 0	34 0	35 0	36 0
37 0	38 0	39 0	40 3	41 3	42 2.62 16 0.7787 1.43	43 0.18 33 0.8403 1.24	44 0.53 22 0.9046 0.97	45 0	46 0	47 0
48 0	49 0	50 1	51 8.51 8 0.7702 1.61	52 3.27 6 0.8142 1.40	53 3.11 23 0.8787 0.97	54 1.03 17 0.8763 1.15	55 1.58 40 0.9020 0.90	56 5.08 26 0.8625 1.17	57 1	58 0
59 0	60 0	61 2	62 2.27 24 0.9482 1.21	63 -3.16 24 0.8812 0.95	64 -3.61 7 0.8457 1.43	65 1.61 38 0.8679 1.01	66 7.41 9 0.7786 1.49	67 2	68 1	69 0
70 0	71 0	72 2	73 4.63 33 0.8188 1.38	74★ 0.14 25 0.8775 1.03	75 -0.65 35 0.8625 1.11	76 0.25 31 0.8443 1.33	77 2.21 13 0.7215 1.77	78 1	79 0	80 0
81 0	82 0	83 1	84 -3.46 7 0.7821 1.76	85 2.83 7 0.7880 1.80	86 -2.10 7 0.8082 1.73	87 -4.70 39 0.8343 1.32	88 -1.06 18 0.8620 0.99	89 7.23 11 0.8362 1.20	90 0	91 0
92 0	93 0	94 2	95 5.04 37 0.8393 1.42	96 0.89 18 0.8457 1.39	97 -3.39 42 0.8869 1.01	98 -2.78 25 0.8748 1.20	99 -1.55 8 0.7919 1.55	100 -3.34 20 0.6786 1.24	101 3	102 0
103 0	104 0	105 0	106 1	107 3	108 -2.37 15 0.8239 1.54	109 -4.68 21 0.8855 1.11	110 0	111 0	112 0	113 0
114 0	115 0	116 0	117 0	118 0	119 1	120 1	121 1	122 0	123 0	124 0

136	137	138	139	140	141	142	143	144	145	146
						-2.91				
0	0	0	0	2	2	5	1	0	0	0
						0.7924				
						1.54				
147	148	149	150	151	152	153	154	155	156	157
						-1.43				
0	0	1	3	1	4	7	1	0	0	0
						0.8860				
						1.39				
158	159	160	161	162	163	164	165	166	167	168
			3.14	-1.59	-3.77	0.83	3.60			
0	0	0	5	5	13	10	22	2	0	0
			0.7423	0.8396	0.8928	0.8575	0.8846			
			1.92	1.80	1.22	1.46	1.31			
169	170	171	172	173	174	175	176	177	178	179
			-1.87	-2.31	-3.67	-2.80	2.48	3.01		
0	1	3	5	9	25	33	36	28	3	1
			0.5691	0.8392	0.8670	0.8920	0.9122	0.9164		
			1.66	1.97	1.29	1.19	1.04	1.17		
180	181	182	183	184	185	186	187	188	189	190
		4.74		-1.23	-6.58	-3.87	-0.82	0.12	2.31	
0	0	6	3	28	18	32	22	17	8	1
		0.5380		0.8870	0.8903	0.9071	0.9355	0.7758	0.8423	
		1.91		1.19	1.19	1.10	1.31	1.60	1.81	
191	192	193	194	195 ★	196	197	198	199	200	201
		3.91	2.57	-3.15	-4.89	-4.59	-2.41			
0	2	5	15	31	26	28	22	2	3	1
		0.8663	0.8931	0.9110	0.9142	0.9134	0.8563			
		2.00	1.70	1.50	1.04	1.17	1.57			
202	203	204	205	206	207	208	209	210	211	212
				-4.49	-3.27	-2.36	2.69	-2.63		
0	0	3	3	22	10	15	19	6	4	0
				0.9108	0.8451	0.9000	0.8823	0.8031		
				1.23	1.79	1.66	1.22	1.82		
213	214	215	216	217	218	219	220	221	222	223
			-1.27	-2.14	0.64	-1.94	0.54	0.87	7.39	
0	2	4	15	26	27	26	25	21	7	0
			0.8480	0.8537	0.8985	0.9238	0.8690	0.7108	0.7740	
			1.99	1.91	1.63	1.45	1.89	1.62	1.87	
224	225	226	227	228	229	230	231	232	233	234
				3.84	-1.60	-1.98				
0	0	2	1	7	13	28	2	1	2	1
				0.8755	0.8660	0.8551				
				1.79	1.38	1.29				
235	236	237	238	239	240	241	242	243	244	245
0	0	1	0	1	1	3	2	1	0	0

Layer 3

Legend:

Block number and station name
Velocity perturbation
Number of hits (rays)
Diagonal of the resolution matrix
Standard errors

257 0	258 0	259 3	260 3	261 2	262 4	263 3	264 2	265 0	266 0	267 0
268 0	269 0	270 1	271 1	272 2	273 -1.37 5 0.7923 1.86	274 3	275 1	276 0	277 0	278 0
279 0	280 1	281 3	282 4	283 -0.26 6 0.8596 1.64	284 1.18 14 0.9073 1.15	285 -1.74 6 0.8634 1.60	286 0.58 20 0.9295 0.94	287 4	288 2	289 0
290 1	291 3	292 3.30 5 0.5542 1.77	293 0.91 6 0.5925 1.81	294 3.14 9 0.8766 1.56	295 -0.02 17 0.9032 1.17	296 -0.88 24 0.9239 1.11	297 -0.80 31 0.9349 1.03	298 -1.16 28 0.9465 0.81	299 3	300 3
301 0	302 1	303 3	304 -2.01 6 0.9008 1.32	305 3.22 25 0.9108 1.14	306 1.07 21 0.9450 0.73	307 -6.33 14 0.9276 1.03	308 -0.11 26 0.9284 1.05	309 2.02 23 0.9608 0.73	310 -1.14 12 0.9231 1.15	311 1
312 2	313 3	314 -2.97 7 0.8537 1.62	315 -3.62 5 0.5442 2.14	316 ★ -1.61 10 0.9168 1.17	317 2.42 15 0.9295 1.03	318 -2.46 15 0.8119 1.23	319 -3.39 18 0.9403 1.42	320 1.99 7 0.7850 1.88	321 4	322 3
323 0	324 1	325 2	326 3	327 1.37 16 0.9180 1.03	328 1.94 19 0.9490 0.74	329 -1.59 18 0.9368 1.01	330 -3.36 23 0.9355 0.90	331 -3.19 8 0.8688 1.52	332 4	333 3
334 1	335 2	336 3.23 7 0.8681 1.96	337 -5.91 8 0.8022 2.00	338 1.25 12 0.9133 1.04	339 3.91 12 0.8599 1.54	340 -3.75 12 0.8716 1.51	341 -2.12 26 0.9242 1.00	342 0.69 20 0.9092 1.06	343 -1.89 14 0.8911 1.27	344 4
345 0	346 1	347 2	348 1	349 0.09 12 0.8843 1.22	350 -2.73 10 0.8568 1.55	351 0.40 20 0.9105 1.19	352 3	353 3	354 1	355 2
356 0	357 0	358 1	359 0	360 1	361 1	362 1.22 9 0.8270 1.59	363 -1.10 7 0.8681 1.45	364 1	365 1	366 1

Layer 4

Legend:

Block number and station name
Velocity perturbation
Number of hits (rays)
Diagonal of the resolution matrix
Standard errors

REFERENCES

Achauer, U., Greene, L., Evans, J.R. and Iyer, H.M., 1986. Nature of the Magma Chamber Underlying the Mono Craters Area, Eastern California, as determined from Teleseismic Travel Time Residuals. J. Geophys. Res., 91, 13873 - 13891.

Aki, K., Christoffersson, A. and Husebye, E.S., 1977. Determination of the three-dimensional seismic structure of the lithosphere. J. Geophys. Res., 82, 277 - 296.

Aki, K. and Richards, P.G., 1980. Quantitative Seismology, Theory and Methods (V. 1 and 2). W. H. Freeman and Company.

Anderssen, R.S. and Cleary, J.R., 1980. Estimation of PKP times from ISC data. Phys. Earth Planet. Inter., 23, 207 - 214.

Avedik, F., 1979. Preliminary results of a seismic refraction study in the Meriadzek - Trevelyan area, Bay of Biscay. DSDP Initial Rept. Leg 48, 1015 -1023.

Baker, B.H., 1958. Geology of the Magadi area. Kenya Geol. Survey. Rept. 42.

Baker, B.H., 1963. Geology of the Baragoi area. Kenya Geol. Survey. Rept. 61.

Baker, B.H. and Wohlenberg, J., 1971. Structure and evolution of the Kenya Rift Valley. Nature, 229, 538 - 542.

Baker, B.H., Mohr, P.A. and Williams, L..J., 1972. Geology of the East African rift system of Africa. Geol Soc of Am., Special paper 136.

Baker, M.R., Braile, L.W. and Smith, R.B, 1982. Amplitude and phase normalisation of seismograms from multiple seismograph recording systems for the Yellowstone-Snake River Plain seismic refraction experiment. J. Geophys. Res., 87, 2611 - 2618.

Bally, A.W., 1982. Musings over sedimentary basin evolution. Phil. Trans. R. Soc. Lond., A 305, 325 - 328.

Bamford, S.A.D., 1972. An example of the iterative approach to time-term analysis. Geophys. J. R. astr. Soc., 31, 365 - 372.

Banks, R.J. and Swain, C.J., 1978. The isostatic compensation of East Africa. Proc. R. Soc. Lond., A 364, 331 - 352.

Banks, R.J. and Beamish, D., 1979. Melting in the crust and upper mantle beneath the Kenya rift: Evidence from geomagnetic deep sounding experiments. J. Geol. Soc. Lond., B 136, 225 - 233.

Berckhemer, H., 1976. Standard Equipment for Deep-Seismic Sounding. In Explosion Seismology in Central Europe, Data and Results. (ed. Giese, P., Prodehl, C. and Stein, A.), 115 - 118. Springer_Verlag, Berlin.

Berry, M.J. and West, G.F., 1966. An interpretation of the first arrival data of the Lake Superior experiment by the time-term method. Bull. Seism. Soc. Am., 56, 141 - 171.

Betchel, T.D., Forsyth, D.W. and Swain, C.J., 1987. Mechanisms of isostatic compensation in the vicinity of the East African Rift, Kenya. Geophys. J. R. astr. Soc., 90, 445 - 465.

Bonjer, K.P., Fuchs, K. and Wohlenberg, J., 1970. Crustal structures of the East African Rift System from spectral response ratios of long period body waves. Z. Geophysik., 36, 287 - 297.

Bott, M.H.P., Formation of sedimentary basins of the graben type by the extension of the continental crust. Tectonophysics, 36, 205 - 222.

Bosworth, W., 1985. Geometry of propagating continental rifts. Nature, 316, 625 - 627.

Bosworth, W., Lambiase, J. and Keisler, R., 1986. A new look at Gregory's rift: The structural style of continental rifting. E. O. S., 67, n.29, 577 - 582.

Bosworth, W., 1987. Off-axis volcanism in the Gregory rift, East Africa: Implications for models of continental rifting. Geology, 15, 397 - 400.

Bott, M.H.P. and Mithen, D.P., 1983. Mechanisms of graben formation - the wedge subsidence hypothesis. Tectonophysics, 94, 11-22.

Braile, L.W., 1977. Interpretation of crustal velocity gradients and Q structure using amplitude-corrected seismic refraction profiles. In The Earth's crust: Its nature and physical properties. Geophys. Monogr. Ser., 20. (ed. Heacock, J.G.), 427 - 439. AGU, Washington, DC.

Brown, L., Wille, D., Zheng, L., DeVoogd, B., Mayer, J., Hearn, T., Sanford, W., Caruso, C., Zhu, T.F., Nelson, D., Potter, C., Hauser, E., Klemperer, S., Kaufman, S. and Oliver, J., 1987. COCORP: new perspective on the deep crust. Geophys. J. R. astr. Soc., 89, 47 - 54.

Bullard, E.C., 1936. Gravity measurements in East Africa. Phil. Trans. R. Soc. Lond., A 135, 265 - 281.

Bullen, K.E., 1963. An introduction to the theory of seismology. Cambridge University Press, Cambridge.

Cerveny, V., 1966. On some kinematic and dynamic properties of reflected and head waves in the case of a layered overburden. Geofyskalni Sbornik, Academia, Prague., 14, 105 - 179.

Cerveny, V., Langer, J. and Psencik, I., 1974. Computation of geometric spreading of seismic body waves in laterally inhomogeneous media with curved interfaces. Geophys. J. R. astr. Soc., 38, 9 - 19.

Cerveny, V., Molotkov, I.A. and Psencik, I., 1977. Ray Method in Seismology. University of Karlova, Prague.

Cooke, P.A.V., 1987. An earthquake study in the Kenyan rift valley. Abstract. Geophys. J. R. astr. Soc., 89, 480.

Crampin, S., Mcgonigle, R., and Ando, M., 1986. Extensive-dilatancy anisotropy beneath Mount Hood, Oregon and the effect of aspect ratio on seismic velocities through aligned cracks. J. Geophys. Res., 91, 12703 - 12710.

Dalheim, H. and Davis, P.M., 1986. Deep velocity structure beneath the East African rift and waveform analysis using teleseismic events. Abstract. E.O.S., 67 No.44, 1103.

Darracott, B.W., Fairhead, J.D. and Girdler, R.W., 1972. Gravity and magnetic surveys in northern Tanzania and southern Kenya. Tectonophysics, 15, 131 - 141.

Dunkelman, T.J., 1986. The structural and stratigraphic evolution of Lakc Turkana, Kenya, as deduced from multichannel reflection data. M.Sc. Thesis. Duke University.

Ellsworth, W.L. and Koyanagi, R.Y., 1977. Three-dimensional crust and mantle structure of Kilauea Vilcano, Hawaii. J. Geophys. Res., 82, 5379 - 5394.

Emerick, C.M. and Duncan, R.A., 1982. Age progressive volcanism in the Comores Archilpelago, western Indian Ocean and implications for Somali plate tectonics. Earth. Planet. Sci. Lett., 60, 415 - 428.

Evans, T.R. and Tammemagi, H.Y., 1974. Heat flow and heat production in northeast Africa. Earth. Planet. Sci. Lett., 23, 349 - 356.

Evans, J.R., 1986. Teleseismic Traveltime Residual Analysis System: A User's Manual. Unpublished U.S.G.S. document.

Fairhead, J.D., 1976. The structure of the lithosphere beneath the Eastern rift, East Africa, deduced from gravity studies. Tectonophysics, 30, 269 - 298.

Fairhead, J.D. and Stuart, G.D., 1982. The seismicity of the East African Rift System and comparison with other continental rifts. In Continental and oceanic rifts. (ed. Palmason, G.), 41 - 61. Am. Geophys. Union.

Freund, R., 1970. Plate tectonics of the Red Sea and East Africa. Naturc, 228, 453.

Girdler, R.W., Fairhead, J.D., Searle, R.C. and Sowerbutts, W.T.C., 1969. The evolution of rifting in Africa. Nature, 244, 1178 - 1182.

Green, W.V. and Meyer, R.P., 1986. KRISP 85 2-D teleseismic recording across the Gregory rift, Kenya. Abstract. E.O.S., 67 No.44, 1103.

Griffiths, D.H., King, R.E., Khan, M.A. and Blundell, D.J., 1971. Seismic refraction line in the Gregory rift. Nature, 229, 69 - 71.

Griffiths, P.S., 1977. The geology of the area around Lake Hannington and the Perkerra River, Rift Valley Province, Kenya. Ph.D. Thesis. University of London.

Grant, F.S and West, G.F., 1965. Interpretation Theory in Applied Geophysics. McGraw-Hill.

Gumper, F. and Pomeroy, P.W., 1970. Seismic wave velocities and earth structure on the African continent. Bull. Seism. Am., 60, 651 - 668.

Hamilton, R.M., Smith, B.E. and Knapp, F., 1973. Earthquakes in geothermal areas near Lakes Naivasha and Hannington, Kenya. UNESCO unpublished report.

Herbert, L. and Langston, C.A., 1985. Crustal thickness estimates at AAE (Addis-Ababa, Ethiopia) and NAI (Nairobi, Kenya) using P-wave conversions. Tectonophysics, 111, 299 - 327.

Herrin, E., 1968. 1968 seismological tables for P phases. Bull. Seism. Soc. Am., 58, 1193 - 1241.

Higham, I.M., 1987. Seismic Data Processing System (version 4): User Manual. Unpublished document, Geology Department, University of Leicester.

Hill, D.P., 1971. Velocity gradients and anelasticity from crustal body wave amplitudes. J. Geophys. Res., 76, 3309 - 3325.

Jacob, A.W.B., 1975. Dispersed shots at optimum depth - an efficient seismic source for lithospheric studies. J. Geophys., 41, 63 - 70.

Jenkins, F.A. and White, H.E., 1976. Fundamentals of optics. McGraw-Hill, 4th Ed.

Kanasewich, E.R., 1975. Time Sequence Analysis in Geophysics. The University of Alberta Press, Alberta, Canada.

Khan, M.A. and Mansfield, J., 1971. Gravity measurements in the Gregory rift. Nature, 229, 72 - 75.

King, B.C. and Chapman, G.R., 1972. Volcanism of the Kenya Rift Valley. Phil. Trans. R. Soc. Lond., A 271, 185 - 208.

King, B.C., 1978. Structural and volcanic evolution of the Gregory Rift Valley. In Geological background to fossil man. (ed. Bishop, W.W.), 29 - 45. Scottish Academic Press Ltd.

Knopoff, L. and Schlue, J.W., 1972. Rayleigh wave phase velocities for the path Addis Ababa - Nairobi. Tectonophysics, 15, 157 - 163.

KRISP working group, 1987. Structure of the Kenya rift from seismic refraction. Nature, 325, 239 - 242.

Kusnir, N.J. and Park R.G., 1987. The extensional strength of the lithosphere : its dependence on geothermal gradient, and crustal compostion and thickness. In Continental extentional tectonics. Geological society special publication No 28. (ed. Coward, M.P., Dewey, J.F. and Hancock, P.L.), 35 - 52. Blackwell Scientific Publications.

Lewis, B.T.R. and Dorman, L.M., 1970. Experimental isostacy 2. J. Geopys. Res., 75, 3367 - 3386.

Lippard, S.J., 1972. The stratigraphy and structure of the Elgeyo Escarpment, southern Kamasia Hills and adjoining regions, Rift Valley Province, Kenya. Ph.D. Thesis. University of London.

Logatchev, N.A., Beloussov, V.V. and Milanovsky, E.E., 1972. East African Rift development. Tectonophysics, 15, 71 - 81.

Long, R.E. and Mitchell, M.G., 1970. Teleseismic P-wave delay time in Iceland. Geophys. J. R. astr. Soc., 20, 41 - 48.

Long, R.E., Backhouse, R.W., Maguire, P.K.H. and Sundaralingham, K., 1972. The structure of East Africa using surface wave dispersion and Durham seismic array data. Tectonophysics, 15, 165 - 178.

Long, R.E. and Backhouse, R.W., 1975. The structure of the western flank of the Gregory rift. Part II. The mantle. Geophys. J. R. astr. Soc., 44, 677 - 688.

Long, R.E., 1987. A P-wave velocity cross-section of the central Kenyan rift. Abstract. Geophys. J. R. astr. Soc., 89, 479.

Maguire, P.K.H., 1974. The crustal structure of East Africa through earthquake seismology. Ph.D. Thesis. University of Durham.

Maguire, P.K.H. and Long, R.E., 1976. The structure of the western flank of the Gregory rift (Kenya). Part I. The crust. Geophys. J. R. Astr. Soc., 44, 661 - 675.

Maguire, P.K.H. and Khan, M.A., 1980. The deep structure and dynamics of the East African Plateau, Kenya Dome and the Gregory Rift. Proc. Geol. Ass., 182, 25 - 31.

McCall, G.J.H., 1967. Geology of the Nakuru - Thompson's Falls - Lake Hanninigton area. Kenya Geol. Survey Rept. 78

McConnel, R.B., 1967. The East Africa Rift System. Nature, 215, 578 - 581.

McKenzie, D.P., Davies, D. and Molnar, P., 1970. Plate tectonics of the Red Sea and East Africa. Nature, 226, 243 - 248.

McKenzie, D.P., 1978. Some remarks on the development of sedimentary basins. Earth Planet. Sci. Lett., 40, 25 - 32.

Middleton, M.F., 1980. A model of intracratonic basin formation entailing deep crustal metamorphism. Geophys. J. R. astr. Soc., 62, 1 - 14.

Mims, C.H. and Sax, R.L., 1965. Rectilinear motion detection (REMODE).Seismic Data Laboratory Report n.118, Teledyne. Inc., Alexandria. report n.118, Teledyne. Inc., Alexandria.

Mohr, P.A., 1970. Plate tectonics of the Red Sea and East Africa. Nature, 228, 547 - 548.

Mohr, P.A., 1982. Musings on continental and oceanic rifts. In Continental and oceanic rifts. (ed. Palmason, G.), 293 - 309. Am. Geopys. Union.

Mohr, P., 1987. Structural style of continental rifting in Ethiopia: Reverse decollements. E. O. S., 68, n.35, 721 - 736.

Montadert, L., Roberts, D.G., De Charpal, O. and Guennoc, P., 1979. Rifting and subsidence of the northern continental margin of The Bay of Biscay. DSDP Initial Rept. Leg 48, 1025 - 1060.

Morelli, A. and Dziewonski, A.M., 1987. Topography of the core-mantle boundary and lateral homogeneity of the liquid core. Nature, 325, 678 - 683.

Morgan, P., 1973. Terrestrial heat flow studies in Cyprus and Kenya. Ph.D. Thesis. University of London.

Morgan, P. and Wheildon, J., 1981. Heat flow measurements across the Kenya rift. Unpublished manuscript.

Morgan,P., 1982. Heat flow in rift zones. In Continental and oceanic rifts. (ed. Palmason, G.), 107 - 122. Am. Geophys. Union.

Mueller, S. and Bonjer, K.P., 1973. Average structure of the crust and upper mantle in East Africa. Tectonophysics, 20, 283 - 293.

Nafe, J.E. and Drake, C.L., 1957. Variations with depth in shallow and deep water marine sediments of porosity, density and the velocities of compressional and shear waves. Geophysics, 22, 523 - 552.

O'Brien, P.N.S., 1960. Seismic energy from explosions. Geophys. J., 3, 29 - 44.

Olsen, K.H., Keller, G.R. and Stewart, J.N., 1979. Crustal structure along the Rio Grande rift from seismic refraction profiles. In Rio Grande Rift: Tectonics and Magmatism. (ed. Riecker, R.E.), 127 - 144. Am. Geophys. Union.

Olsen, K.H., Cash, D.J. and Stewart, J.N, 1982. Mapping the northern and eastern extent of the Socorro midcrustal magma body by wide-angle seismic reflections. New Mexico Geological Society Guidebook.

Olsen, K.H., 1983. The role of seismic refraction data for studies of the origin and evolution of continental rifts. Tectonophysics, 94, 349 - 370.

Pointing, A.J., 1985. Seismicity and lithospheric structure of Northern Kenya. Ph.D. Thesis. University of Leicester.

Pointing, A.J., Maguire, P.K.H., Khan, M.A., Francis, D.J., Swain, C.J., Shah, E.R., and Griffiths, D.H., 1985. Seismicity of the northern part of the Kenya rift valley. J. Geodynamics, 3, 23 - 27.

Prodehl, C., 1981. Structure of the crust and upper mantle beneath the central European rift system. Tectonophysics, 80, 255 - 269.

Puzirev, N.N., Mandelbaum, M.M., Krylov, S.V., Mishenkin, B.P., Krupskaya, G.V. and Petrik, G.V., 1978. Deep structure of the Baikal and other continental rift zones from seismic data. Tectonophysics, 45, 15 - 22.

Rabiner, L.R. and Gold, B., 1975. Theory and application of digital signal processing. Prentice-Hall, Inc., New Jersey.

Raitt, R.R., Shor, G.G., Francis, T.J.G. and Morris, G.B., 1969. Anisotropy of the Pacific Upper Mantle. J. Geophys. Res., 74, 3095 - 3109.

Reasenberg, P., Ellsworth, W. and Walter, A., Teleseismic evidence for a low-velocity body under the Coso geothermal area. J. Geophys. Res., 85, 2471 - 2483.

Robinson, E.A., 1967. Multichannel Time Series Analysis with Digital Computer Programs. Holden-Day, San Fransisco.

Robinson, R. and Iyer, H.M., 1981. Delineation of a low-velocity body under the Roosevelt Hot Springs geothermal area, Utah, using teleseismic P-wave data. Geophysics, 46, 1456 - 1466.

Rooney, D. and Hutton, V.R.S., 1977. A magnetotelluric and magnetovariational study of the Gregory Rift Valley, Kenya. Geophys. J. R. astr. Soc., 51, 91 - 119.

Rosendahl, B.R., Reynolds, P.M., Lorber, P.M., Burgess, C.F., McCill, J., Scott, D., Lambiase, J.J. and Derksen, S.J., 1986. Structural expressions of rifting: lessons from Lake Tanganyika, Africa. In Sedimentation in the African Rifts, Geological Society Special Publication No. 25, 29 - 43.

Rosendahl, B.R., 1987. Architecture of continental rifts with special reference to East Africa. Ann. Rev. Earth. Planet. Sci., 15, 445 - 503.

Rothe, J.P., 1954. La Zone Seismique mediane Indo - Atlantique. Proc. R. Soc. London., A222, 387 - 397.

Rykounov, L.N., Sedov, V.V., Savrina, L.A. and Bourmin, V.J.U., 1972. Study of microearthquakes in the rift zones of East Africa. Tectonophysic, 15, 123 - 130.

Savage, J.E.G., 1979. A seismic investigation of the lithosphere of the Gregory Rift. Ph.D. Thesis. University of Durham.

Savage, J.E.G. and Long, R.E., 1985. Lithospheric structure beneath the Kenya dome. Geopys. J. R. astr. Soc., 82, 461 - 477.

Searle, R.C., 1970. Evidence from gravity anomalies for thinning of the lithosphere beneath the rift valley in Kenya. Geophys. J. R. astr. soc., 21, 13 - 31.

Searle, R.C., 1970. Lateral extension in the East African rift valleys. Nature, 227, 267 - 268.

Shah, E., 1986. Seismicity of Kenya. Ph.D. Thesis. University of Kenya.

Shudofsky, G.N., 1984. Source mechanisms and focal depths of East African earthquakes and Rayleigh phase velocities in Africa. Ph.D. Dissertation. Princeton University.

Smith, T.J., Steinhart, J.S. and Aldrich, L.T., 1966. Lake Superior crustal structure. J. Geophys. Res., 71, 1141 - 1172.

Sowerbutts, W.T.C., 1969. Crustal structure of the East African Plateau and rift valleys from gravity measurements. Nature, 223, 143 - 146.

Sundaralingham, K., 1971. A seismic investigation of the crust and upper mantle of East Africa. Ph.D. Thesis. University of Durham.

Swain, C.J., 1979. Gravity and seismic measurements in Kenya. Ph.D. Thesis. University of Leicester.

Swain, C.J., 1976. Some gravity results from the northern Gregory rift. In Afar between continental and oceanic rifting. (ed. Pilger A. and Rosler A.), 120 -125. Stuttgart.

Swain C.J. and Khan, M.A., 1977. Kenya: A Catalogue of Gravity Measurements. Unpublished catalogue, University of Leicester.

Swain, C.J., Khan, M.A., Wilton, T.J., Maguire, P.K.H. and Griffiths, D.H., 1981. Seismic and gravity surveys in the Lake Baringo - Tungen Hills area, Kenya rift valley. J. Geol. Soc. Lond., 138, 93 - 102.

Telford, W.M., Geldhart, L.P., Sheriff, R.E. and Keys D.A., 1976. In Applied Geophysics, p.61. Cambridge University Press.

Turcotte, D.L. and Emerman, S.H., 1983. Mechanisms of active and passive rifting. Tectonophysics, 94, 39 - 50.

Walsh, J., 1969. Geology of the Eldama Ravine-Kabarnet area. Kenya Geol. Survey Rept. 42.

Wernicke, B. and Burchfiel, B.C., 1982. Modes of extensional tectonics. J. Struct. Geol., 4, 105 - 115.

Whitcombe, D.N., 1979. Seismic studies of the upper crust in Central England. Ph.D. Thesis. University of Leicester.

Whitecombe, D.N. and Maguire, P.K.H., 1979. The response of the time-term method to simulated crustal structures. Bull. Seism. Soc. Am., 69, 1455 - 1473.

Williams, L.A.J., 1970. The volcanics of the Gregory Rift Valley, East Africa. Bull. Volc., 34, 439 -465.

Williamson, K.H., 1975. Terrestrial heat flow studies in Kenya. Ph.D. Thesis. University of London.

Willmore, D.L. and Bancroft, A.M., 1960. The time-term approach to refraction seismology. Geophys. J. R. astr. Soc., 3, 419 - 432.

Wohlenberg, J. and Bhatt, N.V., 1972. Report on airmagnetic surveys of two areas in the Kenya rift valley. Tectonophysics, 15, 143 - 149.

Wohlenberg, J., 1975. Geophysikalische aspekte der ostrafrikanischen graenzonen. Geologisches Jahrbuch, Hannover.

Wright, J.B., 1967. Geology of the Narok area. Kenya Geol. Survey Rept. 80.

Young, J.B. and Gibbs, P.G., 1968. A series of computer programs for deriving information at selected seismic recording sites, for signals from unknown hypocentres. AWRE Report No. 54/68 GEDESS.

Zoeppritz, K., 1919. Uber reflexion und durchgang seismischer wellen durch Unstetigkerlslaschen. Berlin, Uber Erdbebenwellen VII B, Nachrichten der Koniglichen Gesellschaft der Wissenschaften zu Gottingen, math-phys. K1., 57 - 84.